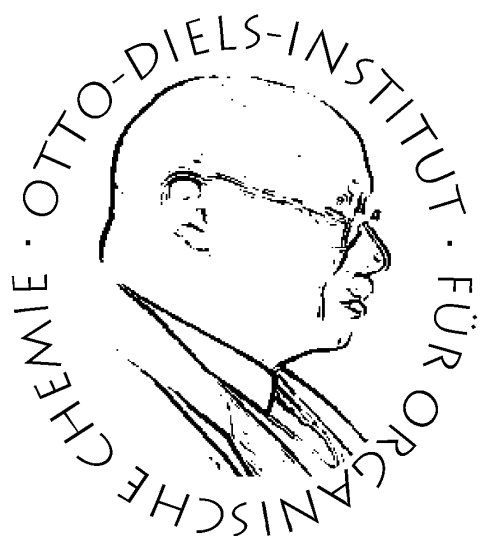


In Silico Design funktionaler Moleküle: Vorhersage und Erklärung molekularen Verhaltens durch Dichtefunktionaltheorie



Dissertation

zur Erlangung des Doktorgrades
der Mathematisch-Naturwissenschaftlichen Fakultät
der Christian-Albrechts-Universität
zu Kiel

vorgelegt von

Fynn Röhricht

Otto Diels-Institut für Organische Chemie
Kiel 2022

Erster Gutachter: Prof. Dr. Rainer Herges
Zweiter Gutachter: Prof. Dr. Frank Sönnichsen

Tag der mündlichen Prüfung: 03. März 2023
Zum Druck genehmigt: 03. März 2023

Die vorliegende Arbeit wurde unter der Anleitung von
Prof. Dr. Rainer Herges
in der Zeit von
Juli 2017 bis Februar 2022
am Otto Diels-Institut für Organische Chemie der
Christian-Albrechts-Universität zu Kiel
angefertigt.

Diese Arbeit ist zu Teilen durch Förderung des
Sonderforschungsbereichs 677 – "Funktion durch Schalten" entstanden.

Hiermit erkläre ich, Fynn Röhricht, an Eides statt, dass ich die vorliegende Doktorarbeit selbstständig und nur mit den angegebenen Hilfsmitteln angefertigt habe. Diese Dissertation ist nach Inhalt und Form - abgesehen von der Beratung durch meinen Betreuer Prof. Dr. Rainer Herges - durch mich eigenständig nach den Regeln guter wissenschaftlicher Praxis der Deutschen Forschungsgemeinschaft verfasst worden. Sie hat weder in Auszügen noch in ganzer Form einer anderen Stelle im Rahmen eines Prüfungsverfahrens vorgelegen. Mir wurde kein akademischer Grad aberkannt. Es handelt sich um meinen ersten Promotionsversuch.

Kiel, 4. Mai 2023

Fynn Röhricht

Danksagung

Bei Ihnen bedanke ich mich klar als erstes: Vielen Dank Herr Herges für die Möglichkeit, eine Doktorarbeit mit so unterschiedlichen und interessanten Projekten erarbeiten und schlussendlich abgeben zu können. Besonders für die Hilfestellung und Motivation auf den schweren letzten Metern bin ich Ihnen sehr dankbar. Auch möchte ich hier Herrn Sönnichsen einen großen Dank für das Zweitgutachten zu meiner Arbeit aussprechen.

Reichlich bedanken möchte ich mich unbedingt bei allen Kooperationsbeteiligten, die mir sehr viele interessante Einblicke in die chemische Forschung und zusätzlich auch erfolgreiche Publikationen beschert haben. Großer Dank gilt auch den Korrektoren! Ihr habt mich und vor allem die Arbeit sehr viel weitergebracht. Danke, natürlich auch jedem aus der Uni, der die eine oder andere Hilfestellung, Diskussion, Kaffeepause und FABs mit mir geteilt hat =) I miss this! Ihr habt mir die Zeit aller bestens versüßt!!

An nächster Stelle danke ich meinem mir sehr wichtigen, privaten Umfeld: Ohne Family und langjährige Freunde geht es einfach für mich nicht. Ihr gebt mir unglaublich viel Kraft und seid immer mein Ausgleich! Ich bin wirklich sehr froh euch zu haben!

Nun zum Schluss folgen nochmal drei direkte Nennungen: Danke dir Nele fürs Aushalten und immense Motivieren. Du machst mich einfach ganz und ich freue mich auf die Zukunft mit dir! Eigentlich am wichtigsten: Danke Mama & Papa - you made me Doktor - sogar vor Papa ;-)



Kurzdarstellung

In dieser Dissertation wurden unterschiedliche Methoden der Dichtefunktionaltheorie verwendet, um eine Reihe von funktionalen Moleküle quantenmechanisch zu beschreiben. Dabei reichen die Themen vom Design neuer Verbindungen über die Vorhersage thermodynamischer, elektronischer und photophysikalischer Eigenschaften bis zur Erklärung von experimentellen Phänomenen. Der Hauptfokus der Arbeit liegt auf der Untersuchung und Entwicklung von Azo-basierten Photoschaltern. So konnte die durch Goldoberflächen beschleunigte Relaxation von Azobenzol (AB) aufgeklärt werden. Diese Spin-Switch-Katalyse konnte durch intelligentes Moleküldesign und die somit einstellbare Kopplung zur Oberfläche nachgewiesen werden. AB erfährt bei ausreichernder Kopplung zum Leitungsband des Substrates ein *intersystem crossing* und die Relaxation wird nicht mehr adiabatisch, sondern durch die quantenmechanische Durchtrittswahrscheinlichkeit bestimmt. Um zu untersuchen, ob dieser Mechanismus auch für ähnliche Systeme gilt, wurden weitere Konzepte entwickelt und experimentell untersucht. Darunter kamen Diazocine (DACs) zum Einsatz, welche eine inverse thermische Stabilität aufweisen. Diese relativ junge Klasse an Schaltern zeigt photophysikalische Eigenschaften, die denen von AB teilweise überlegen sind. So sind nicht nur photostationäre Zustände, Quantenausbeuten und Konversionsraten besser, sondern auch die relevanten *trans*-Absorptionsbanden in das bio-optische Fenster (600 - 900 nm) verschoben. Insbesondere durch die letzte Eigenschaft birgt diese Verbindungsklasse großes Potential für die Anwendung als Pharmakophor. Da das Stammsystem jedoch einige Schwachstellen bezüglich Synthese und Substitution aufweist, wurden in dieser Arbeit durch quantenchemische Rechnungen verschiedene neue DACs entwickelt. Dabei konnte durch berechnete Ringspannungen nicht nur abgeschätzt werden, ob die Zielverbindungen synthetisierbar sind, sondern auch gleichzeitig die thermodynamische Charakterisierung der Systeme vorgenommen werden. Zudem konnten stark separierte, bis in den nahen Infrarot-Bereich reichende Absorptionsbanden vorhergesagt und experimentell bestätigt werden. Außerdem konnte durch die quantenmechanische Untersuchung des konformationellen Raums der Konfigurationen und durch spektroskopische Experimente die Schaltmechanismen der neuen Schalter aufgeklärt werden. Um die Geometrien und auch die Energien möglichst adäquat zu beschreiben, wurden verschiedene Kombinationen aus Funktionalen und Basissätzen angewandt. So konnte anhand der experimentellen Isomerisierungsenthalpie von AB als verwandtes System und über einen Strukturabgleich mit erhaltenen Einkristallen ein guter Kompromiss zwischen Rechenaufwand und Genauigkeit für die quantenmechanische Beschreibung von DACs ermittelt werden. Neben der Untersuchung von Photoschaltern wurde die Anisotropie der induzierten Stromdichte (ACID) Methode verwendet, um verschiedene Konzepte von elektronischer Delokalisierung aufzudecken und zu beweisen. Durch die quantitative und qualitative Auswertung mittels ACID konnte so die Stereo- und Regiochemie von Diels-Alder-Reaktionen an Porphyrinen und Derivaten vorausgesagt und erklärt werden. Zusätzlich half die Methode, Aromatizität in dreifach verdrillten Möbiusstrukturen nachzuweisen sowie Konjugation durch den freien Raum ohne kovalente Bindung visuell aufzuzeigen und somit zu belegen.

Abstract

In this thesis, different DFT methods were used to describe a number of functional molecules quantum mechanically. The topics range from the design of new target molecules and the prediction of their thermodynamic, electronic and photophysical properties, up to the explanation of experimental phenomena. The work is mainly focussed on the investigation and development of azo-based photoswitches. Thus, the relaxation mechanism of azobenzene (AB) accelerated by gold surfaces could be elucidated. This spin-switch catalysis was proven by sophisticated molecular design and the tunable electronic coupling to the surface. Upon coupling to the conduction band of the substrate, AB undergoes an intersystem crossing and the relaxation rate is no longer defined adiabatically by an activation barrier but rather by the quantum mechanical transition probability. In order to investigate whether this mechanism is also applicable to similar systems, further concepts were developed and investigated. Particularly diazocines (DACs) were used, which have an inverse thermal stability. This relatively young class of switches exhibits photophysical properties that are superior to those of ABs. Not only photostationary states, quantum yields and conversion rates are higher, but also the relevant *trans*-absorption bands are shifted into the bio-optical window (600 - 900 nm). Due to the latter property in particular, this class of compounds has a great potential for the use as pharmacophores. To enlarge the range of applications, a number of DAC derivatives were designed and their properties were calculated prior to synthesis in the laboratory. By calculating their ring strain and energies of configurations and conformations the systems were characterized. In addition strongly separated absorption bands reaching into the near infrared region could be predicted and confirmed experimentally after synthesis. In collaboration with spectroscopic experiments, the quantum mechanical analysis of the conformational and configurational space was used to elucidate the switching mechanism of these compounds. To describe the geometries and energies as accurate as possible, various combinations of density functionals and basis sets were benchmarked. Using the experimental isomerisation enthalpy of AB as a closely related system and by comparing the calculated geometries with data from crystal structure analysis, a good compromise between computational effort and accuracy was established.

In an independent project, the anisotropy of the induced current density (ACID) method was used to elucidate and prove different concepts of electronic delocalization. Through the quantitative and qualitative ACID evaluation, the stereo- and regiochemistry of Diels-Alder reactions with porphyrins and derivatives was predicted and explained. Furthermore, the method helped to detect aromaticity in triple twisted Möbius structures and to visually demonstrate and thus prove conjugation through space without covalent bonds.

Inhaltsverzeichnis

1 Einleitung	1
1.1 Molekulare Maschinen	1
1.2 Photoresponsive Schalter	2
1.3 Chemoinformatik	4
2 Aufgabenstellung	9
3 Diazocine	11
3.1 Modifikation des Stamm-Diazocins	12
3.2 Stickstoffverbrückte DACs	14
3.3 Nitrogen Bridged Diazocines: Photochromes Switching within the Near-Infrared Region with High Quantum Yields in Organic Solvents and in Water	15
3.4 Gerichtete Schaltung und erhöhte Effizienz	27
3.5 Efficient Conversion of Light to Chemical Energy: Directional, Chiral Photoswitches with Very High Quantum Yields	28
4 Funktionalisierte Oberflächen	37
4.1 Azobenzol auf Gold(111)	37
4.2 Long-Distance Rate Acceleration by Bulk Gold	40
4.3 Inverse Schaltung auf Gold	47
4.4 Diazocine-functionalized Triazatriangulen (TATA) platforms	48
4.5 Alternative Oberflächenfunktionalisierung	56
4.6 Ordered Adlayers of a Combined Lateral Switch and Rotor	57
5 ACID - Das Multifunktionstool	71
5.1 Porphyrine und Derivate	72
5.2 One-Pot Approach to Chlorins, Isobacteriochlorins, Bacteriochlorins, and Pyrrocophins	73

Inhaltsverzeichnis

5.3	MÖBIUS Topologie und Aromatizität	81
5.4	Cyclic tris-[5]helicenes with single and triple twisted Möbius topologies and Möbius aromaticity	83
5.5	Erweiterte π -Systeme	92
5.6	Twisted Thienylene–Phenylene Structures: Through-Space Orbital Coupling in Toroidal and Catenated Topologies	93
6	Sonstige Publikationen in chronologischer Reihenfolge	105
7	Zusammenfassung und Ausblick	109
7.1	Neue Photoschalter	109
7.2	Schaltverhalten auf Oberflächen	114
7.3	Konzepte von Delokalisierung und Aromatizität	117
8	Anhang	123

1

Einleitung

1.1 Molekulare Maschinen

Anfangen mit dem Zeitalter der Aufklärung und durch die Weiterentwicklung naturwissenschaftlicher Theorien in der industriellen Revolution kann mittlerweile nahezu jeder makroskopische Prozess durch Maschinen erledigt werden. Dem gegenüber stehen die uralten und unverzichtbaren mikroskopischen Maschinen der biologischen Evolution. So wird auf molekularer Ebene in der Photosynthese Sonnenenergie genutzt,^[1,2] in Adenosintriphosphat (ATP) Energie gespeichert,^[3,4] Kraft ausgeübt und Fracht transportiert^[5–8] sowie repliziert, translatiert und transkribiert.^[9–11] In der Gegenwart versucht sich der Mensch nun artifiziell dieser mikroskopischen Ebene mit zwei verschiedenen Ansätzen zu nähern. Einer der Ansätze, die Miniaturisierung von makroskopischen Maschinen, das Verkleinerungsprinzip oder auch *top-down approach* genannt, ist längst Teil der Realität geworden und war im 20. Jahrhundert die vorherrschende Strategie für ganze Industriezweige wie z.B. die Mikroelektronik und Halbleiter-technik. Die Revolution der Mikroelektronik basiert auf diesem Konzept, stößt aber mittlerweile an physikalische Grenzen.^[12,13] Mit immer kleiner werdenden Chips ergeben sich immer größere Probleme wie z.B. bei der Hitzeableitung und Materialauswahl sowie grundsätzlich im Herstellungsprozess.^[14] Diese noch mit dem *top-down approach* eingeläutete Nano-Technik ist eine der Schlüsseltechnologien des 21. Jahrhunderts. Die moderne Analytik und die neuen Synthesemethoden der Chemie bilden die Grundlage für das Vergrößerungsprinzip (*bottom-up approach*).^[15,16] Dieser Ansatz geht davon aus, dass basierend auf kleinsten Teilchen (Atomen oder Molekülen) Strukturen für funktionelle Anwendung generiert werden können. Aus diesem Zusammenhang leitet sich der Begriff molekulare Maschine ab. Diese Konstruktionseinheiten werden durch eine festgelegte Anordnung von Molekülen definiert, welche auf externe Stimuli maschinenähnlich reagieren. So entwickelten Chemiker in den letzten vier Jahrzehnten Prototypen mit anfänglich einfachen Funktionen wie der lichtgesteuerten selektiven Bindung von Alkalimetallkationen in Kronethern,^[17] dem molekularen Shuttle^[18] und der Rotationsbewegung.^[19,20] Auf dieser Grundlage wurden kompliziertere Funktionseinheiten aufgebaut und Aufzüge,^[21,22] Autos,^[23,24] Scheren,^[25] Muskeln,^[26–28] und sogar ein eigenständiger Peptid-synthesizer^[29,30] realisiert. Dieses wichtige Teilgebiet der chemischen Forschung ist spätestens seit dem Nobelpreis 2016 für SAUVAGE, STODDART und FERINGA mit ihrem Design und der

Synthese künstlicher molekularer Maschinen^[31] auch außerhalb der Forschung in der breiten Öffentlichkeit angekommen.^[8,32–36]

1.2 Photoresponsive Schalter

Allen mikroskopischen Maschinen liegt das gleiche Prinzip wie ihrem makroskopischen Vorbild zu Grunde. Auf einen geeigneten Stimulus (Input) folgt eine Reaktion (Output), manchmal als Änderung der elektronischen Struktur, oft als einfache mechanische Bewegung.^[32] Bekannte chemisch bzw. physikalisch umsetzbare Stimuli sind pH-Wert- und Temperaturänderungen sowie elektronisch oder licht-induzierte Impulse.^[35] So lassen sich ein Vielzahl organischer Verbindungsklassen z.B. Spiropyrone, Stilbene, Diarylethene, Fulgide, Norbornadiene und Azobenzole (ABs) durch Licht geeigneter Wellenlängen zwischen verschiedenen Isomeren schalten.^[34]

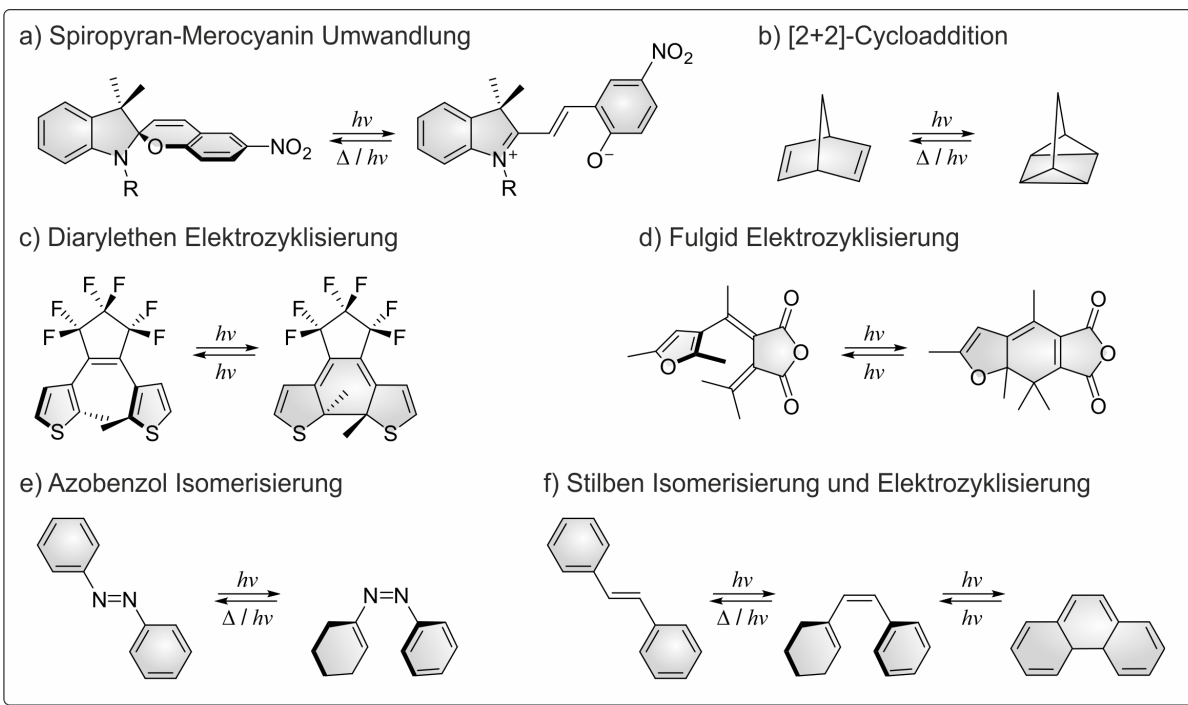


Abb. 1.1: Repräsentative Beispiele photoresponsiver molekularer Schalter. a) Umwandlung des Spiropyrans mit UV-Licht zu seiner in polaren Lösungsmitteln stabilen, zwitterionischen Merocyaninform. b) Die photochemisch erlaubte [2+2] Cycloaddition führt mittels UV-Licht zum Quadricyclan, welches photochemisch, thermisch und katalytisch Cycloreversion eingehen kann. c) Diarylethene unterliegen photochemisch einer reversiblen Elektrocyclisierung des zentralen Hexatriens zum Cyclohexadien. Thermisch ist die Reversion nicht möglich. d) Wie bei den Diarylethenen ist eine photochemische reversible Elektrocyclisierung sowie zusätzlich die *cis/trans*-Isomerisierung um die Doppelbindung möglich. e+f) Die *trans*-Konfiguration der Doppelbindung kann mit UV-Licht zum metastabilen *cis*-Isomer überführt werden. Stilbene können zusätzlich zum Dihydrophenanthren elektrocyclisieren.

Diese durch die photoinduzierte Isomerisierung erlangte strukturelle Veränderung entspricht makroskopisch gesehen einer mechanischen Bewegung. Dabei basieren die Umwandlungen

der Spiropyrone auf einer Interkonversion zum Merocyanin,^[37–39] Diarylethene^[40–43] und Fulgide^[44,45] auf einer Elektrocyclisierung zur geschlossenen Form, Norbornadiene auf der [2+2]-Cycloaddition zu Quadricyclanen^[46,47] und Stilbene^[48–51] sowie ABs^[52] auf der *cis/trans*-Isomerisierung der Doppelbindung (Abb. 1.1). Das besonders populäre AB z.B. kann mit UV-Licht der Wellenlänge 365 nm von der stabilen *trans*- zur metastabilen *cis*-Konfiguration geschaltet werden. Die Rückisomerisierung erfolgt thermisch oder mit Photonen der Wellenlänge 400 nm.^[53–57]

Die oben genannten Photoschalter sind seit Jahrzehnten in verschiedensten Variationen bekannt und ausführlich charakterisiert, die lichtinduzierten strukturellen Veränderungen sind jedoch klein. 1999 wurde dann die Umwandlung von Licht in mechanische Arbeit noch einmal deutlich komplexer umgesetzt.^[31] Die Entwicklung eines Motors auf Basis eines stark gehinderten Alkens (Abb. 1.2) ermöglichte durch axiale Chiralität erstmals eine unidirektionale 360° Drehung auf molekularer Ebene.^[20]

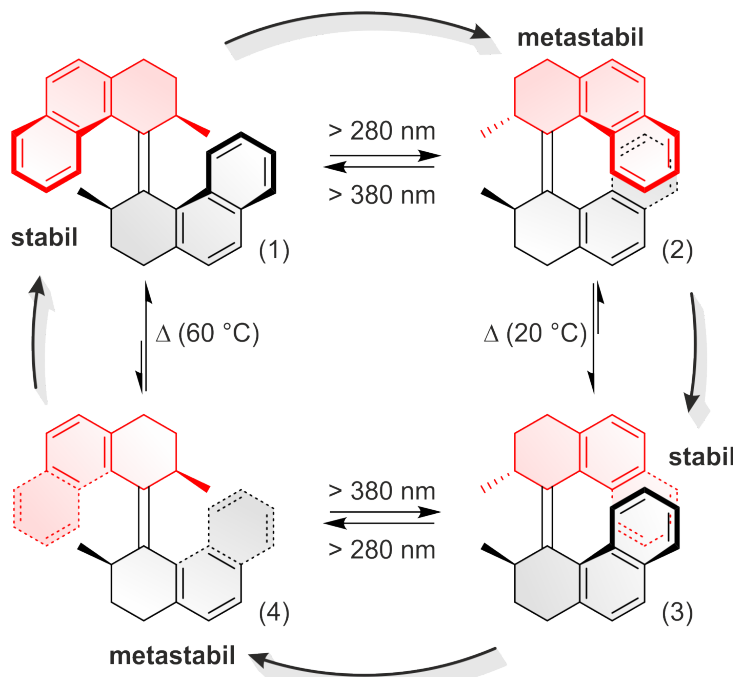


Abb. 1.2: FERINGA's lichtbetriebener molekularer Motor mit unidirektionaler 360°-Drehung dank axialer Chiralität: startend bei der thermodynamisch stabilen (*P,P*)-*trans*-Form (1) erfährt der Motor durch Licht der Wellenlänge $> 280 \text{ nm} < 380 \text{ nm}$ die Isomerisierung zur metastabilen (*M,M*)-*cis*-Konfiguration (2). Diese formt sich zum thermodynamisch stabileren (*P,P*)-*cis*-Isomer (3) um und kann erneut durch Licht mit gleicher Wellenlänge (wie in (1)→(2)) zur metastabilen (*M,M*)-*trans*-Konfiguration (4) isomerisieren. Dieses Isomer relaxiert bei 60 °C und der Rotationsprozess ist abgeschlossen.

All diese Photoschalter sind für sich gesehen noch keine anwendbaren Maschinen, sondern eher als molekulare Bauteile mit maschinenartigem Charakter zu verstehen. Diese können durch externe Stimuli Aufgaben wie z. B. eine direktionale mechanische Bewegung erledigen, eine ganzheitliche Maschine jedoch vereint eine weitere elementare Funktion. Neben dem Energieeintrag, der sie antreibt, der Bewegung der Einzelteile, ihrer Kontrolle und Nachverfolgung, ihrer cyclischen

Wiederholbarkeit und deren Dauer steht eine Anwendung zwangsläufig klar im Fokus.^[32] So ist die Verwendung der Photoschalter im Design hin zu einer zweckmäßigen Maschine je nach gewünschter Anwendung eines der zentralen Forschungsgebiete vieler Arbeitskreise.

1.3 Chemoinformatik

Das Design neuer, funktionaler, molekularer Systeme gehört mit zu den bedeutendsten Aufgaben eines Chemikers. Um so ein Design effektiv zu entwickeln, bedarf es neben viel chemischem Verständnis einer Idee der Anwendung oder falls gewünscht der ganzen Maschine selbst. So ist der Blick zu evolutionär entwickelten, molekularen Maschinen und die Nachahmung solcher von Vorteil.^[58] Die Aufklärung der Funktionsweise und das dadurch gewonnene Verständnis kann so in der Entwicklung und im Design gewinnbringend eingesetzt werden.^[59] Auch die Möglichkeit, vorhandene Systeme zu variieren, ist gängig und zielführend. Aber wie genau das neue Molekül oder die ganze Maschine detailliert und erfolgreich designt werden soll, ist meistens die herausfordernde Fragestellung. Genau deshalb greifen viele Forscher, nicht zuletzt um Arbeitszeit und Material zu sparen, sondern vielmehr um gezielt spezielle Funktionen oder Eigenschaften von molekularen Bauteilen zu verändern oder ganze Maschinen zu konzeptionieren, auf theoretische Methoden zurück.^[60–62] Aus diesen Bemühungen hat sich das Forschungsgebiet der Chemoinformatik hervorgetan, in welchem u. A. die sogenannte Computerchemie Einsicht in die strukturellen und nahezu alle physikalischen Eigenschaften der zu untersuchenden Systeme geben kann. Darüber hinaus können dynamische Einflüsse und Wechselwirkungen mit anderen Molekülen oder Oberflächen simuliert werden. Die Qualität der Ergebnisse hängt dabei stark von der Genauigkeit der ausgewählten Rechenmethode ab. Dabei ist die Auswahl der Methode und innerhalb dieser die Wahl des Niveaus (*level of theory*) nicht trivial. Die Rechenzeit und somit die Kosten der Rechnungen hängen entscheidend von der Größe des zu untersuchenden Systems und den vorhandenen technischen Möglichkeiten ab. Das heißt, je kleiner ein System ist, desto präzisere Methoden und Niveaus können in annehmbarer Zeit bei gleicher technischer Ausstattung verwendet werden. Somit korreliert die Qualität der Ergebnisse direkt mit der aufgewandten Rechenzeit der gewählten Methode bzw. des Niveaus.^[63–65]

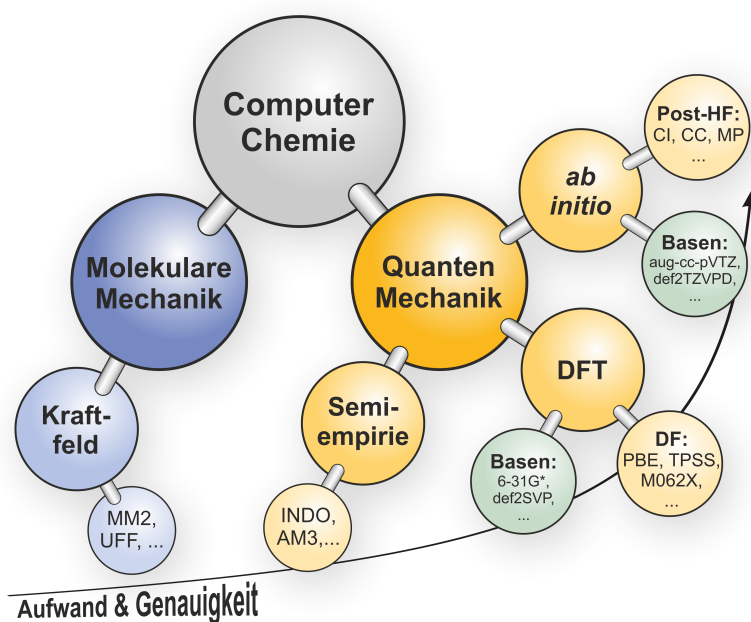


Abb. 1.3: Schematische Darstellung der verschiedenen Methoden der Computerchemie: Der Aufwand (Kosten bzw. Zeit) aber auch die Genauigkeit der angewandten Methoden steigt von links nach rechts oben.

Die Methoden der Computerchemie spalten sich dabei (s. Abb 1.3) grundsätzlich in zwei Gebiete auf: Die molekulare Mechanik (MM) ist der klassisch physikalische Ansatz, in dem Atome wie Kugeln mit bestimmter Masse und Ladung über Federn miteinander verbunden sind. Die Beschreibung des Systems basiert auf parametrisierten Termen, die Bindungsenergien beschreiben und in einem Kraftfeld zusammengefasst sind. Mit den Gesetzen von NEWTON und HOOK kann dann zusätzlich eine Dynamik betrachtet werden. Dies reicht aber nicht aus, um chemische Reaktionen zu beschreiben. Die Methode ist mit aktueller Hardware sehr schnell und ermöglicht Rechnungen mit mehreren Millionen Atomen wie z. B. ganzen Enzymen und wird so häufig für strukturelle Aufklärung von Proteinen etc. eingesetzt. Bindungsbrüche, Aromatizität und angeregte Zustände können mit der MM jedoch nicht beschrieben werden. Diese Methode ist zu simpel und somit inadäquat, um exakte Vorhersagen von kleinen molekularen Bauteilen und deren Verhalten gegenüber externen Stimuli vorherzusagen.

Das zweite Gebiet wird durch die Quantenmechanik (QM) beschrieben. Grundsätzlich basieren hier alle Methoden auf der Lösung der SCHRÖDINGER-Gleichung, sind demnach exakt und kommen ohne empirische Parameter aus. *Ab initio*-Methoden berücksichtigen die Wechselwirkungen der Kerne und Elektronen im Molekülen auf Basis der Quantenmechanik und erlauben so, das Knüpfen und Brechen von Bindungen und angeregte Zustände zu beschreiben. Daher können auch Reaktionen und Verhalten auf äußere Stimuli beschrieben werden, was sie zu idealen Kandidaten für das Entwickeln neuer funktionaler Molekülstrukturen macht. Der hohe Anspruch an die Genauigkeit wird jedoch mit einer sehr hohen Rechenzeit bezahlt. Daher sind solche Methoden nur für relativ kleine Systeme anwendbar. Um mittelgroße Systeme in

annehmbarer Zeit adäquat zu beschreiben, wurden verschiedene Vereinfachungen der *ab initio*-Methode entwickelt. Den im Vergleich einfachste Ansatz der QM stellt die semiempirische Methode dar. Diese basiert auf HARTREE-FOCK (HF)-Rechnungen, wobei bestimmte Integrale durch Approximationen ersetzt oder weggelassen werden. Um die dadurch entstanden Fehler zu kompensieren, ist eine Parametrisierung eingearbeitet, welche auf einen Molekülsatz empirisch angepasst wurde.^[66] Diese Annäherungen machen die Methode extrem schnell, jedoch auch fehleranfällig gegenüber Systemen, die nicht gut parametrisiert sind.^[67]

Einen guten Kompromiss zwischen Rechenaufwand und Genauigkeit stellt die Dichtefunktionaltheorie (DFT) dar.^[68,69] Die Grundlagen dieser Theorie sind die Arbeiten von KOHN und SHAM (KS), welche zeigten, dass die Grundzustandsenergie ausschließlich von der Elektronendichte abhängt.^[70,71] Das exakte Dichtefunktional, welches unbekannt ist und somit genähert werden muss, sollte die exakte Lösung der SCHRÖDINGER-Gleichung für einen Bruchteil der Rechenzeit einer aufwendigen Elektronenkorrelations-, Wellenfunktions-basierten Rechnung darstellen.^[69,72] Ausschlaggebend für die Qualität dieser Näherung ist die Elektron-Elektron-Wechselwirkung, welche durch Austausch-Korrelations-Funktionale (E_{XC}) approximiert werden muss.^[73–75] Im Laufe der DFT-Entwicklung entstanden verschiedene komplexe Annäherungen an diesen Term, welche kategorisch in der Jakobsleiter (Abb. 1.4) zusammengefasst sind.^[76]

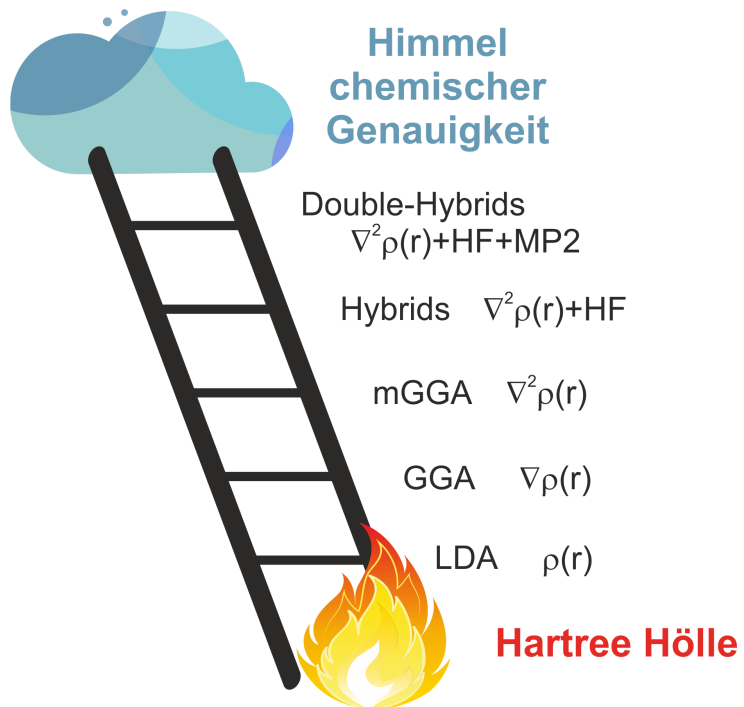


Abb. 1.4: Die Jakobsleiter (nach GOERIGK *et al.*^[69]) zeigt schematisch die Klassifizierung verschiedener Dichtefunctionale. Die Leiter verbindet die HARTREE-Hölle mit dem Himmel der chemischen Genauigkeit.

Die Leiter verbindet dabei die sogenannten HARTREE-Hölle, bei der keine Elektronenwechselwirkungen beschrieben werden, mit dem Himmel chemischer Genauigkeit. Dies bedeutet für

einen Chemiker nicht zwingend die exakte Lösung der SCHRÖDINGER-Gleichung, vielmehr reichen hier akkurate Vorhersagen von Reaktionsenergien oder -barrieren von ca. 1 kcal mol^{-1} , nicht kovalenten Wechselwirkungen von $0.1 \text{ kcal mol}^{-1}$ und Anregungsenergien von 0.1 eV .^[69] Der niedrigste Rang der Leiter wird mit den *local density approximation* (LDA) Funktionalen besetzt. Hier basiert das Austausch-Korrelations-Funktional auf der Austauschwechselwirkung der Partikel im homogenen Elektronengas. Die Elektronendichte in Molekülen ist jedoch kein homogenes Elektronengas, sodass verschiedene Korrekturen eingearbeitet wurden. Die *generalised gradient approximation* (GGA), welche den zweiten Rang darstellt, basiert nicht nur auf der Dichte, sondern beinhaltet nun einen Gradienten dieser ($\nabla\rho$). Hier hängt das Funktional nicht allein von dem Abstand der Teilchen untereinander sondern zusätzlich auch von der Bewegung der Dichte ab.^[77] Bekannte Vertreter der GGAs sind BLYP^[78–80] und PBE,^[81] welche mit vielerorts vorhandener Hardware (ca. 500 GFlops) bereits annehmbar akkurate Geometrien für eine Vielzahl von Systemen bis zu hundert Atomen in kurzer Zeit berechnen können. Mit der nächsten Stufe der *meta-GGA* kommt zusätzlich eine höhere Ableitung der Dichte ($\nabla^2\rho$) und/oder die kinetische Energiedichte der Orbitale (τ) hinzu. Populäre Funktionale sind TPSS^[72] oder M06L,^[82] welche nur geringfügig mehr Genauigkeit bringen, aber im gleichen Maße wenig Mehrkosten verursachen. Diese ersten drei Ränge sind (semi)-lokal, da sie die Elektronendichte ausschließlich an bestimmten Punkten und in ihrer nächsten Umgebung mit lokalen Funktionen beschreiben. Die exakte Austausch-Korrelations-Energie ist aber kein lokales Phänomen und muss demnach anders gelöst werden. Auf dem vierten Rang wird dieses Problem mit einer Kombination aus (semi)-lokalen Dichtefunktionalen und klassisch non-lokalem HF-Austausch angegangen.^[77,83,84] Diese Hybridfunktionale, wie z. B. PBE0,^[85,86] B3LYP^[87] oder M062X^[88] sind rechnerisch deutlich aufwendiger, erzielen jedoch häufig für beispielsweise Reaktionsenergien oder -barrieren schon ausreichend gute Ergebnisse.^[89] Noch einen Schritt weiter auf der Leiter, angekommen bei den doppelten Hybriddichtefunktionalen (DHDF), wird nun zusätzlich ein Anteil der semi-lokalen DFT-Korrelation durch einen orbitalabhängigen, non-lokalen, störungstheoretischen Term zweiter Ordnung ersetzt. Hierfür gibt es verschiedene Möglichkeiten, wie z. B. den in Abb. 1.4 gezeigten Ansatz nach MØLLER-PLESSET (MP2).^[90] Diese DHDF sind rechnerisch jedoch außerordentlich aufwendig und begrenzen sich mit aktueller Hardware nur auf sehr kleine Systeme. Der Vorteil der DFT liegt zusammengefasst in der Möglichkeit, große Systeme von mehreren hundert Atomen zu simulieren und je nach aufsteigender Stufe die Genauigkeit des Ergebnisses zu erhöhen. So eignen sich niedrigere und wenig kostenintensive Stufen für ein generelles Screening von Geometrien und höhere, zeitintensivere Stufen für eine detailliertere Beschreibung der elektronischen Struktur.^[91]

Aufgabenstellung

2

Der Fokus dieser Arbeit liegt auf der Beschreibung, Erklärung und Vorhersage von diversen molekularen Strukturen und ihren Eigenschaften mittels der Dichtefunktionaltheorie (DFT). So wurden zum einen Moleküle mit für die angestrebte Funktion optimalen Eigenschaften entwickelt und die erhaltenen Ergebnisse experimentell bestätigt. Zum anderen wurden experimentell beobachtete Phänomene bereits synthetisierter Systeme quantenchemisch untersucht und aufgeklärt. Die Arbeit unterteilt sich dabei in zwei Gebiete:

Im ersten Teil der Arbeit wird die anwendungsspezifische Modifikation von verbrückten Azo-benzolen, sogenannten Diazocinen dargelegt. Der Fokus liegt dabei auf der Vorhersage der molekularen Struktur, möglichen Photoanregungen, der Synthesierbarkeit und der Analyse des Konformations- und Konfigurationsraum der neuen Systeme. Zusätzlich werden die thermischen Gleichgewichte sowie Schaltmechanismen der neuen Schalter ergründet. Nachfolgend wird der Einfluss von Gold(111)-Oberflächen auf verschiedene, über Plattformen adsorbierte Photoschalter theoretisch untersucht, diskutiert und aufgeklärt.

Der zweite Teil dieser Dissertation beschäftigt sich mit der Delokalisierung von Elektronen in Molekülen. Die Anwendung der ACID-Methode hilft dabei, Reaktionen vorherzusagen und diese zu erklären, Aromatizität zu beschreiben bzw. nachzuweisen und Spezialfälle von Konjugation aufzuzeigen. So werden Stereo- und Regiochemie von Diels-Alder-Reaktionen an porphyrinogenen Systemen untersucht, verschiedene Moleküle auf MÖBIUS-Topologie und Aromatizität getestet und zu guter Letzt mittels qualitativer und quantitativer ACID-Analyse Konjugation durch den freien Raum diskutiert.

3

Diazocine

Dibenzodiazocine (Diazocine) sind direkte Verwandte des Azobenzols (AB) und wurden erstmalig 1910 von DUVAL synthetisiert.^[92] Sie besitzen zusätzlich zu der Azofunktion eine Ethylenbrücke in *ortho*-Position der Phenylringe, durch die sich der für diese Verbindungsklasse charakteristische zentrale Achtring ausbildet. Die dadurch erzeugte Ringspannung verändert die photophysikalischen Eigenschaften im Vergleich zum AB grundlegend.^[93,94] Zusätzlich sorgt der Achtring für vermindernde Freiheitsgrade, da die Phenylgruppen nicht mehr frei rotieren können.

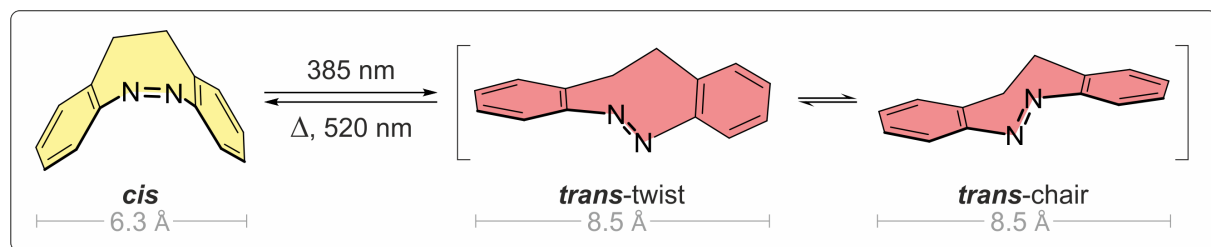


Abb. 3.1: Dibenzodiazocin kann von seiner thermodynamisch stabilen *cis*-Konfiguration durch Belichtung mit 385 nm in seine metastabile *trans*-Form mit zwei verschiedenen Konformationen (twist und chair) isomerisieren. Dabei erfährt das System eine strukturelle Änderung gemessen an der Änderung des Abstandes der Kohlenstoffatome in *para*-Position zur Azofunktion von ca. 2.2 Å. Die Relaxation erfolgt thermisch oder mit Licht der Wellenlänge $\lambda = 520 \text{ nm}$.^[93]

Der größte Unterschied zum AB ist die inverse thermodynamische Stabilität. Mit Licht der Wellenlänge $\lambda = 385 \text{ nm}$ kann die Isomerisierung beim Diazocin (DAC) vom stabilen *cis*- zum metastabilen *trans*-Zustand erfolgen. Die Relaxation erfolgt thermisch ($t = 4.5 \text{ h}, T = 28.5^\circ\text{C}$, Hexan) ähnlich schnell wie bei AB ($t = 4.7 \text{ h}, T = 28.5^\circ\text{C}$, Acetonitril)^[95] oder durch Belichtung ($\lambda = 520 \text{ nm}$).^[93] Auf Grund der guten Bandenseparation ergeben sich photostationäre Zustände (*photostationary states*) (PSS) von 92 % für die Anreicherung der *trans*-Spezies (bei 385 nm in Hexan) und eine quantitative Umsetzung bei der Rückisomerisierung mit 520 nm. Außerdem weist das DAC erhöhte Quantenausbeuten gegenüber dem AB bei Belichtung beider $n\pi^*$ -Banden auf (*cis* \rightarrow *trans*: 72 %, AB: 47 %; *trans* \rightarrow *cis*: 50 %, AB: 32 %).^[93,96] Der durch die Isomerisierung erreichte strukturelle Unterschied ist beim DAC nicht so stark ausgeprägt wie beim AB. Der Abstand der AB-Kohlenstoffatome in *para*-Position zur Azofunktion ändert sich von *trans* mit 9.0 Å zu *cis* mit 6.0 Å.^[97,98] Die Abstandsänderung ist somit im AB (3.0 Å) um 0.8 Å größer als im DAC (2.2 Å).^[99] Der zentrale Achtring bedingt bei der *trans*-Konfiguration

zwei verschiedene Konformere, den twist und den chair. Das chair-Konformer ist gegenüber der twist-Konformation um $2.7 \text{ kcal mol}^{-1}$ benachteiligt und spielt daher eine untergeordnete Rolle.^[100]

3.1 Modifikation des Stamm-Diazocins

Dank dem tricyclischen System und der Ähnlichkeit zu vielen bereits gut untersuchten Pharmakophoren sind DACs eine sehr vielversprechende Verbindungsklasse für pharmakologische Untersuchungen. Eine hierfür besonders positive Eigenschaft des DACs ist die bathochromie Verschiebung der Absorptionsmaxima im Vergleich zum AB von bis zu 100 nm (s. Abb. 3.2). Hiermit reichen die Absorptionsbanden fast bis in den nahen Infrarot (NIR) Bereich. Hierdurch befindet sich die Anregungswellenlänge fast im bio-optischen Fenster, was eine höhere Eindringtiefe bei Belichtung in menschliches Gewebe ermöglichen würde.^[101]

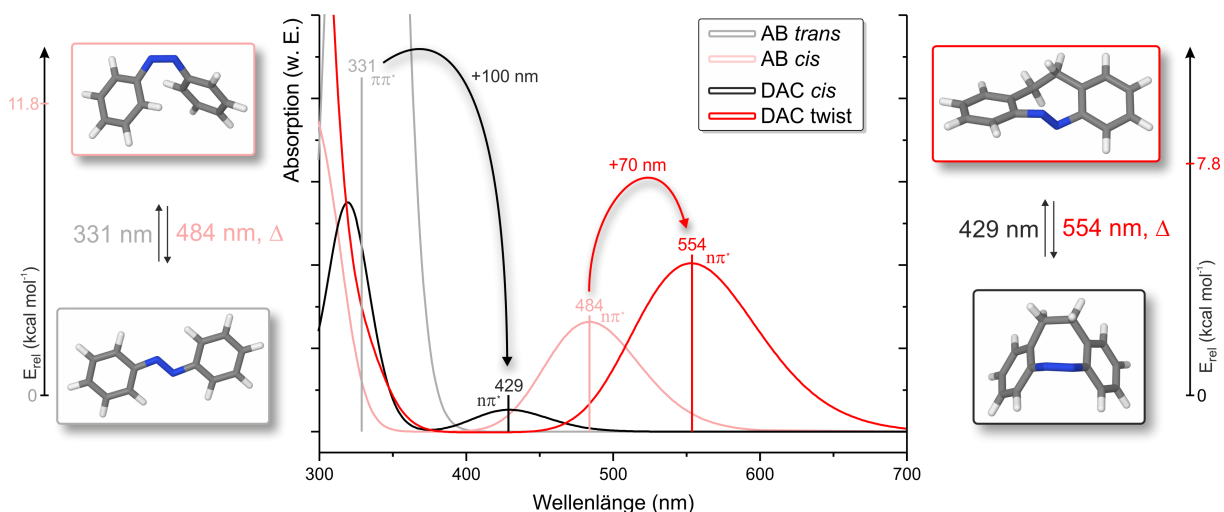


Abb. 3.2: Vergleich der Rechnungen von AB und DAC: in grau/schwarz: thermisch stabile Konfiguration; rötlich/rot: metastabiler Zustand. Die Energien (PBE-D3(BJ)/def2TZVP) und Übergänge (TD-B3LYP/6-31G*/PBE-D3(BJ)/def2TZVP) unterscheiden sich durch die Verbrückung deutlich. Das DAC weist im Vergleich zu AB eine inverse thermische Stabilität sowie bis zu 100 nm bathochrom verschobene Absorptionsbanden auf.

Um die Absorptionsbanden ganz in das bio-optische Fenster zu bringen, könnten Modifikationen an dem Photoschalter vorgenommen werden, wie z. B. das Stammsystem mit verschiedenen elektronenziehenden oder -schiebenden Gruppen zu substituieren. Das Stamm-DAC ist jedoch synthetisch nicht immer konstant zugänglich, die Ausbeuten variieren und die Reproduzierbarkeit ist nicht immer gewährleistet.^[102] Der häufig angewandte symmetrische, statistische Ansatz zu Erzeugung der DACs ist darüber hinaus nicht gut geeignet, um unsymmetrische Substitutionsmuster zu erhalten.^[103]

Aus diesen Gründen wurde 2016 von HAMMERICH *et al.* ein systematischer, unsymmetrischer Ansatz zu Darstellung von Hetero-DACs entwickelt. Das neue Konzept basiert anstatt der *ortho*-

Ethylenverbrückung ($-\text{CH}_2\text{-CH}_2-$) auf einer Ester- bzw. Thioesterbrücke ($-\text{O/S-CH}_2-$). Hierbei wurden vor der Synthese DFT-Rechnungen auf dem weit verbreiteten B3LYP/6-31G*-Niveau eingesetzt, um die neuen Verbindungen zu untersuchen. Die aus isodesmischen Gleichungssystemen erhaltenen Ringspannungsenergien waren dabei indikativ für die Synthesierbarkeit der Zielverbindungen. Gleichzeitig konnte hierdurch die für DACs typische thermische *cis*-Stabilität ermittelt werden. Bei der *trans*-Konfiguration zeigten sich chair- und twist-Konformere. Zeitabhängige (*time-dependent*) DFT (TD-DFT)-Rechnungen (TD-B3LYP/6-31G*) wiesen eine deutliche Bandenseparation der $n\pi^*$ -Anregungsübergänge von mehr als 100 nm für die *cis*- und *trans*-twist-Spezies auf. Lediglich die Spektren der chair-Konformation ähneln dem des *cis*-Isomers. Für eine effektive Photoanreicherung der *trans*-Konfiguration sollte daher der chair energetisch benachteiligt und somit weniger populiert vorliegen. Spektroskopische Untersuchungen konnten für das Sauerstoffdiazocin (*O*-DAC) einen besseren PSS als für das Schwefeldiazocin (*S*-DAC) belegen. Der Grund für den schlechteren PSS liegt in der Isoenergetik der *trans*-Konformere des *S*-DAC. Zusätzlich wurden die im Vergleich zum Stamm-DAC vergrößerte, durch die Rechnungen vorhergesagte Bandenseparation und die Schaltung bis in den fernen Bereich roten Lichts experimentell bestätigt. Insgesamt weisen die Hetero-DACs im Vergleich zum Stammsystem eine systematische Syntheseroute, verbesserte Schalteffizienzen und klare Bandenseparation mit Anregungswellenlängen bis fast zum NIR Bereich auf.

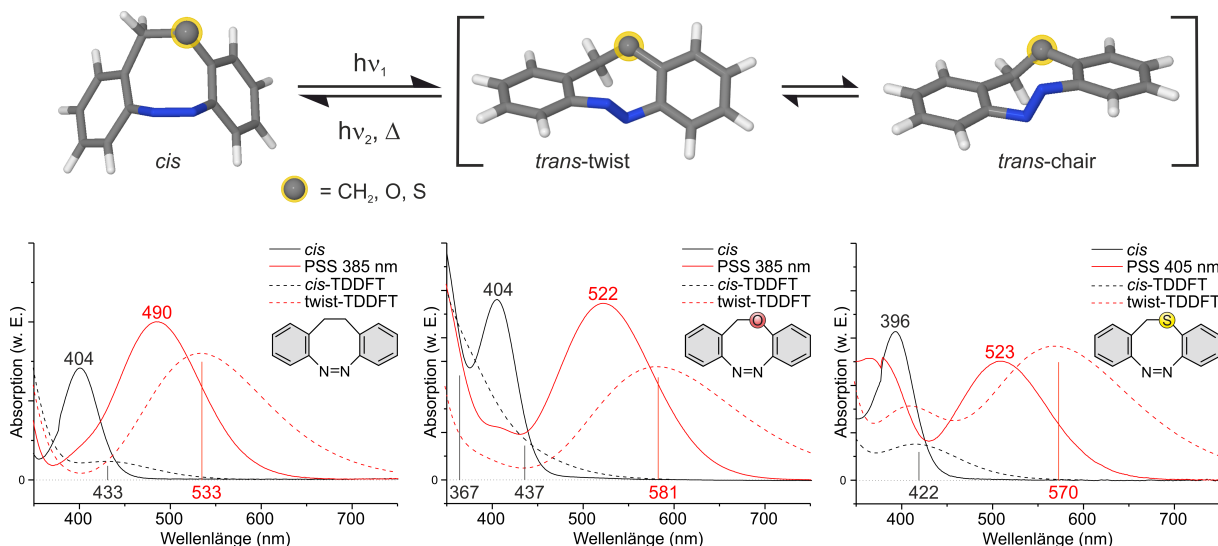


Abb. 3.3: Photoschaltung der Hetero-DACs und des Stamm-DAC: Thermisch stabil in ihrer *cis*-Konfiguration isomerisieren diese zum *trans*-Isomer mittels Belichtung geeigneter Energie ($E_1 = h\nu_1$). Die Rückisomerisierung zur *cis*-Form erfolgt thermisch oder mit Licht anderer Energie ($E_2 = h\nu_2$). Ein Vergleich der exp. sowie berechneten Spektren (TD-B3LYP/6-31G*) zeigt die quantitativ überschätzten Simulationen, welche die Bandenseparation aber qualitativ gut widerspiegeln.

3.2 Stickstoffverbrückte DACs

Neben Sauerstoff und Schwefel stellt die Verbrückung mit dreibindigem Stickstoff nicht nur den nächsten logischen Schritt in der Erforschung sondern auch eine vielversprechende Zielverbindung für die Photopharmakologie dar. Besonders dort können DACs dank der thermischen *cis*-Stabilität besser angewendet werden als AB. Häufig wird ein bioaktiver Inhibitor mittels einer photoschaltbaren Einheit so modifiziert, dass eine Konfiguration aktiv inhibiert und die andere biologisch inaktiv ist. AB passt auf Grund der thermischen stabilen, schlanken *trans*-Form in die meisten Bindetaschen und inhibiert damit aktiv. Wegen häufig unvollständiger Umwandlung zum *cis* kann der Wirkstoff meist nur anteilig inaktiv geschaltet werden und relaxiert nach einer gewissen Zeit wieder zur aktiven Spezies. DACs umgehen dieses Problem intrinsisch, da die sperrige und thermisch stabile *cis*-Spezies nicht in die Bindetasche passt. Der passive Wirkstoff könnte dann ortsaufgelöst mit Licht geeigneter Wellenlänge aktiviert werden und würde sich mit der Zeit thermisch oder durch Belichtung mit anderer Wellenlänge wieder deaktivieren. Die Kontrolle der Wirkstoffaktivität wäre mit dem Einsatz von DACs damit viel genauer.^[104–108]

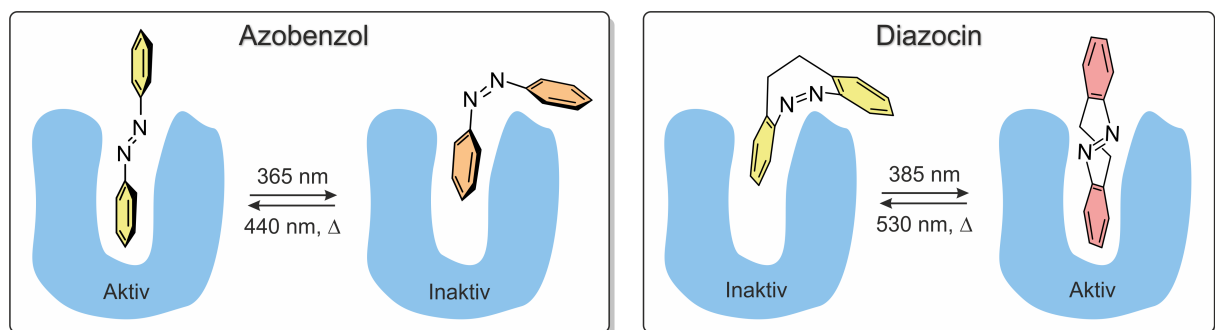


Abb. 3.4: Die meisten AB-derivatisierten Wirkstoffe sind in ihrer thermisch stabileren *trans*-Form in der Bindetasche (blau) gebunden und somit aktiv. Sie können lediglich anteilig durch Licht geeigneter Wellenlänge deaktiviert werden und aktivieren sich thermisch oder Belichtung mit einer anderen Wellenlänge wieder. Dank der inversen thermischen Stabilität der DACs sind diese dauerhaft inaktiv, bis sie mit Licht geeigneter Wellenlänge ort- und zeitaufgelöst aktiviert werden.

Für solche *in vivo* Anwendungen sind allerdings wasserlösliche und auch darin effizient schaltbare Verbindungen notwendig, welche je nach Inhibitor systematisch weiter und auch asymmetrisch modifiziert werden müssten. Hierfür eignen sich die bisher entwickelten DACs nicht, da sie die erforderlichen Eigenschaften nicht aufweisen. Die noch unerforschten stickstoffverbrückten Diazocene (N-DACs) könnten eine Alternative darstellen. Darüber hinaus stellt die strukturelle Verwandtschaft mit tricyclischen Dibenzooazocinen, welche bereits erfolgreich in diversen Pharmazeutika zum Einsatz kamen, ein zusätzliches Potential zur Entwicklung schaltbarer Medikamente wie Antidepressiva, Calciumantagonisten und Antihistaminika dar.

3.3 Nitrogen Bridged Diazocines: Photochromes Switching within the Near-Infrared Region with High Quantum Yields in Organic Solvents and in Water

P. Lentes, E. Stadler, F. Röhricht, A. Brahms, J. Gröbner, F. D. Sönnichsen, G. Gescheidt und
R. Herges

J. Am. Chem. Soc. **2019**, *141*, 13592–13600.

DOI:10.1021/jacs.9b06104

Supporting Information: Anhang Begleitmaterial 8

Wissenschaftliche Beiträge: DFT-Geometrieeoptimierung, Berechnung der Ringspannungsenergien mittels isodesmischer Reaktionen, TD-DFT-Simulationen der UV/Vis-Spektren, konformatio nelle und konfigurationelle Analyse der Potentialhyperfläche (*potential energy surface*) (PES) beinhalteter Diazocine (mit Übergangszustandssuchen (*transition state searches*) (TSS) zur Bestimmung der Aktivierungsenergien (E_a)), Verfassen des Manuskripts (anteilig).

Zusammenfassung

Diese Veröffentlichung zeigt die systematische Entwicklung verschiedener neuer N-DACs mit bathochrom verschobenen Absorptionsbanden bis in den NIR Bereich und hohen Quantenausbeuten. Präsynthetische quantenmechanische DFT-Rechnungen ergaben ähnliche Ergebnisse für die -CH₂-NR- verbrückten DACs wie für die bereits etablierten Hetero-DACs: ähnliche Ringspannungsenergien (isodesmische Reaktion), über 100 nm separierte nπ*-Absorptionsmaxima der *cis*- und *trans*-Konfigurationen (TD-DFT Rechnungen), thermodynamisch favorisierte *cis*-Isomere gegenüber der *trans*-Konfiguration und außerdem stabilere twist- als chair-Konformationen der *trans*-Isomere. Letzteres ist entscheidend für eine effiziente Photoisomerisierung bei unterschiedlichen Wellenlängen, da angenommen wird, dass die Konformere bei Raumtemperatur schnell ineinander konvertieren und die chair-Form ähnliche Absorptionsbanden wie das *cis*-Isomer aufweist.

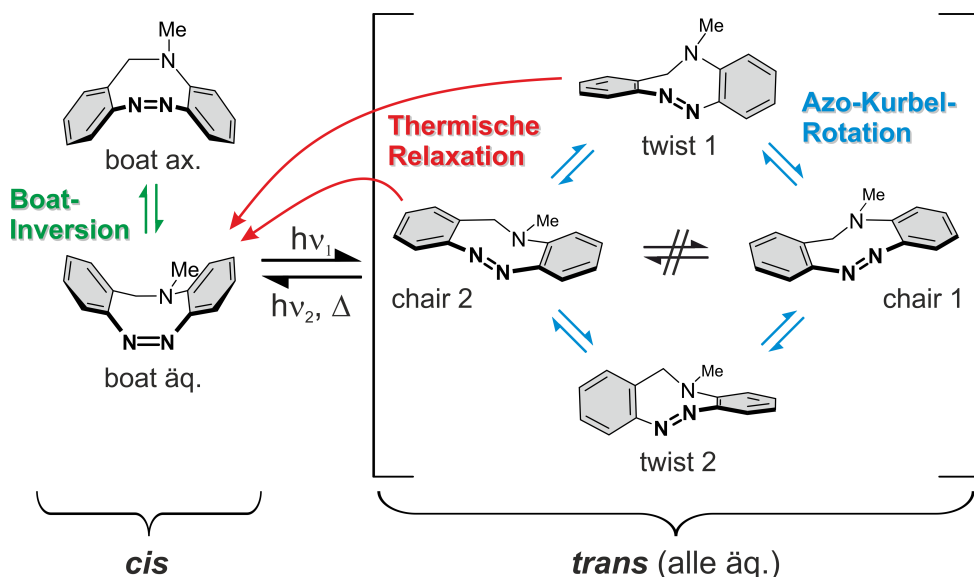


Abb. 3.5: Vereinfachter konformationeller Raum der N-DAC-Konfigurationen am Beispiel von N-Me-DAC: Die ax. oder äq. boat-Konformere der *cis*-Konfiguration können durch eine boat-Inversion des zentralen Achtrings schnell ineinander übergehen. Auf der komplexeren Hyperfläche der *trans*-Konfiguration ist der Übergang zwischen den enantiomeren chair-Konformeren nicht direkt, sondern immer nur über eins der twist-Enantiomere durch eine Rotation der Azofunktion (C-N=N-C) möglich. Analoges gilt für die twist-Enantiomere. Die thermische Relaxation vom metastabilen *trans* zum *cis* geschieht durch nahezu isoenergetische Übergangszustände entweder vom twist oder vom chair.

Der Schwerpunkt dieser Arbeit liegt neben der Synthese und photophysikalischen Charakterisierung der neuen N-DACs auch auf einer konformationellen Analyse der Schalterkonfigurationen. Im Vergleich zu den bisher etablierten DACs ergibt sich durch den verbrückten Stickstoff ein zusätzliches Stereozentrum (neben dem des Achtrings), welches je nach ax. (axial) oder äq. (äquatorial) Substituentenstellung eine andere Konformation der jeweiligen Konfiguration darstellt. Durch den Einsatz von DFT-Rechnungen in Zusammenarbeit mit Protonenkernspinresonanz (*proton nuclear magnetic resonance*, ¹H-NMR)-Experimenten konnte der konformationelle Raum

der Konfigurationen untersucht werden. So unterscheiden sich z.B. durch *boat*-Inversion des *cis*-Isomers die ax. bzw. äq. Konformere eigentlich energetisch, werden jedoch durch eine schnelle Inversion (auf der NMR-Zeitskala) am Stickstoff nicht getrennt voneinander beobachtet. Des weiteren unterteilt sich die *trans*-Konfiguration neben bekannten chair- und twist-Konformeren weiter in je zwei Enantiomere (z.B. twist1 und twist2) und unter Einbezug der Substituentenstellung noch weiter in ax./äq.-Diastereomere (ax. twist1 und äq. twist1 usw.). Da die DFT die Inversion am Stickstoff inadäquat beschreibt,^[109] wurden bei der *trans*-Konfiguration nur die meist thermodynamisch stabileren äq. Enantiomere berücksichtigt. TSS zeigten, bestätigt durch NMR-Experimente, dass zwar bei Raumtemperatur eine schnelle Umwandlung der *trans*-Konformere und Enantiomere ineinander gegeben sein sollte, eine direkte Konversion von $\text{twist1} \rightleftharpoons \text{twist2}$ oder $\text{chair1} \rightleftharpoons \text{chair2}$ (Racemisierung) jedoch nicht möglich ist.

Nitrogen Bridged Diazocines: Photochromes Switching within the Near-Infrared Region with High Quantum Yields in Organic Solvents and in Water

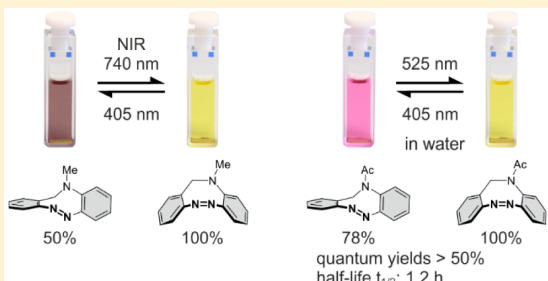
Pascal Lentes,[†] Eduard Stadler,[‡] Fynn Röhricht,[†] Arne Brahms,[†] Jens Gröbner,[†] Frank D. Sönichsen,[†] Georg Gescheidt,[‡] and Rainer Herges^{*†}

[†]Otto Diels-Institute of Organic Chemistry, Christian Albrechts University Kiel, Otto Hahn Platz 4, 24118 Kiel, Germany

[‡]Institute of Physical and Theoretical Chemistry, Graz University of Technology, Stremayrgasse 9, 8010 Graz, Austria

Supporting Information

ABSTRACT: Diazocines are bridged azobenzenes with superior photophysical properties. In contrast to azobenzenes the Z configuration is thermodynamically stable and the E isomer is metastable. We present a new class of nitrogen bridged diazocines with bathochromically shifted switching wavelengths and remarkably high quantum yields ($-\text{NH}-\text{CH}_2-$ bridged diazocine: $\Phi_{Z \rightarrow E} = 0.57$, $\Phi_{E \rightarrow Z} = 0.8$). Z to E isomerization is induced by irradiation with blue light, whereas switching back to the Z isomer is accomplished with light in the near-infrared window (up to 740 nm), which is important for medical applications like photopharmacology (deep tissue penetration). Furthermore, substitution at the bridging nitrogen should provide access to widely applicable tricyclic, photoswitchable pharmacophores. The $-\text{NAC}-\text{CH}_2-$ bridged derivative is soluble in water, and all photophysical properties (conversion rates, quantum yields, and thermal half-lives) are largely retained. Hence, this diazocine is an ideal photoswitch for applications in biochemical systems and in photopharmacology.



INTRODUCTION

Photochromic compounds such as azobenzenes (ABs), spirobifluorenes, and diarylethenes have been used as actuators to switch the properties of catalysts,¹ biomolecules,^{2,3} polymers,³ surfaces,⁴ and pharmacophores.^{2,5,6} Azobenzenes, arguably, are the most frequently used photoswitches because they are small, robust, reliable, and easy to synthesize and to derivatize. However, there are deficiencies in a number of applications. The switching wavelengths are within the UV and visible range (parent azobenzene: 314 nm ($E \rightarrow Z$) and 435 nm ($Z \rightarrow E$)) causing problems in material and medical applications. Quantum yields are moderate (parent AB: $\Phi_{E \rightarrow Z} = 0.11$, $\Phi_{Z \rightarrow E} = 0.56$).⁷ The conformational flexibility (free rotation of phenyl groups) lowers the efficiency of power transmission in applications as motors in molecular machines. Particularly in photopharmacology the fact that the E configuration is more stable than the Z isomer often prevents practical applications. The goal in photopharmacology is to derivatize a known bioactive compound, such as an inhibitor with a photoswitch in such a way that the inhibitor is active in one configuration but inactive in the other form. Hence, the bioactivity can be switched on and off with light. However, it is usually the slender E configuration which fits into the tight binding site of the protein, in contrast to the bent and bulkier Z configuration.^{2,5,6} Hence, the parent resting state is the

bioactive E isomer. It would be, however, of much greater practical value if the inactive state could be converted to its active form using a photo trigger having an appropriate wavelength with a high spatiotemporal resolution. Side-effects in healthy neighboring tissue, thus, would be avoided. Deactivation of the drug would either be induced by thermal back-isomerization or by irradiation with another wavelength.

Analogous requirements hold for applications of photochromes as mechanophores. Here, spirobifluorens have been implemented in polymer backbones or cross-linking units. Macroscopic stretching forces of such polymers are transferred to the molecular mechanophores, which undergo ring-opening, indicating macroscopic stress by a color change.^{3,8} Azobenzenes cannot be used as mechanophores, because their resting state is the stretched E configuration. Tensile forces would convert the bent Z configuration into E, however, not vice versa.

Diazocines do not suffer from this disadvantage, because of their inverse configurational stability. The bent Z configuration is thermodynamically more stable than the E isomer.^{9,10} Hence, diazocines are ideal photoswitches for applications as photopharmacophores^{11,12} and mechanophores.¹³ Moreover,

Received: June 7, 2019

Published: July 31, 2019

Table 1. Comparison of the Photophysical Properties of Parent Azobenzene, Parent Diazocine, O- and S-Diazocine

stable isomer	parent azobenzene		parent diazocine		O-diazocine ¹⁰	S-diazocine ¹⁰
	E	Z	Z	Z	Z	Z
ΔE_{rel}^a	-12.4 ^h	7.9 ^h	12.5 ^h	6.2 ^h		
$\lambda_{\max(Z)}^{b,c}$	435 nm(nπ*) ⁷	404 nm(nπ*) ⁹	385 nm(nπ*)	405 nm(nπ*)		
$\lambda_{\max(E)}^{b,c}$	314 nm(ππ*) ⁷	490 nm(nπ*) ⁹	525 nm(nπ*)	525 nm(nπ*)		
$t_{1/2}^{d,e}$	119 h (25 °C) ¹⁶	4.5 h (28.5 °C) ⁹	89 s (20 °C)	3.5 d (27 °C)		
$\Gamma_{Z \rightarrow E}^{d,e}$	79% (>400 nm) ⁷	92% (385 nm) ⁹	80% (385 nm)	70% (405 nm)		
$\Phi_{Z \rightarrow E}^{d,e}$	0.47 ¹⁷	0.72 ⁹	N/A	N/A		
$\Gamma_{E \rightarrow Z}^{d,e}$	90% (317 nm) ¹⁸	99% (520 nm) ⁹	99% (520 nm)	99% (520 nm)		
$\Phi_{E \rightarrow Z}^{f,g}$	0.16 ¹⁷	0.9 ^h	N/A	N/A		
S_1 lifetime $E \rightarrow Z$	365–400 fs ^{14,19}	30–40 fs ¹⁴	N/A	N/A		

^a $\Delta E_{\text{rel}} = E_E - E_Z$ in kcal · mol⁻¹. ^{b,c} $\lambda_{\max(Z)}$: maximum absorption wavelengths of the excitations used for switching (nπ* or ππ*). ^{d,e} $\Gamma_{Z \rightarrow E}$, $\Gamma_{E \rightarrow Z}$: conversion rates $Z \rightarrow E$ and $E \rightarrow Z$ at the photostationary states upon irradiation at the given wavelengths. ^{f,g} $\Phi_{Z \rightarrow E}$, $\Phi_{E \rightarrow Z}$: quantum yields determined at the given wavelengths. ^hThis work (for details, see the Supporting Information, S VII).

they are superior to azobenzenes in terms of most of their photophysical properties. They exhibit higher quantum yields (parent diazocine $\Phi_{E \rightarrow Z} = 0.9$, $\Phi_{Z \rightarrow E} = 0.72$), more rigid structures, bathochromically shifted switching wavelengths, higher photochemical conversion rates (parent diazocine: 92% ($Z \rightarrow E$) and 100% ($E \rightarrow Z$)),⁹ and a photochemical isomerization time scale that is 1 order of magnitude shorter than in unbridged AB^{14,15} (see Table 1).

Particularly in view of in vivo applications, switching in the far-red or near-infrared is desirable, because light within the range of 680–900 nm has a larger penetration depth in blood supported tissue compared to visible, or UV light.²⁰ There have been several successful attempts to shift the switching wavelengths of azobenzenes into the red region. *ortho*-Substitution of the azobenzene core with heteroatoms N,²¹ O,^{22,23} F,^{16,24} and S²⁵ (mainly investigated by the groups of Woolley²⁶ and Hecht²⁷) leads to a bathochromic shift of the nπ* transition of the *E* isomer and a band separation of the nπ* of *Z* and *E* isomers giving rise to excellent conversion rates in some cases. Further red-shifted and switchable under physiological conditions are *ortho*-substituted azobenzenes forming azonium ions^{28,29} in their *E* configurations. An advantage of the latter systems is that they isomerize from the stable *E* resting state to the metastable *Z* isomer (not vice versa) upon irradiation with far-red light. Provided that the *Z* isomer is the pharmacologically active species and a thermal relaxation leads back to the stable *E* isomer, red light could be used to switch a drug on at the target site.

Heterocyclic azobenzenes³⁰ such as azoimidazoles^{31,32} or azopyrazoles^{33–35} also isomerize upon irradiation with visible light. Strongly red-shifted are the BF₂ adducts^{36,37} of azobenzenes developed by Aprahamian et al. As a rule of thumb, any approach to achieve red-shifted switching wavelengths will compromise (shorten) the half-life of the metastable isomer. However, this is not true for systems with extra internal stabilization such as protonated bisazoimida-zoles³⁸ or the so-called “record player design”, where the metastable *Z* isomer of an azopyridine or azoimidazole is stabilized by coordination to a Ni-porphyrin. A Ni-porphyrin^{39–42} equipped with methoxy substituted azopyridine exhibits perfect switching properties. Conversion rates are quantitative in both directions and the thermal half-life of the *Z* isomer at room temperature extends to several years.⁴³ Switching within the NIR, however, has not yet been achieved.

We previously developed –CH₂O– and –CH₂S– bridged azobenzenes (O-diazocine **2** and S-diazocine **3**, Figure 1,

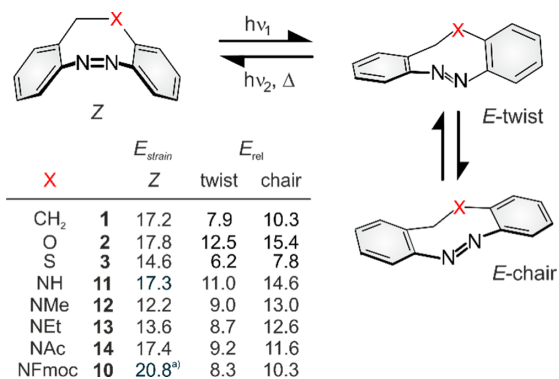


Figure 1. Isodesmic strain energies (E_{strain}) and relative energies (E_{rel}) of the different *E* conformations of ethylene **1**, oxygen **2**, sulfur **3**, and nitrogen **10–14** bridged diazocines in kcal mol⁻¹. E_{rel} is given with respect to the more stable *Z* configuration (for details, see Supporting Information, SII). All calculations were carried out using DFT at the M06-2X(D3)/def2-TZVP level of theory. ^aCalculated with methoxycarbonyl instead of fluorenylmethoxycarbonyl to save computer time.

Table 1) as a new class of heteroatom bridged azobenzenes (heterodiazocines).¹⁰ Compared to the parent diazocine **1**, O-diazocine **2** and S-diazocine **3** exhibit further red-shifted absorptions in their *E* configurations ($\lambda_{\max(E)} = 525$ nm). *E* → *Z* isomerizations are still effective and quantitative upon irradiation with 660 nm, because the *E* nπ* absorption bands extend to the far red. The nπ* absorption of the *Z* isomer and hence the *Z* → *E* isomerization is not effected by introduction of heteroatoms into the bridge ($\lambda_{\max(Z)} \approx 405$ nm). 385 and 405 nm are the most effective wavelengths to switch the O- and S-diazocine **2** and **3** from *Z* to *E* configurations. The *Z* → *E* conversion rates at the photostationary states (PSS) are 80% (O-diazocine **2**) and 70% (S-diazocine **3**). O-diazocine **2** and S-diazocine **3** exhibit drastically different thermal half-lives with 89 s (20 °C) vs 3.5 d (27°). Parent diazocine falls in between (4.5 h, 28.5 °C).

According to our quantum chemical calculations the *E* configuration adopts two different conformations: a twist and a chair geometry, that rapidly interconvert. In all cases investigated so far, the twist form is more stable than the chair species (Figure 1). It is important to note that TD-TDFT calculations predict that the chair conformation displays very

similar $n\pi^*$ absorptions to the Z boat configuration. Therefore, any design of new diazocines should avoid stabilizing the chair versus the twist form.

We now report on $-\text{CH}_2-\text{NR}-$ bridged azobenzenes (N-diazocines). In analogy to azobenzenes, N-substitution should shift the absorption further to the far-red region.^{2,27} Moreover, a number of drugs contain a tricyclic dibenzazocine core such as hydroxysteroid dehydrogenase,⁴⁴ kinase inhibitors,^{45,46} prostanoid receptor ligands,⁴⁷ antiallergics,⁴⁸ anticholinergics,⁴⁸ and analgesics.⁴⁸

The tricyclic cores of these inhibitors differ from our target N-diazocines only by the replacement of a C=C or C=C bond within the central 8-membered ring by a switchable N=N unit. There is a good chance that the bioactivity is retained in the (boat) Z isomer if a C=C bond is replaced by N=N and can be switched off by isomerization to the (twist) E form. Replacement of a C=C bond by N=N should lead to the reverse situation. Trauner et al. recently suggested that such isosteric replacements (azologizations) could be a powerful approach in photopharmacology.⁴⁹

A wide range of tricyclic antidepressants such as Imipramine⁵⁰ or Nortriptyline,⁵¹ calcium antagonists⁵² and anti-histamines, such as Cyproheptadine are structurally related to the diazocines.⁵³ Cyproheptadine is also active against breast cancer growth.⁵⁴ Particularly the biologic activity and the effect of tricyclic agents strongly depends on the angle between the two phenyl rings.⁵⁵ However, the internal conformational flexibility of tricyclic structures related to their activity is not fully understood.⁵⁶ Upon photoisomerization of diazocene 1 and O- and S-diazocene 2 and 3 this angle changes between $\sim 90^\circ$ and $\sim 180^\circ$. Hence, the neurological activity and mode of action should also drastically change.

All tricyclic pharmacophores mentioned above are functionalized in the central 7- or 8-membered ring. Functionalization of the ethylene bridge of diazocines, however, to mimic these tricyclic drugs is difficult. To our knowledge, only a few bridge substituted derivatives are reported.^{57–59} Another motivation to introduce a NH group into the bridge is the fact that a variety of bridge substituted diazocines would become accessible by standard nucleophilic substitution.

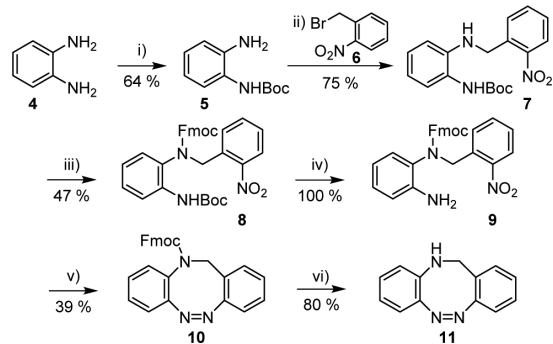
RESULTS AND DISCUSSION

TD-DFT calculations (for details, see the Supporting Information, SII) predict a $n\pi^*$ band separation of more than 100 nm for the Z and E isomers of NH diazocene 11 and all alkyl and acyl derivatives 10, 12–14 (for structures see Figure 1). An efficient photoisomerization at two different wavelengths, therefore, can be expected. All N-diazocines are more stable in their twist than in the chair conformation, which is crucial for effective switching (see above). The calculated strain energies of the eight-membered rings are comparable to previously synthesized diazocines. Therefore, synthesis according to previous procedures seemed feasible.

Synthesis of Nitrogen Bridged Diazocines. Standard procedure for diazocene synthesis is the reductive azo condensation of the nitro precursors.^{10,58,60,61} This strategy depends on the quality of the metals used as a reducing reagent, and a number of further parameters, such as temperature, pH, reaction time, etc., which makes the synthesis hard to reproduce (strongly varying yields).⁶² We therefore used the intramolecular Baeyer-Mills reaction⁶³ as the key step to close the 8-membered ring by azo-condensation. Synthesis was performed by single Boc protection of *o*-phenylenedi-

amine (4)⁶⁴ (Scheme 1) followed by substitution of the free amine 5 with 2-nitrobenzyl bromide (6). The resulting N-

Scheme 1. Synthesis of NH-diazocene 11^a

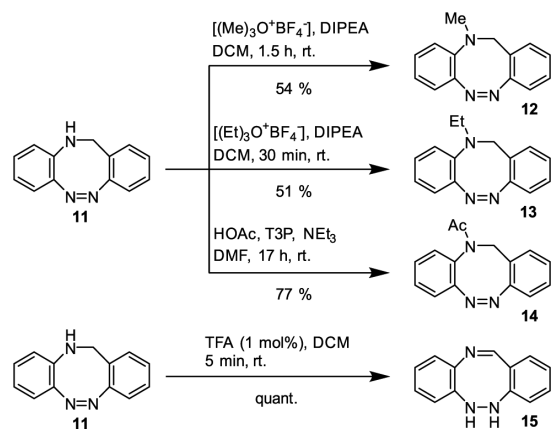


^aReaction conditions: (i) Boc₂O, MeOH, 15 h, rt.; (ii) DIPEA, THF, 18 h, reflux; (iii) Fmoc-Cl, DIPEA, DMF, 43 h, rt.; (iv) DCM/TFA (3:1), 20 h, rt.; (v) 1.) Zn, NH₄Cl, EtOH/H₂O (2:1), 10 min, 70 °C; 2.) FeCl₃, 6 H₂O, 15 min, 0 °C; 3.) acetic acid, 17 h, rt.; (vi) NEt₃ in DCM (50%), 24 h, rt.

benzyl aniline 7 was protected with Fmoc-chloride to accomplish an orthogonal protective group strategy. Removing of the Boc group of 8 with TFA resulted in the mixed precursor 9 for the intramolecular Baeyer-Mills reaction. In a one-pot synthesis, the nitro group of 9 was reduced with zinc/NH₄Cl to form the corresponding hydroxylamine followed by oxidation with iron(III) chloride to the nitroso derivative. After that glacial acetic acid was added and stirred overnight. The resulting Fmoc protected N-diazocene 10 was isolated in 39% yield over three reaction steps. Removal of the Fmoc group with triethylamine gave the NH-diazocene 11 in 80% yield.

Alkylation of the NH-diazocene 11 (Scheme 2) was carried out with Meerwein salts⁶⁵ giving NMe-diazocene 12 in 54% yield and NET-diazocene 13 in 51% yield. Acylation was performed by T3P mediated active ester synthesis⁶⁶ with acetic acid yielding NAc-diazocene 14 in 77%.

Scheme 2. Reaction Conditions for the Substitution and Tautomerization of the NH-Diazocene 11



It should be noted that NH-diazocine **11** undergoes an acid catalyzed two proton tautomerization to yield the imine bridged hydrazine **15** (**Scheme 2**). The first steps in this process, obviously, are the protonation of the bridge NH group and a transannular 1,5-sigmatropic shift of a proton from the NH_2^+ group to the distant nitrogen atom of the $\text{N}=\text{N}$ azo unit (for a tentative mechanism, see the Supporting Information, **SVIII**). Attempts to oxidize the hydrazine to an azo group with HgO , CuCl_2/O_2 or mCPBA were not successful. Apparently, the formation of an 8 electron antiaromatic triazocine ring is not favored.

UV-vis Spectra and Photostationary States of Nitrogen Bridged Diazocines. UV-vis spectra of diazocines **10–14** were recorded in THF at $-20\text{ }^\circ\text{C}$ (**Figure 2**). They generally display two maxima attributable to the individual $n\pi^*$ absorptions of the *Z* ($\sim 400\text{ nm}$) and the *E* isomer ($\sim 550\text{ nm}$). Upon irradiation with 405 nm , the $n\pi^*$ absorption at about 400 nm decreases and the $n\pi^*$ absorption bands of the *E* isomers between 520 and 560 nm grow (**Table 2**, **Figure 2**, for full range spectra from 200 to 800 nm , see the Supporting Information, **SV.7**). The absorption maxima of the *Z* isomers are located around 400 nm , accordingly, 405 nm is a well suited wavelength to achieve efficient *Z* \rightarrow *E* conversion.

For the *E* isomers, the substitution pattern shifts the absorption maximum: Starting from *E*-NFmoc (**10**) at 518 nm the $n\pi^*$ maxima are red-shifted in the order **10** $<$ **14** $<$ **12** $=$ **13** $<$ **11**. The large separation between the *Z* and *E* absorption bands allows to selectively excite the *E* isomer using light $\geq 500\text{ nm}$ leading to a virtually complete (>99%) conversion to the *Z* isomer. In particular, the near-infrared $n\pi^*$ bands of *E*-NMe **12** and NEt **13** extending to $>750\text{ nm}$ allow using red light to induce *E* \rightarrow *Z* switching. Indeed, we observed rapid back-switching with near-infrared light ($\geq 740\text{ nm}$). Such long wavelengths provide the deep light penetration required for applications in blood supported tissue, being ideal for photopharmacological applications.²⁰ An almost complete conversion is achieved within 3 s of irradiation with light of $\geq 740\text{ nm}$ (long pass filter), and a light intensity of $\geq 36\text{ mW cm}^{-2}$.

In contrast to the acylated diazocines NFmoc **10** and NAc **14**, the extrapolated spectra of the *E* isomers (**Figure 2**, blue) of the parent NH-diazocine **11**, and the alkylated diazocines NMe **12** and NEt **13** exhibit additional absorptions at around 400 nm , i.e., close to the absorptions of the corresponding *Z* isomers (NH **11**: 391 nm ; NMe **12**: 424 nm ; NEt **13**: 421 nm). Very likely these weak absorption bands arise from *E* chair conformations, which are in equilibrium with the *E* twist conformation (for further evidence from ^1H NMR see *vide infra*). Previous TD-DFT calculations revealed that the *E* chair and the *E* twist conformations exhibit largely different UV spectra. Only the *E* twist conformation has a large bathochromic shift of the $n\pi^*$ transition, whereas the *E* chair spectrum is more similar to the *Z* boat species. The additional band at $\sim 400\text{ nm}$ of these *E* isomers greatly influences the achievable *Z* \rightarrow *E* conversion with 405 nm light. For compounds **10** and **14** missing this additional band, we obtained the largest *E* conversion (80 and 85%), whereas for compounds **11**, **12**, and **13** with a residual band at $\sim 400\text{ nm}$, conversion was comparatively low (45–65%). Photostationary states (**Table 2**) were explored by ^1H NMR spectroscopy in THF at $-28\text{ }^\circ\text{C}$. The samples were irradiated with 405 nm in a glass dewar at $-78\text{ }^\circ\text{C}$ and then quickly transferred into the spectrometer. The extinction

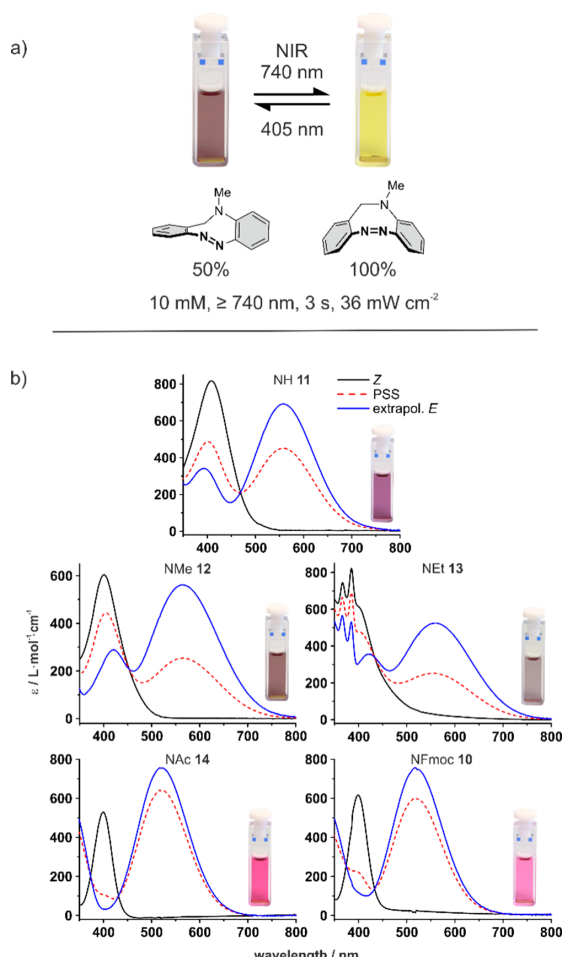


Figure 2. (a) Photochemical switching of NMe-diazocine **12** with blue light and near-infrared ($\geq 740\text{ nm}$). Concentration of **12**: 10 mM in toluene, irradiation wavelength $\geq 740\text{ nm}$, irradiation time 3 s , light intensity 36 mW cm^{-2} . (b) UV-vis spectra of N-diazocines **10–14** in THF at $-20\text{ }^\circ\text{C}$. *Z* spectra (black) were recorded with a sample, which was standing overnight at $40\text{ }^\circ\text{C}$ to ensure complete thermal conversion to the *Z* isomer. Spectra of the photostationary states (dashed red) were recorded after irradiation with 405 nm at $-20\text{ }^\circ\text{C}$ until no change after further irradiation appeared. Extrapolated *E* spectra (blue) were calculated by multiplication of the *Z* spectra (black) with the remaining percentage of *Z* at the photostationary state (**Table 2**) and subtraction from the PSS spectra (red) (for details, see the Supporting Information, **SV.8**). The extrapolated *E* spectra (blue) were also concentration corrected to give the extinction of the pure *E* isomers. All spectra were density corrected to $25\text{ }^\circ\text{C}$ (for details, see the Supporting Information, **SV.6**).

coefficients of the $n\pi^*$ transitions were measured by UV-vis spectroscopy in THF at $-20\text{ }^\circ\text{C}$ (to prevent back-isomerization).

The photochemical quantum yields of the NH-diazocine **11** isomerization were measured via online UV-vis spectroscopy⁶⁷ (for details, see the Supporting Information, **SVII**) by the method utilized by Rau and co-workers.⁶⁸ At 400 nm the quantum yields are $\phi_{Z \rightarrow E} = 0.57$ for the *Z* \rightarrow *E* direction and $\phi_{E \rightarrow Z} = 0.62$ for the reverse process. Using irradiation with 520 nm

Table 2. Photostationary States PSS, Extinction Coefficients ϵ_λ , Thermal Half-Lives of the *E* Isomers $t_{1/2}$, ΔS^\ddagger and ΔH^\ddagger of the $E \rightarrow Z$ Isomerizations of the Nitrogen Bridged Diazocines 10–14^a

	$\Gamma_{Z \rightarrow E}^b$ at 405 nm	$\Gamma_{E \rightarrow Z}^b$ (irradiation wavelengths)	nπ* transitions		$t_{1/2}$ (25 °C) ^d exp.	ΔS^\ddagger / cal mol ⁻¹ K ⁻¹ exp.	ΔH^\ddagger / kcal mol ⁻¹ exp.	ΔH^\ddagger kcal mol ⁻¹ calc.	
			Z λ_{max}^c	ϵ_λ^c				I ^e	II ^f
11	65	>99 (520–690 nm)	409 nm, 722	559 nm, 667	131 s	4.7	19.2	19.6	20.2
12	50	>99 (520–740 nm)	401 nm, 607	554 nm, 519	40 s	14.9	15.4	19.3	20.0
13	45	>99 (520–740 nm)	385 nm, 834	554 nm, 550	22 s	9.3	16.7	20.5	20.6
14	85	>99 (520–590 nm)	400 nm, 582	520 nm, 876	29 min	10.5	19.0	23.0	24.6
10	80	>99 (520–590 nm)	399 nm, 524	518 nm, 776	42 min	11.1	19.0		

^aAll kinetic data were measured in acetone. ^b $\Gamma_{Z \rightarrow E}$, $\Gamma_{E \rightarrow Z}$: conversion rates (%) $Z \rightarrow E$ and $E \rightarrow Z$ at the photostationary states upon irradiation at the given wavelengths. ^c ϵ_λ [L mol⁻¹ cm⁻¹] in THF. ^dExtrapolated from low temperature measurements to 25 °C using the Arrhenius equation (for details, see the Supporting Information, SV.6). ^eMechanism I: *E*(twist) → [TS]_I → *Z*(boat). ^fMechanism II: *E*(twist) → *E*(chair) → [TS]_{II} → *Z*(boat). Calculated activation enthalpies ΔH^\ddagger (calc.) are determined at the M06-2X(D3)/def2-TZVP level of theory.

nm we determined the quantum yield for accelerating the thermal *E* → *Z* isomerization $\phi_{Z \rightarrow E} = 0.8$. In comparison, measured with the same setup, the quantum yields of the parent system **1** are slightly higher.

Thus, the photochemical switching quantum yields of parent diazocine **1** and NH diazocine **11**, are considerably higher than those of other frequently used photocromatic systems (e.g., spiropyran $\Phi_{\text{spiropyran} \rightarrow \text{merocyanine}}$: 0.22;⁶⁸ diarylethenes $\Phi_{\text{ring-close}}$: 0.46, $\Phi_{\text{ring-open}}$: 0.015⁶⁹).

Thermal Back-Isomerization of Nitrogen Bridged Diazocines. The *E* isomers of all N-diazocines (10–14) isomerize back to their *Z* configurations within a period of 20 s and 50 min at room temperature in acetone. Exact half-lives were determined by UV-vis spectroscopy in acetone at 5 different temperatures for each N-diazocine. We found that NAc **14** and NFmoc **10** follow first-order kinetics as expected. Interestingly NH **11** and NMe **12** just exhibit first-order kinetics over the first half-life.

Net **13** exhibits the strongest deviation from Arrhenius behavior. Since the half-lives are not concentration dependent (for details, see the Supporting Information, SVII), we assume that the deviation from Arrhenius behavior is pH dependent and the *Z* isomer is more basic than the *E* isomer.

The activation parameters ΔH^\ddagger and ΔS^\ddagger were calculated from the temperature dependence of the reaction rates (*k*) using the Eyring eq (Table 2, for further details, see the Supporting Information, SV.1–6). Only the linear range of the first order kinetic plots (within the first half-life) was included. Using the NH-diazocine **11** as the parent reference system, the nπ* bands in the UV-vis spectra and the thermal half-lives of the *E* isomer exhibit a systematic behavior as a function of the electronic nature of the substituent at the bridge N atom. Decreasing the electron density with Fmoc **10** and acetyl **14** groups at the bridge nitrogen atom, leads to hypsochromic shifts of the nπ* absorption maxima of the *E* isomers and sharper absorption bands, while the half-lives are significant longer. Electron donating substituents such as methyl (**12**) and ethyl (**13**) lead to bathochromic shifted nπ* absorption maxima and increased broadening and the half-lives are significantly shortened. Consequently, the sharper nπ* bands in acylated **10** and **14** result in higher photochemical *Z* → *E*

conversions due to the reduced overlap of their nπ* transitions.

NAc-diazocine **14** is soluble in water (~1 mM), a crucial point for biochemical and photopharmacological applications. Azobenzene based photopharmaca are susceptible to aggregation in water and have to be solubilized by addition of DMSO,³³ acetonitrile,² or encapsulation in water-soluble molecules.^{70,71} Moreover, photophysical properties of photo-switches such as conversion rates and quantum yields are often significantly lower in water compared to organic solvents. Another frequently observed problem are the shortened thermal half-lives of the metastable isomers in water.^{2,5} We therefore determined the photophysical properties and the kinetic parameters of NAc-diazocine **14** in water and compared these values with those measured in acetone (Table 3).

Table 3. Comparison of the Photophysical Properties and Half-Lives of NAc-Diazocine **14** in Acetone and Water

	NAc-diazocine 14	
	acetone	water
$\lambda_{\text{max}(Z)}^c$, ϵ_λ^a	398 nm, 564	393 nm, 587
$\lambda_{\text{max}(E)}^c$, ϵ_λ^a	516 nm, 850	502 nm, 868
$t_{1/2}$ (25 °C)	27 min	73 min
exp. ΔH^\ddagger / kcal mol ⁻¹	19.0	21.0
$\Gamma_{Z \rightarrow E}^b$ (400 nm)	88% ^c	78% ^d
$\Phi_{Z \rightarrow E}$ (400 nm)	0.48	0.51
$\Gamma_{E \rightarrow Z}^b$ (520 nm)	>99%	>99%
$\Phi_{E \rightarrow Z}$ (520 nm)	0.85	0.85

^a ϵ_λ [L mol⁻¹ cm⁻¹]. ^b $\Gamma_{Z \rightarrow E}$, $\Gamma_{E \rightarrow Z}$: conversion rates (%) $Z \rightarrow E$ and $E \rightarrow Z$ at the photostationary states upon irradiation at the given wavelengths. ^cUsing a 400 nm ± 5 nm bandpass filter. ^d¹H NMR measurement in D₂O/CD₃OD (20 Vol%) for better solubility.

Outstandingly, water as the solvent does virtually not alter the populations of the photostationary states (PSS 405 nm: 88% and 78% *E*, in acetone and H₂O, respectively), the quantum yields hardly change (Table 3) and the thermal half-life of the *E* isomer becomes even longer in water as compared to acetone.

Long-Term Switching Stability. The photostabilities of the NH-diazocines 10–14 (Figure 3 and Figure SV.8) were

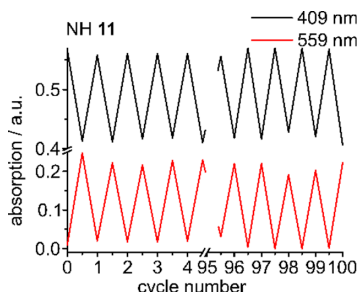


Figure 3. Stability measurements of the N-diazocine **11** in acetone. The sample was irradiated with 405 and 630 nm in an alternating sequence. The absorption was measured at 409 and 559 nm. Irradiation time for each cycle was 30 s.

investigated by irradiating the samples with 405 nm (12 mW cm^{-2}) and 630 nm (10 mW cm^{-2}) in an alternating sequence (switching, 100 cycles). The absorption after irradiation was measured at 409 and 559 nm for the first 5 and the last 5 cycles. No detectable fatigue was observed for any N-diazocine (**10–14**) (for details, see the Supporting Information, **SV.8**).

Conformational Analysis. To investigate the conformational and configurational energy landscape of NMe **12**, we employed quantum chemical calculations at the M06-2X(D3)/def2-TZVP level of density functional theory. All stationary points were checked by harmonic frequency analyses and are confirmed either as minima or saddle points. The Z configuration adopts two boat conformations, which rapidly interconvert under boat inversion with a barrier of 13.3 kcal mol⁻¹ (**Figure 4**). The boat conformation with the

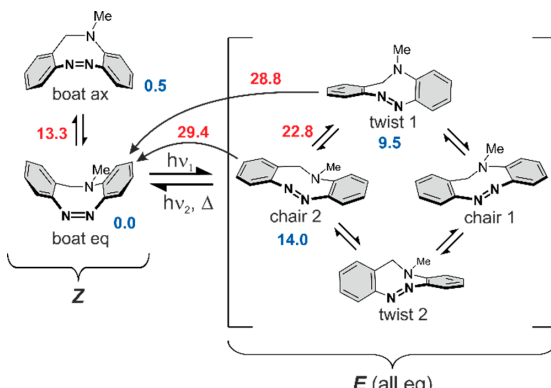


Figure 4. Theoretically calculated potential energy landscape (M06-2X(D3)/def2-TZVP) of NMe diazocine **12**. Relative energies (relative to **Z** (boat) in kcal mol⁻¹) are given underneath the corresponding structures in blue color. Transition state energies are written in red on the reaction arrows and are also relative to the **Z** boat structure. Note that the methyl groups in the **E** isomer are always equatorial.

equatorial methyl group is 0.5 kcal mol⁻¹ more stable compared to the conformation with the methyl group in axial position. Conformational space in the **E** configuration is more complicated. Four species, two twist (enantiomers twist 1 and twist 2) and two chair conformations (enantiomers chair 1 and chair 2), are in equilibrium. The twist conformations are

4.5 kcal mol⁻¹ more stable than the chair conformations. The activation barriers for the twist → chair interconversions are 22.8 kcal mol⁻¹. Thus, the conformational transformations should be fast on the NMR time scale at room temperature. A corresponding conformational analysis was performed for diazocines **11**, **13** and **14** (for details, see the Supporting Information, **SII**).

Thermal **E** → **Z** back-isomerization proceeds either directly from the **E** twist (**TS_I**, **Figure 4**) or via the **E** chair conformation (**TS_{II}**). Transition state analysis revealed that equatorial twist, as well as equatorial chair, are transformed to the equatorial boat conformation. The absolute barriers for both mechanisms are almost isoenergetic.

Our theoretical calculations are in good agreement with experimental results. In the ¹H NMR spectra (**Figure 5**) of the

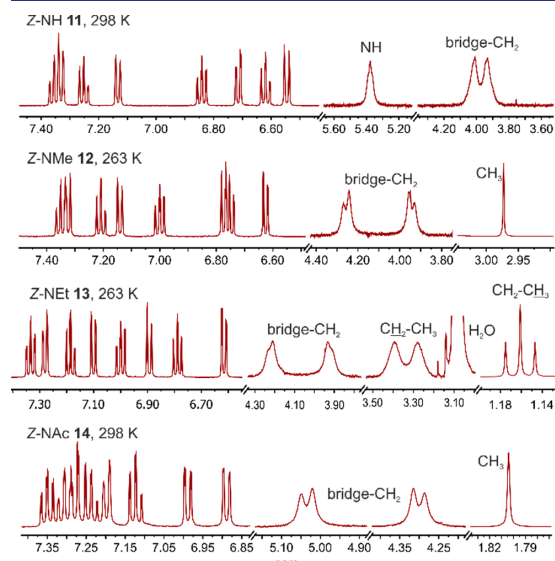


Figure 5. ¹H NMR spectra of the nitrogen bridged diazocines **11–14** in acetone-*d*₆ at different temperatures.

Z diazocines **11–14**, the bridge-CH₂ protons give rise to two separate broad signals (singlets or doublets) in all cases at room temperature. At low temperatures, the signals become sharp with expected multiplicities. We interpret this conformational movement as the boat → boat inversion of the central eight-membered ring. In a normal boat → boat inversion, we would expect an exchange of the axial protons to the equatorial position and vice versa. This was confirmed with 2D ¹H-EEXSY experiments (for details, see the Supporting Information, **SVI**).

However, the fact that the aromatic signals are sharp, and the singlets of the methyl group in NMe **12** and in NAc **14**, as well, are sharp singlets, indicates that the boat inversion interconverts two identical molecules (enantiomers) on the NMR time scale. Since all N-diazocines are unsymmetrical molecules (point group C_1) the two boat conformations would be diastereomers (ax. or eq substituted at the bridge N atom). Hence, there must be a second conformational movement at the bridge nitrogen atom, which is fast on the NMR time scale even at low temperatures, exchanging axial and equatorial positions. This fast process is an inversion at the bridge nitrogen atom.

The conformational space of the *E* isomer includes two twist (enantiomer pair) and two chair (enantiomer pair) conformations, which rapidly interconvert (see Figure 4). *E*-twist and *E*-chair are chemically different so we would expect two *E* signal sets, one for each molecule. This is not the case. Similar to the *Z* isomer, the spectra of the *E* diazocines 11–14 (Figure 6) exhibit one signal set of aromatic protons and

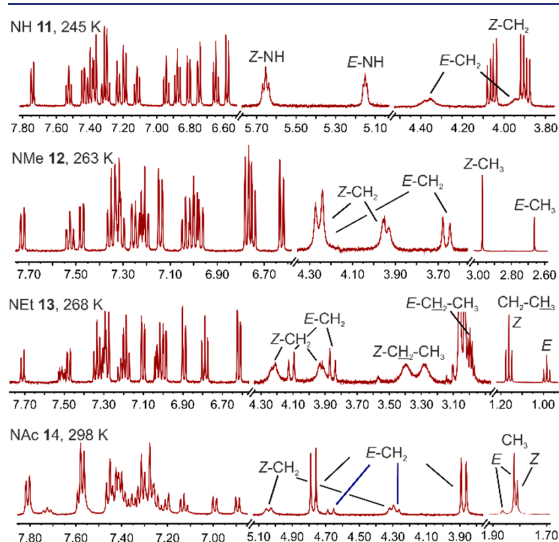


Figure 6. ^1H NMR spectra of the nitrogen bridged diazocines 11–14 in acetone- d_6 at different temperatures after irradiation with 405 nm.

broadened methylene bridge protons. Hence, either there is a fast chair \rightleftharpoons twist interconversion giving rise to a time-averaged signal, or one of the two conformations is considerably more populated than the other and below the detection limit in equilibrium or both. Our calculations (Figure 4) indeed predict, that the twist conformation is up to 4 kcal mol $^{-1}$ more stable than the chair species and the transition states (TS) connecting the chair and twist minima are low in energy (10–14 kcal mol $^{-1}$). It should be noted that a direct twist 1 \rightleftharpoons twist 2 (racemization) is not possible. No transition state (TS) could be located connecting these enantiomers directly. The same is true for the chair 1 \rightleftharpoons chair 2 interconversion (racemization). Racemization of the twist conformation has to proceed via one of the chair conformations and the chair molecules racemize via one of the twist structures, resulting in a cyclic topology as presented in Figure 4. Rapid racemization is in agreement with NMR experiments. The bridge-CH₂ proton axial \rightleftharpoons equatorial exchange was confirmed with 2D ^1H -EXSY experiments. In additional measurements, we found that by decreasing the temperature, these broadened signals are sharpened and form expected multiplicities (for details, see the Supporting Information, SVI). Nevertheless, the spectra of *E* NAc-diazocene 14 exhibit a second set of signals. The two species are in equilibrium as confirmed by 2D ^1H -EXSY experiments. We assign the two species to *E/Z* isomerization of the amide group (pointing toward and away from the neighboring phenyl group), which also is a slow conformational exchange on the chemical shift time scale.

Conclusion. Diazocines are molecular photoswitches with superior photophysical properties, such as very high quantum yields, conversion rates and fatigue resistance. Their higher stability of the *Z* configuration and metastability in their *E* form makes them particularly suitable for applications such as mechanophores in polymers and actuators in molecular machines. This is a major advantage above azobenzenes with their preferred *E* configuration. We now synthesized and investigated diazocines with a –CH₂–NR- bridge (N-diazocines), which are particularly promising for photopharmacology, because their switchable tricyclic structure, resembles a number of pharmacophores, such as hydroxysteroid dehydrogenase inhibitors, kinase inhibitors, prostanoid receptor ligands, antiallergics, anticholinergics, analgesics, serotonin uptake inhibitors and other neuroactive compounds. N-diazocines exhibit excellent switching properties: Their switching wavelengths for the *E* \rightarrow *Z* isomerization lie within the bio-optical window where penetration depth of blood supported tissue is largest. *E* to *Z* isomerization of NMe 12 and NEt 13 diazocene is achieved with light of >740 nm. Isomerization quantum yields of NH-diazocene 11 are $\Phi_{Z \rightarrow E} = 0.57$ (400 nm) and $\Phi_{E \rightarrow Z} = 0.80$ (520 nm) and thus considerably higher than those of the frequently used azobenzenes, spiropyrans or diarylethenes. No fatigue was observed during long-term switching experiments. Depending on the electronic nature of the substituents at the bridge N atom, half-lives for the thermal back-reaction (*E* \rightarrow *Z*) are between 22 s and 73 min (25 °C). Using a combination of NMR spectroscopy and quantum chemical calculations, we elucidated the conformational behavior in *Z* and *E* configuration, which is important in the design of N-diazocines toward applications in photopharmacology. The water-soluble system, NAc-diazocene 14, is a promising candidate for applications as a photoswitch in biochemistry and in photopharmacology. It retains high conversion rates, quantum yields, thermal half-life and fatigue-resistance in aqueous environments.

■ ASSOCIATED CONTENT

● Supporting Information

The Supporting Information is available free of charge on the ACS Publications website at DOI: 10.1021/jacs.9b06104.

DFT-calculations, experimental procedures, ^1H and ^{13}C NMRs of all compounds, photoswitching experiments (^1H NMR and UV-vis), molecule dynamic experiments, and quantum yield determination (PDF)

Photochemical switching of NMe-diazocene 12 with 405 nm (*Z* \rightarrow *E*) and 740 nm (*E* \rightarrow *Z*) (AVI)

Photochemical switching of NAc-diazocene 14 with 405 nm (*Z* \rightarrow *E*) and 520 nm (*E* \rightarrow *Z*) (AVI)

■ AUTHOR INFORMATION

Corresponding Author

*E-mail: rherges@oc.uni-kiel.de.

ORCID

Eduard Stadler: 0000-0003-0672-3165

Frank D. Sönnichsen: 0000-0002-4539-3755

Georg Gescheidt: 0000-0002-6827-4337

Rainer Herges: 0000-0002-6396-6991

Author Contributions

All authors have given approval to the final version of the manuscript.

Notes

The authors declare no competing financial interest.

ACKNOWLEDGMENTS

The authors gratefully acknowledge financial support by the Deutsche Forschungsgesellschaft (DFG) within the Collaborative Research Center SFB 677, "Function by Switching".

REFERENCES

- (1) Neilson, B. M.; Bielawski, C. W. Illuminating Photoswitchable Catalysis. *ACS Catal.* **2013**, *3*, 1874–1885.
- (2) Beharry, A. A.; Woolley, G. A. Azobenzene photoswitches for biomolecules. *Chem. Soc. Rev.* **2011**, *40*, 4422–4437.
- (3) Klajn, R. Spiropyran-based dynamic materials. *Chem. Soc. Rev.* **2014**, *43*, 148–184.
- (4) Katsonis, N.; Lubomska, M.; Pollard, M. M.; Feringa, B. L.; Rudolf, P. Synthetic light-activated molecular switches and motors on surfaces. *Prog. Surf. Sci.* **2007**, *82*, 407–434.
- (5) Szymanski, W.; Beierle, J. M.; Kistemaker, H. A.; Velema, W. A.; Feringa, B. L. Reversible photocontrol of biological systems by the incorporation of molecular photoswitches. *Chem. Rev.* **2013**, *113*, 6114–6178.
- (6) Hüll, K.; Morstein, J.; Trauner, D. In Vivo Photopharmacology. *Chem. Rev.* **2018**, *118*, 10710–10747.
- (7) Ito, Y.; Ito, H.; Matsuura, T. *Trans-cis* Photoisomerization of *meta*-(phenylazo) azobenzenes. *Tetrahedron Lett.* **1988**, *29*, 563–566.
- (8) Qiu, W.; Gurr, P. A.; da Silva, G.; Qiao, G. G. Insights into the mechanochromism of spiropyran elastomers. *Polym. Chem.* **2019**, *10*, 1650–1659.
- (9) Siewertsen, R.; Neumann, H.; Buchheim-Stehn, B.; Herges, R.; Näther, C.; Renth, F.; Temps, F. Highly Efficient Reversible Z-E Photoisomerization of a Bridged Azobenzene with Visible Light through Resolved S1(nπ*) Absorption Bands. *J. Am. Chem. Soc.* **2009**, *131*, 15594–15595.
- (10) Hammerich, M.; Schütt, C.; Stähler, C.; Lentz, P.; Röhricht, F.; Höppner, R.; Herges, R. Heterodiazocines: Synthesis and Photochromic Properties, Trans to Cis Switching within the Bio-optical Window. *J. Am. Chem. Soc.* **2016**, *138*, 13111–13114.
- (11) Thapaliya, E. R.; Zhao, J.; Ellis-Davies, G. C. R. Locked-Azobenzene: Testing the Scope of a Unique Photoswitchable Scaffold for Cell Physiology. *ACS Chem. Neurosci.* **2019**, *10*, 2481–2488.
- (12) Cabré, G.; Garrido-Charles, A.; Gonzalez-Lafont, A.; Moormann, W.; Langbehn, D.; Egea, D.; Lluch, J. M.; Herges, R.; Albes, R.; Busque, F.; Gorostiza, P.; Hernando, J. Synthetic Photoswitchable Neurotransmitters Based on Bridged Azobenzenes. *Org. Lett.* **2019**, *21*, 3780–3784.
- (13) Bowserand, B. H.; Craig, S. L. Empowering mechanochemistry with multi-mechanophore polymer architectures. *Polym. Chem.* **2018**, *9*, 3583–3593.
- (14) Böckmann, M.; Doltsinis, N. L.; Marx, D. Unraveling a Chemically Enhanced Photoswitch: Bridged Azobenzene. *Angew. Chem., Int. Ed.* **2010**, *49*, 3382–3384.
- (15) Siewertsen, R.; Schönborn, J. B.; Hartke, B.; Renth, F.; Temps, F. Superior Z → E and E → Z photoswitching dynamics of dihydrodibenzodiazocine, a bridged azobenzene, by S1(nπ*) excitation at $\lambda = 387$ and 490 nm. *Phys. Chem. Chem. Phys.* **2011**, *13*, 1054–1063.
- (16) Knie, C.; Utecht, M.; Zhao, F.; Kulla, H.; Kovalenko, S.; Brouwer, A. M.; Saalfrank, P.; Hecht, S.; Bléger, D. *ortho*-Fluoroazobenzenes: Visible Light Switches with Very LongLived Z Isomers. *Chem. - Eur. J.* **2014**, *20*, 16492–16501.
- (17) Ladányi, V.; Dvořák, P.; Al Anshori, J.; Vetráková, L.; Wirz, J.; Heger, D. Azobenzene photoisomerization quantum yields in methanol redetermined. *Photochem. Photobiol. Sci.* **2017**, *16*, 1757–1761.
- (18) Bortolus, P.; Monti, S. *Cis-trans* photoisomerization of azobenzene. Solvent and triplet donors effects. *J. Phys. Chem.* **1979**, *83*, 648–652.
- (19) Jiang, C.-W.; Xie, R.-H.; Li, F.-L.; Allen, R. E. Comparative Studies of the trans-cis Photoisomerizations of Azobenzene and a Bridged Azobenzene. *J. Phys. Chem. A* **2011**, *115*, 244–249.
- (20) Pansare, V. J.; Hejazi, S.; Faenza, W. J.; Prud'Homme, R. K. *Chem. Mater.* **2012**, *24*, 812–827.
- (21) Sadovski, O.; Beharry, A. A.; Zhang, F.; Woolley, G. A. Spectral tuning of azobenzene photoswitches for biological applications. *Angew. Chem., Int. Ed.* **2009**, *48*, 1484–1486.
- (22) Beharry, A. A.; Sadovski, O.; Woolley, G. A. Azobenzene Photoswitching without Ultraviolet Light. *J. Am. Chem. Soc.* **2011**, *133*, 19684–19687.
- (23) Samanta, S.; Beharry, A. A.; Sadovski, O.; McCormick, T. M.; Babalhavaeji, A.; Tropepe, V.; Woolley, G. A. Photoswitching Azo Compounds in Vivo with Red Light. *J. Am. Chem. Soc.* **2013**, *135*, 9777–9784.
- (24) Bléger, D.; Schwarz, J.; Brouwer, A. M.; Hecht, S. o-Fluoroazobenzenes as Readily Synthesized Photoswitches Offering Nearly Quantitative Two-Way Isomerization with Visible Light. *J. Am. Chem. Soc.* **2012**, *134*, 20597–20600.
- (25) Samanta, S.; McCormick, T. M.; Schmidt, S. K.; Seferos, D. S.; Woolley, G. A. Robust visible light photoswitching with *ortho*-thiol substituted azobenzenes. *Chem. Commun.* **2013**, *49*, 10314–10316.
- (26) Dong, M.; Babalhavaeji, A.; Samanta, S.; Beharry, A. A.; Woolley, G. A. Red-Shifting Azobenzene Photoswitches for in Vivo Use. *Acc. Chem. Res.* **2015**, *48*, 2662–2670.
- (27) Bléger, D.; Hecht, S. Visible-Light-Activated Molecular Switches. *Angew. Chem., Int. Ed.* **2015**, *54*, 11338–11349.
- (28) Samanta, S.; Babalhavaeji, A.; Dong, M.; Woolley, G. A. Photoswitching of *ortho*-substituted azonium ions by red light in whole blood. *Angew. Chem., Int. Ed.* **2013**, *52*, 14127–14130.
- (29) Dong, M.; Babalhavaeji, A.; Collins, C.; Jarrah, K.; Sadovski, O.; Dai, Q.; Woolley, G. A. Near-Infrared Photoswitching of Azobenzenes under Physiological Conditions. *J. Am. Chem. Soc.* **2017**, *139*, 13483–13486.
- (30) Crespi, S.; Simeth, N. A.; Koenig, B. Heteroaryl azo dyes as molecular photoswitches. *Nature Rev. Chem.* **2019**, *3*, 133–146.
- (31) Wendler, T.; Schütt, C.; Näther, C.; Herges, R. Photoswitchable Azoheterocycles via Coupling of Lithiated Imidazoles with Benzenediazonium Salts. *J. Org. Chem.* **2012**, *77*, 3284–3287.
- (32) Schehr, M.; Ianes, C.; Weisner, J.; Heintze, L.; Müller, M. P.; Pichlo, C.; Charl, J.; Brunstein, E.; Ewert, J.; Lehr, M.; Baumann, U.; Rauh, D.; Knippschild, U.; Peifer, C.; Herges, R. 2-Azo-, 2-diazocine-thiazols and 2-azooimidazoles as photoswitchable kinase inhibitors: limitations and pitfalls of the photoswitchable inhibitor approach. *Photochem. Photobiol. Sci.* **2019**, *18*, 1398–1407.
- (33) Weston, C. E.; Richardson, R. D.; Haycock, P. R.; White, A. J.; Fuchter, M. J. Arylazopyrazoles: Azoheteroarene Photoswitches Offering Quantitative Isomerization and Long Thermal Half-Lives. *J. Am. Chem. Soc.* **2014**, *136*, 11878–11881.
- (34) Calbo, J.; Weston, C. E.; White, A. J. P.; Rzepa, H. S.; Contreras-García, J.; Fuchter, M. J. Tuning Azoheteroarene Photoswitch Performance through Heteroaryl Design. *J. Am. Chem. Soc.* **2017**, *139*, 1261–1274.
- (35) Gibson, R. S. L.; Calbo, J.; Fuchter, M. J. Chemical Z-E Isomer Switching of Arylazopyrazoles Using Acid. *ChemPhotoChem* **2019**, *3*, 372–377.
- (36) Yang, Y.; Hughes, R. P.; Aprahamian, I. Visible Light Switching of a BF₂-Coordinated Azo Compound. *J. Am. Chem. Soc.* **2012**, *134*, 15221–15224.
- (37) Yang, Y.; Hughes, R. P.; Aprahamian, I. Near-Infrared Light Activated Azo-BF₂ Switches. *J. Am. Chem. Soc.* **2014**, *136*, 13190–13193.

- (38) Weston, C. E.; Richardson, R. D.; Fuchter, M. J. Photoswitchable basicity through the use of azoheteroarenes. *Chem. Commun.* **2016**, *52*, 4521–4524.
- (39) Venkataramani, S.; Jana, U.; Dommaschk, M.; Söennichsen, F. D.; Tuczek, F.; Herges, R. Magnetic bistability of molecules in homogeneous solution at room temperature. *Science* **2011**, *331*, 445–448.
- (40) Dommaschk, M.; Peters, M.; Gutzeit, F.; Schütt, C.; Näther, C.; Söennichsen, F. D.; Tiwari, S.; Riedel, C.; Boretius, S.; Herges, R. Photoswitchable Magnetic Resonance Imaging Contrast by Improved Light-Driven Coordination-Induced Spin State Switch. *J. Am. Chem. Soc.* **2015**, *137*, 7552–7555.
- (41) Heitmann, G.; Dommaschk, M.; Löw, R.; Herges, R. Modular Synthetic Route to Monofunctionalized Porphyrin Architectures. *Org. Lett.* **2016**, *18*, 5228–5231.
- (42) Dommaschk, M.; Näther, C.; Herges, R. Synthesis of Functionalized Perfluorinated Porphyrins for Improved Spin Switching. *J. Org. Chem.* **2015**, *80*, 8496–8500.
- (43) Gutzeit, F.; Dommaschk, M.; Levin, N.; Buchholz, A.; Schaub, E.; Plass, W.; Näther, C.; Herges, R. Structure and Properties of a Five-Coordinate Nickel(II) Porphyrin. *Inorg. Chem.* **2019**, in press. DOI: [10.1021/acs.inorgchem.9b00348](https://doi.org/10.1021/acs.inorgchem.9b00348)
- (44) Fink, B. E.; Gavai, A. V.; Tokarski, J. S.; Goyal, B.; Misra, R.; Xiao, H.-J.; Kimball, S. D.; Han, W.-C.; Norris, D.; Spires, T. E.; You, D.; Gottardis, M. M.; Lorenzi, M. V.; Vite, G. D. Identification of a novel series of tetrahydridobenzazocines as inhibitors of 17 β -hydroxysteroid dehydrogenase type 3. *Bioorg. Med. Chem. Lett.* **2006**, *16*, 1532–1536.
- (45) Arnold, L. A.; Guy, R. K. Synthesis of highly substituted dibenzo[b,f]azocines and their evaluation as protein kinase inhibitors. *Bioorg. Med. Chem. Lett.* **2006**, *16*, 5360–5363.
- (46) Fink, B. E.; Gavai, A. V.; Vite, G. D.; Han, W.-C.; Misra, R. N.; Xiao, H.-Y.; Norris, D.-J.; Tokarski, J. S. Fused tricyclic compounds as inhibitors of 17 β -hydroxysteroid dehydrogenase 3; U.S. Patent 2005250753, 2008.
- (47) Ruel, R.; Lacombe, P.; Abramovitz, M.; Godbout, C.; Lamontagne, S.; Rochette, C.; Sawyer, N.; Stocco, R.; Tremblay, N.-M.; Metters, K.-M.; Labelle, M. New class of biphenylene dibenzazocinones as potent ligands for the human EP1 prostanoid receptor. *Bioorg. Med. Chem. Lett.* **1999**, *9*, 2699–2704.
- (48) Yale, H. L.; Sowinski, F. A. 5-(Substituted Amino-Lower Alkylene)-5,6-Dihydridobenz[b,f]Azocines; U.S. Patent 3514443, 1970.
- (49) Morstein, J.; Awale, M.; Reymond, J.-L.; Trauner, D. Mapping the Azolog Space Enables the Optical Control of New Biological Targets. *ACS Cent. Sci.* **2019**, *5*, 607–618.
- (50) Villani, F. J.; Ellis, C. A.; Teichman, C.; Bigos, C. Dialkylaminoalkyl Derivatives of 10,11-Dihydro-SH-dibenzo[a,d]-cycloheptene and Related Compounds. *J. Med. Pharm. Chem.* **1962**, *5*, 373–383.
- (51) Stach, K.; Bickelhaupt, F. Beiträge zur Entwicklung psychotroper Stoffe, 2. Mitt.: Basisch substituierte Dibenzo-oxepin-, Dibenzo-thiepin- und Dibenzo-cycloocten-Derivate. *Monatsh. Chem.* **1962**, *93*, 896–904.
- (52) Kurokawa, M.; Sato, F.; Fujiwara, I.; Hatano, N.; Honda, Y.; Yoshida, T.; Naruto, S.; Mastumoto, J.; Uno, H. A new class of calcium antagonists. 2. Synthesis and biological activity of 11-[4-[4-(4-fluorophenyl)-1-piperazinyl]butyryl]amino]-6,11-dihydridobenz[b,e]thiepin maleate and related compounds. *J. Med. Chem.* **1991**, *34* (3), 927–934.
- (53) Lee, E. E.; Maibach, H. I. Treatment of Urticaria. An evidence-based evaluation of antihistamines. *Am. J. Clin. Dermatol.* **2001**, *2*, 27–32.
- (54) Takemoto, Y.; Ito, A.; Niwa, H.; Okamura, M.; Fujiwara, T.; Hirano, T.; Handa, N.; Umehara, T.; Sonoda, T.; Ogawa, K.; Tariq, M.; Nishino, N.; Dan, S.; Kagechika, H.; Yamori, T.; Yokoyama, S.; Yoshida, M. Identification of Cyproheptadine as an Inhibitor of SET Domain Containing Lysine Methyltransferase 7/9 (Set7/9) That Regulates Estrogen-Dependent Transcription. *J. Med. Chem.* **2016**, *59*, 3650–3660.
- (55) Wilhelm, M. The chemistry of polycyclic psycho-active drugs—serendipity or systematic investigation? *Pharm. J.* **1975**, *214*, 414–416.
- (56) Casarotto, M. G.; Craik, D. J. Ring Flexibility within Tricyclic Antidepressant Drugs. *J. Pharm. Sci.* **2001**, *90*, 713–721.
- (57) Paudler, W. W.; Zeiler, A. G. Diazocine chemistry. VI. Aromaticity of 5,6-dihydridobenz[b,f][1,2]diazocine. *J. Org. Chem.* **1969**, *34*, 3237–3239.
- (58) Deo, C.; Bogliotti, N.; Métivier, R.; Retailleau, P.; Xie, J. A Visible Light Triggered Conformational Diastereomer Photoswitch in a Bridged Azobenzene. *Chem. - Eur. J.* **2016**, *22*, 9092–9096.
- (59) Tellkamp, T.; Shen, J.; Okamoto, Y.; Herges, R. Diazocines on Molecular Platforms. *Eur. J. Org. Chem.* **2014**, *2014*, 5456–5461.
- (60) Duval, H. Recherches sur la benzidination. *Bull. Soc. Chim. Fr.* **1910**, *7*, 727–732.
- (61) Moormann, W.; Langbehn, D.; Herges, R. Solvent-Free Synthesis of Diazocine. *Synthesis* **2017**, *49*, 3471–3475.
- (62) Joshi, D. K.; Mitchell, M. J.; Bruce, D.; Lough, A. J.; Yan, H. Synthesis of cyclic azobenzene analogues. *Tetrahedron* **2012**, *68*, 8670–8676.
- (63) Schehr, M.; Hugenbusch, D.; Moje, T.; Näther, C.; Herges, R. Synthesis of mono-functionalized S-diazocines via intramolecular Baeyer–Mills reactions. *Beilstein J. Org. Chem.* **2018**, *14*, 2799–2804.
- (64) Choi, A. W.-T.; Yim, V. M.-W.; Liu, H. W.; Lo, K. K.-W. Rhodium(I) Polypyridine Diamine Complexes as Intracellular Phosphogenic Sensors: Synthesis, Characterization, Emissive Behavior, Biological Properties, and Nitric Oxide Sensing. *Chem. - Eur. J.* **2014**, *20*, 9633–9642.
- (65) Meerwein, H.; Hinz, G.; Hofmann, P.; Kroning, E.; Pfeil, E. Über tertiäre Oxoniumsalze, I. *J. Prakt. Chem.* **1937**, *147*, 257–285.
- (66) Valeur, E.; Bradley, M. Amide bond formation: beyond the myth of coupling reagents. *Chem. Soc. Rev.* **2009**, *38*, 606–631.
- (67) Stadler, E.; Eibel, A.; Fast, D.; Freiheit, H.; Holly, C.; Wiech, M.; Moszner, N.; Gescheidt, G. A versatile method for the determination of photochemical quantum yields via online UV-Vis spectroscopy. *Photochem. Photobiol. Sci.* **2018**, *17*, 660–669.
- (68) Rau, H.; Greiner, G.; Gauglitz, G.; Meier, H. Photochemical quantum yields in the A (+hv) ⇌ (B (+hv, Δ)) system, when only the spectrum of A is known. *J. Phys. Chem.* **1990**, *94*, 6523–6524.
- (69) Irie, M. Diarylethenes for Memories and Switches. *Chem. Rev.* **2000**, *100*, 1685–1716.
- (70) Wang, D.; Wagner, M.; Butt, H.-J.; Wu, S. Supramolecular hydrogels constructed by red-light-responsive host–guest interactions for photo-controlled protein release in deep tissue. *Soft Matter* **2015**, *11*, 7656.
- (71) Wang, D.; Wagner, M.; Butt, H.-J.; Wu, S. Supramolecular hydrogels constructed by red-light-responsive host–guest interactions for photo-controlled protein release in deep tissue. *Soft Matter* **2015**, *11*, 7656.

3.4 Gerichtete Schaltung und erhöhte Effizienz

Die Erforschung artifizieller photochemischer Schalter ist für die Anwendung nicht nur in Pharmazeutika, sondern auch ganz allgemein in molekularen Maschinen, Motoren, Pumpen, Sensoren oder Aktuatoren enorm wichtig. Essentiell für einen erfolgreichen Einsatz sind neben Ermüdungsresistenzen, chemischer Robustheit und hohen Umsatzraten zwischen den meta- und stabilen Zuständen auch die für bestimmte technische Vorgänge wichtige gerichtete Schaltbewegung. Die meisten bisher etablierten schaltbaren Systeme weisen entweder keine direktionale Bewegung auf (achiral) oder sind schwer zugänglich bzw. modifizierbar. Die direktionale Umwandlung und somit die gezielte Anreicherung über nur einen Reaktionsweg würde zusätzlich einen weiteren wichtigen Faktor für den Einsatz in molekularen Maschinen begünstigen: die Effizienz der Konversion von Licht in chemische Energie oder besonders in nutzbare Arbeit. Diese hängt dabei von Anregungswellenlänge, Quantenausbeute und direkt von der Menge erzeugter Energie oder Arbeit ab.

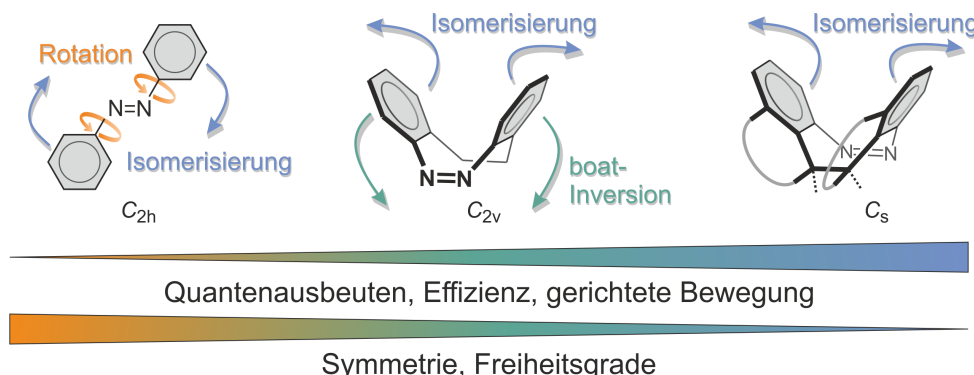


Abb. 3.6: Überlegungen zur systematischen Verbesserung der photophysikalischen Eigenschaften von AB (links) durch verschiedene Verbrückungen: Die *ortho*-Ethinylverbrückung im DAC (mittig) erniedrigt die Symmetrie/Freiheitsgrade und steigert die Quantenausbeuten/Konversionsraten. Eine doppelte Überbrückung (rechts) könnte die Freiheitsgrade noch weiter reduzieren und dadurch eine gerichtete Schaltbewegung mit hoher Effizienz bedingen.

Die systematische Überarbeitung vom am häufigsten eingesetzten Photoschalter AB hin zum DAC war der erste Schritt in der Optimierung: bathochrom verschobene Absorptionsbanden, höhere Quantenausbeuten und verbesserte Konversionsraten bei gleichzeitig leichter Zugänglichkeit und bei den Hetero-DACs auch Modifizierbarkeit. Doch eine gerichtete Schaltbewegung weisen auch die bisher etablierten DACs nicht auf. Um diese Klasse der photochromen Schalter weiter in ihren konformationellen Freiheitsgraden einzuschränken und damit eine direktionale Bewegung zu ermöglichen, könnte der zentrale Achtring des tricyclischen Systems chiral modifiziert werden (s. Abb. 3.7). Ein solches Design sollte neben der Vermeidung nicht zielführender Schaltprozesse eine Erhöhung der Quantenausbeute und somit der Konversionsrate ermöglichen. Das Resultat wäre eine gesteigerte Effizienz der Konversion von Licht in chemische Energie und somit ein vielversprechender Kandidat als Antrieb in molekularen Maschinen.

3.5 Efficient Conversion of Light to Chemical Energy: Directional, Chiral Photoswitches with Very High Quantum Yields

W. Moormann, T. Tellkamp, E. Stadler, F. Röhricht, C. Näther, R. Puttreddy, K. Rissanen, G. Gescheidt und R. Herges

Angew. Chem. **2020**, *59*, 15081-15086.

DOI:10.1002/anie.202005361

Deutsche Version: DOI:10.1002/ange.202005361

Supporting Information: Anhang Begleitmaterial 8

Wissenschaftliche Beiträge: Benchmarking verschiedener DFT-Niveaus an der exp. bestimmten Isomerisierungenthalpie von AB und durch Geometrieabweichung zu Diindandiazocinen (DIDs)-Kristallstrukturen, Geometrieoptimierung der ABs, DACs und Diindandiazocine (DIDs), TSS der Isomerisierung der *meso*- und *rac*-DIDs, Verfassen von Manuskriptteilen, Übersetzung des Manuskripts ins Deutsche.

Zusammenfassung

Die Entwicklung des Stamm-DAC hin zum Diindandiazocin (DID) führt mit hohen Quantenausbeuten und Konversionsraten (stabil → metastabil) zu Umwandlungseffizienzen, die AB um das mehr als 10-fache sowie das Stamm-DAC um fast das 3-fache übersteigen. Hierfür wurden Ethylenbrücken so eingeführt (s. Abb. 3.7), dass mit zwei Stereozentren zwei Konstitutionsisomere, ein *meso*- sowie ein *racemisches* DID, vorliegen. Diese Formen können nicht ineinander konvertieren, was es möglich macht, die Strukturen und deren konformationellen Raum getrennt voneinander zu untersuchen. Um möglichst aussagekräftige Werte für die Umwandlung von Licht in chemische Energie zu erhalten, wurde ein Benchmarking verschiedener Niveaus von DFT-Rechnungen an der exp. Isomerisierungsenthalpie von AB sowie ein struktureller Abgleich optimierter Geometrien mit den in dieser Arbeit erhaltenen Kristallstrukturen durchgeführt.

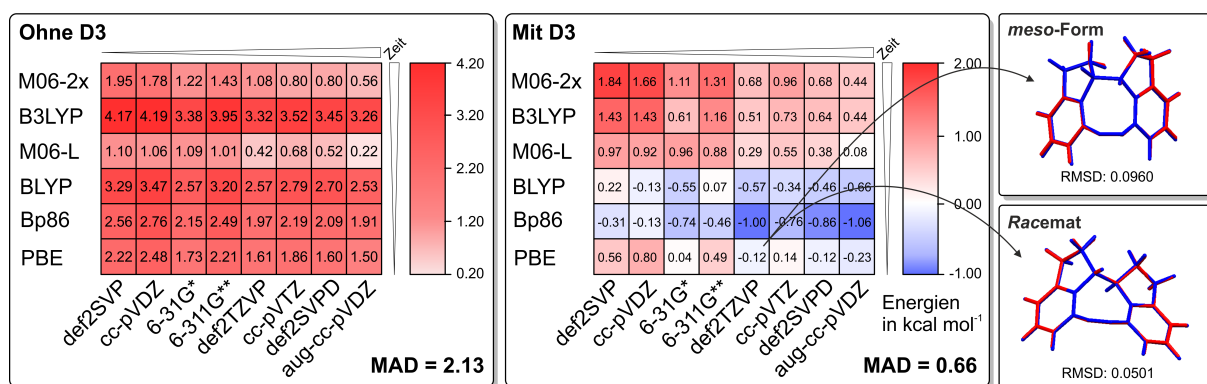


Abb. 3.7: Benchmarking verschiedener Niveaus an der Isomerisierungsenthalpie von AB: Dargestellt ist die Abweichung von diesem Wert. Der MAD zeigt wie vorteilhaft insgesamt der Einsatz von Dispersionskorrektur (D3) ist, da alle Ergebnisse näher am Experiment liegen. Den besten Kompromiss liefert PBE-D3(BJ)/def2TZVP, da zusätzlich im Einkristallstrukturvergleich (Einkristall: blau, DFT-Optimierung: rot) die geringsten Abweichungen (RMSD, *root mean square deviation*) festgestellt werden.

Das Benchmarking zeigt über die mittlere absolute Abweichung (*mean absolute deviation*) (MAD), dass der Einsatz der Dispersionskorrektur (D3) deutlich bessere Werte liefert als ohne Korrektur. Aus den vielversprechendsten Kombinationen stellt sich durch die geringste Abweichung mit der Kristallstruktur das Niveau PBE-D3(BJ)/def2TZVP als bester Kompromiss zwischen Rechenaufwand und Genauigkeit dar. Die Rechnungen belegen die *a priori* Idee: Die *cis*-boat-Inversion sowie die Inversion der twist-Isomere ist nicht zu beobachten, da die dabei entstehenden Konformationen energetisch extrem gespannt und ungünstig sind. Dies ist entscheidend für die gerichtete Schaltbewegung. Im Falle der *meso*-Verbindung entsteht neben der direktonalen Isomerisierung durch die zusätzliche Spannung einer Indanverbrückung eine potentielle Energie von 18.5 kcal mol⁻¹ (PBE-D3(BJ)/def2TZVP). Allein dies ist im Vergleich zum StammDAC bei gleicher Anregungswellenlänge eine mehr als doppelt so hohe Energieumwandlung von Licht in chemische Energie.

Efficient Conversion of Light to Chemical Energy: Directional, Chiral Photoswitches with Very High Quantum Yields

Widukind Moermann, Tobias Tellkamp, Eduard Stadler, Fynn Röhricht, Christian Näther, Rakesh Puttreddy, Kari Rissanen, Georg Gescheidt, and Rainer Herges*

Abstract: Photochromic systems have been used to achieve a number of engineering functions such as light energy conversion, molecular motors, pumps, actuators, and sensors. Key to practical applications is a high efficiency in the conversion of light to chemical energy, a rigid structure for the transmission of force to the environment, and directed motion during isomerization. We present a novel type of photochromic system (diindane diazocines) that converts visible light with an efficiency of 18% to chemical energy. Quantum yields are exceptionally high with >70% for the *cis*-*trans* isomerization and 90% for the back-reaction and thus higher than the biochemical system rhodopsin (64%). Two diastereomers (*meso* and *racemate*) were obtained in only two steps in high yields. Both isomers are directional switches with high conversion rates (76–99%). No fatigue was observed after several thousands of switching cycles in both systems.

Photochemically induced *cis*-*trans* isomerizations (e.g. of retinal) are the key processes in the perception of light and for retinal-based photosynthesis (pumping protons through ion channels in halophilic bacteria).^[1] Notwithstanding the very different functions (sensing and directed motion), both

systems are based on the same reversible chemical reaction: the photoisomerization of retinal.^[2–4] Nature has optimized these systems for more than 2 billion years to achieve high quantum yields (64–67%), conversion rates (between the (meta)stable states), and fatigue resistance.^[5] Within the last four decades a number of artificial photoswitches have been developed and optimized, aiming at a plethora of applications, such as motors, pumps, actuators, switchable drugs, sensors, and switchable liquid crystals. However, to the best of our knowledge, the quantum yields of biological systems are still unmatched (Figure 1)^[6] with the exception of diazocene, which was developed by our group.^[7]

Whereas previous artificial systems exhibit high conversion rates and fatigue resistance, their energy conversion process is not adequately efficient. The efficiency of converting light into chemical energy or to perform work is a function of the wavelength λ of the absorbed light, the quantum yield Φ , and the amount of energy E or work W produced. Particularly for the conversion of light into useful work, further properties such as directional motion (e.g. chiral switch) and sufficient rigidity for the transmission of the molecular force to the environment are prerequisites. Additional important parameters are conversion rates (photostationary states, PSS) and fatigue resistance (long-term stability). We therefore set out to systematically improve the performance of the most frequently used artificial photoswitch azobenzene **1** and have been successful in enhancing all above parameters. The conversion wavelengths are shifted into the visible range, the quantum yields improved to 70–90% (surpassing even the most efficient biological system rhodopsin), the strain energy produced increased to 18 kcal mol⁻¹, the molecular switching movement is directional, the molecular framework is rigid (no conformational degrees of freedom), and the fatigue resistance amounts to at least a few thousand cycles.

Moreover, our new switches (**3** and **4**) presented here are accessible from commercially available starting materials in only two steps at high yields. Figure 1b compares the efficiency of converting light into chemical energy (strain) of azobenzene **1** (1.4%), diazocene **2** (7.6%), and *meso*-diindanediazocene **3** (18.1%) upon irradiation at their peak absorption wavelengths 317, 385, and 400 nm. *meso*-Diindanediazocene **3** is not suitable for immediate long-term chemical energy storage,^[15] however, the short lifetime of the metastable state and the superior photophysical properties make it an ideal motor for ATP-synthase type light-driven synthesis^[16] and other light-to-chemical-energy conversion systems.^[17]

* Dr. W. Moermann, Dr. T. Tellkamp, F. Röhricht, Prof. Dr. R. Herges
Otto-Diels-Institut für Organische Chemie
Christian-Albrechts-Universität zu Kiel
Otto-Hahn-Platz 4, 24118 Kiel (Germany)

E-mail: rherges@oc.uni-kiel.de

Dr. E. Stadler, Prof. Dr. G. Gescheidt
Institute of Physical and Theoretical Chemistry
Graz University of Technology
Stremayrgasse 9, 8010 Graz (Austria)

Prof. Dr. C. Näther
Institut für Anorganische Chemie
Christian-Albrechts-Universität zu Kiel
Max-Eyth-Str. 2, 24118 Kiel (Germany)

Dr. R. Puttreddy, Prof. Dr. K. Rissanen
University of Jyväskylä, Department of Chemistry
P.O. Box 35, 40014 Jyväskylä (Finland)

Dr. R. Puttreddy
Smart Photonic Materials, Faculty of Engineering and Natural Sciences, Tampere University
P. O. Box 541, 33101, Tampere (Finland)

Supporting information and the ORCID identification number(s) for the author(s) of this article can be found under:
<https://doi.org/10.1002/anie.202005361>.

© 2020 The Authors. Published by Wiley-VCH Verlag GmbH & Co. KGaA. This is an open access article under the terms of the Creative Commons Attribution License, which permits use, distribution and reproduction in any medium, provided the original work is properly cited.

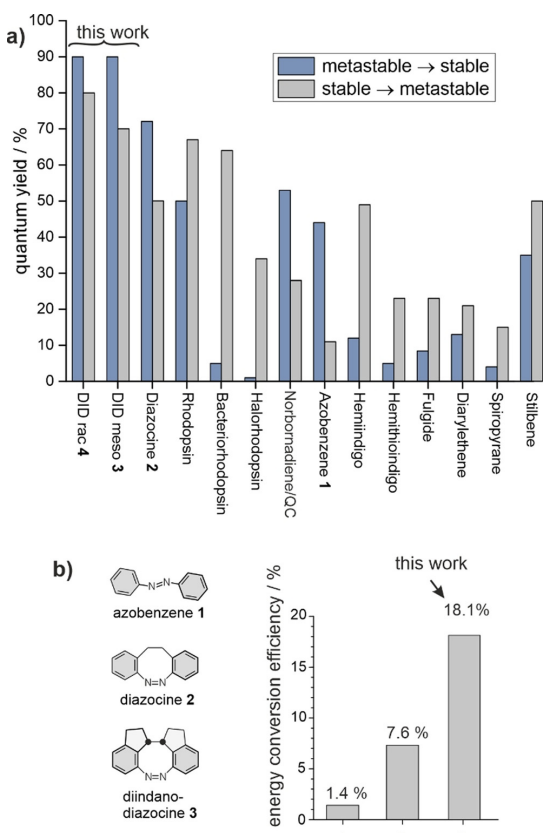


Figure 1. Switching properties of selected photochromic compounds. a) Quantum yields of diindane diazocines (DID meso 3 and DID rac 4) presented in this work compared to frequently used artificial photoswitches and natural systems.^[3,4,6,8–14] For an extended list of photoswitches and quantum yields see Supporting Information Table S1. b) Efficiency of the conversion of light to chemical energy (strain energy, see Supporting Information Figure S28).

Arguably, the most frequently used artificial photoswitch is azobenzene **1**. Azobenzene derivatives are easily accessible, robust, reliable, chemically inert, and fatigue resistant. However, UV light is needed for the isomerization of the *trans* to the *cis* isomer, conversion rates are usually not high, and quantum yields are relatively low.^[10,18] By the introduction of ethylene bridges between the *o,o'* positions of azobenzenes, we have been able to improve the photophysical properties considerably.^[7] Compared with **1**, these diazocines **2** exhibit enhanced quantum yields, switching wavelengths in the visible range, and very high conversion rates. Moreover, diazocines **2** are thermodynamically more stable in their bulkier *cis* configuration, which is of advantage in applications such as photopharmacology and mechanosensing.^[19–22]

However, neither the parent azobenzene **1** nor diazocine **2** are directional switches and are therefore unable to induce directional motion (Figure 2a,b, curved arrows in **3** and **4** indicate the directionality of the molecular movement during

isomerization). Introduction of additional bridges into the tricyclic diazocine system should further reduce conformational movements and introduces directionality into the switching motion. Moreover, the elimination of conformational degrees of freedom should concomitantly increase the quantum yields of the switching processes by preventing unproductive relaxation pathways.^[23,24]

Aiming at the improvement of our parent diazocine switches along the above lines, we pursued a design strategy based on ring strain. Figure 2c illustrates our approach by means of a simplified model. Starting from the parent *cis* and *trans* diazocine **2** and introducing two ethylene bridges between positions 1–11 and 10–12, 8 different isomers of bridged diazocines (diindanodiazocines) are conceivable (Figure 2c). Concomitant introduction of two stereocenters leads to a *meso* compound (*m*) **3** and a racemate (*r*) **4**. *Cis* and *trans* isomers are denoted with *c* and *t*. *Syn* annelations are favorable (*f*) and *anti* annelations are strained and unfavorable (*u*). Hence, four *meso* isomers result: *m-c-uu*, *m-c-ff*, *m-t-uf*, and *m-t-fu*. Analogously, the racemate comes as *r-c-uu*, *r-c-ff*, *r-t-uf*, and *r-t-fu*. *Meso* **3** and racemate **4** do not interconvert because that would imply an inversion at a sp^3 carbon. Hence, the conformational degrees of freedom of meso **3** and rac **4** can be analyzed separately. Besides *cis-trans* isomerization, there two conceivable conformational transitions: ring inversion of the *cis*-boat, and twist- and twist-chair inversion of the *trans* isomer. Simple molecular model considerations reveal that the inversion at azo nitrogen atom 5 induces a rotation of the 12 methylene group and thus a change from a favorable (*f*) to an unfavorable bridge (*u*) or vice versa. Likewise the inversion at N6 (atom numbering see Figure 2b) interconverts the pseudo axial and pseudo equatorial hydrogen atoms at position 11 and thus changes the strain of the corresponding bridge. Both boat inversion and twist inversion change both bridges from favorable to unfavorable or vice versa. From these simple model considerations, the reaction network shown in Figure 2c,d can be derived. The relative energies of the 8 isomers can be estimated as well without explicit calculations. The *cis* isomer of diazocine is approximately 8 kcal mol⁻¹ more stable than *trans*, and if we assume that an unfavorable bridge induces about 10 kcal mol⁻¹ strain, the most stable *meso cis* structure *m-c-ff* is about 18 kcal mol⁻¹ more stable than its *trans* isomer, whereas the *cis* (*r-c-uf*) and *trans* (*r-t-ff*) racemate should be almost isoenergetic. Structures *m-c-uu* and *r-t-uu* with two strained bridges are extremely unfavorable and probably not accessible. We should not observe the *r-c-uf* ⇌ *r-c-fu* ring inversion and the *m-t-uf* ⇌ *m-t-fu* twist inversion because a high activation barrier can be expected, since both conformational movements include the simultaneous change of the strain of two bridges. Explicit DFT calculations at the PBE(D3(BJ))/def2TZVP level of density functional theory (Supporting Information Figures S26 and S27, Table S7) support our qualitative picture (blue numbers in Figure 2a–c). Upon irradiation, the *meso cis* compound (*m-c-ff*) should convert into a high-energy *trans* isomer (*m-t-uf*) with a strain energy of 18.5 kcal mol⁻¹. The *cis* and *trans* isomers of the racemate are close in energy (3.5 kcal mol⁻¹ in favor of the *cis* isomer). Transition state calculations confirm the expected high

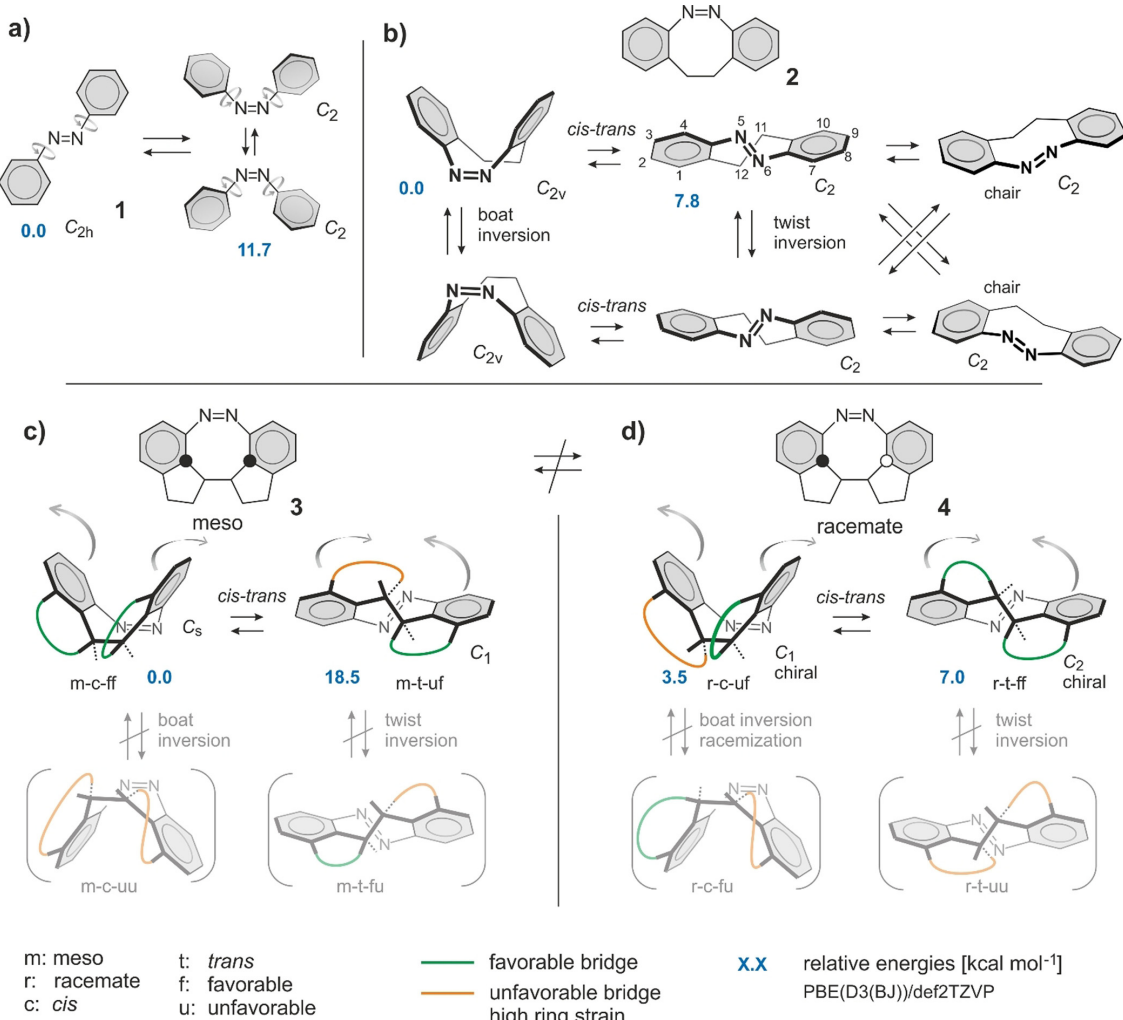


Figure 2. Stepwise reduction of conformational degrees of freedom by the introduction of bridges into azobenzene. a) azobenzene **1**, b) diazocine **2**, and c,d) doubly bridged diazocines (diindane diazocines) **3** and **4**. a) *trans* azobenzene **1** (C_{2h}), upon irradiation, gives two enantiomeric *cis*-azobenzenes **1** (C_2) that rapidly interconvert at room temperature by almost free rotation of the phenyl groups. b) In diazocine **2** the phenyl rings are fixed by an ethylene bridge connecting the two rings. Conformational movements are restricted to twist inversions and twist-chair inversions of the *trans* configuration. The *cis* configuration undergoes boat inversion at room temperature. c,d) There are two diastereomers of diindane diazocine: *meso* **3** and *racemate* **4**. Both compounds are conformationally rigid. There is no boat inversion and no twist inversion, which restricts each of the *cis* and the *trans* isomers to only one conformation. The $-\text{CH}_2-\text{CH}_2-$ bridge is either favorable (*syn* annelation, green) or strained (*anti* annelation, orange). Relative energies (kcal mol^{-1}) at the PBE(D3(BJ))/def2TZVP level of density functional theory are given in blue numbers. Structures m-c-uu and r-t-uu could not be located as minima on the potential energy surface, probably because of very high strain. The curved arrows in **3** and **4** indicate the directionality of the isomerization. Other molecular movements, for example, flapping in the reverse direction, are prohibited by the molecular framework.

barriers for boat and twist inversions (Figure 2c,d, Supporting Information Figures S26 and S27). The bridging strategy in diindane diazocines **3** and **4** restricts the conformational degrees of freedom to only one conformation in each configuration.

The synthesis of the *meso* compound **3** and racemate **4** of diindane diazocine (DID) is quite straightforward. It includes

only two steps starting from commercially available 4-nitro-indane **5**. Treatment of 4-nitroindane **5** with *tert*-butoxide and bromine afforded a mixture of the dinitro compounds **6** and **7**, which were separated by crystallization. The dinitro compounds **6** and **7** were converted into the diazocines **3** and **4** (Figure 3). The yields are 53 % for the *meso* compound **3** and 70 % for the racemic mixture **4**. An X-ray crystal structure of

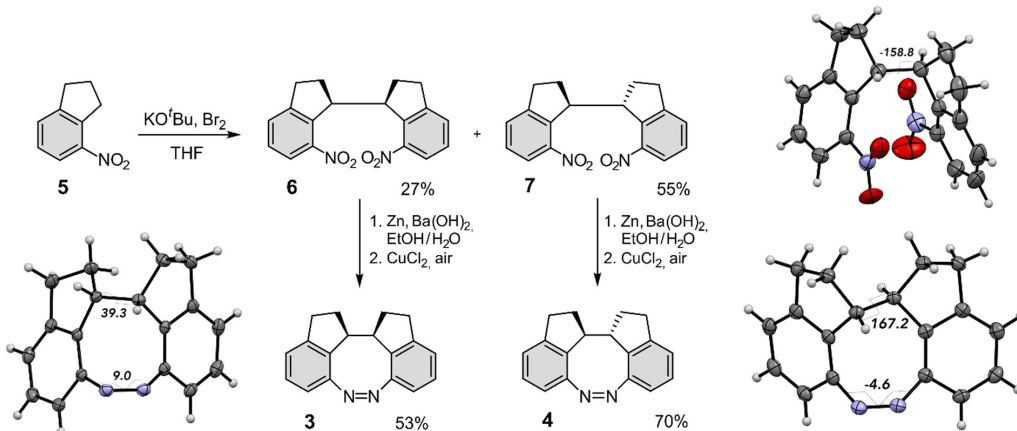


Figure 3. The diindane diazocines **3** and **4** were obtained by oxidative C–C coupling of 4-nitroindane **5**, followed by reductive azo cyclization of the corresponding dinitro compounds **6** and **7**. The thermal ellipsoids of the X-ray crystal structures are shown at the 50 % probability level.

the dinitro compound **7** reveals that the two nitro groups are suitably oriented for ring closure (Figure 3, top right), which explains the high yield (70%) of the azo cyclization. The single-crystal X-ray diffraction study of diazocines **3** and **4** (Figure 3, bottom left and right, respectively, Supporting Information Table S6) proves the markedly different molecular geometries between the m-c-ff form of **3** and the r-t-ff form of **4**. The *cis* configuration of the -HC-CH- bridge with the H–C–C–H torsion angle of 39.3° in the diazocene **3** causes increased steric hindrance of the CH hydrogens and results in a slightly more twisted azo group (C=N=N–C torsion of 9.0°). The r-t-ff form of **4** is more relaxed with H–C–C–H torsion angle of 167.2° and C=N=N–C torsion of -4.6°.

The highly strained diindane diazocines **3** and **4** exhibit unusual properties regarding the half-lives of their thermal relaxation. While the half-life of the racemic mixture **4** is about four times longer than the half-life of the parent system **2** (117 h vs. 27.6 h), the thermal relaxation for the *meso* compound **3** is about four orders of magnitudes faster than the parent system **2** (3 s). This is due to the high strain of the pincer-shaped molecule **3**.

Half-lives and photostationary states (PSS) were determined via NMR experiments in acetone (Table 1, Supporting Information Figures S13–S16). The half-life of the *meso* compound **3** was extrapolated from low-temperature meas-

urements via Arrhenius plots (Supporting Information Figure S14). Additionally the thermal relaxation of the *trans*→*cis* isomerization was monitored via low-temperature UV spectroscopy at 233 K (Figure 4a). The UV spectrum of the *meso* diazocene **3** shows almost completely separated maxima for the n–π* transitions, (*cis* 411 nm, *trans* 468 nm), resulting

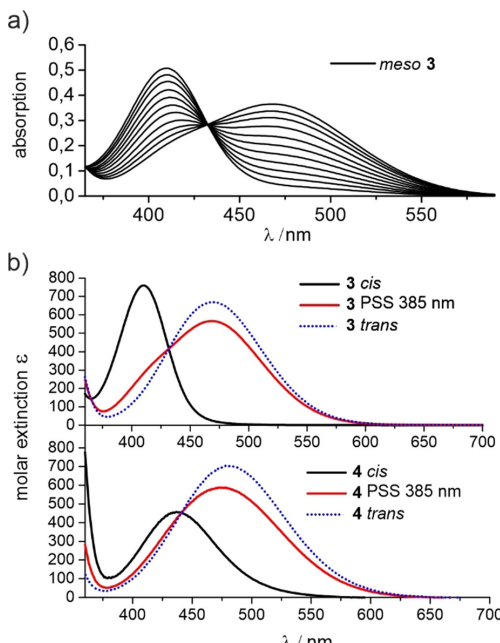


Figure 4. a) Selected UV spectra of the thermal relaxation of the *meso* diazocene **3** in THF at 233 K after irradiation at 385 nm. b) UV spectra of the n–π* transition of the diazocenes **3** (top) and **4** (bottom) before and after irradiation at 385 nm in THF at 298 K. The UV spectra of the pure *trans* isomers **3** and **4** were obtained through extrapolation.

in a PSS of 84 %, which is consistent with the PSS of the parent system **2** (Figure 4b). The racemic diazocine **4** exhibits a *cis*→*trans* conversion of 76 % (385 nm). The n–π* transition for the *cis*→*trans* isomerization has a bathochromic shift resulting in a maximum at 431 nm and because the *trans*→*cis* n–π* transition is not shifted equally (478 nm), resulting in an overlap of absorption bands (Figure 4b). *Trans*→*cis* conversions of **3** and **4** are achieved upon irradiation with green light (530 nm) and are quantitative within the limits of detection (UV and ¹H NMR).

The photostabilities of compounds **3** and **4** were determined via long-term irradiation experiments. The photo-switching of the racemic diazocine **4** in acetonitrile was monitored via UV spectroscopy. The solution was irradiated at 385 nm and 530 nm for 30 seconds each in an alternating sequence. After 5000 cycles, UV spectra of several additional irradiation cycles were recorded showing no loss of absorption (Figure 5a). The *meso* diazocine **3** was irradiated at 400 nm for 3.5 days (stirred solution 800 rpm, concentration: 1 mM, path length 1 cm, light intensity: 0.3 mWcm⁻²). This corresponds to ca. 2900 *cis*→*trans* isomerizations of one single molecule based on the molar absorption and the photon flux. The comparison of the UV spectra before and after illumination shows no sign of fatigue (Figure 5b). The photochemical quantum yields of the isomerization of diindane diazocine **3** and **4** were measured in an online UV/Vis spectroscopy experiment (Supporting Information Figures S20–S25 and Tables S2–S4) as described by Rau and co-

workers.^[25,26] Both diindane diazocines **3** and **4** have exceptionally high quantum yields confirming our strategy (Table 1). High-temperature NMR measurements (Supporting Information Figures S17–S19) confirm the rigidity of the diindane diazocines **3** and **4** in comparison to the parent diazocine **2**. When diazocine **2** is heated from 298 K to 343 K the signal of the ethylene bridge protons is broadened, confirming a boat inversion at higher temperatures. The relevant signals of the diindane diazocines **3** and **4**, on the other hand, exhibit no broadening from 298 K to 343 K.

Stepwise and systematic elimination of the conformational flexibility from azobenzene **1** to diazocine **2** drastically improved the photophysical properties. We introduced further bridges into the diazocine framework, preventing all conformational degrees of freedom leading to unproductive relaxation (boat, twist, and twist-chair inversions) leaving only a well-defined pincer-type molecular movement for the *cis*→*trans* isomerization. The quantum yields of these diindanodiazocines **3** and **4** surpass even the natural systems rhodopsin, bacteriorhodopsin, and halorhodopsin. Concomitantly, we have been able to introduce considerable strain into the *meso* isomer of diindane diazocine **3**. The *trans* configuration is 18.5 kcal mol⁻¹ higher in energy than the *cis* isomer. The high quantum yield (70 %) combined with the large ring strain that builds up upon *cis*→*trans* isomerization of *meso* diindanodiazocine **3**, leads to an exceptionally high light-to-chemical-energy conversion efficiency of 18 %. The syntheses of *meso* **3** and *rac* **4** diindane diazocine include only two steps from commercially available chemicals. Multigram amounts can be prepared within a few days with standard laboratory equipment. Moreover, no fatigue has been observed over thousands of switching cycles. In contrast to azobenzene and most other photochromes, the molecular motion during isomerization is directional. Thus, *meso* diindanodiazocines (such as **3**) are ideal actuators to power molecular machines. *Rac* diindane diazocine **4** is the smallest chiral photoswitch known to date. It is also ideally suited as a component to switch chiroptical properties and to control the chirality of liquid crystals.^[27–30]

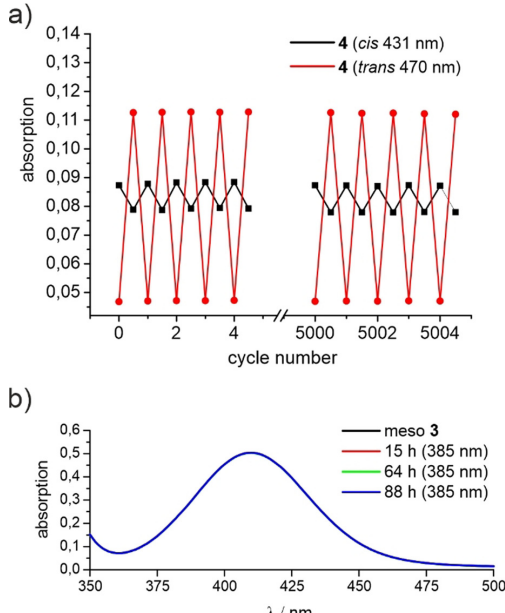


Figure 5. a) Absorption of the n–π* transitions of compound **4** at 431 nm (*cis*, black) and at 470 nm (*trans*, red) after alternating irradiation at 385 nm and 530 nm. b) UV spectrum of the *meso* compound **3** before (black) and after (blue) irradiation at 400 nm for 3.5 d.

Acknowledgements

We gratefully acknowledge financial support by the Deutsche Forschungsgesellschaft (DFG) within the Sonderforschungsbereich 677, “Function by Switching”. E.S. and G.G. thank NAWI Graz for support.

Conflict of interest

The authors declare no conflict of interest.

Keywords: diazocine · energy conversion · photochemistry · photochromism · quantum yields

[1] J. L. Spudich, *Trends Microbiol.* **2006**, *14*, 480–487.

- [2] V. I. Prokhorenko, A. M. Nagy, S. A. Waschuk, L. S. Brown, R. R. Birge, R. J. D. Miller, *Science* **2006**, *313*, 1257–1261.
- [3] T. Suzuki, R. H. Callender, *Biophys. J.* **1981**, *34*, 261.
- [4] D. Oesterhelt, P. Hegemann, J. Tittor, *EMBO J.* **1985**, *4*, 2351.
- [5] M. A. Ostrovsky, *Paleontol. J.* **2017**, *51*, 562.
- [6] S. Wiedbrauk, H. Dube, *Tetrahedron Lett.* **2015**, *56*, 4266.
- [7] R. Siewertsen, H. Neumann, B. Buchheim-Stehn, R. Herges, C. Näther, F. Renth, F. Temps, *J. Am. Chem. Soc.* **2009**, *131*, 15594.
- [8] A. Dreos, Z. Wang, B. E. Tebikachew, K. Moth-Poulsen, J. Andréasson, *J. Phys. Chem. Lett.* **2018**, *9*, 6174.
- [9] J. Tittor, D. Oesterhelt, *FEBS Lett.* **1990**, *263*, 269.
- [10] H. M. D. Bandara, S. C. Burdette, *Chem. Soc. Rev.* **2012**, *41*, 1809.
- [11] C. Petermayer, H. Dube, *J. Am. Chem. Soc.* **2018**, *140*, 13558.
- [12] K. Uchida, M. Irie, *Chem. Lett.* **1995**, *24*, 969.
- [13] C. S. Santos, A. C. Miller, T. C. S. Pace, K. Morimitsu, C. Bohne, *Langmuir* **2014**, *30*, 11319.
- [14] G. Tomasello, M. Garavelli, G. Orlandi, *Phys. Chem. Chem. Phys.* **2013**, *15*, 19763.
- [15] “Molecular systems for solar thermal energy storage and conversion”: K. Moth-Poulsen, *Organic Synthesis and Molecular Engineering* (Ed.: B. Nielson), Wiley, Hoboken, New Jersey, USA, **2014**, Chapter 6, pp. 179–196.
- [16] H. Sell, A. Gehl, D. Plaul, F. D. Sönnichsen, C. Schütt, F. Köhler, K. Steinborn, R. Herges, *Commun. Chem.* **2019**, *2*, 3468.
- [17] X. Wang, F. Wang, Y. Sang, H. Liu, *Adv. Energy Mater.* **2017**, *7*, 1700473.
- [18] E. Merino, *Chem. Soc. Rev.* **2011**, *40*, 3835.
- [19] G. Cabré, A. Garrido-Charles, À. González-Lafont, W. Moormann, D. Langbehn, D. Egea, J. M. Lluch, R. Herges, R. Alibés, F. Busqué, et al., *Org. Lett.* **2019**, *21*, 3780.
- [20] J. B. Trads, K. Hüll, B. S. Matsuura, L. Laprell, T. Fehrentz, N. Görldt, K. A. Kozeck, C. D. Weaver, N. Klöcker, D. M. Barber, et al., *Angew. Chem. Int. Ed.* **2019**, *58*, 15421; *Angew. Chem.* **2019**, *131*, 15567.
- [21] P. Paoletti, G. C. R. Ellis-Davies, A. Mourot, *Nat. Rev. Neurosci.* **2019**, *20*, 514.
- [22] S. Li, G. Han, W. Zhang, *Macromolecules* **2018**, *51*, 4290.
- [23] R. Siewertsen, J. B. Schönborn, B. Hartke, F. Renth, F. Temps, *Phys. Chem. Chem. Phys.* **2011**, *13*, 1054.
- [24] M. Böckmann, N. L. Doltsinis, D. Marx, *Angew. Chem. Int. Ed.* **2010**, *49*, 3382; *Angew. Chem.* **2010**, *122*, 3454.
- [25] E. Stadler, A. Eibel, D. Fast, H. Freiße, C. Holly, M. Wiech, N. Moszner, G. Gescheidt, *Photochem. Photobiol. Sci.* **2018**, *17*, 660.
- [26] H. Rau, G. Greiner, G. Gauglitz, H. Meier, *J. Phys. Chem.* **1990**, *94*, 6523.
- [27] Y. Wang, Q. Li, *Adv. Mater.* **2012**, *24*, 1926.
- [28] M. Mathews, N. Tamaoki, *J. Am. Chem. Soc.* **2008**, *130*, 11409.
- [29] R. A. van Delden, T. Mecca, C. Rosini, B. L. Feringa, *Chem. Eur. J.* **2004**, *10*, 61.
- [30] M. J. Moran, M. Magrini, D. M. Walba, I. Aprahamian, *J. Am. Chem. Soc.* **2018**, *140*, 13623.

Manuscript received: April 13, 2020

Accepted manuscript online: April 29, 2020

Version of record online: June 8, 2020

4

Funktionalisierte Oberflächen

Grenz- und Oberflächen sind gleich für mehrere naturwissenschaftliche Arbeitsbereiche wie Physik, Chemie, Biologie, aber auch in spezialisierten Bereichen wie Klimaforschung, Biogeochemie und in der Industrie von außerordentlich großem Interesse. Die Erde besteht an ihrer Oberfläche zu zwei Dritteln aus einer flüssig/gasförmigen Grenzfläche, welcher nicht nur im Zuge der Klimaerwärmung eine besondere Rolle beikommt.^[110–112] Die chemische Industrie arbeitet in diversen Bereichen mit heterogener Katalyse, d.h. Reaktionen an unterschiedlichen Phasen bzw. Grenzflächen, ohne die Chemikalien im Megatonnen-Maßstab nicht hergestellt werden könnten.^[113–122] Die aktuelle Forschung in der Chemie hat nicht nur auf Grund der Katalyse ein besonders großes Interesse, sich mit Oberflächen bzw. Grenzflächen zu beschäftigen. Vielmehr gibt es einen speziellen Bereich, der die gezielte Funktionalisierung von und Reaktionssteuerung auf Oberflächen entwickelt und untersucht.

4.1 Azobenzol auf Gold(111)

Für die Umsetzung von Oberflächenfunktionalisierung wurde im Arbeitskreis HERGES das Plattform-Konzept entwickelt. Die Basis dieses Konzepts bilden Triaza- (TATA) oder Trioxatriangulen (TOTAL), welche auf Substratoberflächen physisorbiert können. Durch den Einsatz von modifizierbaren, vertikalen Spacern und im Falle der TATA-Plattformen mit veränderbarem lateralem Abstand durch Seitenketten können diverse funktionelle Gruppen durch Substitution am zentralen Kohlenstoff auf ein Substrat aufgebracht werden.^[123–132] Dieses modulare Konzept bildet selbst organisierende Monolagen (*self-assembled monolayers*) (SAMs) mit freistehenden Funktionalisierungen wie z.B. AB als photochromem Schalter. Die Eigenschaften dieser Azobenzol-Ethynyl-Triazatriangulene (AB-TATAs) Moleküle wurden sowohl auf Goldnanopartikeln^[133] als auch auf Gold(111)-Oberflächen mit verschiedenen Oberflächen-sensitiven Methoden untersucht.^[125,134–136] Dabei konnte die reversible, lichtinduzierte Schaltung sowie Monolagen mit orthogonaler Ausrichtung des AB nachgewiesen werden. Bei der kinetischen Vermessung der thermischen Relaxation von AB-TATA auf einem Gold(111)-Substrat wurde jedoch ein bisher unbekanntes Phänomen beobachtet. Trotz eines deutlichen Abstands zur Oberfläche und keiner sterischen Hinderung durch Nachbarmoleküle in der Monolage relaxiert das AB von *cis* nach *trans* um mehrere Größenordnungen schneller als in Lösung.^[137,138]

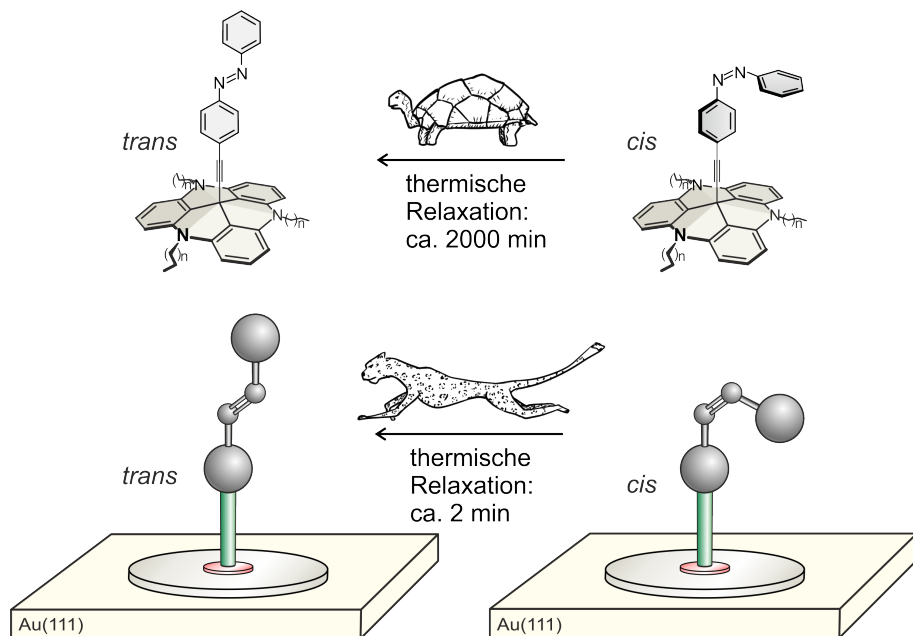


Abb. 4.1: Modulares Plattform-Konzept mit Ethynyl-Spacer und AB-Funktionalisierung: In Lösung (oben) relaxiert das AB von der metastabilen *cis*-Konfiguration in das stabile *trans*-Isomer mit einer Halbwertszeit von ca. 2000 min. Auf Gold(111) adsorbierte Moleküle (schematisch, unten) relaxieren trotz großer Entfernung zu Oberfläche um mehrere Größenordnungen schneller.

Die thermische Rückisomerisierung von AB ist grundsätzlich über viele Wege möglich, es gibt jedoch zwei Hauptmechanismen: die reine Rotation der Azofunktion (Torsionswinkel: C-N=N-C), welche bekanntermaßen in eine konische Durchschneidung mit der angeregten Singulett-Hyperfläche (S_1)^[55,56,139,140] führt oder die Inversion an den Stickstoffatomen (Winkel: C-N=N), welche energetisch dem experimentellen Mechanismus in Lösung am nächsten kommt und auch in quantenchemischen Studien mit hohem Niveau den energetisch niedrigsten Übergangszustand (*transition state*) (TS) lieferte.^[55,95] Anderen Studien zufolge kommt es häufig auch zu einem gemischten Mechanismus, welcher hauptsächlich über eine Inversion abläuft und teilweise durch Rotation begleitet wird.^[141–143] Viele dieser quantenmechanischen Untersuchungen berechnen auch die hypothetische Rotation auf der Triplet-Hyperfläche (T_1) und überdenken Mechanismen, welche die eigentlich spinverbotene *intersystem crossing* (ISC) aufweichen und so über $S_0 \rightarrow T_1 \rightarrow S_0$ relaxieren.^[137,139,144] Da diese Hyperfläche einen Pfad liefert, der energetisch deutlich unterhalb der Singulettinversion liegt, würde ein ISC die Aktivierungsbarriere drastisch herabsetzen. Da dieser Übergang jedoch verboten ist, müsste genauer erörtert werden, wie das Spinverbot aufgehoben wird und die ISC erlaubt wird.

Eine Erklärung der Gold(111)-Substrat-vermittelten, beschleunigten Relaxation wäre ein Mechanismus, bei dem das AB trotz großer Entfernung zur Oberfläche durch Konjugation mit der TATA-Plattform eine elektronische Kopplung mit dem Leitungsband des Substrats eingeht. Diese Kopplung könnte störungstheoretisch als Erklärung für die Aufweichung des ISC-Verbots dienen. Diese theoretische Überlegung zum Mechanismus mit quantenchemischen Methoden zu belegen, ist aber nicht trivial, da je nach Methode entweder das Substrat oder das organi-

sche Molekül unzureichend adäquat beschrieben wird.^[144–146] Um sich dem Problem trotzdem theoretisch zu nähern und die Kopplung genauer zu beschreiben, könnte das Substrat zunächst vernachlässigt werden und lediglich die Konjugation, also die Möglichkeit der elektronischen Kopplung vom AB zur adsorbierten TATA-Plattform, genauer untersucht werden. Hier können synthetische und theoretische Chemie beim Design verschiedener stark konjugierter Systeme zusammenarbeiten und Moleküle entwickeln, welche die Konjugation und somit die Kopplung zum Gold systematisch variieren und somit das Phänomen besser untersuchbar machen.

4.2 Long-Distance Rate Acceleration by Bulk Gold

A. Schlimm, R. Löw, T. Rusch, F. Röhricht, T. Strunkus, T. Tellkamp, F. Sönnichsen, U. Mathe, O. Magnussen, F. Tuczek und R. Herges

Angew. Chem. Int. Ed. **2019**, *58*, 6574–6578.

DOI:10.1002/anie.201814342

Supporting Information: Anhang SI 8

Wissenschaftliche Beiträge: DFT-Geometrieeoptimierungen der Moleküle, IR-Spektrensimulationen, Spindichtebestimmung der Triplettsstrukturen, Unterstützend bei: Datenbeschaffung, -integration, -auswertung, -validierung, Review und Änderung des Manuskripts (siehe SI).

Zusammenfassung

In dieser Veröffentlichung wird die Aufklärung des Mechanismus der Gold-katalysierten Relaxation von AB auf TATA-Plattformen dargelegt. Das drastische Abweichen der Isomerisierungs-kinetik in Lösung (¹H-NMR- und UV/Vis-Spektroskopie) im Vergleich zu der auf Gold(111)-Oberflächen (IRRAS) konnte bereits mit den etablierten AB-TATA-Molekülen, welche Konjugation über das ganze Molekül aufweisen, beobachtet, aber nicht erklärt werden. Ausschlaggebend für die Aufklärung des Mechanismus sind die eingesetzten Verbindungseinheiten, welche die Konjugation zwischen Plattform und Schalter variieren. Hierfür wurden verschiedene *ortho*-substituierte Biphenyleinheiten, die mit steigender Verdrillung Konjugation reduzieren, und ein nahezu komplett isolierender cyclischer Orthoester eingesetzt.

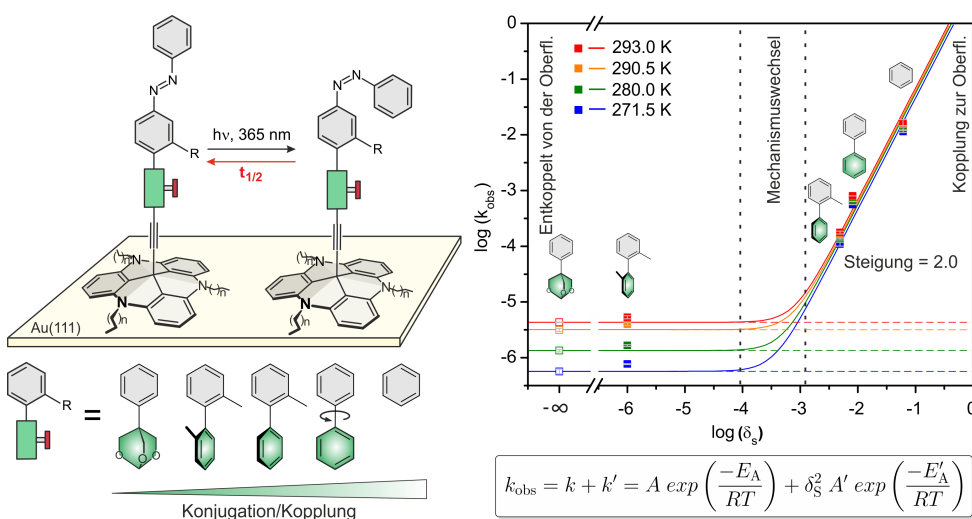


Abb. 4.2: Links: Darstellung der untersuchten AB-TATAs mit unterschiedlichen Verbindungseinheiten zur Regulierung der Konjugation innerhalb des Moleküls. Rechts: Temperaturabhängige Korrelation der observierten Ratenkonstante (k_{obs}) mit dem quadratischen Anteil an delokalisierte Spindichte (δ_s) des Triplet-Zustands (T_1) in der TATA-Plattform (Kopplung des AB zur Oberfläche).

So konnten die unterschiedlich stark beschleunigten Relaxationen in Abhängigkeit der Konjugation innerhalb des Moleküls vermessen werden. Die auf Gold observierte Reaktionskinetik weist dabei einen zweigeteilten Mechanismus auf: Standard Arrhenius-Verhalten (entkoppelt von der Oberfläche) und quadratische Abhängigkeit von der delokalisierten Wellenfunktion (δ_s) des *Triplet-Zustands* (T_1) in der TATA-Plattform (Kopplung des AB zur Oberfläche). DFT-Rechnungen haben im Vorfeld und bei der Auswertung durch exakte Werte der Delokalisierung in die Plattform maßgeblich zum Design der untersuchten Verbindungseinheiten und der Aufklärung des Mechanismus beigetragen. Der nicht adiabatische Teil beruht auf dem Gold-vermittelten elektronischen Übergang ($S_0 \rightarrow T_1 \rightarrow S_0$), also der Kopplung des Schalters mit dem Leitungsband des Goldes, welche das in Lösung verbotene quantenmechanische *intersystem crossing* (ISC) erlaubt. Die Reaktionsgeschwindigkeit ist damit nahezu temperaturunabhängig und wird durch die quantenmechanische Übergangswahrscheinlichkeit definiert. Dies beschreibt somit einen völlig neuen Katalysetyp unabhängig von chemischen Bindungen und direkter Umgebung.

Reaction Kinetics

International Edition: DOI: 10.1002/anie.201814342
 German Edition: DOI: 10.1002/ange.201814342

Long-Distance Rate Acceleration by Bulk Gold

Alexander Schlimm, Roland Löw, Talina Rusch, Fynn Röhricht, Thomas Strunskus,
 Tobias Tellkamp, Frank Sönnichsen, Uwe Manthe, Olaf Magnussen,* Felix Tuczek,* and
 Rainer Herges*

Abstract: We report on a very unusual case of surface catalysis involving azobenzenes in contact with a Au(111) surface. A rate acceleration of the *cis*–*trans* isomerization on gold up to a factor of 1300 compared to solution is observed. By using carefully designed molecular frameworks, the electronic coupling to the surface can be systematically tuned. The isomerization kinetics of molecules with very weak coupling to the metal is similar to that found in solution. For their counterparts with strong coupling, the relaxation rate is shown to depend on the spin-density distribution in the triplet states of the molecules. This suggests that an intersystem crossing is involved in the relaxation process. Aside from their impact on catalytic processes, these effects could be used to trigger reactions over long distances.

The majority of chemical processes in nature and in industry involve catalysis. Often, there is no other way to form stable products from stable reactants under mild conditions. Most technologically relevant reactions employ heterogeneous catalysis, where the reacting molecules interact with atoms or ions on surfaces, forming intermediates.^[1] This opens up reaction pathways with lower barriers and faster reaction rates than in the uncatalyzed processes. A number of reactions on surfaces have been studied and their mechanisms have been elucidated in detail.^[1,2] Here, we report on a very unusual case of surface catalysis involving azobenzene units in

contact with a Au(111) surface. We observe a drastic rate acceleration (up to a factor of 1300 compared to solution) of *cis*–*trans* isomerization on gold, even though the reacting N=N double bonds are located 14 Å above and are separated by eleven covalent bonds from the Au(111) surface. To elucidate this extraordinary long-range acceleration of the reaction rate, we employ carefully designed molecular frameworks.^[3] The modularity of this unique system allows a precise adjustment of intermolecular distances and coupling.^[4,5] Furthermore, the electronic coupling to the surface is systematically tuned by changing the π-conjugation of the coupling unit, while the distance between the gold surface and the azobenzene unit remains almost the same. Surprisingly, the isomerization kinetics of molecules with strong coupling to the metal follows a different mechanism than the one observed for their counterparts with no or very weak coupling. Specifically, activation energies drop to very low values and frequency factors become explicitly dependent on an electronic matrix element that can be correlated with the spin-density distribution in the triplet states of the molecules. Besides their impact on catalytic processes, these effects could be used to trigger chemical reactions over a long distance. Similar remote effects have not been considered in catalytic processes so far. However, they could be operative in a number of reactions on metallic surfaces or nanoparticles.

Catalysts increase the rates of chemical reactions by creating a new and energetically more favorable reaction path with lower activation energies. In heterogeneous catalysis, this new path involves the adsorption of reactants at a surface, where chemical bonds within the molecule are broken and new bonds with surface atoms are formed. Although the majority of chemical reactions follow the Eyring theory or RKKM-type transition state theories, there are a few examples of chemical reactions that substantially deviate from the theoretically predicted behavior.^[6] Their reaction rates mainly depend on quantum-mechanical transition probabilities and not the height of an energy barrier. Characteristic features are apparently small frequency factors and low activation energies, corresponding to reaction rates that are almost temperature-independent. Such processes have mostly been observed at low temperatures (<50 K).^[7] Herein, we show that bulk gold can mediate similar phenomena at temperatures around 300 K. Moreover, by modifying the electronic coupling between the reaction center and the Au surface, we are able to shift the isomerization kinetics from a classical, solution-like behavior to a new regime involving a drastically lowered barrier and increased reaction rates.

In our studies, we employ azobenzene-functionalized TATA (azo-TATA) molecules (Figure 1, top). The *cis*–*trans*

[*] A. Schlimm, Prof. Dr. F. Tuczek

Christian Albrechts University Kiel, Institute of Inorganic Chemistry
 Max-Eyth-Str. 2, 24118 Kiel (Germany)
 E-mail: ftuczek@ac.uni-kiel.de

R. Löw, F. Röhricht, Dr. T. Tellkamp, Prof. Dr. F. Sönnichsen,
 Prof. Dr. R. Herges

Christian Albrechts University Kiel, Institute of Organic Chemistry
 Otto-Hahn-Platz 4, 24118 Kiel (Germany)
 E-mail: rherges@oc.uni-kiel.de

T. Rusch, Prof. Dr. O. Magnussen
 Christian Albrechts University Kiel
 Institute of Experimental and Applied Physics
 Leibnizstr. 19, 24118 Kiel (Germany)
 E-mail: magnussen@physik.uni-kiel.de

Dr. T. Strunskus
 Christian Albrechts University Kiel, Institute for Materials Science
 Kaiserstr. 2, 24143 Kiel (Germany)

Prof. Dr. U. Manthe
 University of Bielefeld, Institute of Theoretical Chemistry
 Universitätsstr. 25, 33501 Bielefeld (Germany)

 Supporting information and the ORCID identification number(s) for
 the author(s) of this article can be found under:
<https://doi.org/10.1002/anie.201814342>.

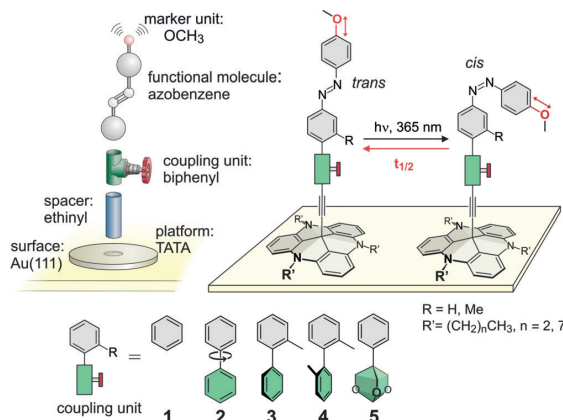


Figure 1. Modular design to tune the electronic coupling of azobenzene units with the metal surface: TATA platforms define the intermolecular distances on the surface (by the size of the side chain: $a = \text{octyl}$, $b = \text{propyl}$) and ethynyl spacers provide a freestanding upright orientation of the reacting azobenzene molecules. Coupling units (green) control the electronic coupling of azobenzenes with the surface. Methoxy groups allow to identify the configuration of the azobenzene (*cis* or *trans*) by IRRAS.

isomerization kinetics of **1a** and **2a** have recently been investigated in solution and for adsorbed monolayers, finding that the thermal *cis*-to-*trans* relaxation of the molecules

adsorbed on bulk Au(111) is considerably faster than in solution.^[8–10] Assuming that this rate acceleration involves electronic coupling to the metal,^[8] we synthesized three new azo-TATA compounds with different coupling units inserted between the TATA platform and the azobenzene unit (Figure 1 and Supporting Information). Biphenyl groups were chosen to tune the electronic coupling of the azo group to the surface, because 4,4'-substituted biphenyls retain the upright alignment of the azobenzene with respect to the surface and, most importantly, upon addition of an increasing number of methyl groups ($n = 0\text{--}4$) in *ortho* position, the phenyl groups are twisted out of coplanarity, which decreases their conductivity (Supporting Information, Figure S124).^[11] To shut off π -conjugation completely, we inserted a trioxabicyclo[2.2.2] unit which separates the π -systems of azobenzene and the ethynyl spacer with sp^3 -hybridized C and O atoms. The new compounds (**3a**–**5a**, **1b**, **2b**, **5b**) were completely characterized in solution and bulk material with NMR, UV/Vis, and vibrational spectroscopy (see Supporting Information). Scanning Tunneling Microscopy (STM) shows that, in agreement with previous results,^[3,4,12] optimized self-assembly conditions result in monolayers of **1a**–**5a** with $(\sqrt{19} \times \sqrt{19})$ R23.4° superstructures and low defect densities (see Figures 2 and S125). X-ray spectroscopy studies (XPS, NEXAFS) prove that the adlayers are of high purity with the molecules being oriented perpendicular to the surface, as shown in Figure 2 (Figures S126 and S127). The vertical alignment of the azobenzene with respect to the surface has

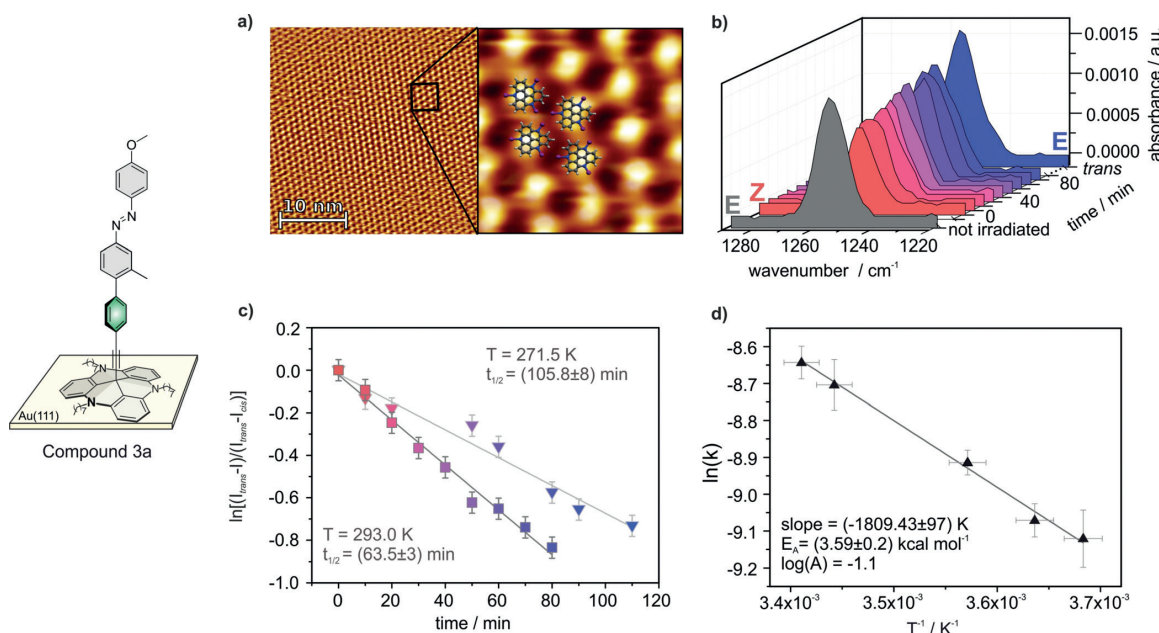


Figure 2. a) STM image and model of a monolayer of azo-TATA **3a** on Au(111). The molecules exhibit an intermolecular distance of 12.6 Å. b) PM-IRRAS signal of the C–O stretching vibration region before irradiation (gray) and after irradiation with light of 365 nm as a function of time (red to blue). The blue spectrum was obtained after irradiation with 440 nm light. In both cases, the irradiation time was 10 min. c) PM-IRRAS intensity of the C–O stretching vibration as a function of time at two different temperatures (271.5 K and 293.0 K). Half-lives ($t_{1/2}$) are derived by a linear regression. d) Arrhenius plot of reaction rates k at five different temperatures. The activation barrier E_a and the frequency factor A are derived by a linear regression.

been confirmed in previous studies as well (tilt angle: $6 \pm 16^\circ$).^[12]

The well-defined molecular orientation together with the surface selection rule allows to monitor the photochemical (365 nm) *trans*-to-*cis* isomerization as well as the ensuing thermal *cis*-to-*trans* relaxation by Infrared Reflection Absorption Spectroscopy (IRRAS).^[13] The relaxation leads to orientational changes of the C_{phenyl}–O_{methoxy} bond relative to the surface and thus, temporal changes in the intensity of the corresponding band in the IRRA spectrum. The rates of the thermal *cis*-to-*trans* relaxation were determined at five different temperatures (Figures 2 and S129). From these data, activation energies and frequency factors were obtained for compounds **1a**–**5a** (Figures 3 and S128). For adsorbate layers of compounds **1a**, **2a**, and **3a** on Au(111), the rates show only small changes in the investigated temperature range. Correspondingly, the activation energies and frequency factors are exceptionally small and typical for non-adiabatic reactions, where the rates are controlled by quantum-mechanical transition probabilities rather than classical energy barriers. On the contrary, the largely decoupled compounds **4a** and **5a** show a significantly stronger temperature dependence of the reaction rate, close to the rates observed in solution. The combined surface-kinetic data thus show that at a fixed temperature, the half-life of the adsorbed species can be changed by up to four orders of magnitude through adjusting the electronic coupling between the platform and the azo unit. In contrast, the half-lives of the five compounds in solution vary only slightly with the coupling unit.

The fundamental change in the *cis*-to-*trans* reaction observed across compounds **1a**–**5a** can be correlated with the degree of electronic coupling to the surface. Particularly remarkable is the change in kinetics between compounds **3a** and **4a** (Figure 3, right). Since both are structurally closely related and only differ in a methyl group, the kinetic data in solution are very similar. Adsorbed on the metal surface, however, their half-lives ($t_{1/2}$), frequency factors (A), and activation energies (E_A) differ drastically (Figure 3). Electronic coupling to the metal surface is still operative in **3a**, whereas the almost orthogonal arrangement of the phenyl rings in **4a** interrupts π -conjugation and electronic coupling. The change from non-standard kinetics in **3a** to classical Arrhenius behaviour in **4a** is thereby clearly related to the breakdown of molecule–substrate coupling. The different activation energies of the compounds **4a**–**5a** in solution and adsorbed on a surface can be explained by the dissimilar environments.

Different hypotheses for the acceleration of *cis*-to-*trans* relaxation processes in molecular adsorbates were discussed. It is known that dense monolayers of azobenzenes on surfaces exhibit increased *cis*-to-*trans* isomerization rates, because intermolecular steric repulsion is larger in the bent *cis* than in the more straight *trans* configuration.^[14] Even though this is unlikely to account for the large rate accelerations, we performed further experiments to probe this hypothesis. The large octyl side groups at the TATA platform were replaced by smaller propyl groups (**1b**, **2b**, **5b**), which results in a smaller intermolecular distance in the self-assembled

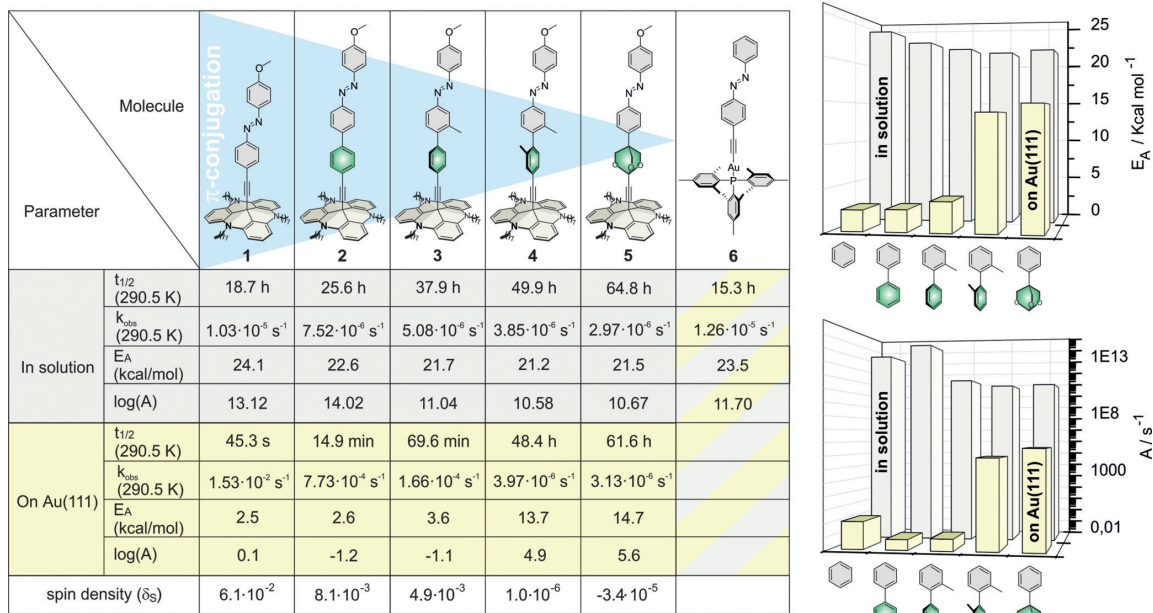


Figure 3. Kinetic data of the *cis*-to-*trans* isomerization of compounds **1a**–**5a** and **6** in solution and adsorbed on Au(111). Half-lives ($t_{1/2}$), observed rates (k_{obs}), activation energy (E_A), and frequency factors (A) for azo-TATA compounds (sorted by decreased coupling between platform and azobenzene) are determined in solution (gray), and adsorbed on Au(111) (yellow). Spin densities (δ_s) of **1a**–**5a** in the triplet state are calculated with DFT (M08HX/def2-TZVP) and integrated over all atoms within the platform unit and the ethynyl spacer. For compound **6**, $t_{1/2}$, E_A , and A are presented in solution. More data points and error margins are given in the Supporting Information (Figure S129).

monolayers on Au(111) (octyl: 12.6 Å vs. propyl 10.4 Å).^[3–5,10] However, the measured rate accelerations on gold are similar (Figure S129). Steric constraints can therefore be excluded. Moreover, steric confinement would not explain the very low barriers and frequency factors. Traces of absorbed water are also not responsible for the rate acceleration.^[15] On the contrary, coincidental water on adsorbed azobenzenes decreases the relaxation rate.^[16] Added water also slows down the reaction rates in solution (Figure S133). It is known that charge transfer can accelerate the *cis-trans* isomerization rates of azobenzenes. Azobenzenes that are either oxidized to the corresponding radical cations or reduced to the radical anions exhibit very fast thermal isomerization rates.^[17] The low *cis-trans* activation barriers of azobenzenes directly absorbed on gold nanoparticles^[18,19] or lying flat on Au(111)^[20] or Bi(111)^[21] surfaces have been explained by a transfer of electron density from the azobenzene to the metal.^[19] To investigate if such a charge transfer would be operative in our system, we synthesized azobenzene **6**, where an Au⁺ ion is directly connected to the ethynyl group (Scheme S5). According to the NBO analysis of **6**, the azoethynyl group carries approximately half an elementary charge (-0.508 e). Kinetic analysis, however, reveals that the activation energy (20.3 kcal mol⁻¹) and the frequency factor ($\log(A/\text{s}^{-1}) = 13.78$; see Figure 3, right) are in the usual range expected for undisturbed azobenzenes.^[22] The strongest argument against static charge transfer is the fact that the IR vibrational frequencies of the *cis* and the *trans* azo-TATA molecules in solution and absorbed on the surface are virtually identical (Figure S123).

The appearance of two different regimes in Figure 3 suggests the existence of two distinct mechanisms. It will be shown that the delocalization of the electronic wavefunction of the azobenzene unit over the entire molecule into the gold plays a key role in this context. A convenient measure of the delocalization is the spin density δ_s at the TATA platform computed for the triplet state (Figure S124): the wavefunction amplitude localized in the bulk gold is approximately proportional to the square root of δ_s for the triplet (T_1) as well as for the singlet (S_0) electronic state (see Supporting Information, Section 1). The plot of $\log(k_{\text{obs}})$ vs. $\log(\delta_s)$ shown in Figure 4 reveals that the observed rate constant k_{obs} can be written as a sum of a rate constant k , which is associated with a thermally activated process exhibiting standard Arrhenius-type behaviour, and a rate constant k' , which additionally depends upon the square of the spin density at the TATA platform:

The parameters A ($10^{5.6}\text{ s}^{-1}$) and E_A (14.7 kcal mol⁻¹) for the regime associated with k are taken from compound **5a**, serving as a reference system for a surface-deposited azo-TATA molecule with an electronically decoupled azobenzene unit (Figure 3). For k' , a significantly reduced apparent barrier height E'_A of $2.7 \pm 0.1\text{ kcal mol}^{-1}$ and a prefactor A' of $894 \pm 110\text{ s}^{-1}$ are found by fitting our data to Equation (1) (Figures S130 and S131).

$$k_{\text{obs}} = k + k' = A \exp\left(\frac{-E_A}{RT}\right) + \delta_s^2 A' \exp\left(\frac{-E'_A}{RT}\right) \quad (1)$$

The described findings strongly suggest that an electronic transition mediated by the bulk gold is involved in the

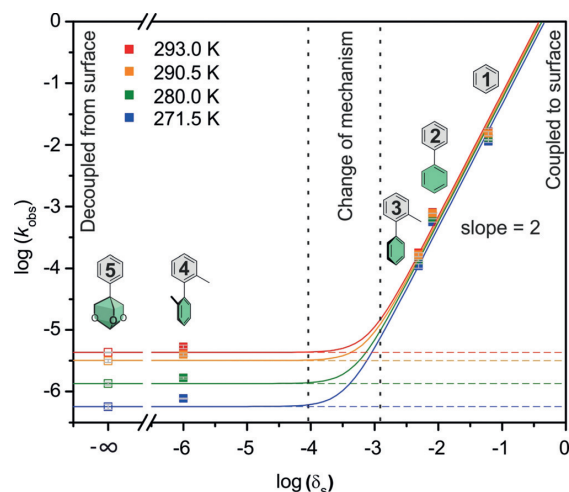


Figure 4. $\log(k_{\text{obs}})$ as a function of $\log(\delta_s)$ for compounds **1a–5a**. δ_s is the spin density of the triplet state of **1a–5a** integrated over all atoms of the platform and the ethynyl spacer, calculated with DFT (M08H/def2-TZVP). Compound **5** serves as a reference molecule without electronic coupling to the surface and a very small value for δ_s (dashed lines). Continuous lines are fitted according to Equation (1).

reaction mechanism associated with the rate constant k' . Two different mechanisms can be imagined: a gold-mediated intersystem crossing (ISC) between the singlet (S_0) and triplet (T_1) states of the azobenzene or a transient charge transfer (CT) between the gold and azo-TATA. By considering the coupling between the different electronic states to be a weak perturbation, k' can be assumed to be proportional to the square of the coupling element that enables the electronic transition (see Supporting Information, Section 1). Since the ISC as well as the CT are enabled by the coupling to the bulk gold, the value of the coupling element is determined by the respective wavefunction amplitudes localized in the bulk gold. The coupling matrix element for the ISC involves the S_0 and T_1 wavefunctions and is thus proportional to δ_s . In contrast, the coupling matrix element for the CT involves the S_0 wavefunction and the wavefunction of the CT state and is proportional to the square root of δ_s (see Supporting Information, Section 1). Thus, only the ISC mechanism is consistent with the observed quadratic δ_s dependence of k' .

The rate enhancement induced by bulk gold described above represents a new type of catalysis. Unlike in conventional heterogeneous catalysis, there is no direct chemical involvement of the surface (no chemical bonds to the surface are made or broken). Instead, the bulk metal opens an alternative pathway with almost vanishing barriers by the mixing of molecular states with the quantum states of gold. Particularly exceptional is the fact that the state transitions occur at room temperature, without photochemical activation, and over a large distance (14 Å, 11 bonds). We used a well-defined, controllable environment to investigate these non-classical effects systematically and propose that a change in spin state is responsible for the drastic rate acceleration. It is quite likely that similar effects are operative in a number of

catalytic processes where molecules react at metal surfaces. Likewise, the controlled coupling of molecules to the conducting band of materials could open new ways to trigger reactions with spatiotemporal control. Such effects may also be exploited to efficiently catalyze chemical reactions or to remote-control molecular machines on surfaces.^[23]

Acknowledgements

We thank the Deutsche Forschungsgemeinschaft (SFB 677) for funding this research, the Helmholtz-Zentrum Berlin for the supply of beamtime at the HE-SGM beamline (XPS and NEXAFS measurements), and Martin Kirk for fruitful discussions.

Conflict of interest

The authors declare no conflict of interest.

Keywords: azobenzene · catalysis · self-assembled monolayers · surface spectroscopy · vibrational spectroscopy

How to cite: *Angew. Chem. Int. Ed.* **2019**, *58*, 6574–6578
Angew. Chem. **2019**, *131*, 6646–6650

- [1] G. Ertl, H. Knözinger, F. Schütt, J. Weitkamp, *Handbook of Heterogeneous Catalysis*, Wiley-VCH, Weinheim, **2008**.
- [2] G. Ertl, *Angew. Chem. Int. Ed.* **2008**, *47*, 3524; *Angew. Chem.* **2008**, *120*, 3578.
- [3] B. Baisch, D. Raffa, U. Jung, O. M. Magnussen, C. Nicolas, J. Lacour, J. Kubitschke, R. Herges, *J. Am. Chem. Soc.* **2009**, *131*, 442.
- [4] S. Lemke, S. Ulrich, F. Claußen, A. Bloedorn, U. Jung, R. Herges, O. M. Magnussen, *Surf. Sci.* **2015**, *632*, 71.
- [5] S. Kuhn, B. Baisch, U. Jung, T. Johannsen, J. Kubitschke, R. Herges, O. Magnussen, *Phys. Chem. Chem. Phys.* **2010**, *12*, 4481.
- [6] B. G. Gowenlock, *Q. Rev. Chem. Soc.* **1960**, *14*, 133.
- [7] a) A. Hauser, *Coord. Chem. Rev.* **1991**, *111*, 275; b) J. N. Harvey, *Phys. Chem. Chem. Phys.* **2007**, *9*, 331; c) P. R. Schreiner, H. P. Reisenauer, F. C. Pickard, A. C. Simmonett, W. D. Allen, E. Mátyus, A. G. Császár, *Nature* **2008**, *453*, 906.
- [8] U. Jung, C. Schütt, O. Filinova, J. Kubitschke, R. Herges, O. Magnussen, *J. Phys. Chem. C* **2012**, *116*, 25943.
- [9] N. R. Krekiehn, M. Müller, U. Jung, S. Ulrich, R. Herges, O. M. Magnussen, *Langmuir* **2015**, *31*, 8362.
- [10] H. Jacob, S. Ulrich, U. Jung, S. Lemke, T. Rusch, C. Schütt, F. Petersen, T. Strunkus, O. Magnussen, R. Herges, et al., *Phys. Chem. Chem. Phys.* **2014**, *16*, 22643.
- [11] a) A. Mishchenko, L. A. Zotti, D. Vonlanthen, M. Bürkle, F. Pauly, J. C. Cuevas, M. Mayor, T. Wandlowski, *J. Am. Chem. Soc.* **2011**, *133*, 184; b) A. Mishchenko, D. Vonlanthen, V. Meded, M. Bürkle, C. Li, I. V. Pobelov, A. Bagrets, J. K. Viljas, F. Pauly, F. Evers, et al., *Nano Lett.* **2010**, *10*, 156; c) M. L. Kirk, D. A. Shultz, D. E. Stasiw, G. F. Lewis, G. Wang, C. L. Brannen, R. D. Sommer, P. D. Boyle, *J. Am. Chem. Soc.* **2013**, *135*, 17144.
- [12] S. Ulrich, U. Jung, T. Strunkus, C. Schütt, A. Bloedorn, S. Lemke, E. Ludwig, L. Kipp, F. Faupel, O. Magnussen, et al., *Phys. Chem. Chem. Phys.* **2015**, *17*, 17053.
- [13] a) X. Yu, Z. Wang, M. Buchholz, N. Fullgrabe, S. Grosjean, F. Bebensee, S. Bräse, C. Wöll, L. Heinke, *Phys. Chem. Chem. Phys.* **2015**, *17*, 22721; b) R. G. Greenler, *J. Chem. Phys.* **1966**, *44*, 310.
- [14] a) M. Kaneta, T. Honda, K. Onda, M. Han, *New J. Chem.* **2017**, *41*, 1827; b) S. D. Evans, S. R. Johnson, H. Ringsdorf, L. M. Williams, H. Wolf, *Langmuir* **1998**, *14*, 6436.
- [15] A. Muždalo, P. Saalfrank, J. Vreede, M. Santer, *J. Chem. Theory Comput.* **2018**, *14*, 2042.
- [16] T. Moldt, D. Przyrembel, M. Schulze, W. Bronsch, L. Boie, D. Brete, C. Gahl, R. Klajn, P. Tegeder, M. Weinelt, *Langmuir* **2016**, *32*, 10795.
- [17] a) A. Goulet-Hanssens, M. Utecht, D. Mutruc, E. Titov, J. Schwarz, L. Grubert, D. Bléger, P. Saalfrank, S. Hecht, *J. Am. Chem. Soc.* **2017**, *139*, 335; b) X. Tong, M. Pelletier, A. Lasia, Y. Zhao, *Angew. Chem. Int. Ed.* **2008**, *47*, 3596; *Angew. Chem.* **2008**, *120*, 3652.
- [18] G. L. Hallett-Tapley, C. D'Alfonso, N. L. Pacioni, C. D. McTiernan, M. González-Béjar, O. Lanzalunga, E. I. Alarcon, J. C. Scaiano, *Chem. Commun.* **2013**, *49*, 10073.
- [19] E. Titov, L. Lysyakova, N. Lomadze, A. V. Kabashin, P. Saalfrank, S. Santer, *J. Phys. Chem. C* **2015**, *119*, 17369.
- [20] S. Hagen, P. Kate, M. V. Peters, S. Hecht, M. Wolf, P. Tegeder, *Appl. Phys. A* **2008**, *93*, 253.
- [21] C. Bronner, P. Tegeder, *New J. Phys.* **2014**, *16*, 053004.
- [22] P. Bortolus, L. Flamigni, S. Monti, M. Bolte, G. Guyot, *J. Chem. Soc. Faraday Trans.* **1991**, *87*, 1303.
- [23] a) T. Kudernac, N. Ruangsrapichat, M. Parschau, B. Maciá, N. Katsonis, S. R. Harutyunyan, K.-H. Ernst, B. L. Feringa, *Nature* **2011**, *479*, 208; b) R. A. van Delden, M. K. J. ter Wiel, M. M. Pollard, J. Vicario, N. Koumura, B. L. Feringa, *Nature* **2005**, *437*, 1337.

Manuscript received: December 18, 2018

Revised manuscript received: January 30, 2019

Accepted manuscript online: February 22, 2019

Version of record online: April 12, 2019

4.3 Inverse Schaltung auf Gold

Durch die Aufklärung der beschleunigten Relaxation von AB-TATA Molekülen auf Gold(111)-Substraten wurde der Grundstein für eine neue Art Oberflächenkatalyse gelegt.^[147] Da dieses Phänomen jedoch bisher nur für den Photoschalter AB untersucht ist, wäre es von Interesse, andere Schalter oder genereller andere Reaktionen auf den Einfluss der Gold-vermittelten Spin-Switch-Katalyse zu untersuchen. Bisher ist bekannt, dass die thermische Rückisomerisierung von *cis* nach *trans* je nach Kopplung mit dem Substrat adiabatisch oder durch ein ISC von $S_0 \rightarrow T_1 \rightarrow S_0$ und somit durch die quantenmechanische Durchtrittswahrscheinlichkeit kontrolliert wird. Dank der inversen thermischen Stabilität von Diazocinen könnte dieser Katalysemechanismus auch auf dem Relaxationspfad von *trans* nach *cis* untersucht werden. Für eine erfolgreiche Untersuchung bedarf es unterschiedlicher Grundlagen. Zunächst wäre es von Vorteil, ein System möglichst nah am Vorbild zu entwickeln, welches zur Überwachung der Kinetik detektierbar für Oberflächen-sensitive Messmethoden (z.B. Infrarot-Reflexions-Absorptions-Spektroskopie (*infrared reflection absorption spectroscopy*, IRRAS) ist. Hierbei können im Vorwege quantenchemische Rechnungen die Grundlage bieten, um Geometrien, Energien, Schwingungs-, Absorptionsspektren und Übergangszustände zu liefern. Außerdem wäre wieder eine variable Konjugation von Vorteil, um den Effekt erneut in Abhängigkeit der Kopplung erfassen zu können. Ein möglichst analoger Aufbau wäre die Ethinyl-TATA-Plattform als Grundlage mit dem Stamm-DAC als photochromen Schalter. Um die Konjugation und damit die Kopplung synthetisch möglichst einfach einzustellen, kann das Diazocin entweder in *meta*- oder in *para*-Position zur Azofunktion substituiert werden. Das System der delokalisierten Elektronen sollte in *para*-Position deutlich besser konjugiert sein und somit eher zur beschleunigten Relaxation auf Gold-Oberflächen neigen als das *meta*-Analogon.

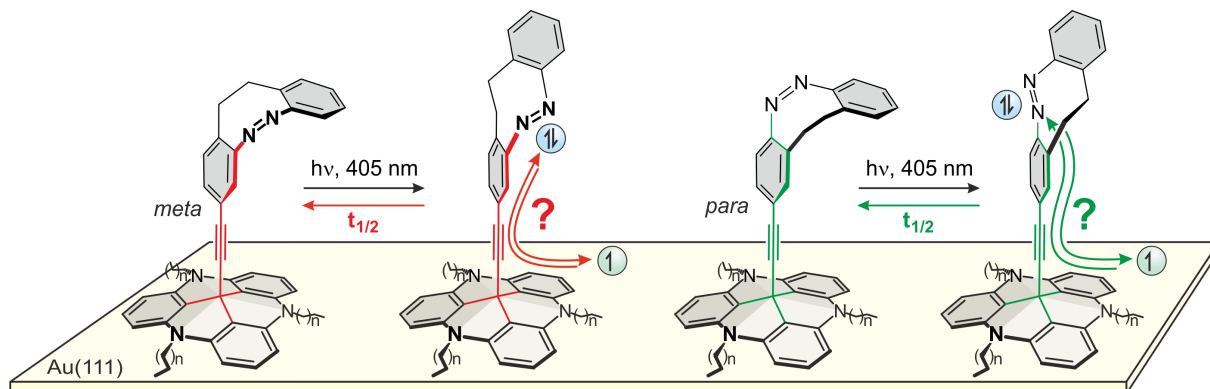


Abb. 4.3: Konzept zur Untersuchung der Spin-Switch-Katalyse auf die Rückisomerisierung von *trans*→*cis* mit Diazocin-basierten Systemen auf Gold(111)-Oberflächen. Die unterschiedliche Substitutionsposition (*meta*: schwach konjugiert, *para*: stark konjugiert) sollte die Konjugation und somit die Kopplung mit dem Goldsubstrat einstellen.

4.4 Diazocine-functionalized TATA platforms

R. Löw, T. Rusch, F. Röhricht, O. Magnussen und R. Herges

Beilstein J. Org. Chem. **2019**, *15*, 1485–1490.

DOI:10.3762/bjoc.15.150

Supporting Information: Anhang SI 8

Wissenschaftliche Beiträge: DFT-Geometrieoptimierungen der funktionalisierten TATA-Plattformen, TSS der *cis-trans*-Isomerisierung, (anteilig) Verfassen des Manuskripts.

Zusammenfassung

Diese Publikation knüpft an die Aufklärung der Gold-katalysierten thermischen Relaxation von AB an, welches orthogonal entfernt (14 Å) von der Oberfläche um mehrere Größenordnungen schneller isomerisiert als in Lösung. Der Mechanismus basiert dabei auf dem nicht adiabatischen, quantenmechanischen Übergang von $S_0 \rightarrow T_1 \rightarrow S_0$, welcher durch Kopplung des AB durch 11 konjugierte Bindungen zum Goldsubstrat moderiert wird. Um diesen vorher unbekannten Mechanismus weiter zu untersuchen, wurde in dieser Arbeit das AB des Grundgerüsts analog zur vorherigen Untersuchung durch das photoschaltbare Stamm-Diazocin (DAC) substituiert. Der Unterschied in diesem Aufbau liegt zum einen in der unterschiedlichen Bindungssituation des Schalters an die Plattform (*meta* und *para* zur Azofunktion: schwache und starke Konjugation) und zum anderen in der intrinsisch thermodynamisch stabileren *cis*-Konfiguration des DACs. Trotz veränderter Geometrie sollte die unterscheidbare Detektion von *trans* und *cis* mittels IRRAS dank Methoxykopfgruppe möglich sein.

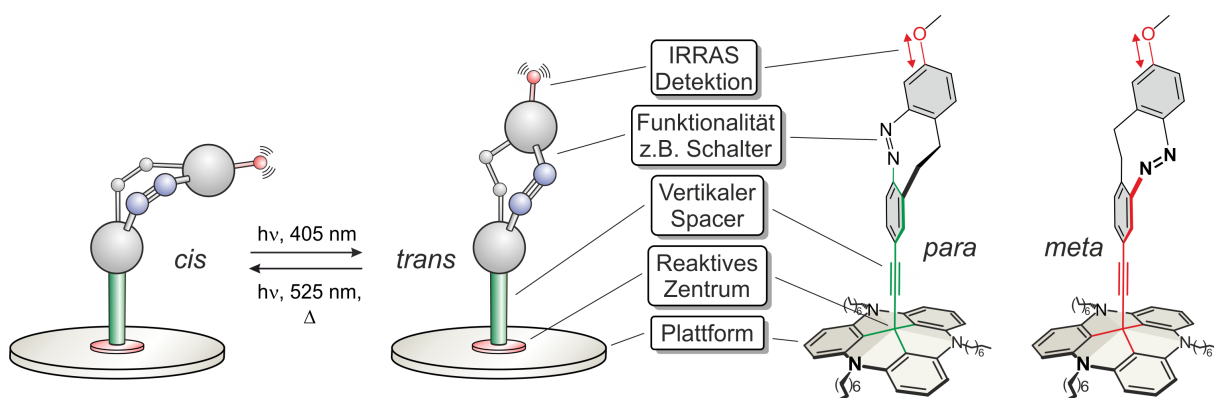


Abb. 4.4: Konzept der Untersuchung auf Spin-Switch-Katalyse mit inverser Schaltung; Links: schematische Darstellung des modularen Plattform-Konzeptes mit dem Diazocin als schaltbare Gruppe und Kopfgruppe zur Detektion mittels IRRAS; Rechts: Moleküldesign mit starker (grün) und schwacher (rot) Konjugation des Schalters bis in die TATA-Plattform.

DFT-Rechnungen konnten im Voraus Geometrien (Detektierbarkeit IRRAS), *cis*-Stabilität und nahezu gleiche Aktivierungsbarriere für die thermische Relaxation in Lösung für beide Moleküle vorhersagen. UV/Vis- und ^1H -NMR-Ergebnisse belegten die Rechnungen mit thermodynamischer *cis*-Stabilität und Aktivierungsenergien von ca. 20 kcal mol $^{-1}$. Darüber hinaus konnten bereits erfolgreich SAMs der Plattformen mittels Rastertunnelmikroskop (*scanning tunneling microscope*, STM) auf Gold(111)-Oberflächen nachgewiesen werden. Dieses Konzept ergibt die außerordentlich interessante Möglichkeit, die Schaltung von *trans*→*cis* auf einen Gold-vermittelten, nicht-adiabatischen Mechanismus zu untersuchen.



Diazocine-functionalized TATA platforms

Roland Löw¹, Talina Rusch², Fynn Röhricht¹, Olaf Magnussen² and Rainer Herges^{*1}

Full Research Paper

Open Access

Address:

¹Otto Diels Institute of Organic Chemistry, University of Kiel,
Otto-Hahn-Platz 4, 24118 Kiel, Germany and ²Institute for
Experimental and Applied Physics, University of Kiel, Leibnizstraße
19, 24098 Kiel, Germany

Beilstein J. Org. Chem. **2019**, *15*, 1485–1490.

doi:10.3762/bjoc.15.150

Received: 17 April 2019

Accepted: 28 June 2019

Published: 05 July 2019

Email:

Rainer Herges* - rherges@oc.uni-kiel.de

This article is part of the thematic issue "Molecular switches".

* Corresponding author

Guest Editor: W. Szymanski

Keywords:

cis–*trans* isomerization; diazocine; molecular switch; photochrome;
self-assembled monolayers; TATA platform

© 2019 Löw et al.; licensee Beilstein-Institut.

License and terms: see end of document.

Abstract

Recently, it has been shown that the thermochemical *cis*→*trans* isomerization of azobenzenes is accelerated by a factor of more than 1000 by electronic coupling to a gold surface via a conjugated system with 11 bonds and a distance of 14 Å. The corresponding molecular architecture consists of a platform (triazatriangulenium (TATA)) which adsorbs on the gold surface, with an acetylene spacer standing upright, like a post in the middle of the platform and the azobenzene unit mounted on top. The rate acceleration is due to a very peculiar thermal singlet–triplet–singlet mechanism mediated by bulk gold. To investigate this mechanism further and to examine scope and limitation of the “spin-switch catalysis” we now prepared analogous diazocine systems. Diazocines, in contrast to azobenzenes, are stable in the *cis*-configuration. Upon irradiation with light of 405 nm the *cis*-configuration isomerizes to the *trans*-form, which slowly returns back to the stable *cis*-isomer. To investigate the thermal *trans*→*cis* isomerization as a function of the conjugation to the metal surface, we connected the acetylene spacer in *meta* (weak conjugation) and in *para* (strong conjugation) position. Both isomers form ordered monolayers on Au(111) surfaces.

Introduction

Catalysts increase chemical reaction rates by lowering the activation energies and thus create more favorable reaction pathways [1–4]. However, there are very few reactions which do not follow the classical Eyring theory [5,6]. The rate of these reactions is not dependent on an activation barrier but controlled by quantum mechanical transition probabilities between two quantum states [7–10]. The majority of these quantum chemically forbidden reactions are photochemical processes or transition metal reactions including transitions between spin states or

electronic states. We recently discovered a purely organic system in the ground state, whose reaction rate is accelerated from days to seconds by electronic coupling to a bulk gold surface via a conjugated linker over 11 bonds and 14 Å [11]. Thermal *cis*→*trans* isomerizations of azobenzenes are usually slow with half-lives of the *trans*-isomer within the range of hours to days at room temperature (parent azobenzene: 4–5 d at 25 °C) [12]. Rotation around the N=N bond is a symmetry-forbidden process and the slow isomerization proceeds via inversion at the

Beilstein J. Org. Chem. 2019, 15, 1485–1490.

N atoms [13]. The rate of isomerization is temperature dependent and follows a classical Arrhenius type behavior [12]. However, the rate and the mechanism change dramatically if the azobenzenes are electronically coupled to bulk gold [14–17]. To investigate the *cis*→*trans* isomerizations of azobenzenes as a function of electronic coupling systematically, we used the so-called platform approach [18]. The azobenzenes are not directly adsorbed on the surface, but covalently mounted on “TATA” (triazatriangulenium) platforms which adsorb on Au(111) surfaces. A spacer, such as an ethynyl group is connected to the central carbon atom like a post and the azobenzene is mounted on top of the spacer. After preparation of an ordered self-assembled monolayer on gold, the azobenzene units are freestanding upright on the surface. The platform defines the lateral distance between next neighbors and provides the free volume for unhindered isomerization of the azobenzene units [19,20]. The length and electronic nature of the spacer units control the distance from the surface and define the electronic coupling with the metal surface [11,18]. With increasing π -conjugation from the azobenzene into the platform, and thus coupling to the gold surface, the activation barrier drops to almost zero ($\approx 8 \text{ kJ mol}^{-1}$) and the frequency factors ($\log A$) become negative [11]. Vanishing barriers and low frequency factors are typical for non-adiabatic reactions [9]. The mechanism was elucidated as a singlet–triplet–singlet spin change process, which is forbidden in solution but mediated by coupling to the conduction band of the bulk gold. We are now exploring scope and limitations of this peculiar spin catalysis. To investigate if the reverse isomerization process from the *trans* to the *cis*-configuration would also be accelerated, and to further scrutinize the coupling effects, we prepared analogous diazocine systems. Diazocines are bridged azobenzenes [21]. Imposed by the ring strain of the central eight-membered ring, the *cis*-configuration (boat conformation) is more stable than the *trans*-isomer (twist conformation). Upon irradiation with $\approx 400 \text{ nm}$ the *cis*-form switches to the *trans*-isomer, and irradiation with $\approx 500 \text{ nm}$ or heating leads back to the *cis*-form [22]. Hence, the diazocines are quasi reversed azobenzenes that are more stable in their *trans*-configurations [23].

To investigate the electronic coupling effects, we synthesized two diazocine derivatized TATA platforms with ethynyl spacers (diazocine-TATAs). In compound **1** the diazocine is connected to the platform with the ethynyl group in *para*-position to the azo group, providing a full π -conjugation path of the N=N unit through the ethynyl spacer into the platform. Diazocine-TATA **2** is connected in *meta*-position and thus interrupting conjugation [24,25]. Both diazocine-TATAs are equipped with methoxy groups, which serve as “reporter units” indicating the configuration of the molecules on metal surfaces [15]. In **1** the OMe group is attached *para* and in **2** the methoxy

group is *meta* with respect to the azo group. Model calculations predict that the C_{phenyl}–O bonds in the *cis*-isomers thus are parallel, and in the *trans*-isomers orthogonal to the surface (Figure 1). Previous investigations have shown that IRRAS (infrared absorption reflection spectroscopy) in combination with the surface selection rules (stretching mode orthogonal to the surface→high intensity, parallel to the surface→low intensity) is a suitable method to determine the configuration and to measure kinetics on surfaces [15]. The C–O stretching frequencies proved to be ideal reporter signals to determine the configuration and to measure kinetics in monolayers of azo-TATAs on surfaces.

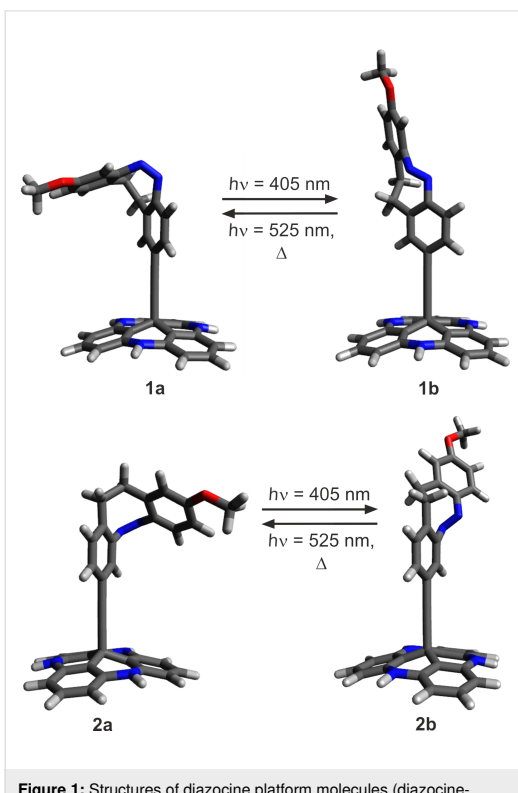


Figure 1: Structures of diazocine platform molecules (diazocine-TATAs) **1** and **2** in *cis* (**1a**, **2a**) and *trans*-configuration (**1b**, **2b**) (octyl side chains are replaced by protons for simplification). The *cis*-diazocines (**1a**, **2a**) isomerize upon irradiation with 405 nm to the metastable *trans*-diazocines (**1b**, **2b**) and with 525 nm or thermally back to the *cis*-diazocines (**1a**, **2a**).

Results and Discussion

To obtain information on preferred conformations of **1** and **2** in their *cis* and *trans*-configurations and to predict thermodynamic and kinetic stabilities, we performed DFT calculations at the M06-2X/def2-TZVP level of theory (Table 1, for details see Supporting Information File 1, chapter VI). As expected for

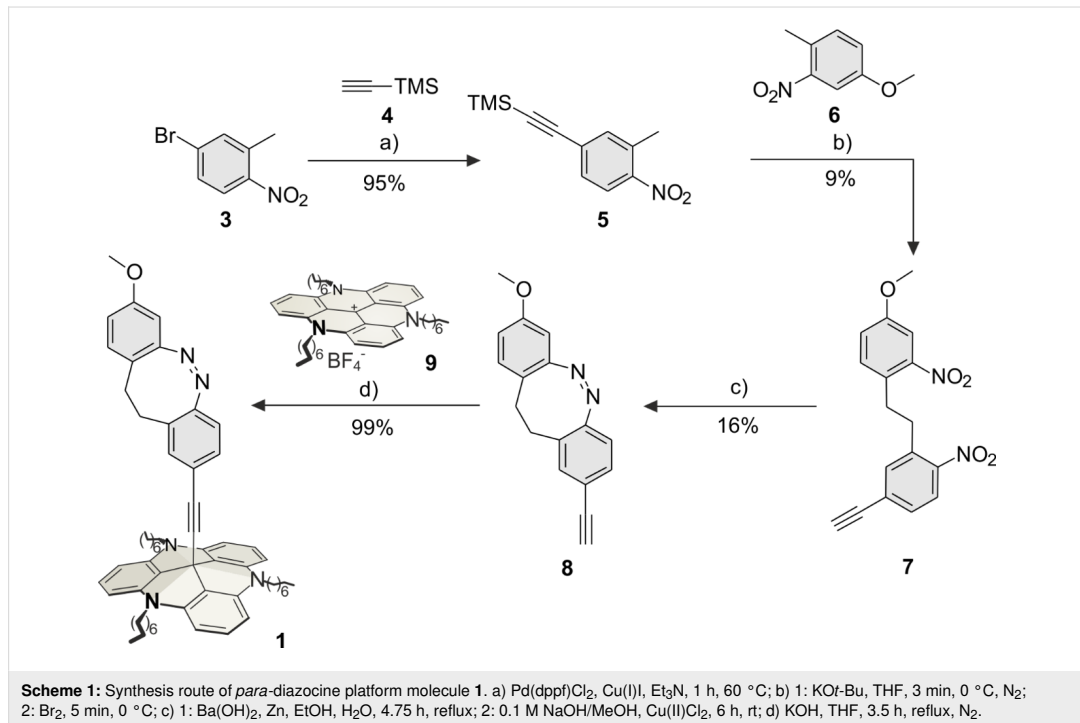
diazocine-based molecules our calculations predict the *cis* configuration for both compounds as the thermodynamically most stable isomers. For the corresponding *trans*-configuration two different conformations were found: the twist and the chair structures. The twist conformation is about 2.5 kcal mol⁻¹ more stable than the chair conformation. Our calculations predict reaction barriers (*trans*-twist→*cis*-boat) for both compounds of approximately 23 kcal mol⁻¹ (96 kJ mol⁻¹). Obviously, the TATA platform and the ethynyl spacer have only marginal effects on the isomerization process. Hence, the diazocines **1** and **2** are ideal candidates to investigate the effect of bulk gold as a function of electronic coupling (conjugation) of the azo unit to gold.

Table 1: Calculated quantum chemical energies E_{rel} (M06-2X/def2-TZVP) of the twist and chair conformation of the *trans*-configuration of *para*-ethynyl-substituted diazocene **1b** (*para*-diazocene), and *meta*-diazocene **2b**, relative to the boat conformation of the *cis*-isomers **1a** and **2a**. ΔH^\ddagger are the calculated reaction barriers (*trans*-twist→*cis*-boat). All energies are given in kcal mol⁻¹.

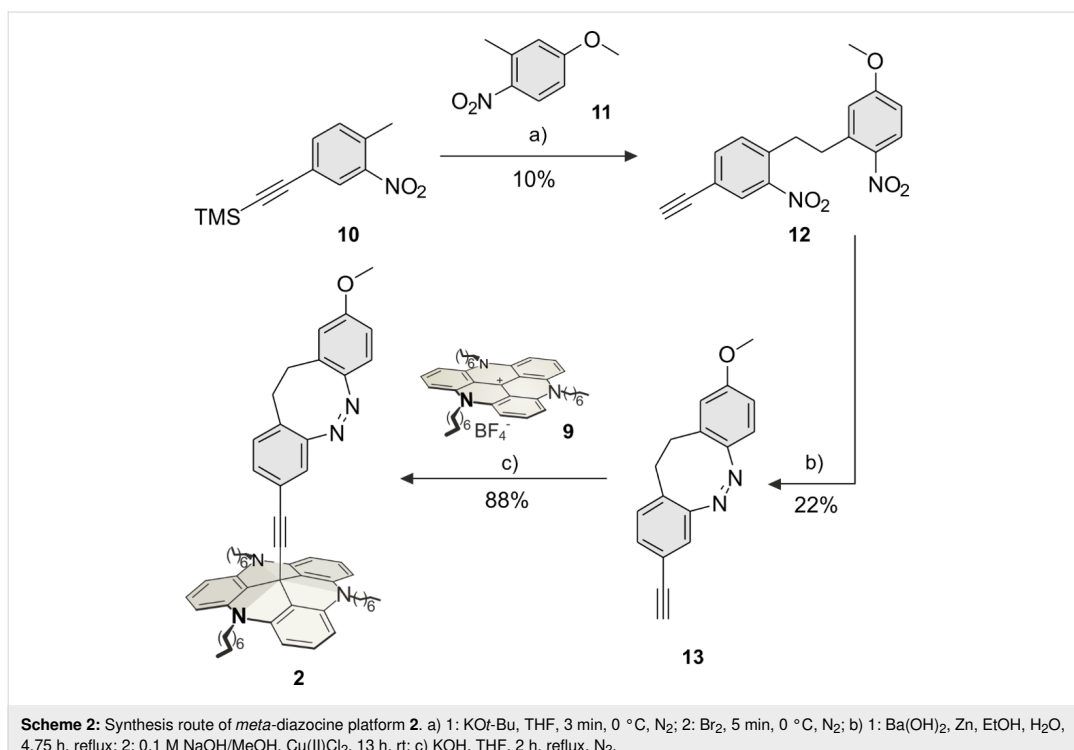
	E_{rel} <i>trans</i> twist	E_{rel} <i>trans</i> chair	ΔH^\ddagger
<i>para</i> -diazocene 1	7.9	10.6	22.6
<i>meta</i> -diazocene 2	8.0	10.3	23.0

The *para*-diazocene-TATA **1** was synthesized in a 5-step synthesis route (Scheme 1). Bromotoluene **3** was synthesized as described [26]. In a Sonogashira cross-coupling reaction acetylene **4** (95%) was prepared from bromotoluene **3** with TMS-protected acetylene **4** (95%). The C–C bond formation of **5** and **6** to give dibenzoyl **7** was achieved with potassium butoxide and elemental bromine (9%) according to a literature procedure [27]. The *para*-ethynyl diazocene **8** was obtained by reduction of both nitro groups, followed by oxidation of the formed hydrazine (16%). The unprotected ethynyl diazocene **8** was deprotonated with potassium hydroxide and connected to the central carbon atom of the TATA platform **9** (synthesized according to Laursen and Krebs [28]) to obtain target *para*-diazocene mounted on the octyl-substituted TATA platform **1** (99%).

The synthesis of the *meta*-diazocene platform molecule **2** was achieved in a 4-step synthesis route (Scheme 2). Nitrotoluene **10** was synthesized as described in literature [29]. The reaction of ethynyltoluene **10** with methoxytoluene **11** gave dibenzoyl **12** (10%) according to the same procedure as for dibenzoyl **7** (Scheme 1). Diazocene **13** was obtained by reduction and oxidation in moderate yields (22%). The reaction of diazocene **13** with the TATA ion **9** gave the target diazocene **2** (88%, Scheme 2).



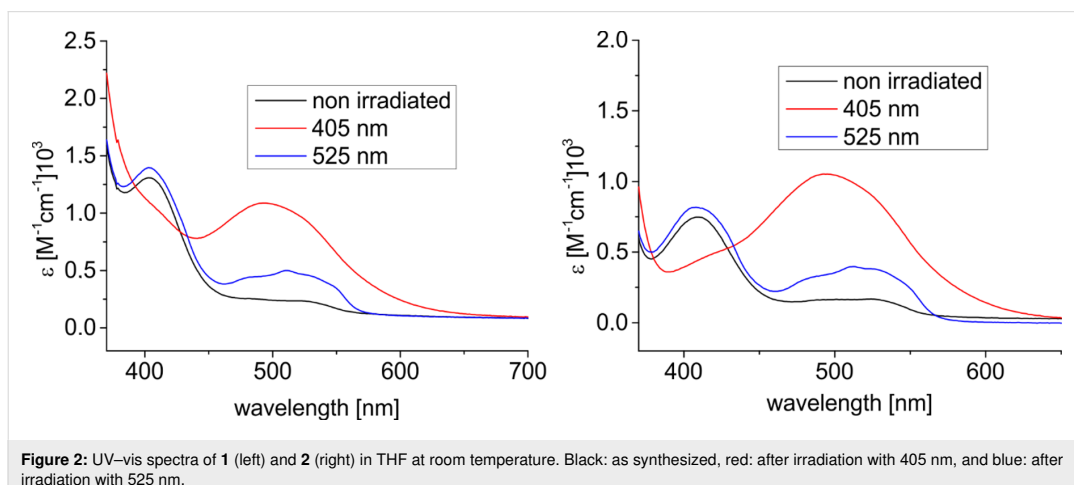
Beilstein J. Org. Chem. 2019, 15, 1485–1490.



The photophysical properties and the switching behavior of **1** and **2** were determined in solution (THF). The UV-vis spectra of **1** and **2** are shown before and after irradiation with 405 nm and 525 nm. Both diazocine-TATAs **1** and **2** exhibit similar UV spectra. The $n \rightarrow \pi^*$ transition of *cis*-**1** appears at 403 nm and at 494 nm in the *trans*-isomer. The corresponding absorption

maxima in diazocine-TATA **2** are 409 nm (*cis*) and 493 nm (*trans*) (Figure 2).

The photostationary states of **1** and **2** were determined in toluene- d_8 by ^1H NMR measurements (Table 2). Optimal wavelengths for the *cis* \rightarrow *trans* isomerization are 405 nm (**1**: 53%



trans, **2**: 65% *trans*). Back-isomerization to the *cis*-isomer with 525 nm is nearly quantitative. The half-lives (298 K) are similar for both systems (2.12 h for **1** and 2.32 h for **2**). The lack of conjugation between the azo function and the ethynyl spacer of **2** yields in a slightly higher half-life, which is in agreement with earlier results [11].

Table 2: Photostationary states (PSS) of *para*-diazocine-TATA **1** (2.05 mmol/L) and *meta*-diazocine-TATA **2** (2.27 mmol/L) upon irradiation with light of 405 nm, 525 nm and thermal isomerization half-life ($t_{1/2}$) determined with ^1H NMR spectroscopy (in deuterated toluene). The activation energies (E_A) are calculated from the linear fit of an Arrhenius plot.

	<i>para</i> -diazocine 1	<i>meta</i> -diazocine 2
PSS (405 nm)	53% (<i>trans</i>)	65% (<i>trans</i>)
PSS (525 nm)	93% (<i>cis</i>)	93% (<i>cis</i>)
$t_{1/2}$ (290.5 K)	5.27 h	5.76 h
$t_{1/2}$ (298 K)	2.12 h	2.32 h
$t_{1/2}$ (308 K)	0.69 h	0.73 h
E_A (kJ mol $^{-1}$)	86.5	84.7

STM Measurements

The adsorption behavior of the diazocine-TATA molecules on Au(111) surfaces was studied by STM at room temperature (Figure 3). Adlayers of both compounds show a hexagonally ordered superstructure with lattice constants of **1** and **2** being (12.2 ± 0.6) Å and (12.1 ± 0.5) Å, respectively. Additionally, two rotational domains with an angle of $(15 \pm 4)^\circ$ are observed. Altogether these parameters are in good agreement with a $(\sqrt{19} \times \sqrt{19}) R23.4^\circ$ superstructure which has been also observed in previous STM investigations of TATA and azobenzene-TATA molecules with octyl ligands [18,20,30].

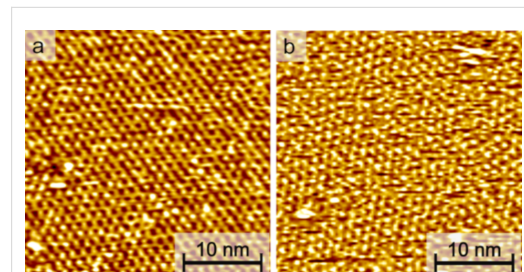


Figure 3: STM images (30×30 nm 2 , $U_{\text{bias}} = 0.3$ V, $I_t = 40$ pA) of self-assembled monolayers of (a) compound **1** and (b) compound **2** on Au(111).

Conclusion

In summary, we present the syntheses of two different diazocines mounted on TATA platforms (**1**, **2**). The photochem-

ical switching between the stable *cis* and metastable *trans*-isomers was investigated. Upon irradiation with light of 405 nm diazocine-TATAs **1** and **2** convert to their *trans*-configurations in moderate to good yields. The metastable *trans*-isomers of **1** and **2** isomerize back to the *cis*-isomer with half-lives of 2.12 h and 2.32 h at 298 K. The *trans* \rightarrow *cis* activation energies with 86.5 kJ mol $^{-1}$ for **1** and with 84.7 kJ mol $^{-1}$ for **2** are similar to the structurally related azobenzenes [11]. Both diazocine-TATAs form highly ordered monolayers on Au(111) surfaces. Further studies will include IRRAS measurements to determine the *trans* \rightarrow *cis* isomerization kinetics on Au(111) surfaces.

Experimental

For detailed experimental procedures, including NMR, UV-vis and MS spectra see Supporting Information File 1, chapters I–IV, for kinetic studies see Supporting Information File 1, chapter V.

Supporting Information

Supporting Information File 1

Analytical methods, experimental procedures, NMR and UV spectra, kinetic studies and DFT calculations.
[<https://www.beilstein-journals.org/bjoc/content/supporting/1860-5397-15-150-S1.pdf>]

Acknowledgements

The authors gratefully acknowledge financial support by the Deutsche Forschungsgesellschaft within the Sonderforschungsbereich 677, “Function by Switching”.

ORCID® iDs

Roland Löw - <https://orcid.org/0000-0002-3051-7831>
Talina Rusch - <https://orcid.org/0000-0001-8123-6792>
Fynn Röhricht - <https://orcid.org/0000-0001-9935-9256>
Rainer Herges - <https://orcid.org/0000-0002-6396-6991>

Preprint

A non-peer-reviewed version of this article has been previously published as a preprint doi:10.3762/bxiv.2019.11.v1

References

- Hauffe, K., Ed. *Katalyse*; DE GRUYTER: Berlin, New York, 1976; p 119. doi:10.1515/9783110829990
- Ostbald, W. *Z. Phys. Chem.* **1894**, 15, 705–706.
- Oyama, S. T.; Somorjai, G. A. *J. Chem. Educ.* **1988**, 65, 765–769. doi:10.1021/ed065p765
- Shriver, D. F.; Atkins, P. W.; Langford, C. H. In *Anorganische Chemie*, 2nd ed.; Heck, J.; Kain, W.; Weidenbruch, M., Eds.; Wiley-VCH: Weinheim, Germany, 1997; p 692.
- Eyring, H. *J. Chem. Phys.* **1935**, 3, 107–115. doi:10.1063/1.1749604

Beilstein J. Org. Chem. **2019**, *15*, 1485–1490.

6. Gowenlock, B. G. *Q. Rev., Chem. Soc.* **1960**, *14*, 133–145.
doi:10.1039/qr9601400133
7. Hauser, A. *Coord. Chem. Rev.* **1991**, *111*, 275–290.
doi:10.1016/0010-8545(91)84034-3
8. Xie, C.-L.; Hendrickson, D. N. *J. Am. Chem. Soc.* **1987**, *109*, 6981–6988. doi:10.1021/ja00257a013
9. Harvey, J. N. *Phys. Chem. Chem. Phys.* **2007**, *9*, 331–343.
doi:10.1039/b614390c
10. Schreiner, P. R.; Reisenauer, H. P.; Pickard IV, F. C.; Simmonett, A. C.; Allen, W. D.; Matyus, E.; Császár, A. G. *Nature* **2008**, *453*, 906–909. doi:10.1038/nature07010
11. Schlamm, A.; Löw, R.; Rusch, T.; Röhricht, F.; Strunkus, T.; Tellkamp, T.; Sönnicthen, F.; Manthe, U.; Magnussen, O.; Tuczek, F.; Herges, R. *Angew. Chem., Int. Ed.* **2019**, *58*, 6574–6578.
doi:10.1002/anie.201814342
12. Hartley, G. S. *J. Chem. Soc.* **1938**, 633–642.
doi:10.1039/jr9380000633
13. Shinkai, S.; Kusano, Y.; Shigematsu, K.; Manabe, O. *Chem. Lett.* **1980**, *9*, 1303–1306. doi:10.1246/cl.1980.1303
14. Jung, U.; Schütt, C.; Filinova, O.; Kubitschke, J.; Herges, R.; Magnussen, O. *J. Phys. Chem. C* **2012**, *116*, 25943–25948.
doi:10.1021/jp310451c
15. Jacob, H.; Ulrich, S.; Jung, U.; Lemke, S.; Rusch, T.; Schütt, C.; Petersen, F.; Strunkus, T.; Magnussen, O.; Herges, R.; Tuczek, F. *Phys. Chem. Chem. Phys.* **2014**, *16*, 22643–22650.
doi:10.1039/c4cp03438d
16. Krekienh, N. R.; Müller, M.; Jung, U.; Ulrich, S.; Herges, R.; Magnussen, O. M. *Langmuir* **2015**, *31*, 8362–8370.
doi:10.1021/acs.langmuir.5b01645
17. Hagen, S.; Kate, P.; Peters, M. V.; Hecht, S.; Wolf, M.; Tegeder, P. *Appl. Phys. A: Mater. Sci. Process.* **2008**, *93*, 253–260.
doi:10.1007/s00339-008-4831-5
18. Baisch, B.; Raffa, D.; Jung, U.; Magnussen, O. M.; Nicolas, C.; Lacour, J.; Kubitschke, J.; Herges, R. *J. Am. Chem. Soc.* **2009**, *131*, 442–443. doi:10.1021/ja807923f
19. Ulrich, S.; Jung, U.; Strunkus, T.; Schütt, C.; Bloedorn, A.; Lemke, S.; Ludwig, E.; Kipp, L.; Faupel, F.; Magnussen, O.; Herges, R. *Phys. Chem. Chem. Phys.* **2015**, *17*, 17053–17062.
doi:10.1039/c5cp01447f
20. Kuhn, S.; Baisch, B.; Jung, U.; Johannsen, T.; Kubitschke, J.; Herges, R.; Magnussen, O. *Phys. Chem. Chem. Phys.* **2010**, *12*, 4481.
doi:10.1039/b922882a
21. Duval, H. *Bull. Soc. Chim. Fr.* **1910**, *7*, 727.
22. Siewertsen, R.; Neumann, H.; Buchheim-Stehn, B.; Herges, R.; Näther, C.; Renth, F.; Temps, F. *J. Am. Chem. Soc.* **2009**, *131*, 15594–15595. doi:10.1021/ja906547d
23. Hartley, G. S. *Nature* **1937**, *140*, 281. doi:10.1038/140281a0
24. Yaliraki, S. N.; Ratner, M. A. *Ann. N. Y. Acad. Sci.* **2002**, *960*, 153–162.
doi:10.1111/j.1749-6632.2002.tb03030.x
25. Mayor, M.; Büschel, M.; Fromm, K. M.; Lehn, J.-M.; Daub, J. *Ann. N. Y. Acad. Sci.* **2002**, *960*, 16–28.
doi:10.1111/j.1749-6632.2002.tb03022.x
26. Wahhab, A.; Therrien, E. Small Molecule Inhibitors of Protein Arginine methyltransferases. PCT Pat. Appl. WO2008104077 A1, Feb 28, 2007.
27. Moermann, W.; Langbein, D.; Herges, R. *Synthesis* **2017**, *49*, 3471–3475. doi:10.1055/s-0036-1590685
28. Laursen, B. W.; Krebs, F. C. *Chem. – Eur. J.* **2001**, *7*, 1773–1783.
doi:10.1002/1521-3765(20010417)7:8<1773::aid-chem17730>3.0.co;2-f
29. Park, K.; Lee, B. M. Novel phenylethynyl benzamide glucokinase activator and method for preparing same. PCT Pat. Appl. WO2014112798 A1, Jan 16, 2013.
30. Lemke, S.; Ulrich, S.; Claußen, F.; Bloedorn, A.; Jung, U.; Herges, R.; Magnussen, O. M. *Surf. Sci.* **2015**, *632*, 71–76.
doi:10.1016/j.susc.2014.08.028

License and Terms

This is an Open Access article under the terms of the Creative Commons Attribution License (<http://creativecommons.org/licenses/by/4.0>). Please note that the reuse, redistribution and reproduction in particular requires that the authors and source are credited.

The license is subject to the *Beilstein Journal of Organic Chemistry* terms and conditions:
(<https://www.beilstein-journals.org/bjoc>)

The definitive version of this article is the electronic one which can be found at:
[doi:10.3762/bjoc.15.150](https://doi.org/10.3762/bjoc.15.150)

4.5 Alternative Oberflächenfunktionalisierung

Neben dem Plattformkonzept gibt es bereits eine Vielzahl anderer Konzepte zur Funktionalisierung von Oberflächen. Verwendete Ansätze zielen dabei meist auf einen definierten Abstand zur Oberfläche ab, da ein Schalter wie z.B. AB ohne Substitution flach auf Gold adsorbiert.^[148] Dort koppelt dieser mit dem Bulkmaterial elektronisch, wird in der Photoanregung gequencht und zusätzlich durch die Physisorption an der Isomerisierung gehindert.^[149–151] Mit der Einführung von sterisch anspruchsvollen Substituenten entsteht ein Abstand zur Oberfläche (s. Abb. 4.5 A) und eine Schaltung wird möglich.^[148,152–156] Die Anreicherung des *cis*-Isomers gelingt jedoch deutlich ineffizienter^[149,157] und die Rückisomerisierung ist im Vergleich zu der in Lösung drastisch beschleunigt.^[153] Konzepte, welche die elektronische Kopplung umgehen, sind z.B. wohl geordnete SAMs aus vertikal chemisorbierten Alkanthiolen (s. Abb. 4.5 B). Da die Schaltung durch auftretende sterische Hinderung in der Monolage eingeschränkt ist,^[158–161] wurden sowohl sperrige Substituenten in die Alkylketten^[159] als auch Coadsorptionsexperimente mit unfunktionalisierten Ketten verwendet (s. Abb. 4.5 C), um freie Isomerisierung für AB zu ermöglichen.^[158,161–167] Um auftretende Aggregation und Phasenseparation zu verhindern, wurden Tripods (s. Abb. 4.5 D) entwickelt,^[168] welche ähnlich der TATA-Plattform einzeln adressierbare^[169] und in der gesamten SAM schaltbare ABs zeigen.^[170,171]

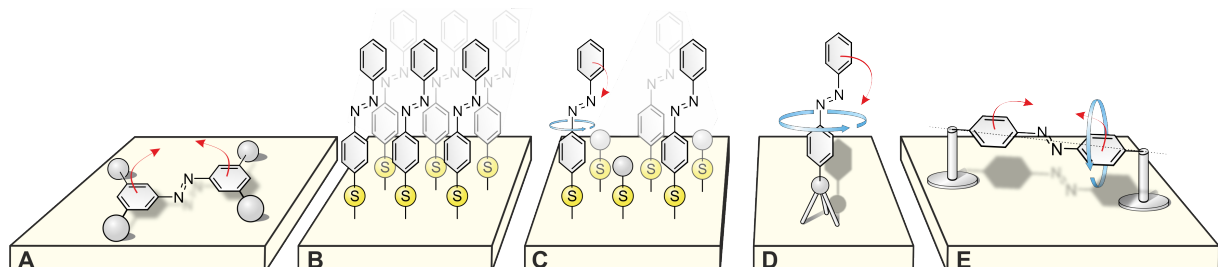


Abb. 4.5: Alternative Konzepte zur Oberflächenfunktionalisierung: A) laterale, eingeschränkte Schaltung, B) kovalente Thiol-Bindung: keine Schaltung, C) Coadsorption von un- und funktionalsierten Thiolen: vertikale Schaltung, D) Tripodansatz: vertikale Schaltung, E) Konzept für laterale Schaltung und altitudinale Rotation: TATA-Plattformen dienen als Pfeiler für ein photoschaltbares, rotierbares AB.

Ein bisher wenig erforschter Bereich in der Oberflächenfunktionalisierung sind horizontale Schalter und altitudinale Rotoren. Um so seltene Konstruktionen^[172–176] zu ermöglichen, muss das Design mehrere Faktoren berücksichtigen. Für eine freie altitudinale Rotation wäre eine Art Aufhängung in Form von zwei Pfeilern (s. Abb. 4.5 E), die Abstand zur Oberfläche garantieren, von Vorteil. Setzt man in dieser Konstruktion einen konjugationsisolierten Photoschalter mit Rotationsachse ein, könnte man dank Abstand Kopplung zur Oberfläche und somit Quenching der Anregung sowie strukturelle Einschränkungen der Isomerisierung ausschließen. AB mit intrinsischer Rotationsachse bei zweifacher *para*-Substitution sollte freie Rotation und Photoschaltbarkeit gewährleisten. Um so ein Design umzusetzen, wurden TATA-Plattformen mit Phenylethinylaufbau über AB verbunden, sodass bei Adsorption der TATAs auf einer Oberfläche zwei Pfeiler den Photoschalter auf einer Rotationsachse tragen sollten.^[177]

4.6 Ordered Adlayers of a Combined Lateral Switch and Rotor

T. R. Rusch, A. Schlimm, N. R. Krekiehn, B. M. Flöser, F. Röhricht, M. Hammerich, I. Lautenschläger, T. Strunskus, R. Herges, F. Tuczek und O. Magnussen

J. Phys. Chem. C **2019**, *123*, 13720–13730.

DOI:10.1021/acs.jpcc.9b02469

Supporting Information: Anhang SI 8

Wissenschaftliche Beiträge: Coverabbildung, Verfassen des Manuskripts (anteilig), quantenchemische Rechnungen des DFT-Teils.

Zusammenfassung

Bei dieser Arbeit wird anders als bei anderen Oberflächenfunktionalisierungen AB als lateraler Schalter und altitudinaler Rotor in geordneten Monolagen auf Gold(111)-Oberflächen aufgebracht und untersucht. Das molekulare Konzept basiert auf zwei TATA-Plattformen mit orthogonal zur Oberfläche stehenden Phenylethinylen-Pfeilern, welche über den Photoschalter AB lateral verknüpft sind. Die makroskopische Betrachtung des Systems auf Gold mittels STM-Experimenten zeigt eine hoch geordnete hexagonale Überstruktur, welche jedoch durch Photoisomerisierung keine Veränderung erfuhr. Um die dreidimensionale Anordnung der Moleküle und deren Schaltung aufzuklären, wurden verschiedene oberflächenspektroskopische und theoretische Methoden angewandt.

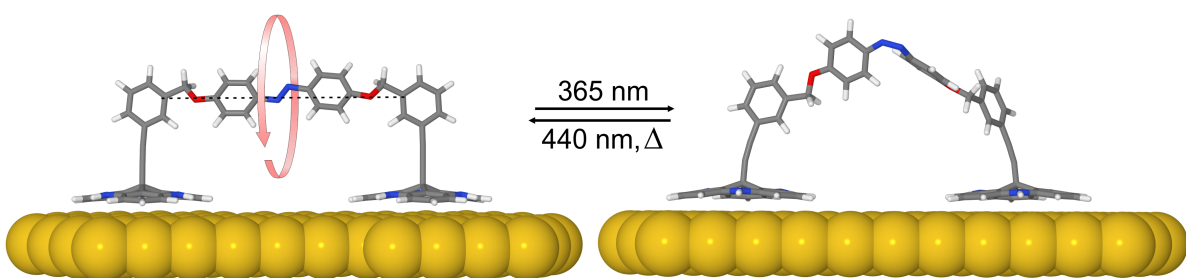


Abb. 4.6: Vereinfachte Strukturvorschläge des Moleküls (ohne Seitenketten) beider Isomere auf einer Gold(111)-Oberfläche. Die *trans*-Konfiguration bietet intrinsisch eine Rotationsachse, welche durch Isomerisierung mit 365 nm zum *cis*-Isomer entfällt.

Spektroskopische Ergebnisse belegen intakte Moleküle auf der Oberfläche (XPS) sowie reversible Photoisomerisierung des ABs mit Kinetik ähnlich der in Lösung und demnach einer Entkopplung von der Oberfläche (UV/Vis). Zudem konnten Röntgen-Nahkanten-Absorptions-Spektroskopie (*near-edge x-ray absorption fine structure*, NEXAFS) Experimente dies bestätigen und freie Drehbarkeit der zentralen funktionellen Gruppe für die *trans*-Konfiguration nachweisen. Die theoretische Struktursuche konnte mehrere *trans*-Strukturen mit dem durch die Überstruktur vorgegebenen intramolekularen TATA-Abstand (18.5 Å) finden. Der theoretisch unbeschränkte Abstand 19.8 Å ist geringfügig größer. Trotzdem sind diese Strukturen alle nahezu isoenergetisch und weisen für *trans*-AB eine lineare Rotationsachse auf. Zusätzlich konnte ein *cis*-Isomer bei gleichem TATA-Abstand energetisch mit knapp 19 kcal mol⁻¹ (rel. zum *trans*) gefunden werden. Diese Struktur zeigt zwar durch Biegung der Pfeiler eine gewisse Spannung, ist jedoch im Vergleich zu einem anderen *cis*-Konformer, bei dem das AB Richtung Substrat zeigt, energetisch favorisiert und weniger gespannt. Da keine lineare Rotationsachse bei den *cis*-Strukturen ersichtlich ist und andere Konformere der *cis*-Konfiguration energetisch ungünstig, scheint diese Bewegung unterbunden. Dies steht in guter Übereinkunft mit den NEXAFS-Ergebnissen. Die gefundenen Strukturen ergeben mit den experimentellen Daten somit eine umfassende Charakterisierung des Systems auf Gold.

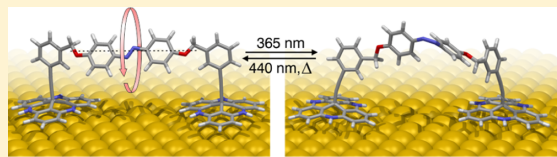
Ordered Adlayers of a Combined Lateral Switch and Rotor

Talina R. Rusch,[†] Alexander Schlimm,[‡] Nicolai R. Krekiehn,[†] Benedikt M. Flöser,[‡] Fynn Röhricht,[§] Melanie Hammerich,[§] Irene Lautenschläger,[‡] Thomas Strunskus,[§] Rainer Herges,^{*,||} Felix Tuczek,^{*,‡} and Olaf M. Magnussen^{*,†}

[†]Institute of Experimental and Applied Physics, [‡]Institute of Inorganic Chemistry, [§]Otto Diels Institute of Organic Chemistry, and ^{||}Institute for Materials Science, Christian Albrechts University Kiel, Kiel 24118, Germany

Supporting Information

ABSTRACT: Rotors and switches are elementary building blocks of molecular machines. To achieve more advanced functions, these units have to be integrated into solid-state devices, which triggered interest in mounting these functional units in well-defined geometries onto surfaces. While vertically oriented switches and rotors have been obtained by various strategies, the design of surface-parallel switches and of altitudinal rotors with an in-plane oriented rotation axis has proven to be more difficult. We here demonstrate a molecular adlayer system with highly defined geometry and laterally oriented functional groups that combines facile photoswitching and rotation. We employ a custom-designed molecule with two platforms and pillars that span an azobenzene unit between them. The molecules form well-ordered monolayers on Au(111) with the azobenzene units parallel to and above the surface. Spectroscopic data and density functional calculations suggest that in the trans configuration, at room temperature, the azo unit is freely rotating. Upon irradiation with UV light, the azo unit switches to the bent cis configuration and rotation stops. Irradiation with 430 nm restores the rotating trans state. Notably, the photochemistry is not quenched by the metal surface. This approach offers a promising strategy to operate molecular machines on metal surfaces with light, which is still a major problem in molecular nanotechnology.



INTRODUCTION

Similar to their counterparts in the macroscopic world, molecular motors and machines must be properly embedded in their environment to achieve sophisticated functions. The first step in building artificial molecular machines thus is the integration of functional molecular units into solids or onto surfaces. Extensive advances in this field have already been made, especially in the attachment of molecular rotors and switches to surfaces via self-assembly. Free rotation and molecular switching are among the most fundamental functions achievable in self-assembled layers on surfaces, but applications of such systems for more complex machinelike functions are still limited. For this, systems with precisely defined positions and orientations have to be developed. That requires going beyond conventional self-assembly approaches, such as surface attachment of functional units via flexible alkanethiol or siloxane-based molecules.

Several strategies have been used to mount molecular switches or rotors perpendicular or parallel to solid surfaces, which in the case of rotors correspond to an azimuthal or altitudinal rotation axis, respectively (Figure 1a).

Both geometries have been realized (Figure 1b,c).^{1–3} Azimuthal rotors on surfaces were demonstrated by Michl and co-workers, who used vertical channels in crystal surfaces to insert the axes of rotors.⁴ Alternative approaches to mount rotors and switches perpendicular to surfaces use molecular building blocks that ensure a vertical geometry, e.g.,

tripods,^{5,6} bulky spacer groups,^{7–10} or the platform concept developed by our group (Figure 1b, right).^{11–16} The latter employs planar units that adsorb on the surface in the form of highly ordered monolayers and provide posts for vertical functions that are freely rotating and, with suitable functional groups, photoswitchable.

Altitudinal rotors and surface-parallel switches require a different construction strategy.^{1,3,17–19} Zheng et al. have been the first to present a concept for such systems.¹⁷ They employed two vertical poles to mount an altitudinal rotor parallel to the surface. However, apart from this seminal work, very few examples of such systems exist.^{1,18,20} In the case of molecular switches on metals, azobenzenes and other photocromes adsorb in a planar geometry,^{21,22} but their photochemistry is quenched by electronic coupling to the substrate. Several approaches have been developed to decouple the photoactive parts from the surface and thus restore the photochemistry.^{23–25} Tegeder et al. employed azobenzene units with large substituents as vertical spacers (airbag approach),^{26–29} but distortions of the molecule upon adsorption lead to strong suppression of the photoisomerization. Furthermore, cyclophane-type structures were used to enforce a distance between the metal surface and the

Received: March 15, 2019

Revised: May 15, 2019

Published: May 16, 2019

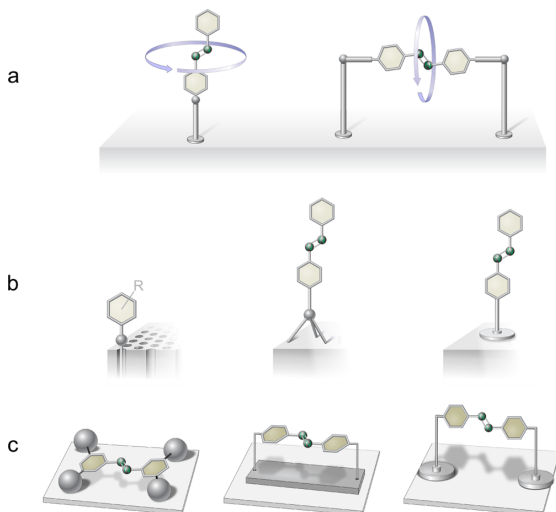


Figure 1. Schematic illustrations of (a) surface-mounted molecular switches and rotors with vertical and lateral orientation. Concepts for realizing these (b) vertical and (c) lateral functions on surfaces.

photoactive part of the molecule to prevent electronic coupling.³⁰ Switching or rotation of the decoupled units was not reported, however.

In this work, we demonstrate that modification of our platform concept allows vertical mounting of a functional unit while retaining its capability to both switch and rotate. Here, two platforms with two pillars span the axis of a rotor, consisting of a photoswitchable p,p'-substituted azobenzene unit (Figure 1c, right). This is realized using compound 1, which we recently introduced.³¹ In this molecule, an azobenzene is spanned between two phenyl-functionalized triazatriangulenium (TATA) platforms (Figure 2). Ether

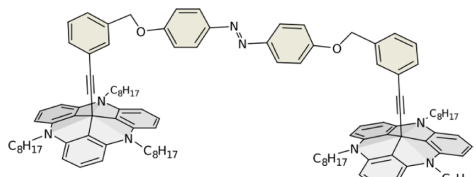


Figure 2. Studied compound 1: an azobenzene unit spanned between two phenyl posts, mounted on TATA platforms.

bridges attached the meta positions of phenyls on both sides to the para positions of azobenzene. The alkoxy group interrupts the conjugation between the platform and azobenzene and decouples the azo unit from the metal surface. According to photophysical experiments in solution, azobenzene is still reversibly switchable with a high switching efficiency and low fatigue.

In the following, we present a detailed study of the adlayers structure and photoswitching by scanning tunneling microscopy (STM), X-ray photoelectron spectroscopy (XPS), near-edge X-ray absorption fine structure spectroscopy (NEXAFS), ultraviolet-visible (UV-vis) spectroscopy, and supporting quantum chemical calculations. Preparation of molecular monolayers with a well-defined adsorption geometry and

long-range order is nontrivial for complex nonplanar molecules, such as compound 1. We show that by optimizing the self-assembly conditions ordered adlayers with high packing density of these molecules can be prepared on Au(111) surfaces, in which the azobenzene units are oriented parallel to the surface and to each other. Furthermore, we provide evidence that azobenzene is rotatable in the slender trans configuration. Upon irradiation with UV light, reversible isomerization to the bent cis configuration occurs, which appears to block the rotation.

EXPERIMENTAL SECTION

Adlayer Preparation. The synthesis of 1,2-bis[4-[3-(4,8,12-tris-n-octyl-4,8,12-triazatriangulenium-benzyloxy)-12c-ethynyl]phenyl]diazene (1) has been described in detail in a previous publication.³¹ The crude product was purified by column chromatography, and according to NMR analysis, there are no major signs for impurities. For the STM, XPS, and NEXAFS measurements, circular Au(111) single crystals with surface diameters of 10–12 mm, oriented within 0.3° (MaTeck), were used as substrates for the self-assembled monolayer (SAM) formation. The single crystals were cleaned before each preparation by flame-annealing in butane gas. UV-vis experiments were performed on ultrathin Au films of 10 nm nominal thickness with a 1–2 nm Ti adhesion layer on quartz glass (Phasis Sarl), described in more detail in a previous publication.³² The substrates were cleaned by repeated rinsing with acetone (Uvasol, spectroscopy grade, Merck). The glassware used for all of the preparations of the SAMs was cleaned in piranha solution (1/3 hydrogen peroxide, 2/3 sulfuric acid) and thoroughly rinsed with Milli-Q water prior to use. The adsorbate layers were then prepared by immersion of the substrate in 50–100 μm solutions in acetone for 1–3 days at 20–25 °C. Afterward, the samples were rinsed with pure acetone to remove excess molecules physisorbed on top of the SAM, dried under ambient conditions, and immediately transferred into the experimental setup.

STM. STM studies were performed under ambient conditions with a PicoPlus STM (Agilent, Santa Clara) and mechanically cut Pt/Ir (70:30) tips. The measurements were carried out in a constant current mode at tunneling currents of 20–90 pA and bias voltages of 200–700 mV. The STM data was analyzed using Scanning Probe Imaging Processor Software (SPIP, Image Metrology). Lateral drift was corrected with dedicated software, developed by our group. Radial distribution functions were obtained from sets of 14–30 images with sizes ranging from 3600 to 8100 nm² using Matlab R2016a.

XPS. The XPS and NEXAFS measurements were performed at the BESSY II synchrotron radiation facility using the PREVAC endstation at the beamline HE-SGM. The experimental station is equipped with a hemispherical VG Scienta R3000 photoelectron analyzer. The energy resolution E/DE of the beamline with 150 μm slits is 800. XP survey spectra were recorded at 700 eV photon energy using an analyzer pass energy of 100 eV, whereas for the C 1s and N 1s spectra, the photon energies were 350 and 500 eV, respectively, with a pass energy of 50 eV. All spectra were recorded at normal electron emission. For determination of the relative composition of the TATA adlayers, the XP spectra were energy-corrected using the Au 4f_{7/2} line at a binding energy of 84.0 eV as a reference. Background correction was performed using a Shirley background for the Au 4f signals and

a linear background for all other signals. Peak fitting was performed using the CASA XPS Tool. The fitting parameters are shown in the Supporting Information (Table S4). For the quantitative determination of the adlayer coverage, the peaks were integrated and normalized by the number of recorded scans to obtain the intensity per scan (IPS). To secure that small changes in beam energy and beam spot size do not influence the comparison, the IPS values were divided by the respective IPS of the gold peaks, measured directly after the N 1s or C 1s signal.

NEXAFS. The NEXAFS spectra were normalized by setting the pre-edge background to 1 (i.e., for the C K edge determined at 275.0 ± 2.5 eV and the N K edge at 388.75 ± 2.5 eV). To correct for the photon flux, all spectra were divided by the spectrum obtained for a freshly sputtered clean gold substrate and then edge-step normalized (using the average intensities for the C K edge between 275 ± 0.5 and 325 ± 0.5 eV and for the N K edge between 395 ± 0.5 and 420 ± 0.5 eV as pre- and postedge). The normalized spectra were fitted employing a step function for the absorption edge and Gaussians for the π^* and σ^* resonances to determine the intensity I of specific resonances (Figure S4). The series of spectra of a specific sample measured at different angles of incidence were fitted with the same parameter set, i.e., the energies of the resonances were allowed to vary in maximum by 0.2 eV and the half-widths at full maximum by 0.3 eV, as in agreement with the estimated experimental resolution. For determination of the orientation of the molecular orbitals, the dependence of the intensities I of the π^* resonances on the angle of incidence θ was finally fitted to model functions

$$I = A \cdot \left[P \cos^2 \theta \cdot \left(1 - \frac{3}{2} \sin^2 \alpha \right) + \frac{1}{2} \sin^2 \alpha \right] \quad (1)$$

with the specific amplitudes of the resonances A , the degree of polarization $P = 0.91$, and the tilt angle of the transition dipole moment of the molecule with respect to the surface normal α .

UV/Vis. The UV/vis spectroscopy measurements were carried out with a Cary 4000 double-beam spectrometer (Varian Inc.) using the methodology of our previous studies.³² The intensities of the spectrometer beam were less than 10^{-7} mW cm⁻², i.e., 6 orders of magnitude lower than those employed for the photoisomerization. The spectra were recorded under ambient conditions and in transmission, with the Au thin film oriented perpendicular and the quartz backside of the sample facing toward the incident monochromatic probe beam. The trans–cis and cis–trans photoisomerizations in the SAM were induced by irradiating the sample from the backside at an angle of 45° with light-emitting diodes with emission maxima at 365 nm (Nichia Corporation) and 455 nm (Luxeon), respectively. This resulted in intensities of up to 0.41 mW cm⁻² (365 nm) and 0.38 mW cm⁻² (455 nm) at the sample. Photoisomerization of the molecules in solution was recorded with the same setup, using a cuvette with a thickness of 1 mm in the place of the quartz sample holder. In all spectral measurements, the spectral resolution $\Delta\lambda$ was set to 1 nm with an integration time of 0.1 s. The spectral bandwidth was 5 nm. To reduce the contribution of the substrate, the initially obtained absorption spectrum of the pristine nonfunctionalized substrate was subtracted. The photoisomerization kinetics were measured by monitoring the absorption of the sample at a fixed wavelength of 355 nm with a time resolution of 1 s. While probing the molecules, UV

and blue lights were alternately turned on and off, which was accompanied by instantaneous jumps of the signal, caused by stray light. These jumps were removed in the presented data.

Calculations. All semiempirical geometry optimizations were conducted with the code GFN-xTB (version 1, as published in JCTC 2017),³³ designed for accurate geometries, frequencies, and noncovalent interactions. Simulated annealing was performed as implemented in the code with three annealing blocks with electronic temperatures of 149, 650, and 1000 K, respectively, and a run time of 50 ps each, also making use of the SHAKE algorithm³⁴ for all bonds. Single-point energy calculations were performed with ORCA 4.0.1.³⁵ For the single-point energies, the ω B97X-D3³⁶ density functional approximation (DFA) was used in conjunction with a large def2-TZVPP orbital basis set,³⁷ as this DFA performed well in Grimme's latest study on noncovalent interactions.³⁸ To speed up the calculations, density fitting together with the chain of spheres approximations as implemented in ORCA (RJCOSX)³⁹ was used, with a fine grid (gridX6 in ORCA nomenclature) and the all-purpose def2 fitting basis set (def2/J in ORCA terminology).⁴⁰

Density functional theory (DFT) geometry optimizations without the underlying Au(111) surface were conducted with the standard level of theory B3LYP⁴¹ and a 6-31G* basis set⁴² with Gaussian09 revision D01.⁴³ For single-point energies, the Minnesota density functional M06-2X⁴⁴ with dispersion correction (D3)⁴⁵ was used with a large triple ζ basis def2-TZVPP.³⁷ These calculations were carried out with Turbomole7.2⁴⁶ and the usage of resolution-of-identity (RI) with multipole accelerated RI-J (marij) to speed up the calculations. For the DFT calculations on a single layer of Au(111), Turbomole7.2 was used with the same adjustments as above but with the time-saving generalized gradient approximation Perdew–Burke–Ernzerhof (PBE),^{47–50} dispersion correction (D3), and a small def2-SVP basis set.³⁷ Afterward, single-point calculations [M06-2X(D3)/def2-TZVPP] were carried out by removing the gold slab to obtain comparable energies of the isomers.

RESULTS

STM. A high coverage and low defect density are preferable to determine the overall adsorption geometry of **1** on the Au(111) surface as well as the adsorption sites. To identify the preparation condition that yields the SAM most suitable to achieve this goal, several samples prepared via three different methods were studied by STM. Characteristic examples of the appearance of these samples are presented in Figure 3.

In all STM images, discrete maxima of uniform size are observed. As we will demonstrate below, these can be attributed to individual molecules of **1**. In addition, larger features are observed, which can be assigned to small Au monolayer islands, caused by the lifting of the Au(111) surface reconstruction during adlayer formation.¹⁴

Preparation by immersion for 48 h at 20 °C (method I, Figure 3a) results in a largely disordered monolayer, in which only small patches exhibit hexagonal order. It can be assumed that in this case compound **1** adsorbs in the thermodynamically stable trans configuration on the surface. On samples prepared with additional permanent irradiation during the immersion with 365 nm (method II, Figure 3b), we find larger hexagonally ordered patches with some disordered areas at the edges of those patches. Uncovered areas between the ordered domains can also be observed. Although one expects the

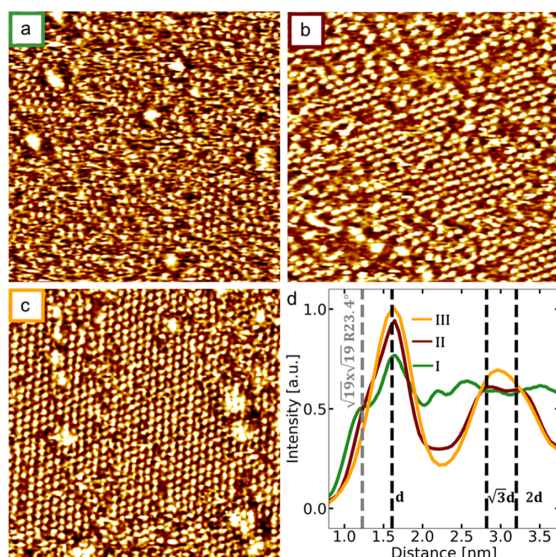


Figure 3. STM images of **1** adlayers on Au(111), prepared by (a) method I, (b) method II, and (c) method III ($50 \times 50 \text{ nm}^2$, $U_{\text{bias}} = 0.3 \text{ V}$, $I_t = 30 \text{ pA}$). (d) Corresponding radial distribution functions. The dashed vertical lines highlight the first three intermolecular distances for $(\sqrt{31} \times \sqrt{31}) \text{ R}8.9^\circ$ superstructure and the nearest-neighbor distance for the unfunctionalized platforms [$(\sqrt{19} \times \sqrt{19}) \text{ R}23.4^\circ$ superstructure].

majority of the adsorbed molecules **1** to be in the *cis* state under these preparation conditions, the better ordering is most probably caused by a slight heating of the sample rather than due to photoisomerization of the molecules. Nonirradiated samples that were heated to 25 °C during the preparation and immersed for 72 h (method III, Figure 3c) exhibited even better order with large hexagonally ordered domains and only a few disordered areas, mainly at areas between different rotational domains. Preparation at even higher temperatures resulted in adlayers of low coverages without ordered structures and thus was not studied in more detail.

The increasing order in the adlayer is corroborated by a quantitative analysis of the hexagonally ordered domains in larger sets of STM images. Here, the average number of molecules per domain increases from 28 to 45 for adlayers prepared by methods I and II, whereas for method III, even 280 molecules per domain were found. The same trend manifests in the intermolecular distances, which were determined from the radial distribution function of the molecule positions, calculated from the STM data (Figure 3d). All studied samples show a pronounced peak at about 1.6 nm, which corresponds to the nearest-neighbor distance of the molecules in the hexagonally ordered domains. From the well-ordered samples prepared by method III, an intermolecular distance of $d = 1.62 \pm 0.04 \text{ nm}$ is determined. This distance as well as the experimentally measured angle between rotational domains of $17 \pm 3^\circ$ is in good agreement with a $(\sqrt{31} \times \sqrt{31}) \text{ R}8.9^\circ$ superstructure on the Au(111) substrate. For samples of type II and III, also the corresponding distances to next-nearest neighbors and beyond (at $\sqrt{3}d$, $2d$) manifest as clear peaks in the pair correlation function, further supporting this structure. However, interesting deviations are found in the

more disordered areas, specifically in the samples prepared by method I. For these, the radial distribution function shows an additional edge, located at about 1.25 nm, i.e., below the 1.6 nm intermolecular spacing of the ordered domains. An intermolecular distance of 1.25 nm was also found for adlayers of bare and functionalized octyl-TATA.^{14,51} We assign this spacing to shorter distances between molecules of **1** in the disordered regions, where a greater variability in the local environment exists and the distance between the molecules thus may vary. In type II samples, only a very weak shoulder in the correlation function is visible at 1.25 nm; in type III samples, this distance is not observable at all.

The surface coverage of **1** increases with the degree of order. Specifically, type I samples have a coverage θ of $0.26 \pm 0.03 \text{ nm}^{-2}$, type II samples $0.33 \pm 0.03 \text{ nm}^{-2}$, and type III samples $0.36 \pm 0.02 \text{ nm}^{-2}$. The latter is $\approx 80\%$ of the ideal coverage of a $(\sqrt{31} \times \sqrt{31}) \text{ R}8.9^\circ$ superstructure of $0.45 \pm 0.02 \text{ nm}^{-2}$ but in good agreement with the experimental coverages obtained by XPS (see below). Because type III adlayers had unsurpassed high coverage and low defect density, this method was employed for the preparation of the adlayers in all spectroscopic studies. The decrease in coverage with reduced long-range order reflects the lower surface density in the disordered areas. Nevertheless, as just discussed, the lowest intermolecular distances of 1.25 nm are found only in those locations. That seemingly paradoxical situation originates in the specific molecular geometry and will be discussed in more detail below. For all preparation methods, the observed adlayer structures strongly differ from that of bare octyl-TATA or octyl-TATA platforms with vertical functions, which all form well-ordered $(\sqrt{19} \times \sqrt{19}) \text{ R}23.4^\circ$ adlayers.^{12,14,51,52} This indicates that the molecule, especially the azobenzene bridge between the two TATA platforms, remains intact upon adsorption.

High-resolution STM images, obtained at higher bias voltages (500–700 mV), reveal the intramolecular structure of the molecules. Figure 4a, recorded in the center of an

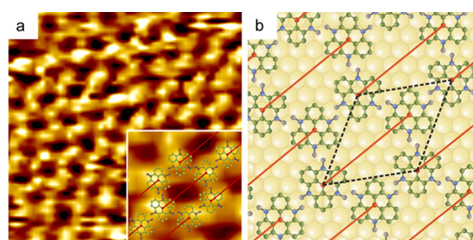


Figure 4. (a) High-resolution STM image of a **1** adlayer, revealing the intramolecular structure ($15 \times 15 \text{ nm}^2$, $U_{\text{bias}} = 0.7 \text{ V}$, $I_t = 50 \text{ pA}$). (b) Model of the in-plane arrangement of the TATA platforms of **1** in the adlayer on the Au(111) surface. For clarity, only the first C atom of the octyl side chains is shown (in gray). The suggested positions of the vertical phenyl–azobenzene–phenyl units are indicated by red lines. The inset in (a) shows the proposed structure overlaid on a $2.2 \times 2.2 \text{ nm}^2$ area of the STM image.

extended $(\sqrt{31} \times \sqrt{31}) \text{ R}8.9^\circ$ domain, shows two peaks in each $(\sqrt{31} \times \sqrt{31}) \text{ R}8.9^\circ$ unit cell, arranged in a honeycomb structure. We assign each of those peaks to one of the two TATA units of **1**, corresponding to one molecule **1** per unit cell. The attached azobenzene unit is not directly visible in these STM images due to the electronic decoupling. The

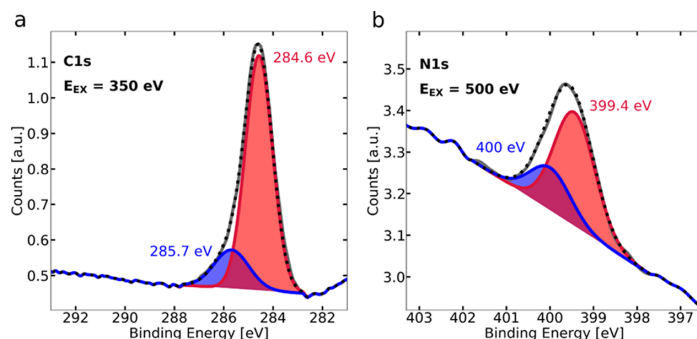


Figure 5. XP spectra of the **1** monolayer on Au(111), showing the (a) C 1s and (b) N 1s lines.

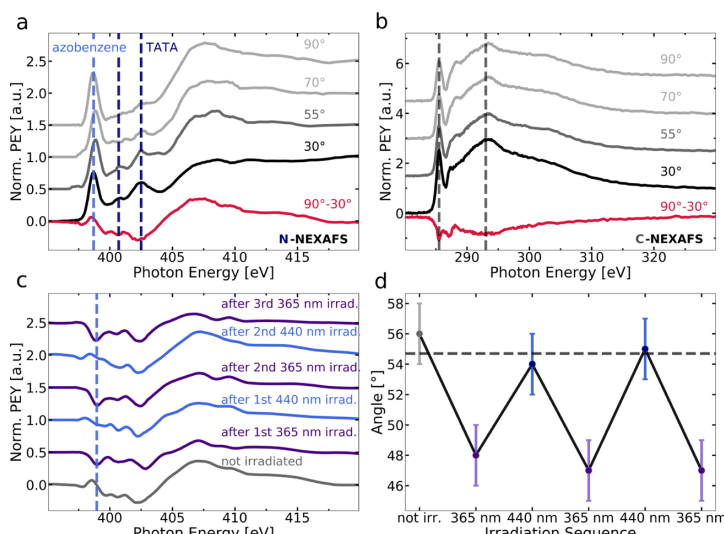


Figure 6. NEXAFS of the **1** adlayer on Au(111). (a) N and (b) C K edge at different angles. The red lines show the differences of the spectra recorded at 90 and 30°. (c) Changes of the N K edge difference spectra during an experiment, where the sample was alternately irradiated by UV (365 nm) and blue (440 nm) light, resulting in transitions between the trans and cis state of the azobenzene unit. (d) Calculated effective angle between the transition dipole moment of the N 1s core level excitation to the azobenzene's lowest unoccupied molecular orbital (LUMO) and the surface normal for the sequence of spectra shown in (c). The dashed line indicates the magic angle for an isotropically oriented dipole moment.

surface density of the adsorbing octyl-TATA platforms in this arrangement is 23% higher than in the well-ordered ($\sqrt{19} \times \sqrt{19}$) $R23.4^\circ$ adlayers of bare octyl-TATA.

Only in the more disordered areas, where the local coverage of **1** is lower, the characteristic $\sqrt{19}$ distance of 1.25 nm can be apparently achieved (e.g., by a parallel arrangement of both molecules where both TATA units are offset by the same 1.25 nm distance from the corresponding TATA units of the neighboring molecule, Figure S1). On the basis of these data, we propose an arrangement as indicated in Figure 4b, where the TATA platforms adopt a honeycomb structure with a nearest-neighbor distance of 0.92 nm. We assume that the azobenzene bridge links the two TATA platforms on opposite sides of the honeycomb (Figure 4b, red lines), as their distance of 18.5 Å is close to the natural spacing of these units in the free molecule **1**. Further rationalization for this adsorbate structure will be provided in the Discussion.

For the free molecule in solution, the spacing between the two platforms of each **1** molecule in cis state differs from that

in the trans state. To assess whether the **1** adlayer structure, especially the spacing between the two TATA groups of an adsorbed molecule, was influenced by photoisomerization, the samples were irradiated with 365 nm light. No differences were found, i.e., STM images of irradiated samples exhibit the same inter- and intramolecular distances as nonirradiated samples. Since the two states cannot be distinguished by STM, NEXAFS and UV-vis spectroscopy measurements were conducted to establish whether the molecules can switch reversibly between the trans and the cis state. Prior to the NEXAFS and UV-vis studies, XPS experiments were carried out to validate the surface coverage and confirm that the adsorbed molecules are intact.

XPS. High-resolution XP spectra of the C 1s (Figure 5a) and N 1s regions (Figure 5b) were used to probe the adlayer composition. In the N 1s spectra, two species can be recognized under the main line. The one with the lower binding energy at 399.4 eV (red line) can be assigned to nitrogen atoms directly connected to carbon atoms represent-

ing the nitrogens of the TATA platform,^{16,53} whereas the other signal with higher binding energy at 400.0 eV (blue line) refers to nitrogen atoms directly bonded to another nitrogen atom. According to the literature, this signal corresponds to the nitrogen atoms of the azo moiety.^{54,55} This clearly indicates that the azo group is still intact after the adsorption process. The ratio of the relative intensities (2.7:1) almost conforms to the expected value (3:1), which was calculated based on the molecular structure. The small deviation is within the error bars of the fit. The slightly lower value may result from attenuation of the signal of TATA nitrogens by atoms located above the TATA platforms.

The high-resolution C 1s spectrum contains two signals. The most prominent signal at 284.6 eV (red line) corresponds to the aliphatic and aromatic carbon atoms with only carbon–carbon bonds and the signal at 285.7 eV (blue line) is due to the carbon atoms, which have bonds to nitrogen or oxygen atoms. Actually, two different species (C–O) and (C–N) for the second signal would be anticipated, but the resolution of the spectrum is insufficient to separate them. However, within the error bars of the quantitative analysis, the ratio of the relative intensities (4.8:1) fits approximately to the values expected on the basis of the molecular composition (5:1).

To confirm the adlayer coverage inferred from the STM measurements, quantitative XPS measurements were employed. For this, a well-known azo-TATA compound, (*E*)-12c-[4-(4-methoxyphenyldiaz恒)-phenyl]ethynyl-4,8,12-tri-*n*-octyl-4,8,12-triazatriangulene, **2** was used as a reference.⁵³ Self-assembled monolayers of **2** form a highly ordered ($\sqrt{19} \times \sqrt{19}$) R23.4° superstructure on Au(111) surfaces with an ideal coverage of 0.73 molecules per nm⁻², corresponding to 3.6 N atoms per nm⁻² and 42.4 C atoms per nm⁻². Because the defect densities of optimally prepared **1** and **2** monolayers are similar according to the STM studies, comparison with this reference should provide the local coverage of **1** in the ideal ordered adlayer structure. For both compounds, **2** and **1**, N 1s and C 1s spectra were recorded on the same Au(111) single crystal and subsequently fitted. From the intensity ratio of the N 1s peaks for **1** and **2** (see Tables S2 and S3), a surface coverage of 0.45 molecules per nm⁻² was obtained, which is in good agreement with the ideal coverage of a ($\sqrt{31} \times \sqrt{31}$) R8.9° superstructure with one molecule **1** per unit cell. The surface coverage obtained from the C 1s peaks is ≈30% lower (0.32 molecules per nm⁻²). However, this quantity is expected to be more inaccurate than that obtained from the N 1s spectra since the transfer of the samples into the vacuum could lead to an uptake of carbon-containing impurities.

NEXAFS. NEXAFS spectra (Figure 6) were recorded at the carbon and nitrogen K edges for **1** monolayers on Au(111) single crystals. The C K edge of **1** (Figure 6b) shows one intensive π^* resonance at 285.5 eV. Above the edge, several broad σ^* resonances can be observed, the most pronounced one located at 293 eV. Measurements with different angles of incidence indicate an angular dependency of the π^* resonance, where the intensity slightly decreases at an angle of 90°. These results are in accordance with previous studies of TATA compounds.¹⁶ The spectra of the N K edge of nonirradiated **1** monolayers on Au(111) (Figure 6a) exhibit three π^* resonances. The smaller resonances at 400.7 and 402.5 eV originate from the TATA platform nitrogen atoms and show the same polarization as observed for the pure platform

molecule.¹⁶ With higher angles of incidence, the intensity of these π^* resonances decreases, which also is well known for adsorbed TATA platforms.

The energy position (398.7 eV) of the first π^* resonance corresponds well to the characteristic π^* resonance reported in the literature for azobenzene units¹⁶ and thus is assigned to the N 1s $\rightarrow \pi^*$ transition of the azo moiety, i.e., the excitation from the N 1s core level to the LUMO. Its intensity depends on the direction of the electric field vector of the incident polarized light relative to the direction of the transition dipole moment of this excitation, which varies with the angle of incidence of the polarized X-ray beam. It is thus expected that the intensity of this azo-resonance depends on this angle if the molecule and the transition dipole moment of the considered resonance show a preferred orientation to the surface. However, in contrast to adlayers with vertically oriented azobenzene groups, a significant change of the azo-resonance at 398.7 eV with incident angle is missing for the studied range of 30–90° (Figure 6a).

Quantitative calculation of the angle of the transition dipole moment of this resonance (excitation from the N 1s core level to the LUMO of the azobenzene) relative to the surface normal yields a nominal value of 56° (eq 1 and Figure S4). Within the experimental error, this is identical to the so-called “magic angle” (54.7°), which would be obtained for an isotropic orientation of the dipole moment. Taking into account that the azobenzene unit is mounted at the same height above the surface at the two phenyl-TATA moieties and its axis thus is oriented parallel to the surface, this result indicates that the azobenzene unit is freely rotatable around the C_{azob.}–O bonds.

To study the photoisomerization of adsorbed **1**, the sample was irradiated with UV light of 365 nm, which results in clear changes in the polarization of the first π^* resonance at 398.7 eV (Figure 6c). Specifically, the intensity of this azo-resonance decreases at an angle of 90° in comparison to that at 30°. This corresponds to a decrease in the calculated dipole moments angle to 47°, indicating a change in orientation of the azobenzene groups of the molecule **1**. This change in geometry can be assigned to a trans–cis isomerization of the azobenzene and is fully reversible: if the sample is subsequently irradiated with light of 440 nm, the polarization of the π^* resonance at 398.7 eV switches back, indicating that the orientation of the transition dipole moment is reverted to the original state. The high reversibility of this process is proven by repetitive irradiation experiments, where the angle of the dipole moment to the surface alternated reproducible between approximately 55 and 47° during photoinduced changes between the cis and trans state (Figure 6d). Besides the change in intensity, a shift of the respective azo- π^* resonance from 398.7 to 398.9 eV could be observed after irradiation with light of 365 nm. As shown by Moldt et al.,⁵⁶ this small peak shift can be attributed to a binding energy change of the N 1s core level upon the cis–trans isomerization of the azobenzene. After irradiation with light of 440 nm, the peak shifts back to 398.7 eV, confirming again the high reversibility of photoisomerization of **1** in the adlayer.

UV/Vis. Further confirmation and kinetic data on the photoswitching were obtained by UV/vis spectroscopy. Spectra of **1** in cyclopentane solution (Figure 7a, dashed lines) are shown for the photostationary state (PSS) after 365 and 455 nm irradiation, corresponding to a state containing predominantly cis- and trans-azobenzene, respectively. In good

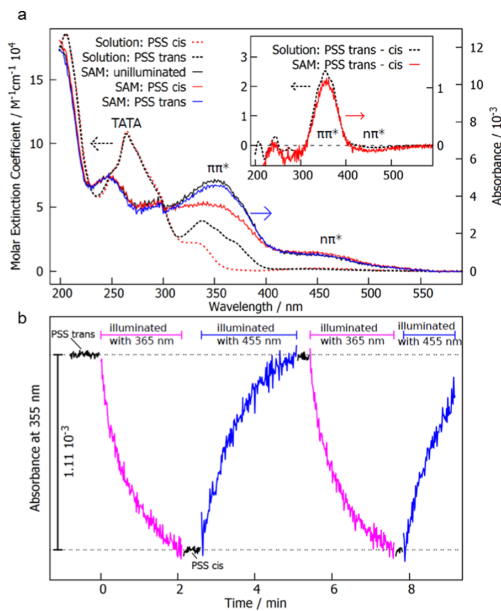


Figure 7. (a) UV-vis spectra of **1** in cyclopentane solution (dashed lines, axis on the left side) and as an adlayer on Au films (solid lines, axis on the right side), recorded directly after preparation and in the cis and trans state, prepared by irradiation with UV (365 nm, $2.69 \pm 0.07 \text{ mW cm}^{-2}$ for solution, $0.41 \pm 0.02 \text{ mW cm}^{-2}$ for SAM) and blue light (455 nm, $2.63 \pm 0.15 \text{ mW cm}^{-2}$ for solution, $0.38 \pm 0.05 \text{ mW cm}^{-2}$ for SAM), respectively. Background signals of the solvent or substrate are subtracted. The inset shows the trans–cis difference spectra in solution (dashed line) and in the adlayer (solid line). (b) Time-dependent changes of the absorbance signal at 355 nm of the **1** adlayer during irradiation with UV and blue light, showing fast and highly reversible photoswitching.

agreement with previous data of azobenzene-functionalized TATA derivatives,³² the $\pi-\pi^*$ (~ 300 – 400 nm) and the $n-\pi^*$ (~ 400 – 500 nm) bands are observed. Photoisomerization to the cis state results in a significant reduction of the $\pi-\pi^*$ and a slight increase of the $n-\pi^*$ band. Additionally, a band centered at 264 nm is observed, which belongs to the TATA moiety (in the following called TATA band) but is blue-shifted by 21 nm with respect to that of TATA platforms with vertically oriented azobenzene groups.³²

In UV-vis spectra of **1** adlayers on Au (Figure 7a, solid lines), the $\pi-\pi^*$ transition can be clearly resolved. The spectra change in a similar way upon irradiation with UV and blue light as those obtained in solution, confirming the photo-switching of the adsorbed molecules. Even the change in the $n-\pi^*$ band can be observed. Compared to solution, the $n-\pi^*$ band is more pronounced relative to the $\pi-\pi^*$ band, whereas the TATA band is significantly less pronounced. In addition, the TATA band is even more blue-shifted (from 264 to 246 nm) than in solution. For a better comparison of the photo-switching of **1** in solution and in the monolayer, the difference between the UV-vis spectra in the trans and cis state is shown for both cases in the inset of Figure 7a. In contrast to TATAs with vertically mounted azobenzene groups,³² the $\pi-\pi^*$ band maxima in the difference spectra of the **1** adlayer and **1** in solution are not shifted with respect to each other.

Furthermore, the larger relative change of the $n-\pi^*$ band in the **1** adlayer as compared to **1** in solution becomes apparent.

From the spectral data, the surface coverage of **1** on the Au surface can be estimated by comparison of the absorbance of the **1** adlayer with the extinction coefficient ϵ of **1** in solution.³² For this, the areas under a band in the difference spectra of solution and adlayer were determined. Here, we assume that the extinction change $\Delta\epsilon$ of the SAM is similar to that in solution. This seems justified in view of the identical spectral position of the $\pi-\pi^*$ band and the very similar photo-isomerization cross sections (see below) of **1** in the SAM and in solution, which indicate an effective decoupling of the azobenzene switch from the surface. For the calculation of the surface concentration of **1** from these data, it must be taken into account that the molecules are isotropically distributed in solution, whereas the adsorbed molecules and thus their transition dipole moments have a defined orientation. Due to the structure of the molecules, a planar orientation of the platforms and azobenzene units and thus of the $\pi-\pi^*$ dipole moment is expected, resulting in appropriate correction factors (for the employed spectrometer geometry, 3/2 for the solution and 1 for the adlayer). From the measured signals, a coverage θ of $0.37 \pm 0.04 \text{ nm}^{-2}$ is obtained, which is in excellent agreement with the STM and XPS results.

The photoisomerization kinetics of adsorbed **1** on gold was studied by monitoring the absorption as a function of time during alternating irradiation by UV (365 nm) and blue light (455 nm). The experiments were performed at a fixed wavelength $\lambda = 355$ nm, where the change of the $\pi-\pi^*$ band is the largest. Highly reversible and reproducible absorption changes were observed (Figure 7b). Fits of these data by single-exponential decay functions (not shown) perfectly describe the experimental curves, revealing that the trans–cis photoisomerization in the adlayer can be described by well-defined first-order transitions. The corresponding effective photoisomerization cross sections are $\sigma_{\text{eff,trans-cis}} = (28 \pm 7) \times 10^{-18} \text{ cm}^2$ for the trans–cis and $\sigma_{\text{eff,cis-trans}} = (20 \pm 3) \times 10^{-18} \text{ cm}^2$ for the cis–trans transition. These values are very similar to those for azobenzene-TATA compounds in solution and adlayers of TATA-based molecules with vertically attached azobenzenes,³² indicating effective electronic decoupling of the azobenzene unit from the Au substrate.

In the same way, the thermal relaxation of **1** adlayers from the cis to the trans state was measured. Because of the slow kinetics of this process and temporal drift in the small signal from the monolayer, only a rough estimation of the characteristic relaxation time of ≤ 150 min at room temperature could be obtained. Nevertheless, these experiments demonstrate that the adsorbed molecules **1** have a similar stability against thermal backisomerization as the molecules in solution.

Quantum Chemical Calculations. To assist the determination of the complex three-dimensional (3D) adlayer structure, quantum chemical calculations were performed, using a two-pronged approach. First, semiempirical calculations were used to obtain the energetically most favorable geometric conformation of the entire **1** molecule, including the six octyl side chains, by simulated annealing. Then, the side chains were neglected and the geometry of the simplified molecule was calculated by density functional theory, using standard local geometry optimization techniques. This allows the advantages of both approaches to be combined, i.e., the capability of exhaustive conformer searches by semiempirics

and the increased accuracy of DFT. In the following, we will present and compare the results of both approaches.

In the semiempirical approach, a geometry optimization for molecule **1** on a single layer of Au(111) was carried out, with the distance of the two central carbon atoms of the TATA platforms being fixed to the 18.5 Å, obtained from the STM measurements. Although geometry optimization of the free unrestrained molecule **1** in the trans configuration with DFT (B3LYP/6-31G*) finds 19.8 Å for this distance (Figure S6), the state with 18.5 Å is only 0.5 kcal mol⁻¹ higher in energy [at the M06-2X(D3)/def2-TZVPP level], indicating that the molecules can easily accommodate the strain induced by the geometric constraints, resulting from the in-plane arrangement of the TATA platforms. In the next step, the gold surface was removed, the internal coordinates of the TATA platforms fixed, and the most stable thermally accessible conformer determined by simulated annealing (Figure S5). With the thus-obtained structures, single-point energies were calculated by DFT (ω B97X-D3/def2-TZVPP) to obtain more accurate relative conformer energies. From these single-point energies, the most stable conformer was determined, redeposited on an Au(111) surface and reoptimized to account for molecule–surface interactions. The geometries obtained in this manner were used to judge whether the trans configuration can freely rotate. In both trans and cis states, the molecule is strained, manifesting in a slight bending of the phenyl pillars (on an average 12 and 10° relative to the surface normal for the cis and trans isomer, respectively). This strain results from the imperfect match of the length of the azobenzene bridge with the spacing of the corresponding TATA platforms in the tightly packed honeycomb lattice and is more pronounced for the bent cis than for the straight trans configuration.

The geometry optimizations conducted with DFT employed a simplified version of **1**, where the octyl side chains were substituted by protons. This approach is based on the assumption that the flexible alkyl side chains interact only weakly with the azobenzene bridge. In addition, the gold surface was initially omitted and the positions of the TATA platforms were geometrically constrained by keeping the outer carbon atoms of the platforms in a virtual plane simulating the surface and fixing the distance of the central TATA carbon atoms to 18.5 Å. Within this approach, three trans isomer conformations were obtained, which differ significantly in geometry, especially also in the altitudinal orientation of the azobenzene, but are isoenergetic within the precision of the calculations (Figure S6, top). The four most stable conformers of the cis isomer (Figure S6, bottom) vary more in energy due to larger structural variations of the azo group geometry. For a final optimization of selected conformations, the virtual surface was replaced by a single Au(111) layer with fixed positions of the gold atoms. The resulting trans isomer (Figure 8a) stays nearly the same. This indicates a negligible influence of the metal substrate, as may be expected for the rather large and uniform azobenzene–metal spacing (\approx 9 Å relative to the topmost Au layer). For the cis isomer, two configurations were considered, with the azo group pointing either toward or away from the surface (Figure 8b,c). The latter is lower in energy and additionally supported by the facile photoswitching of the molecule, observed in the NEXAFS and UV/vis measurements. In the former conformation, the azo group is physisorbed on the Au surface, which should quench the isomerization process.⁵⁷ Isomerization could still be possible for this configuration via indirect transient excitation.^{58,59}

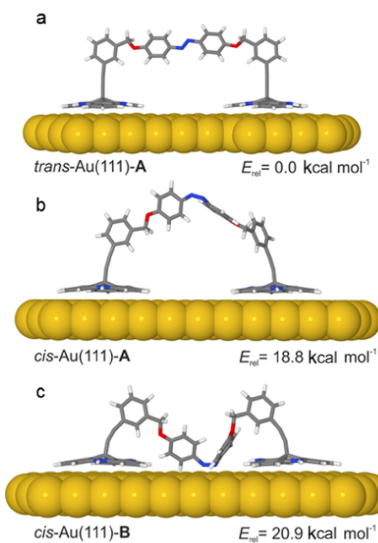


Figure 8. Optimized [PBE(D3)/def2-SVP] structures of the (a) trans and (b, c) cis isomer of **1** on the Au surface. Relative energies were calculated by DFT single-point energy calculations [M06-2X(D3)/def2-TZVPP] with a removed Au layer.

However, a configuration where the *cis*-azo group is pointing away from the surface is more likely because the intramolecular excitation process still occurs according to the UV/vis data. Overall, the resulting structures obtained by the semiempirical and by the DFT calculations are very similar.

These results support a free rotation of the azobenzene in the trans configuration. In the cis isomer, the strongly bent conformation probably restricts this rotation geometrically. Unfortunately, this cannot easily be proven by the current calculations, due to the many degrees of freedom of molecule **1**. Especially, the presence of the six octyl side chains, including the side chains of neighboring molecules in the densely packed monolayer, is expected to significantly influence the rotation of the bridging azobenzene (see below).

■ DISCUSSION

The results obtained by the various microscopic, spectroscopic, and computational methods provide a comprehensive characterization of **1** monolayers on Au(111). On the basis of these studies, a detailed microscopic picture emerges, which demonstrates the successful design of a system with combined vertical switching and altitudinal rotation as well as defined long-range order. In the following, we discuss first the molecular arrangement and then rotation and switching in the adlayer.

The observed lateral arrangement in the adlayer is in good agreement with expectations based on the molecular geometry. Like all other TATA-based compounds, the TATA moieties of the molecules **1** adsorb planar on Au(111) substrates, with the vertical attached units pointing away from the surface. Under optimized preparation conditions, the molecules arrange in a densely packed, hexagonal ($\sqrt{3}1 \times \sqrt{3}1$) R8.9° superstructure with one molecule **1** in the unit cell. The TATA surface density in this structure is substantially higher than that for bare octyl-TATA platforms under ambient conditions. However, it has been shown that the packing density in TATA adlayers is

variable and depends on the space requirements of the alkyl side chains.⁵¹ In particular, for octyl-TATA adlayers in electrochemical environment, an even $\approx 30\%$ denser ($2\sqrt{3} \times 2\sqrt{3}$) structure was found at negative potentials, where the octyl chains were extended away from the surface.⁶⁰ That the arrangement proposed in Figure 4b is sterically feasible was also confirmed by quantum chemical calculations.

The honeycomb lattice of TATA units in the ($\sqrt{31} \times \sqrt{31}$) 88.9° adlayer has never been observed for adlayers of pure TATA or molecules, consisting of a single TATA platform with a vertically attached group. We rationalize this by a lateral structure, in which the adsorbed 1 molecules are parallel but staggered with respect to each other. This type of arrangement has also been found for planar dumbbell-shaped molecules.⁶¹ Taking into account the high flexibility and the many degrees of freedom of 1, the formation of adlayers with large well-ordered domains is unusual. In many cases, a much more disordered arrangement was found for similarly complex, anisotropic 3D molecules.¹⁷ We attribute the good in-plane order to the pronounced self-assembly and high room-temperature mobility of the TATA platforms on Au(111). Apparently, these enable ordering even in this system, where two platforms are interconnected by a molecular bridge. However, the defect density in the 1 adlayer is much more sensitive to the self-assembly conditions and even in the optimal case much larger than for molecules with a single TATA platform.

As demonstrated by the DFT and quantum chemical calculations, a ($\sqrt{31} \times \sqrt{31}$) 88.9° honeycomb structure, in which the azobenzene is parallel to the surface and spans across the remaining empty surface site (Figure 4b), is in good agreement with the natural dimensions of the trans isomer of 1. It implies a geometry where the *trans*-azobenzene is oriented parallel to the Au(111) surface and well separated from it. However, the space between the azobenzene unit and the metal is not empty but largely filled by the alkyl side chains of the TATA platforms. These most likely physisorb on the Au surface due to dispersive interactions and may lead to additional lateral binding between neighboring 1 adsorbates. Considering that six octyl chains are present in each ($\sqrt{31} \times \sqrt{31}$) 88.9° unit cell and assuming a similar density as in liquid alkanes, the average height of this physisorbed layer is ≈ 9 Å, i.e., the bridge should already be partially embedded.

Adlayers of 1 exhibit fast and highly reversible photoisomerization between the trans and cis state. This is in marked contrast to pure azobenzene and tetra-*tert*-butyl-azobenzene, which also feature a planar adsorption geometry on Au(111) surfaces^{21,22,29} but strongly hindered photoisomerization in the adsorbed state.^{26–28,57,62} The facile photoswitching in our system can be attributed to the larger spatial and electronic decoupling of the azobenzene unit from the metal substrate. The latter is also supported by the UV/vis spectra of adsorbed 1, which are even less affected than those of azobenzene mounted vertically on TATA platforms³² and indistinguishable from those of 1 in solution. Altogether, our data demonstrate that our platform-based method is a highly successful approach to mount vertically oriented photoswitches on metal surfaces.

In the ($\sqrt{31} \times \sqrt{31}$) 88.9° adlayer, the trans–cis isomerization does not induce changes in the positions of the TATA units of molecules on the surface. This is understandable in view of the tight TATA packing and the high flexibility of the vertical functional unit. Even if the molecules are adsorbed in

the cis state (i.e., prepared by method II), the same structure is formed. Probably, the arrangement of the TATA units into the honeycomb arrangement is preferred over an in-plane geometry with a shorter distance between the two TATA units of the molecule, which would only be sterically possible by breaking the hexagonal symmetry of the adlayer structure. Nevertheless, photoinduced changes between the two TATA units may in principle be possible for isolated molecules at low coverage since the surface mobility of TATA on a clean Au(111) surface is high. However, such experiments would require STM measurements on 1 at cryogenic temperatures, which is outside the scope of this study.

According to the NEXAFS results, azobenzene is isotropically oriented in the trans isomer of 1, suggesting that it is rotatable around its main axis. This is supported by the calculations and expected in view of the flexible mounting on the phenyl pillars. In contrast, the cis isomer clearly shows a preferred orientation. The corresponding configurations are strongly bent and, contrary to the trans isomer, the azo group thus is located far away from the rotation axis. Rotation of the *cis*-azobenzene should therefore be strongly impeded by the octyl side chain. For a similar reason, an orientation where the azo group is orientated toward the Au surface (as in Figure 8c) seems unlikely. The latter should also strongly quench the photoisomerization, which is at variance with the spectroscopic studies. Finally, the NEXAFS data also provide clear evidence that photoisomerization leads to highly reversible changes in the angular distribution. This is only possible if the orientation of the trans isomer is redistributed after backisomerization, corroborating that the *trans*-azobenzene bridge not only is rotatable, as suggested by DFT and quantum chemical calculations, but indeed rotates at room temperature.

CONCLUSIONS

With this study, we demonstrated the successful assembly of a combined lateral photoswitch and altitudinal rotor on a metal surface. By extending our platform concept to molecules containing several platform units, we could mount the functional azobenzene groups parallel to the Au(111) substrate at a distance defined by the height of the molecular phenyl pillars attached to the TATA platforms. This approach leads to electronic decoupling of the azobenzene from the surface, enabling facile photoswitching. Because the azobenzene is rotatable in the trans but not in the cis state, we can fully reversibly switch the altitudinal rotation on and off by irradiation with UV and blue light, respectively. This capability may be of interest for the realization of higher molecular functions. For example, one may attach additional functions to the rotor unit, which would be either permanently oriented in a defined direction (e.g., toward or away from the surface) or have an isotropic orientation, dependent on the switching state. This would allow switching the chemical availability of these functions to species in the environment above the metal surface. Furthermore, the well-ordered adlayer structure allows mounting the molecules in arrays with parallel arranged functional units. This may enable higher functions that employ cooperative effects. Using intrinsically anisotropic substrates, e.g., Au(110) surface, even macroscopic directionality may seem feasible.

■ ASSOCIATED CONTENT

§ Supporting Information

The Supporting Information is available free of charge on the ACS Publications website at DOI: [10.1021/acs.jpcc.9b02469](https://doi.org/10.1021/acs.jpcc.9b02469).

Model of adsorbed molecules on Au(111); results from quantitative XPS measurements; fitting parameters for XPS data; XP spectra showing the survey; N 1s NEXAFS spectra of the LUMO resonance of the azo moiety; N-NEXAFS spectra; and models of calculated local energy minima ([PDF](#))

■ AUTHOR INFORMATION

Corresponding Authors

*E-mail: rherges@oc.uni-kiel.de (R.H.).

*E-mail: ftuczek@ac.uni-kiel.de (F.T.).

*E-mail: magnussen@physik.uni-kiel.de (O.M.M.).

ORCID

Talina R. Rusch: [0000-0001-8123-6792](#)

Thomas Strunkus: [0000-0003-3931-5635](#)

Rainer Herges: [0000-0002-6396-6991](#)

Felix Tuczak: [0000-0001-7290-9553](#)

Olaf M. Magnussen: [0000-0003-4900-0880](#)

Notes

The authors declare no competing financial interest.

■ ACKNOWLEDGMENTS

We gratefully acknowledge financial support by the Deutsche Forschungsgemeinschaft (DFG) via the collaborative research centre SFB677, project B09. Furthermore, we would like to thank the HZB for provision of beamtime at the BESSY II/HE-SGM and Christof Wöll for the provision of the Prevac endstation. RH is grateful for support by SPP 1928.

■ REFERENCES

- (1) Magnera, T. F.; Michl, J. *Molecular Machines*; Springer-Verlag, 2005; pp 63–97.
- (2) Carroll, G. T.; Pollard, M. M.; van Delden, R.; Feringa, B. L. Controlled Rotary Motion of Light-Driven Molecular Motors Assembled on a Gold Film. *Chem. Sci.* **2010**, *1*, 97.
- (3) Valášek, M.; Mayor, M. Spatial and Lateral Control of Functionality by Rigid Molecular Platforms. *Chem. – Eur. J.* **2017**, *23*, 13538–13548.
- (4) Kopr, L.; Zhao, K.; Shen, Y.; Comotti, A.; Bracco, S.; Shoemaker, R. K.; Sozzani, P.; Clark, N. A.; Price, J. C.; Rogers, C. T.; Michl, J.; et al. Inclusion Compound Based Approach to Arrays of Artificial Dipolar Molecular Rotors. A Surface Inclusion. *J. Am. Chem. Soc.* **2012**, *134*, 10122–10131.
- (5) Ito, M.; Wei, T. X.; Chen, P.-L.; Akiyama, H.; Matsumoto, M.; Tamada, K.; Yamamoto, Y. A Novel Method for Creation of Free Volume in a One-Component Self-Assembled Monolayer. Dramatic Size Effect of Para-Carborane. *J. Mater. Chem.* **2005**, *15*, 478.
- (6) von Wrochem, F.; Scholz, F.; Gao, D.; Nothofer, H.-G.; Yasuda, A.; Wessels, J. M.; Roy, S.; Chen, X.; Michl, J. High-Band-Gap Polycrystalline Monolayers of a 12-Vertex p-Carborane on Au(111). *J. Phys. Chem. Lett.* **2010**, *1*, 3471–3477.
- (7) Yao, Y.; Tour, J. M. Facile Convergent Route to Molecular Caltraps. *J. Org. Chem.* **1999**, *64*, 1968–1971.
- (8) Jian, H.; Tour, J. M. En Route to Surface-Bound Electric Field-Driven Molecular Motors. *J. Org. Chem.* **2003**, *68*, 5091–5103.
- (9) Zhu, S.-E.; Kuang, Y.-M.; Geng, F.; Zhu, J.-Z.; Wang, C.-Z.; Yu, Y.-J.; Luo, Y.; Xiao, Y.; Liu, K.-Q.; Meng, Q.-S.; et al. Self-Decoupled Porphyrin with a Tripodal Anchor for Molecular-Scale Electroluminescence. *J. Am. Chem. Soc.* **2013**, *135*, 15794–15800.
- (10) Valášek, M.; Lindner, M.; Mayor, M. Rigid Multipodal Platforms for Metal Surfaces. *Beilstein J. Nanotechnol.* **2016**, *7*, 374–405.
- (11) Laursen, B. W.; Krebs, F. C. Synthesis, Structure, and Properties of Azatriangulenium Salts. *Chem. – Eur. J.* **2001**, *7*, 1773–1783.
- (12) Baisch, B.; Raffa, D.; Jung, U.; Magnussen, O. M.; Nicolas, C.; Lacour, J.; Kubitschke, J.; Herges, R. Mounting Freestanding Molecular Functions onto Surfaces: The Platform Approach. *J. Am. Chem. Soc.* **2009**, *131*, 442–443.
- (13) Kubitschke, J.; Näther, C.; Herges, R. Synthesis of Functionalized Triazatriangulenes for Application in Photo-Switchable Self-Assembled Monolayers. *Eur. J. Org. Chem.* **2010**, *2010*, 5041–5055.
- (14) Kuhn, S.; Baisch, B.; Jung, U.; Johannsen, T.; Kubitschke, J.; Herges, R.; Magnussen, O. Self-Assembly of Triazatriangulenium-Based Functional Adlayers on Au(111) Surfaces. *Phys. Chem. Chem. Phys.* **2010**, *12*, 4481.
- (15) Otte, F. L.; Lemke, S.; Schütt, C.; Krekiehn, N. R.; Jung, U.; Magnussen, O. M.; Herges, R. Ordered Monolayers of Free-Standing Porphyrins on Gold. *J. Am. Chem. Soc.* **2014**, *136*, 11248–11251.
- (16) Ulrich, S.; Jung, U.; Strunkus, T.; Schütt, C.; Bloedorn, A.; Lemke, S.; Ludwig, E.; Kipp, L.; Faupel, F.; Magnussen, O.; et al. X-Ray Spectroscopy Characterization of Azobenzene-Functionalized Triazatriangulenium Adlayers on Au(111) Surfaces. *Phys. Chem. Chem. Phys.* **2015**, *17*, 17053–17062.
- (17) Zheng, X.; Mulcahy, M. E.; Horinek, D.; Galeotti, F.; Magnera, T. F.; Michl, J. Dipolar and Nonpolar Altitudinal Molecular Rotors Mounted on an Au(111) Surface. *J. Am. Chem. Soc.* **2004**, *126*, 4540–4542.
- (18) London, G.; Carroll, G. T.; Landaluce, T. F.; Pollard, M. M.; Rudolf, P.; Feringa, B. L. Light-Driven Altitudinal Molecular Motors on Surfaces. *Chem. Commun.* **2009**, 1712.
- (19) Carroll, G. T.; London, G.; Landaluce, T. F.; Rudolf, P.; Feringa, B. L. Adhesion of Photon-Driven Molecular Motors to Surfaces via 1,3-Dipolar Cycloadditions: Effect of Interfacial Interactions on Molecular Motion. *ACS Nano* **2011**, *5*, 622–630.
- (20) Murphy, C. J.; Smith, Z. C.; Pronchinski, A.; Lewis, E. A.; Liriano, M. L.; Wong, C.; Ivimey, C. J.; Duffy, M.; Musial, W.; Therrien, A. J.; et al. Ullmann Coupling Mediated Assembly of an Electrically Driven Altitudinal Molecular Rotor. *Phys. Chem. Chem. Phys.* **2015**, *17*, 31931–31937.
- (21) Alemani, M.; Peters, M. V.; Hecht, S.; Rieder, K.-H.; Moresco, F.; Grill, L. Electric Field-Induced Isomerization of Azobenzene by STM. *J. Am. Chem. Soc.* **2006**, *128*, 14446–14447.
- (22) Alemani, M.; Selvanathan, S.; Ample, F.; Peters, M. V.; Rieder, K.-H.; Moresco, F.; Joachim, C.; Hecht, S.; Grill, L. Adsorption and Switching Properties of Azobenzene Derivatives on Different Noble Metal Surfaces: Au(111), Cu(111), and Au(100). *J. Phys. Chem. C* **2008**, *112*, 10509–10514.
- (23) Visser, J.; Katsonis, N.; Vicario, J.; Feringa, B. L. Two-Dimensional Molecular Patterning by Surface-Enhanced Zn-Porphyrin Coordination. *Langmuir* **2009**, *25*, 5980–5985.
- (24) Matino, F.; Schull, G.; Kohler, F.; Gabutti, S.; Mayor, M.; Berndt, R. Electronic Decoupling of a Cyclophane from a Metal Surface. *Proc. Natl. Acad. Sci. U.S.A.* **2011**, *108*, 961–964.
- (25) Bléger, D.; Ciesielski, A.; Samori, P.; Hecht, S. Photoswitching Vertically Oriented Azobenzene Self-Assembled Monolayers at the Solid-Liquid Interface. *Chem. – Eur. J.* **2010**, *16*, 14256–14260.
- (26) Hagen, S.; Leyssner, F.; Nandi, D.; Wolf, M.; Tegeder, P. Reversible Switching of Tetra-tert-butyl-azobenzene on a Au(111) Surface Induced by Light and Thermal Activation. *Chem. Phys. Lett.* **2007**, *444*, 85–90.
- (27) Óvári, L.; Wolf, M.; Tegeder, P. Reversible Changes in the Vibrational Structure of Tetra-tert-butyl-azobenzene on a Au(111) Surface Induced by Light and Thermal Activation. *J. Phys. Chem. C* **2007**, *111*, 15370–15374.
- (28) Tegeder, P.; Hagen, S.; Leyssner, F.; Peters, M.; Hecht, S.; Klamroth, T.; Saalfrank, P.; Wolf, M. Electronic Structure of the

- Molecular Switch Tetra-*tert*-butyl-azobenzene Adsorbed on Ag(111). *Appl. Phys. A* **2007**, *88*, 465–472.
- (29) Tegeder, P. Optically and Thermally Induced Molecular Switching Processes at Metal Surfaces. *J. Phys.: Condens. Matter* **2012**, *24*, No. 394001.
- (30) Scheil, K.; Lorente, N.; Bocquet, M.-L.; Hess, P. C.; Mayor, M.; Berndt, R. Adatom Coadsorption with Three-Dimensional Cyclophanes on Ag(111). *J. Phys. Chem. C* **2017**, *121*, 25303–25308.
- (31) Hammerich, M.; Herges, R. Laterally Mounted Azobenzenes on Platforms. *J. Org. Chem.* **2015**, *80*, 11233–11236.
- (32) Krekienh, N. R.; Müller, M.; Jung, U.; Ulrich, S.; Herges, R.; Magnussen, O. M. UV/Vis Spectroscopy Studies of the Photoisomerization Kinetics in Self-Assembled Azobenzene-Containing Adlayers. *Langmuir* **2015**, *31*, 8362–8370.
- (33) Grimme, S.; Bannwarth, C.; Shushkov, P. A Robust and Accurate Tight-Binding Quantum Chemical Method for Structures, Vibrational Frequencies, and Noncovalent Interactions of Large Molecular Systems Parametrized for All spd-Block Elements ($Z = 1$ –86). *J. Chem. Theory Comput.* **2017**, *13*, 1989–2009.
- (34) Ryckaert, J.-P.; Ciccotti, G.; Berendsen, H. J. Numerical Integration of the Cartesian Equations of Motion of a System with Constraints: Molecular Dynamics of n-Alkanes. *J. Comput. Phys.* **1977**, *23*, 327–341.
- (35) Neese, F. Software Update: The ORCA Program System, Version 4.0. *Wiley Interdiscip. Rev.: Comput. Mol. Sci.* **2017**, *8*, No. e1327.
- (36) Chai, J.-D.; Head-Gordon, M. Long-Range Corrected Hybrid Density Functionals with Damped Atom–Atom Dispersion Corrections. *Phys. Chem. Chem. Phys.* **2008**, *10*, 6615.
- (37) Weigend, F.; Ahlrichs, R. Balanced Basis Sets of Split Valence, Triple Zeta Valence and Quadruple Zeta Valence Quality for H to Rn: Design and Assessment of Accuracy. *Phys. Chem. Chem. Phys.* **2005**, *7*, 3297.
- (38) Goerigk, L.; Hansen, A.; Bauer, C.; Ehrlich, S.; Najibi, A.; Grimme, S. A Look at the Density Functional Theory Zoo with the Advanced GMTKN55 Database for General Main Group Thermochemistry, Kinetics and Noncovalent Interactions. *Phys. Chem. Chem. Phys.* **2017**, *19*, 32184–32215.
- (39) Neese, F.; Wennmohs, F.; Hansen, A.; Becker, U. Efficient, Approximate and Parallel Hartree–Fock and Hybrid DFT Calculations. A ‘Chain-of-Spheres’ Algorithm for the Hartree–Fock Exchange. *Chem. Phys.* **2009**, *356*, 98–109.
- (40) Weigend, F. Accurate Coulomb-Fitting Basis Sets for H to Rn. *Phys. Chem. Chem. Phys.* **2006**, *8*, 1057.
- (41) Becke, A. D. Density-Functional Thermochemistry. III. The Role of Exact Exchange. *J. Chem. Phys.* **1993**, *98*, 5648–5652.
- (42) Ditchfield, R.; Hehre, W. J.; Pople, J. A. Self-Consistent Molecular-Orbital Methods. IX. An Extended Gaussian-Type Basis for Molecular-Orbital Studies of Organic Molecules. *J. Chem. Phys.* **1971**, *54*, 724–728.
- (43) Frisch, M. J.; Trucks, G. W.; Schlegel, H. B.; Scuseria, G. E.; Robb, M. A.; Cheeseman, J. R.; Scalmani, G.; Barone, V.; Petersson, G. A.; Nakatsuji, H. et al. *Gaussian* 16, revision B.01; Gaussian, Inc., 2016.
- (44) Zhao, Y.; Truhlar, D. G. The M06 Suite of Density Functionals for Main Group Thermochemistry, Thermochemical Kinetics, Noncovalent Interactions, Excited States, and Transition Elements: Two New Functionals and Systematic Testing of Four M06-Class Functionals and 12 Other Functionals. *Theor. Chem. Acc.* **2007**, *120*, 215–241.
- (45) Grimme, S.; Antony, J.; Ehrlich, S.; Krieg, H. A Consistent and Accurate Ab Initio Parametrization of Density Functional Dispersion Correction (DFT-D) for the 94 Elements H–Pu. *J. Chem. Phys.* **2010**, *132*, No. 154104.
- (46) TURBOMOLE V7.0 2015, A Development of University of Karlsruhe and Forschungszen-trum Karlsruhe GmbH, 1989–2007; TURBOMOLE GmbH, 2015. Since 2007, available from <http://www.turbomole.com> (accessed May 13, 2019).
- (47) Dirac, P. A. M. Quantum Mechanics of Many-Electron Systems. *Proc. R. Soc. A* **1929**, *123*, 714–733.
- (48) Slater, J. C. A Simplification of the Hartree-Fock Method. *Phys. Rev.* **1951**, *81*, 385–390.
- (49) Perdew, J. P.; Wang, Y. Accurate and Simple Analytic Representation of the Electron-Gas Correlation Energy. *Phys. Rev. B* **1992**, *45*, 13244–13249.
- (50) Perdew, J. P.; Burke, K.; Ernzerhof, M. Generalized Gradient Approximation Made Simple. *Phys. Rev. Lett.* **1996**, *77*, 3865–3868.
- (51) Lemke, S.; Ulrich, S.; Claßen, F.; Bloedorn, A.; Jung, U.; Herges, R.; Magnussen, O. M. Triazatriangulenium Adlayers on Au(111): Superstructure as a Function of Alkyl Side Chain Length. *Surf. Sci.* **2015**, *632*, 71–76.
- (52) Schlimm, A.; Löw, R.; Rusch, T.; Röhricht, F.; Strunkus, T.; Tellkamp, T.; Sönnichsen, F.; Manthe, U.; Magnussen, O.; et al. Long-Distance Rate Acceleration by Bulk Gold. *Angew. Chem., Int. Ed.* **2019**, *58*, 6574–6578.
- (53) Jacob, H.; Ulrich, S.; Jung, U.; Lemke, S.; Rusch, T.; Schütt, C.; Petersen, F.; Strunkus, T.; Magnussen, O.; Herges, R.; et al. Monitoring the Reversible Photoisomerization of an Azobenzene-Functionalized Molecular Triazatriangulene Platform on Au(111) by IRAS. *Phys. Chem. Chem. Phys.* **2014**, *16*, 22643–22650.
- (54) Chandrasekaran, V.; Jacob, H.; Petersen, F.; Kathirvel, K.; Tuczek, F.; Lindhorst, T. K. Synthesis and Surface-Spectroscopic Characterization of Photoisomerizable Glyco-SAMs on Au(111). *Chem. – Eur. J.* **2014**, *20*, 8744–8752.
- (55) Jung, U.; Kuhn, S.; Cornelissen, U.; Tuczek, F.; Strunkus, T.; Zaporozchenko, V.; Kubitschke, J.; Herges, R.; Magnussen, O. Azobenzene-Containing Triazatriangulenium Adlayers on Au(111): Structural and Spectroscopic Characterization. *Langmuir* **2011**, *27*, 5895–5908.
- (56) Moldt, T.; Przyrembel, D.; Schulze, M.; Bronsch, W.; Boie, L.; Brete, D.; Gahl, C.; Klajn, R.; Tegeder, P.; Weinelt, M. Differing Isomerization Kinetics of Azobenzene-Functionalized Self-Assembled Monolayers in Ambient Air and in Vacuum. *Langmuir* **2016**, *32*, 10795–10801.
- (57) Bronner, C.; Schulze, M.; Hagen, S.; Tegeder, P. The Influence of the Electronic Structure of Adsorbate–Substrate Complexes on Photoisomerization Ability. *New J. Phys.* **2012**, *14*, No. 043023.
- (58) Maurer, R. J.; Reuter, K. Bistability Loss as a Key Feature in Azobenzene (Non-)Switching on Metal Surfaces. *Angew. Chem., Int. Ed.* **2012**, *51*, 12009–12011.
- (59) Maurer, R. J.; Reuter, K. Computational Design of Metal-Supported Molecular Switches: Transient Ion Formation during Light- and Electron-Induced Isomerisation of Azobenzene. *J. Phys.: Condens. Matter* **2018**, *31*, No. 044003.
- (60) Lemke, S.; Chang, C.-H.; Jung, U.; Magnussen, O. M. Reversible Potential-Induced Switching of Alkyl Chain Aggregation in Octyl-Triazatriangulenium Adlayers on Au(111). *Langmuir* **2015**, *31*, 3115–3124.
- (61) Marschall, M.; Reichert, J.; Seufert, K.; Auwärter, W.; Klappenberger, F.; Weber-Bargioni, A.; Klyatskaya, S.; Zoppellaro, G.; Nefedov, A.; Strunkus, T.; et al. Supramolecular Organization and Chiral Resolution of p-Terphenyl-m-Dicarbonitrile on the Ag(111) Surface. *ChemPhysChem* **2010**, *11*, 1446–1451.
- (62) Comstock, M. J.; Levy, N.; Kirakosian, A.; Cho, J.; Lauterwasser, F.; Harvey, J. H.; Strubbe, D. A.; Fréchet, J. M. J.; Trauner, D.; Louie, S. G.; et al. Reversible Photomechanical Switching of Individual Engineered Molecules at a Metallic Surface. *Phys. Rev. Lett.* **2007**, *99*, No. 038301.

ACID - Das Multifunktionstool

5

Delokalisierung, Konjugation und Aromatizität sind außerordentlich wichtige Konzepte in der Chemie und werden häufig für die Vorhersage und Interpretation von chemischen sowie physikalischen Eigenschaften verwendet. Von entscheidender Wichtigkeit ist die Quantifizierung und Bestimmung der delokalisierten Elektronen. Hierfür wurden verschiedene Ansätze entwickelt. Eigenschaften wie die Erhöhung der magnetischen Suszeptibilität,^[178] deren Anisotropie^[179] oder die *nucleus-independent shifts* (NICS)^[180–182] sind lediglich auf cyclische Systeme anwendbar und ergeben nur einen einzigen Wert zur Beschreibung. Ein anderer auf Geometrie basierender Ansatz des *harmonic oscillator model of aromaticity* (HOMA)^[183,184] ist theoretisch auch auf nicht-cyclische Systeme anwendbar, ergibt jedoch ebenso nur einen Wert und ist stark abhängig von der Referenz. Ein räumlich aufgelöstes Verfahren ist die detaillierte Erstellung von Stromdichtekarten (*current density maps*),^[182,185–195] welches jedoch auch einige Nachteile mit sich bringt. Die graphische Auswertung ist auf zwei Dimensionen beschränkt, da die Stromdichte ein Vektorfeld ist. Außerdem ist die Stromdichte abhängig von der relativen Ausrichtung des Moleküls und dem Magnetfeld. Eindeutige Ergebnisse liefert diese Methode daher nur für planare Systeme.

1998 nutzen WALLENBORN *et al.* die Anisotropie der induzierten Stromdichte, um die Aromatizität eines TS zu beweisen.^[196] HERGES und GEUENICH entwickelten daraus die generelle Methode Anisotropie der induzierten Stromdichte (*anistropy of the induced current density*, ACID) zur Repräsentation und Quantifizierung von Delokalisierung, Konjugation und Aromatizität in jedem molekularen System.^[197,198] Die Vorteile dieses Konzepts sind das Skalarfeld, welches invariant in Bezug auf die relative Ausrichtung der Moleküle zum Magnetfeld ist, die direkte Visualisierung und der ausschließlich quantenchemische Ansatz ohne empirische Parameter. Außerdem besteht unter Einbezug des Magnetfeldvektors die Möglichkeit, durch die Stromdichtevektoren direkt para- oder diatropo Ringströme des π -Systems anzuzeigen. Die ACID-Methode ist aber nicht nur direkt für die Quantifizierung und Darstellung von delokalisierte Elektronensystemen gut geeignet. Ebenso interessant ist die Verwendung bei der Erklärung von stereoelektronischen Phänomenen wie dem anomeren Effekt oder der Regio- und Stereochemie von pericyclischen Reaktionen wie z.B. für DIELS-ALDER-Reaktionen.

5.1 Porphyrine und Derivate

Porphyrine und dessen Derivate sind nicht nur in der Natur omnipräsent, wie z.B. im Chlorophyll als Magnesiumkomplex und im Hämoglobin oder Cytochrom als Eisenkomplex. Auch der synthetische Einsatz in diversen Anwendungen ist dank großer Variabilität von enormer Bedeutung für die chemische Forschung.^[199] Anwendungen gibt es in medizinischen Bereichen wie z.B. Kontrastmitteln für die Magnet-Resonanz-Tomographie (MRT) (schaltbare magnetische Bistabilität)^[200–207] oder dem Einsatz als Photosensibilisator in der photodynamischen Therapie (PDT) durch Erzeugung von Singulett-Sauerstoff zur lokalen Tumorbehandlung.^[208–214] Auch in technischen Lösungen wie molekularen Drähten,^[215–220] Ladungstrennern für die Photovoltaik,^[221,222] Chromophoren für künstliche Photosynthese^[223–225] und weiteren photonischen, elektronischen oder optoelektronischen Anwendungen werden Porphyrine eingesetzt.^[226,227]

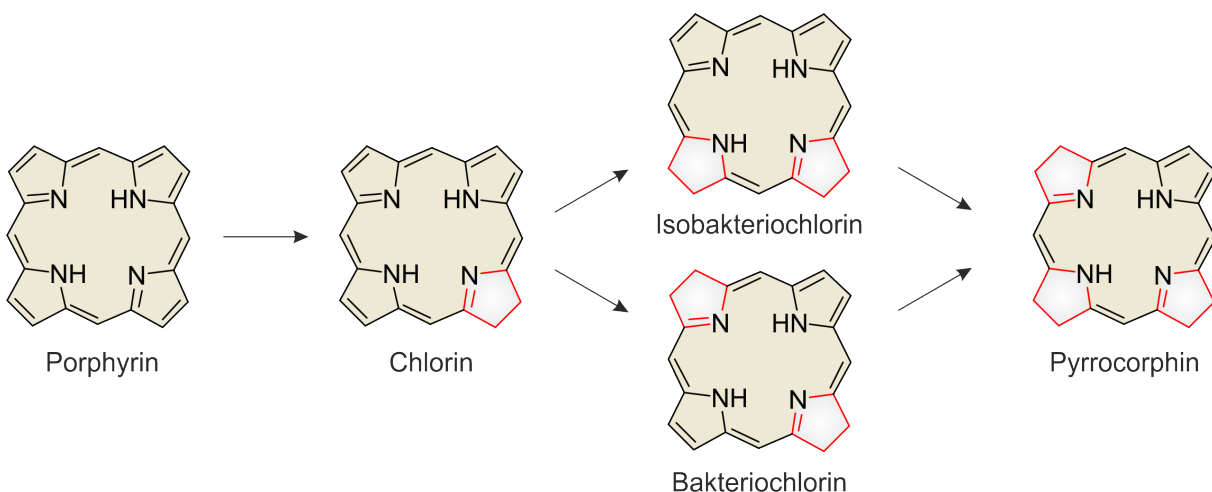


Abb. 5.1: Schematischer Reaktionspfad für die Reduktion von Porphyrin zu den verschiedenen Hydroporphyrinen (hydrierte Pyrrolringe sind farblich markiert).

Von besonderem Interesse sind die Hydroporphyrine, da sie deutlich bathochrom verschobene Absorptionsbanden bis in den NIR-Bereich aufweisen.^[228] Die Synthese ist jedoch auf drei generelle Wege limitiert, welche nicht ausreichend selektiv verlaufen. Grundsätzlich wird meist vom Porphyrin ausgegangen und entweder über eine direkte Hydrierung, eine Oxidation oder über eine Cycloaddition derivatisiert.^[229] Bei der 1,3-dipolaren Cycloaddition wird meist auf Grund der geringen Reaktivität der $\beta\beta'$ -Position der pyrrolischen Doppelbindung mit sehr reaktiven Spezies gearbeitet.^[203,230–232] Auch DIELS-ALDER-Reaktionen sind möglich, die Produkte jedoch neigen zu Pyrrolrückaromatisierung und Oxidationslabilität.^[233–235] Grundsätzlich fehlt aber besonders nach dem ersten Schritt zum Chlorin eine Strategie zur weiteren und selektiven Synthese zum Iso- bzw. Bakteriochlorin sowie die Vorhersage und Erklärung der Regiochemie der Addition. Hochinteressant sind in diesem Zusammenhang auch Unterschiede in der Reaktion mit der freien Base und dem Metallkomplex.

5.2 One-Pot Approach to Chlorins, Isobacteriochlorins, Bacteriochlorins, and Pyrrocorphins

M. K. Peters, F. Röhricht, C. Näther und R. Herges

Org. Lett. **2018**, *20*, 7879–7883.

DOI:10.1021/acs.orglett.8b03433

Supporting Information: Anhang SI 8

Wissenschaftliche Beiträge: Benchmarking verschiedener DFT-Niveaus durch Geometrieabweichung zu Kristallstrukturen, Geometrieoptimierung aller Edukte (bzw. vdW-/CT-Komplexe) und Produkte, TSS aller DIELS-ALDER-TS, ACID-Plots der Edukte, (anteilig) Verfassen des Manuskripts.

Zusammenfassung

Diese Veröffentlichung zeigt die Vorhersage, Durchführung und Aufklärung der Regiochemie von DIELS-ALDER-Reaktionen mit dem Ziel, kontrolliert und systematisch Porphyrine zu Chlorinen, Isobakteriochlorinen, Bakteriochlorinen und Pyrrocorphinen zu reduzieren. Dafür wurde das als Dien extrem reaktive Isobenzofuran (IBF) *in situ* hergestellt, welches anschließend in hohen Ausbeuten mit Porphyrinen zu Chlorinen und nachfolgend in einem weiteren Cycloadditionsschritt zu Iso- und Bacteriochlorinen reagieren kann. Eine große Rolle bei DIELS-ALDER-Reaktionen mit solchen Systemen spielt die *endo/exo*-Isomerie und die Regiochemie. So entsteht aus dem metallfreien Chlorin bei weitere Cycloaddition selektiv ein Bacterichlorin und aus dem Nickelchlorin eine Isobacteriochlorin.

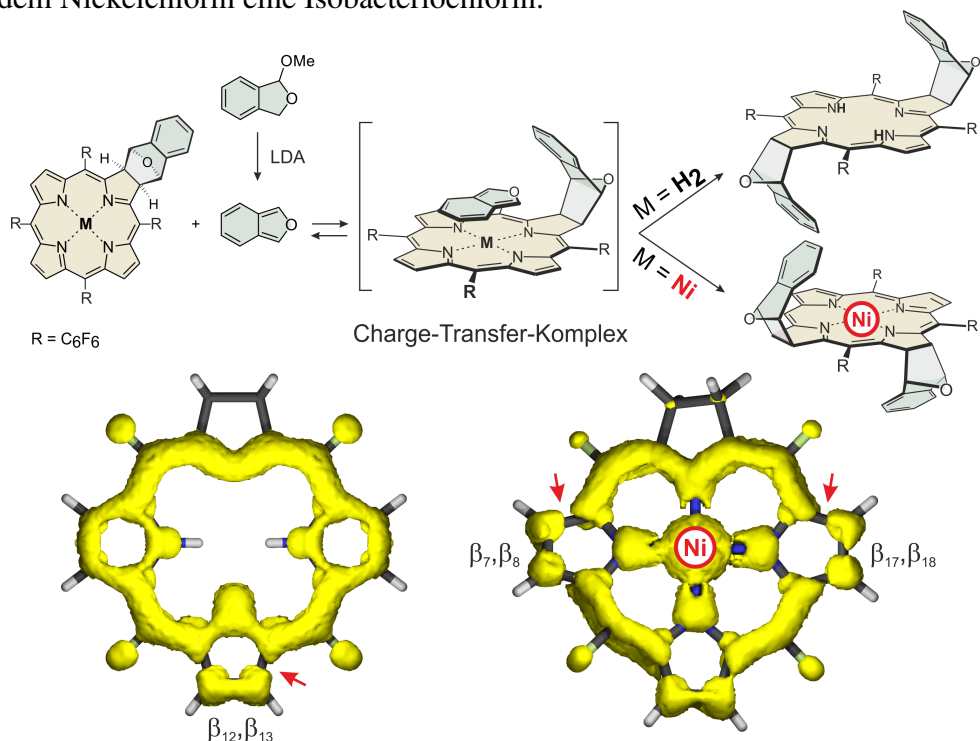


Abb. 5.2: Verlauf der Addition von IBF an Chlorine mit und ohne Metallzentrum. Die ACID-Darstellung liefert die Erklärung des Ausgangs der Reaktion.

Da bei der Reaktion eine Präorganisation der Reaktanden als Charge-Transfer-Komplex (vdW-Komplex) auftritt, muss für eine adäquate Beschreibung Dispersion berücksichtigt werden. Die durchgeführten Rechnungen auf dem durch Struktur-Benchmarking mit erhaltenen Einkristallstrukturen ermittelte Niveau konnten eindeutig die *endo/exo*-Konfiguration der kinetisch (TSS) und thermodynamisch kontrollierten Addition von IBF an Porphyrine und auch die Regio- und Stereochemie der weiteren Addition an Nickel-Chlorine vorhersagen. Zusätzlich zur Vorhersage konnte die ACID-Methode eine Erklärung für die Regiochemie der zweiten Addition geben: die β_{12},β_{13} -Doppelbindung bei metallfreiem Chlorin ist nahezu isoliert vom aromatischen Annulensystem und somit reaktiver als die anderen Bindungen (Produkt: Bakteriochlorin). Bei Chlorinen mit eingelagertem Nickelzentrum ist dies genau andersherum: hier sind die β_{7},β_{8} -

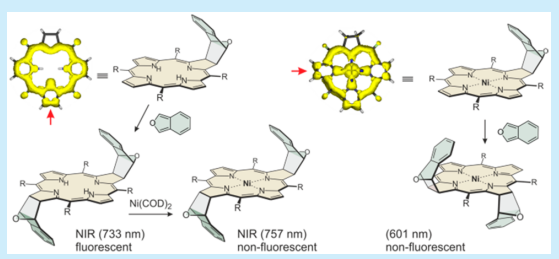
bzw. die β_{17},β_{18} -Doppelbindung schwächer konjugiert, was die Reaktion zum Isobakteriochlorin erklärt.

One-Pot Approach to Chlorins, Isobacteriochlorins, Bacteriochlorins, and Pyrrocorphins

Morten K. Peters,[†] Fynn Röhricht,[†] Christian Näther,[‡] and Rainer Herges^{*,†}[†]Otto Diels-Institute of Organic Chemistry, Christian Albrechts University Kiel, Otto Hahn Platz 4, 24118 Kiel, Germany[‡]Institut für Anorganische Chemie, Christian Albrechts University Kiel, Max-Eyth-Strasse 2, 24118 Kiel, Germany

Supporting Information

ABSTRACT: A Diels–Alder strategy is reported to synthesize the complete set of hydroporphyrins: chlorins, bacteriochlorins, isobacteriochlorins, and pyrrocorphins. Porphyrins and Ni-porphyrins react with isobenzofuran in very high yields at 70 °C to form the corresponding chlorins. Electron-deficient porphyrins react with a second equivalent of isobenzofuran yielding exclusively bacteriochlorin (82%), and Ni-porphyrin gives only isobacteriochlorin (99%). All cycloadditions are completely regio- and stereoselective. The regiochemistry is correctly predicted using the ACID method.



Porphyrins and their reduced derivatives (chlorins, bacteriochlorins, isobacteriochlorins, and pyrrocorphins; Scheme 1) are ubiquitous in nature, and more than 50 000 synthetic analogues have been synthesized so far.¹ Besides stability and catalytic activity, their photophysical properties,² found a wide range of applications. Porphyrin and hydroporphyrin derivatives have been used as photosensitizers for photodynamic therapy,^{3–5} as light-harvesting antennae in artificial photosynthesis,^{6,7} as chromophores in dye-sensitized solar cells,⁸ for multiphoton microscopy⁹ and for the design of a number of molecular photonic devices and materials.¹⁰

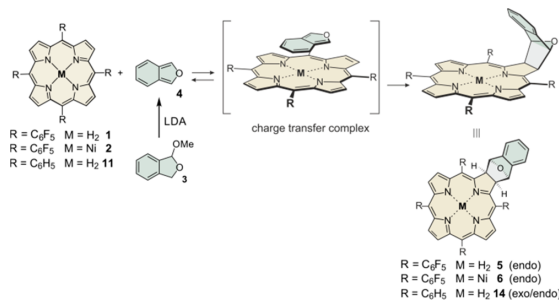
Even though hydroporphyrins such as chlorins and bacteriochlorins are the most important pigments in the photosynthetic systems of green plants and bacteria, their favorable absorption maxima in the visible and NIR range notwithstanding, examples of synthetic hydroporphyrins decrease with increasing hydrogenation state (porphyrins: 45 000, chlorins: 5100, bacteriochlorins: 576, isobacteriochlorins: 180, pyrrocorphins: 68).¹ Most of the bacterio- and isobacteriochlorins are semi-synthetic derivatives of natural products¹¹ because the number of fully synthetic methods is limited.¹² There are three general synthetic approaches to chlorins and (iso)bacteriochlorins starting from porphyrins.¹³

Scheme 1. Schematic Structures of Tetrapyrrolic Compounds Including 18 Electron Annulene Substructures^a



^aHydrogenated pyrrole rings are shown in gray.

Scheme 2. [4 + 2] Cycloaddition of Isobenzofuran 4 with Free-Base H₂TPPF₂₀ (1), NiTPPF₂₀ (2), and TPP (11) Forming the Corresponding Chlorins



The conversion of β,β' pyrrolic double bonds can be achieved by (1) direct reduction, (2) oxidation, and (3) cycloadditions. Direct reduction (1) leads to chlorins that rapidly oxidize back to the porphyrins. Oxidation (2) is usually performed with OsO₄ and leads to the dihydroxylated chlorins, which are further derivatized. Cycloadditions (3), while providing a convenient, one-step access to chlorins, suffer from the low reactivity of the β,β' pyrrolic double bond. Only very reactive 1,3-dipoles, such as azomethine ylides,^{14–16} nitrile oxides,¹⁷ and nitronates¹⁸ react via 1,3-dipolar cycloadditions. Diels–Alder reactions are restricted to highly reactive quinodimethanes as dienes, which have to be generated at very high temperatures *in situ*, leading to chlorins and (iso)bacteriochlorins that are susceptible to oxidation to porphyrins^{19,20} under air, limiting applications in photodynamic therapy.

Received: October 26, 2018

Published: December 11, 2018

Scheme 3. Synthesis of Different Porphyrin Derivatives via [4 + 2] Cycloadditions

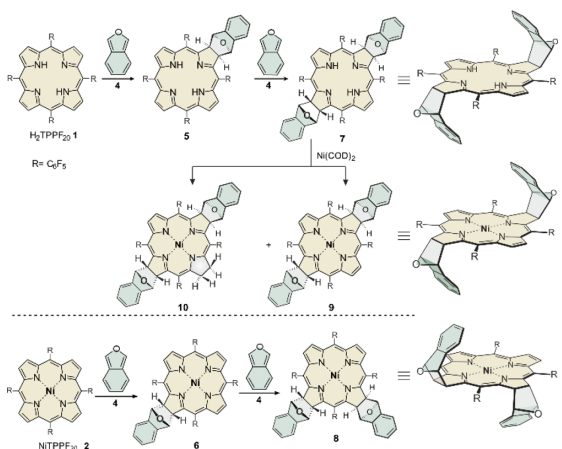


Table 1. Diels-Alder Reactions of Different Porphyrins with IBF at 70 °C^a

tetrapyrrole	eq of IBF	yield (%)			
		remaining starting material	monoadduct	bisadduct	
H ₂ TPPF ₂₀ 1	5	1 (6)	5 (88)	7 (6)	
H ₂ TPPF ₂₀ 1	15	1 (9)	5 (26)	7 (65)	
H ₂ TPCF ₂₀ 5	10	5 (2)	5 (16) ^b	7 (82)	
Ni-TPPF ₂₀ 2	5	2 (1) ^d	6 (14)	8 (83)	
Ni-TPPF ₂₀ 2	10	—	— ^d	8 (99)	
H ₂ P 13	10	not isolated	—	—	
H ₂ TPP 11	10	11 (21) ^d	14 (72) ^c	—	
Ni-TPP 12	10	not isolated	—	—	

^aReaction time was 36 h in all cases; anhydrous benzene was used as a solvent; and in all experiments, 50 mg of porphyrin was used (except H₂P).

^bSome product was lost through retro Diels–Alder reactions.

^cexo 53%, endo 19%. ^dSome product was lost during column chromatography.

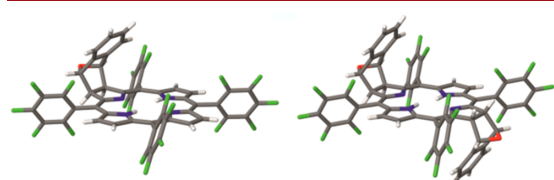


Figure 1. Crystal structure of endo free-base chlorin 5 and the anti-endo free-base bacteriochlorin 7.

Driving force for oxidation is the rearomatization of the newly formed cyclohexene ring. In principle, re-oxidation could be prevented if stable, cyclic quinodimethanes such as the commercially available 1,3-diphenylisobenzofuran (DBPF) would be applied because a bridged cyclohexene would be formed that is not susceptible to rearomatization. Unfortunately, in our hands, DBPF does not react even with electron-poor porphyrins such as tetrakis(pentafluorophenyl)porphyrin **1**. Model calculations reveal that the phenyl substituents in DBPF impose severe sterical hindrance with the aryl groups at

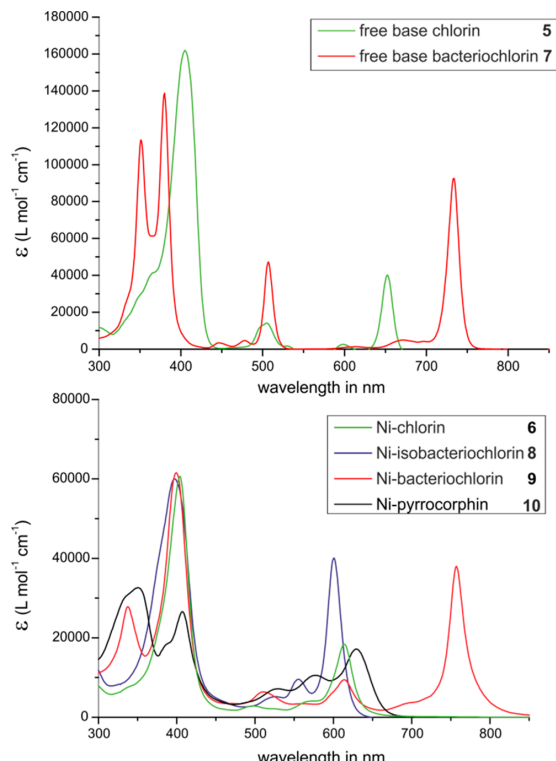


Figure 2. Electronic absorption spectra of chlorin 5 and bacteriochlorin 7 and their reduced derivatives 6, 8, 9, and 10 at 25 °C in acetonitrile (tetrapyrrole concentration of 10 μM).

the *meso* position of the porphyrin. It was therefore straightforward to use the parent isobenzofuran **4** (IBF) as the diene in the Diels–Alder reaction with porphyrins. IBF **4** is considerably more reactive than DBPF and concomitantly sterically less hindered. On the downside, IBF is less stable than DBPF and has to be freshly prepared before use. We recently published a convenient synthesis of pure IBF **4**, which can be stored indefinitely as a solid at –20 °C.²¹ We here report on the high reactivity and selectivity of IBF **4** in Diels–Alder reactions with free-base porphyrins and Ni-porphyrins, forming chlorins (1:1 addition products) and (iso)-bacteriochlorins (2:1 addition) with complete regio and stereoselectivity.

We selected tetrakis(pentafluorophenyl)porphyrin (H₂TPPF₂₀) **1** and Ni-tetrakis(pentafluorophenyl)porphyrin (Ni-TPPF₂₀) **2** as dienophiles because they are readily accessible and have been previously subjected to cycloadditions. We reacted both porphyrins with freshly prepared IBF **4** for 36 h at 70 °C in benzene. After workup, 1:1 (chlorins), and 2:1 cycloaddition adducts (bacterio- and isobacteriochlorins) were isolated (Schemes 2 and 3). The electron-rich IBF and electron-deficient porphyrins form charge-transfer complexes in a pre-equilibrium preceding the cycloaddition. The formation of porphyrin charge-transfer complexes is typically indicated by the quenching of the fluorescence of the porphyrin.^{22,23} The fluorescence of H₂TPPF₂₀ **1** (emissions at 643 and 702 nm) is indeed quenched upon addition of IBF **4** (see the Supporting

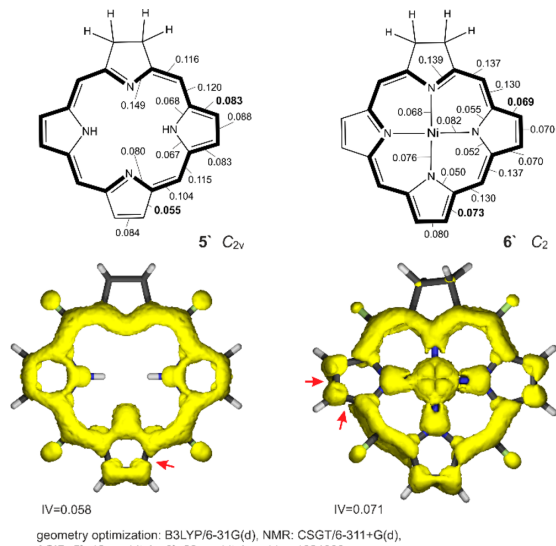


Figure 3. ACID plots predicting the regiochemistry of the Diels–Alder reaction of free base chlorin **5'** and the Ni-chlorin **6'** with isobenzofuran (IBF, **4**). Both chlorins include an aromatic 18 -annulene subunit (highlighted with bold lines) and are represented as contiguous isosurfaces in the ACID plot, leaving one double bond isolated, i.e., olefinic in nature and, thus, more reactive toward a cycloaddition (indicated with red arrows). For the sake of simplicity and to save computer time, the pentafluorophenyl substituents are replaced by fluorine, and the 1,3-dihydroisobenzofuran unit is replaced by two hydrogen atoms. Critical isosurface values (CIV) are given for all conjugated C–C and C–N bonds. Large CIV values represent bonds with strong conjugation.

Information).²⁴ The formation of stable charge-transfer complexes is further corroborated by density functional theory calculations (see the *vide infra* results).

Ni-porphyrin **2** is more reactive than the corresponding free-base porphyrin **1** and forms higher amounts of 2:1 products (see Table 1). NMR spectra and a crystal structure analysis (Figure 1) reveal that only *endo* products are formed. Remaining starting material (porphyrin), 1:1 (chlorins), and 2:1 products can be easily separated by column chromatography (see the *Supporting Information*). We attribute the strong *endo* stereospecificity to the pre-orientation of IBF **4** in the charge-transfer complex (**Scheme 2**). Electron-rich H₂TPP **11** forms a much-weaker complex with IBF **4**, and therefore, both *endo* and *exo* products are formed.

With a higher excess (10–15 equiv) of IBF **4** (at 70 °C), predominantly 2:1 products are formed. Free-base porphyrin **1** exclusively forms the corresponding bacteriochlorin **7** with an 82% yield, and Ni-porphyrin **2** gives 99% Ni-isobacteriochlorin **8**. Compared to previously published cycloadditions, both yields are exceptional. Moreover, both cycloadditions are completely regio- and stereoselective. Among the 12 conceivable isomers (iso/bacteriochlorin, *endo/exo*, and *syn/anti*), only one isomer is formed. Nuclear magnetic resonance and a crystal-structure analysis (Figure 1) prove that only the *anti* and *endo–endo* products of the free base bacterio- and Ni-isobacteriochlorin are isolated. To gain access to the complete series of Ni-tetrapyrroles: Ni-porphyrin, Ni-chlorin, Ni-isobacteriochlorin, Ni-bacteriochlorin, and Ni-pyrocor-

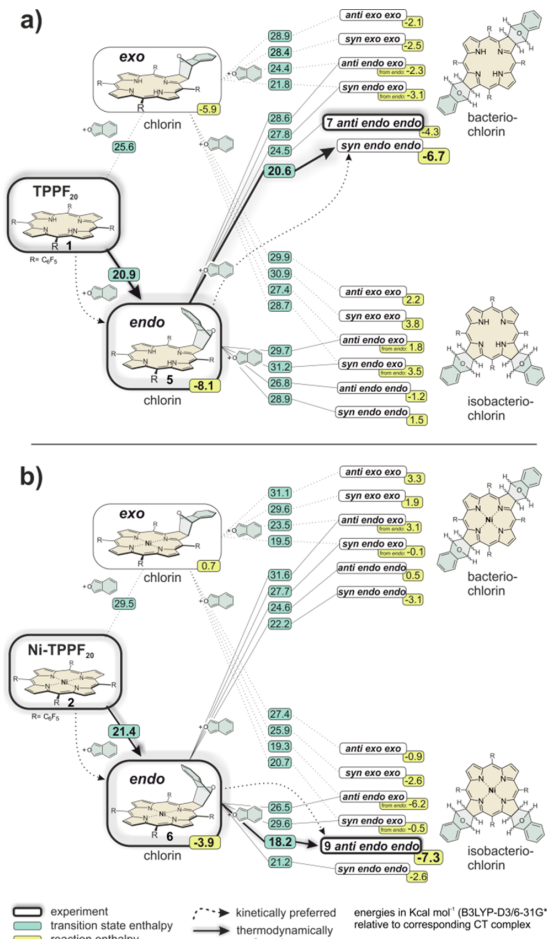


Figure 4. (a) DFT calculations of the Diels–Alder reactions of the free base porphyrin TPPF₂₀ **1** with isobenzofuran (IBF, **4**) yielding the corresponding chlorins **5** in *endo* and *exo* configurations and the subsequent Diels–Alder reactions with a second molecule of IBF (**4**) to form all 12 conceivable isomers of the 2:1 addition products (bacterio- and isobacteriochlorins) in *exo*, *endo*, *anti*, and *syn* configurations. (b) DFT calculations of the Ni-porphyrin Ni-TPPF₂₀ **2** analogous to that shown in panel a). All reaction energies and activation barriers are given relative to the corresponding charge-transfer (van der Waals) complex from which the cycloaddition starts. The experimentally observed pathways and products are highlighted. Predicted and observed products are identical with one exception. According to experiment, the cycloaddition of IBF to the free base chlorin **5** gives *anti*, *endo*, and *endo* bacteriochlorin **7**. DFT calculations favor the formation of the *syn*, *endo*, and *endo* isomers based on kinetic as well as thermodynamic data.

phin,^{25,26} we inserted Ni into bacteriochlorin **7** (**Scheme 3**; for UV–vis spectra, see Figure 2).

Ni²⁺ insertion into **7** following conventionally procedures such as treatment with Ni(OAc)₂ in DMF at 150 °C were unsuccessful because cycloreversion took place at high temperatures. We therefore used a previously published method that allows Ni²⁺ insertion under mild conditions. Treatment of **7** with Ni(COD)₂ at 20 °C yielded the Ni-

bacteriochlorin **9** and Ni-pyrrocorphin **10**.²⁷ The Ni-pyrrocorphin **10** can be converted to the Ni-bacteriochlorin **9** using trifluoroacetic acid under air (see the Supporting Information).

To explore the scope and limitation of our new method, we subjected tetraphenylporphyrin **11** (TPP), Ni-tetraphenylporphyrin **12** (Ni-TPP), and parent porphyrin **13** (H_2P) to cycloadditions with IBF **4**. TPP gives chlorin **14** with *endo* and *exo* configurations that can be separated by column chromatography. However, no 2:1 products are formed. Ni-TPP and parent porphyrin also give chlorins that have not been further characterized because of very poor solubility (Table 1). The Diels–Alder reactions also proceed at room temperature; however, reaction times until complete conversion are several days.

A similar regioselectivity in the cycloadditions of electron-deficient free-base chlorins yielding bacteriochlorins and of the corresponding Ni-chlorins forming isobacteriochlorins has been previously observed upon reaction of TPPF₂₀ and Ni-TPPF₂₀ with two equivalents of azomethine ylides, quinodimethanes, and hydrogenation.^{19,25,28} Bruhn and Brückner explain this regioselectivity based on their average ionization energy (ALIEs) procedure.²⁸ We here apply our ACID method that is known to reliably predict stereoelectronic effects.^{29,30} The ACID scalar field is interpreted as the density of delocalized electrons, which is represented as an isosurface (just as the total electron density). The degree of conjugation between atoms or bonds can be quantified by the critical isosurface value (CIV). CIV is defined as the ACID value at points where the gradient of the ACID scalar field is zero and the Laplacian has two negative and one positive eigenvalues. High CIV values indicate strong conjugation. ACID applied to the chlorins **5'** and **6'** gives an intuitive and conclusive picture. Both chlorins include ¹⁸annulene subunits (bold lines in Figure 3, top), which are aromatic with $4n + 2$ delocalized electrons. The ACID plot of free base chlorin **5'** clearly reflects this classical view. The aromatic subsystem is readily identifiable as a contiguous ACID isosurface (yellow surface in Figure 3, bottom, left). Separate and isolated from this ¹⁸annulene unit is the β_{12}/β_{13} double bond, opposite to the hydrogenated C–C bond (indicated with a red arrow, Figure 3). This double bond is rather olefinic (CIV: 0.055) and, hence, more reactive as a dienophile in Diels–Alder reactions or any other reaction converting this C=C double bond into a single bond. The C=C bonds participating in the aromatic system (CIV: 0.083) are less reactive, which explains the experimental finding that exclusively the bacteriochlorin is formed. The situation is more complicated in Ni-chlorin **6'**. A pair of degenerate, symmetry-equivalent valence bond substructures can be drawn to describe the aromatic ¹⁸annulene subunit (one of them is shown in Figure 3 top, right). Here the β_7/β_8 and β_{17}/β_{18} double bonds (indicated with red arrows, Figure 3 bottom right) are more isolated (CIV: 0.069) compared to the β_{12}/β_{13} double bond (CIV: 0.073), which explains the experimentally observed formation of the isobacteriochlorins.

To further elucidate the reason for the remarkable stereo- and regioselectivity of our cycloadditions, we performed calculations at the B3LYP-D3/6-31G* level of density functional theory (DFT), including dispersion.³¹ Reaction enthalpies and activation barriers were determined relative to the charge-transfer (van der Waals) complex from which the cycloaddition starts. These complexes are stable minima on the potential energy hypersurface. The results are summarized in

Figure 4. Thermodynamic and kinetic data are within the expected range for Diels–Alder reactions proceeding at room temperature or slightly elevated temperatures. Our calculations correctly predict the stereo- and regiochemistry except for the experimentally observed formation of *anti*, *endo*, *endo* bacteriochlorin **7**. According to the DFT calculations, the formation of the corresponding *syn* product should be preferred (Figure 4 a). This discrepancy can be explained by the fact that our calculations do not include entropy. The formation of the *syn* isomer is entropically disfavored because the attack of IBF at the porphyrin π hemisphere, which is already shielded by the first IBF addition, is disfavored. Cycloaddition therefore takes place from the less-hindered side.

In summary, we present a convenient, high-yielding, regio- and stereoselective synthesis of chlorins, bacteriochlorins, isobacteriochlorins, and pyrrocorphins (hexahydroporphyrins). With Ni²⁺ in the tetrapyrrolic core, the whole series of hydropporphyrins has been prepared and characterized. In particular, bacteriochlorins are highly interesting chromophores because they exhibit strong absorption bands in the near-infrared. At these wavelengths, blood-supported tissue is relatively transparent. Free-base bacteriochlorin **7** is strongly fluorescent and stable toward oxidation, and with a strong absorption band at 733 nm, it is a good candidate for applications in photodynamic therapy. The corresponding Ni-bacteriochlorin **9** is non-fluorescent and a stable NIR dye with a strong absorbance at 757 nm. Both compounds are good starting points for further derivatization because the penta-fluorophenyl rings are susceptible to aromatic substitution with nucleophiles, including water-solubilizing groups.³²

■ ASSOCIATED CONTENT

S Supporting Information

The Supporting Information is available free of charge on the ACS Publications website at DOI: [10.1021/acs.orglett.8b03433](https://doi.org/10.1021/acs.orglett.8b03433).

Experimental procedures and spectral data, details of computational studies, and crystallographic data (PDF)

Accession Codes

CCDC entries nos. **1851406** and **1851407** contain the supplementary crystallographic data for this paper. These data can be obtained free of charge via www.ccdc.cam.ac.uk/data_request/cif, by e-mailing data_request@ccdc.cam.ac.uk, or by contacting The Cambridge Crystallographic Data Centre, 12 Union Road, Cambridge CB2 1EZ, U.K.; fax: +44 1223 336033.

■ AUTHOR INFORMATION

Corresponding Author

*E-mail: rherges@oc.uni-kiel.de.

ORCID

Christian Näther: [0000-0001-8741-6508](https://orcid.org/0000-0001-8741-6508)

Rainer Herges: [0000-0002-6396-6991](https://orcid.org/0000-0002-6396-6991)

Notes

The authors declare no competing financial interest.

ACKNOWLEDGMENTS

The authors gratefully acknowledge financial support by the Deutsche Forschungsgesellschaft (DFG) within the Sonderforschungsbereich 677, “Function by Switching”.

REFERENCES

- (1) Reaxys database May 2018.
- (2) *Porphyrins: Optical spectra and electronic structure of porphyrins and related rings*; Gouterman, M.; Dolphin, D., Eds.; Academic Press: Boston, 1978; Vol 3 (Part A), pp 1–165.
- (3) Bonnett, R. *Chem. Soc. Rev.* **1995**, *24*, 19–33.
- (4) Sternberg, E. D.; Dolphin, D.; Bruckner, C. *Tetrahedron* **1998**, *54*, 4151–4202.
- (5) Mazor, O.; Brandis, I.; Plaks, V.; Neumark, E.; Rosenbach-Belkin, V.; Salomon, Y.; Scherz, A. *Photochem. Photobiol.* **2005**, *81*, 342–351.
- (6) Gust, D.; Moore, T. A.; Moore, A. L. *Acc. Chem. Res.* **2009**, *42*, 1890–1898.
- (7) Esswein, A. J.; Nocera, D. G. *Chem. Rev.* **2007**, *107*, 4022–4047.
- (8) Li, L.-L.; Diau, E. W.-G. *Chem. Soc. Rev.* **2013**, *42*, 291–304.
- (9) Konig, K. J. *Microsc. Microanal.* **2000**, *200*, 83–104.
- (10) Holten, D.; Bocian, D. F.; Lindsey, J. S. *Acc. Chem. Res.* **2002**, *35*, 57–69.
- (11) Scheer, H. An Overview of Chlorophylls and Bacteriochlorophylls: Biochemistry, Biophysics, Functions and Applications. *Advances in Photosynthesis and Respiration* **2006**, *25*, 1–26.
- (12) Pandey, R. K.; Zheng, G. *Porphyrin Handbook (Porphyrins as photosensitizers in photodynamic therapy)*; Kadish, K. M.; Smith, K. M.; Guilard, R., Eds.; Academic Press: Boston; Vol 6, Chapter 43, pp 157–230.
- (13) Taniguchi, M.; Lindsey, J. S. *Chem. Rev.* **2017**, *117*, 344–535.
- (14) Silva, A. M. G.; Tomé, A. C.; Neves, M. G. P. M. S.; Silva, A. M. S.; Cavaleiro, J. A. S. *J. Org. Chem.* **2005**, *70*, 2306–2314.
- (15) Silva, A. M. G.; Tome, A. C.; Neves, M. G. P. M. S.; Silva, A. M. S.; Cavaleiro, J. A. S. *Chem. Commun.* **1999**, 1767–1768.
- (16) Silva, A. M. G.; Tomé, A. C.; Neves, M. G. P. M. S.; Silva, A. M. S.; Cavaleiro, J. A. S. *J. Org. Chem.* **2002**, *67*, 726.
- (17) Liu, X.; Li, C.; Peng, X.; Zhou, Y.; Zeng, Z.; Li, Y.; Zhang, T.; Zhang, B.; Dong, Y.; Sun, D.; Cheng, P.; Feng, Y. *Dyes Pigm.* **2013**, *98*, 181–189.
- (18) Ebrahim, M. M.; Moreau, M.; Senge, M. O. *Heterocycles* **2011**, *83*, 627–630.
- (19) Tomé, A. C.; Lacerda, P. S. S.; Neves, M. G. P. M. S.; Cavaleiro, J. A. S. *Chem. Commun.* **1997**, 1199–1200.
- (20) Vicente, M. G. H.; Cancilla, M. T.; Lebrilla, C. B.; Smith, K. M. *Chem. Commun.* **1998**, 2355–2356.
- (21) Peters, M. K.; Herges, R. *Beilstein J. Org. Chem.* **2017**, *13*, 2659–2662.
- (22) Gouterman, M.; Stevenson, P. E. *J. Chem. Phys.* **1962**, *37*, 2266–2269.
- (23) Aoki, T.; Sakai, H.; Ohkubo, K.; Sakanoue, T.; Takenobu, T.; Fukuzumi, S.; Hasobe, T. *Chem. Sci.* **2015**, *6*, 1498–1509.
- (24) Rahman; Harmon, H. J. *Spectrochim. Acta, Part A* **2006**, *65*, 901–906.
- (25) Ide, Y.; Kuwahara, T.; Takeshita, S.; Fujishiro, R.; Suzuki, M.; Mori, S.; Shinokubo, H.; Nakamura, M.; Yoshino, K.; Ikeue, T. J. *Inorg. Biochem.* **2018**, *178*, 115–124.
- (26) Sehwesinger, R.; Waditschatka, R.; Rigby, J.; Nordmann, R.; Schweizer, W. B.; Zass, E.; Eschenmoser, A. *Helv. Chim. Acta* **1982**, *65*, 600–610.
- (27) Peters, M. K.; Herges, R. *Inorg. Chem.* **2018**, *57*, 3177–3182.
- (28) Bruhn, T.; Brückner, C. *J. Org. Chem.* **2015**, *80*, 4861–4868.
- (29) Geuenich, D.; Hess, K.; Köhler, F.; Herges, R. *Chem. Rev.* **2005**, *105*, 3758–3772.
- (30) Herges, R.; Geuenich, D. *J. Phys. Chem. A* **2001**, *105*, 3214–3220.
- (31) Grimme, S.; Antony, J.; Ehrlich, S.; Krieg, H. *J. Chem. Phys.* **2010**, *132*, 154104.
- (32) Dommaschk, M.; Gutzeit, F.; Boretius, S.; Haag, R.; Herges, R. *Chem. Commun.* **2014**, *50*, 12476–12478.

5.3 Möbius Topologie und Aromatizität

MÖBIUS-Objekte begegnen einem ständig im Leben wie etwa das Recyclinglogo (♻). Die Merkmale sind einfach beschrieben: nicht unterscheidbare Ober- und Unterseiten wie z.B. bei einem geschlossenen einseitigen Band. Dennoch handelt es sich um einen hochkomplexen Sachverhalt, dem sich das Teilgebiet der Mathematik Topologie annimmt. Es beschäftigt sich mit den geometrischen Eigenschaften, die bei stetigen Änderungen invariant bleiben. Klebe-, Schnitt- und Bohroperationen sind somit nicht erlaubt und würden die extrinsischen Parameter des Gebildes als das Verhalten im 3D-Raum ändern. Stauch- und Strecktransformation sind jedoch möglich und führen zu homöomorphen Gebilden mit intrinsisch unterschiedlichen Parametern. Ein Loch in einem ringförmigen Band z.B. ist eine extrinsische Eigenschaft und definiert die Topologiekasse.^[236–240] Die Verdrillung des Bandes wird jedoch durch intrinsische Parameter wie dem *Twist* (T_w) oder *Writhe* (W_r) beschrieben. Der T_w beschreibt dabei die Summe aller Diederwinkel der Normalvektoren auf der Oberfläche des Bandes. Ein Verdrillung um 180° linksherum bedeutet einen $T_w = -1$ (rechtsherum: $T_w = +1$). Der W_r ist komplizierter zu verstehen und beschreibt die mittlere Anzahl der Selbstüberschneidungen ($W_r = C_x + C_y + C_z$).^[241] Auch dieser ist richtungsabhängig und wird in $\pi = 180^\circ$ angegeben. Diese Werte sind teilweise ineinander überführbar und somit unbrauchbar für eine extrinsische Beschreibung der Struktur. Verknüpft über das CĂLUGĂREANU-WHITE-FULLER-Theorem,^[242] vereinfacht über die *Linking Number* ($L_k = T_w + W_r$) wird so extrinsisch z.B. Ein- oder Zweiseitigkeit definiert.^[243–245]

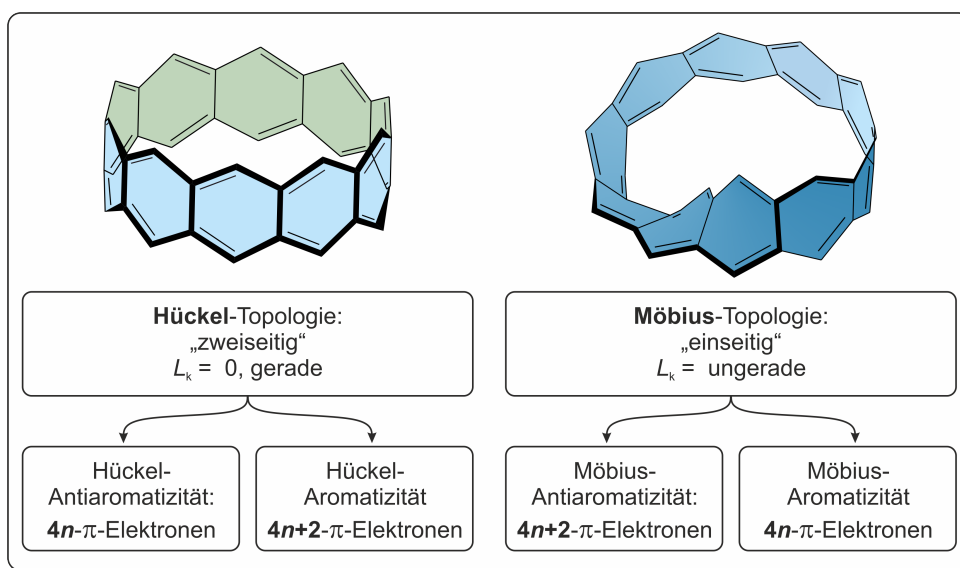


Abb. 5.3: Übersicht von HÜCKEL- und MÖBIUS-Topologie und -aromatizität am Beispiel von [10]Cyclacenen. Betrachtet man die Fläche des verdrillten MÖBIUS-[10]Cyclacenbandes, zeigt sich eindeutig Einseitigkeit somit MÖBIUS-Topologie, die exakte Betrachtung der elektronischen Pfade zeigen jedoch anderes (mehr dazu Kapitel 7, Abb. 7.9).

MÖBIUS-Topologie liegt dann vor wenn der L_k -Wert ungerade ist. Besonders interessant wird diese bei konjugierten Systemen. 1964 postulierte HEILBRONNER auf einer theoretischen Grundlage die Umkehrung der HÜCKEL-Aromatizität.^[246] Im Vergleich zu der HÜCKEL-Regel^[247,248] sollten MÖBIUS-Annulene mit $4n$ - im Vergleich zu $4n + 2$ - π -Elektronen stabilisiert und aromatisch sein. 2003 konnten HERGES *et al.* ein MÖBIUS-Aromaten mit einer $L_k = 1$ publizieren.^[249] Mehrfach verdrillte ($L_k > 1$) MÖBIUS-Aromaten sind jedoch in der Umsetzung auf molekularer Ebene durch eine erhöhte Ringspannung durch die Verdrillung und zudem in der Überlappung der p -Orbitale für eine ausreichende Elektronendelokalisierung besonders schwierig in der Synthese. Grundlage für ein solch ausgeklügeltes Design und zur Bestimmung besagter Parameter sind deshalb häufig quantenmechanische Rechnungen.

5.4 Cyclic tris-[5]helicenes with single and triple twisted Möbius topologies and Möbius aromaticity

G. Naulet, L. Sturm, A. Robert, P. Dechambenoit, F. Röhricht, R. Herges, H. Bock und F. Durola

Chem. Science **2018**, 9, 8930–8936.

DOI:10.1039/c8sc02877j

Supporting Information: Anhang SI 8

Wissenschaftliche Beiträge: DFT-Geometrieoptimierungen der MÖBIUS-topologischen Makrocyclen, (anteilig) Verfassen des Manuskripts, ACID-Plots, Orbitalplots und -auswertung, NICS und HOMA, Berechnung der *Twist-* (T_w), *Writhe-* (W_r) und Verknüpfungszahl (linking number, L_k)-Werte.

Zusammenfassung

In dieser Publikation wird die Synthese und Bestimmung von MÖBIUS-aromatischen Systemen mit einfacher und dreifacher Verdrillung gezeigt. Die Moleküle setzen sich dabei je nach helikaler Chiralität der [5]Helicenutereinheiten zu einem PMM und MMM Cyclo-tris-[5]helicen zusammen. Herausfordernd für MÖBIUS-Topologien grundsätzlich ist das Design des Moleküls: Bei stark verdrillten Systemen treten oft Probleme im Bereich hoher Ringspannung und der geringfügigen Überlappung der p -Orbitale auf. Die Lösung dieser Probleme stellt das Homöomorphie-Prinzip dar. Eigentlich extrem gespannte Systeme ($|L_k| = |T_w|$) mit kaum Konjugation formen sich durch Projektion des *Twists* (T_w) in *Writhe* (W_r) in günstigere Geometrien ($|L_k| = |W_r|$) um. Die Parameter wie ungerade Verknüpfungszahl (L_k) und die Ausbildung geringer Torsionswinkel für eine ausreichend große Überlappung zwischen den beteiligten p -Orbitalen ($L_k = T_w + W_r$) definieren laut Theorie die MÖBIUS-Aromatizität.

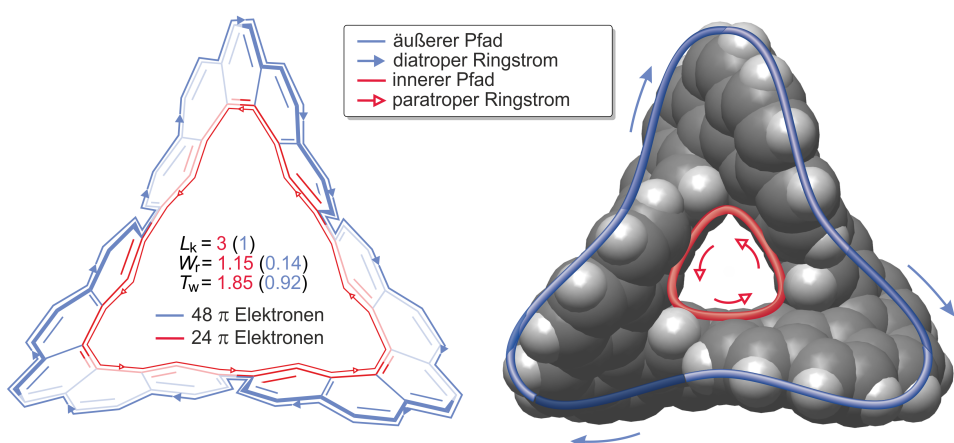


Abb. 5.4: Darstellung des MMM Cyclo-tris-[5]Helicen mit innerem und äußerem Elektronenpfad: links: Parameter der Untersuchung auf MÖBIUS-Topologie und -aromatizität. rechts: Ergebnisse der ACID-Analyse zeigen äußeren diatropen Ringstrom, welcher sich durch den gleichstarken inneren paratropen Strom aufhebt.

So konnten mit Hilfe des Programms ANEWWRITHM die topologischen Parameter der synthetisierten Moleküle exakt bestimmt werden. Die Topologie der Konjugation ist dabei abhängig vom Pfad innerhalb des cyclischen π -Systems. Der innere Pfad setzt sich aus 24 und der äußere Pfad aus 48 π -Elektronen zusammen. Beide Systeme weisen ungerade L_k -Werte, $4n \pi$ -Elektronen und intakte Konjugation auf, welche durch Bestimmung der Verdrillungswinkelmaxima der p -Orbitale bestimmt wurden. Diese Fakten weisen eindeutig auf MÖBIUS-Aromatizität hin. Die ACID-Methode jedoch zeigte komplexere Details: Wie in klassischen Aromaten zeigt der innere Pfad paratropen und der äußere Pfad diatropen Ringstrom. Diese heben sich größtenteils gegenseitig auf, was durch ^1H -NMR-Experimente sowie die theoretische Bestimmung von NICS- und HOMA-Werten bestätigt wird.

EDGE ARTICLE

[View Article Online](#)
[View Journal](#) | [View Issue](#)

[Check for updates](#)
Cite this: *Chem. Sci.*, 2018, **9**, 8930

All publication charges for this article have been paid for by the Royal Society of Chemistry

Cyclic tris-[5]helicenes with single and triple twisted Möbius topologies and Möbius aromaticity†

Guillaume Naulet,^a Ludmilla Sturm,^a Antoine Robert,^a Pierre Dechambenoit,^a Fynn Röhricht,^b Rainer Herges,^{ID *b} Harald Bock^a and Fabien Durola^{ID *a}

A number of singly (180°) twisted, largely single-stranded and thus conformationally rather fragile, Möbius molecules have been synthesized within the last 15 years, which are aromatic with $4n$ electrons, thus violating the Hückel rule. Annulenes with significantly higher twist (e.g. 540°) that retain a full cyclic conjugation path have been elusive, mainly because of the high strain and loss of orbital overlap. Recently, a topological strategy was devised to project the "twist" into "writhe", thus reducing the strain. However, orbital overlap was still severely reduced within the flexible building blocks. We now present a single and a triple twisted annulene with fully conjugated peripheries. They are unique in their pronounced band shape and conformational robustness as they are made up of three fully kata-condensed [5]helicene fragments. The triple twisted molecule exhibits a strong diatropic ring current in the outer periphery, even though the π system includes $4n$ electrons. The diatropic current is counterbalanced by a paratropic current in the σ system, resulting in no net manifestation of macrocyclic aromaticity. The key step of the synthesis of both Möbius compounds is a Perkin condensation of complementary bifunctional bismaleates leading to a flexible macrocycle containing alternating benzene and biphenyl fragments. Subsequent photocyclization yields a separable mixture of rigid diastereomeric tris-helicene macrocycles of the above topologies.

Received 29th June 2018
Accepted 14th November 2018
DOI: 10.1039/c8sc02877j
rsc.li/chemical-science

Introduction

According to the Hückel rule, annulenes are aromatic with $4n + 2$ electrons and antiaromatic with $4n$ electrons delocalized in a cyclic topology.^{1,2} Heilbronner in 1964 predicted that the Hückel rule should be reversed in Möbius annulenes.³ The latter structures can be envisioned by formally cutting a bond in a "normal" annulene, giving one end a 180° twist, and rejoining both ends. Möbius annulenes were predicted to be aromatic with $4n$ electrons and antiaromatic with $4n + 2$ electrons. Heilbronner further pointed out that the severe strain induced by the twist should decrease at ring sizes >20 . It took 40 years until the first Möbius annulene was synthesized, and Heilbronner's electron count rules were experimentally confirmed.^{4–6} Within the last 15 years a number of $4n$ electron aromatic Möbius annulenes with a 180° twist were prepared. The majority of these systems are extended porphyrins.⁷ Heilbronner's electron

count rules should also formally hold for higher twisted systems, or more precisely, for any annulene with an odd number of twists ($n \cdot 180^\circ$, $n = 1, 3, 5, \dots$). However, the severe strain induced by multiple twists is expected to prevent synthesis or at least should drastically reduce overlap between neighbouring p orbitals. We recently pointed out that there are strategies to overcome these problems.^{6,8,9} The decisive topological parameter determining aromaticity is not the number of twists T_w , but the linking number L_k .¹⁰ Hückel systems have an even linking number ($L_k = 0, 2, 4, \dots$) and Möbius objects exhibit an odd linking number ($L_k = 1, 3, 5, \dots$). T_w and L_k are connected by Calugareanu's theorem: $L_k = T_w + W_r$ (W_r = writhe).¹¹ Besides the precise mathematical definition, Calugareanu's theorem can be demonstrated by an everyday life experiment. If a band e.g. a two-core power cord is twisted and both ends are joined, the band would wind around itself. Thus, the strain induced by the twists T_w is released, and projected into writhe W_r without changing the linking number L_k . Similar arguments hold for molecules. The topological transformation can be used as a strategy to reduce strain, while keeping the topological parameter L_k constant. We recently used this strategy to synthesize the first triply twisted Möbius annulene.⁸ Unfortunately, the building block diethynyl-binaphthalene is too flexible to provide a smooth distribution of dihedral angles along the periphery of the annulene and the conjugation was interrupted by torsional angles close to 90° . We now present the

^aCentre de Recherche Paul Pascal, CNRS, Université de Bordeaux, 115 av. Schweitzer, 33600 Pessac, France. E-mail: durola@crpp-bordeaux.cnrs.fr

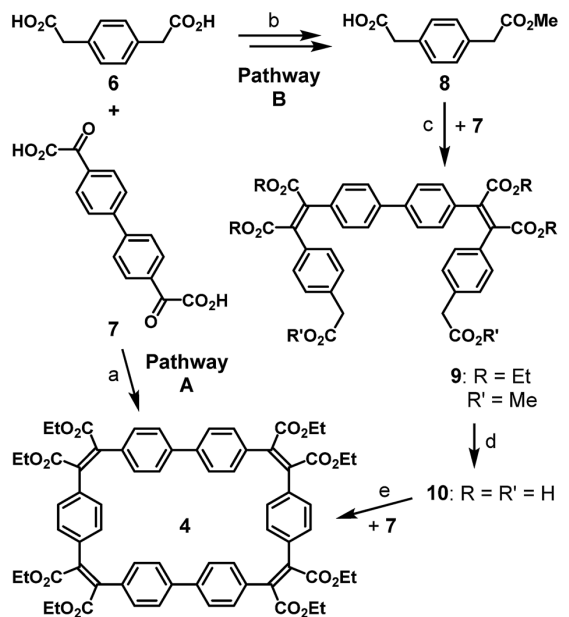
^bOtto-Diels-Institut für Organische Chemie, Christian-Albrechts-Universität Kiel, Kiel 24119, Germany. E-mail: rherges@oc.uni-kiel.de

† Electronic supplementary information (ESI) available: Synthetic procedures, NMR spectra, 2D NMR spectra, single crystal X-ray diffraction, ACID plots, orbital plots, cartesian coordinates of B3LYP/6-31G* optimized structures. CCDC 1826373 and 1826374. For ESI and crystallographic data in CIF or other electronic format see DOI: 10.1039/c8sc02877j

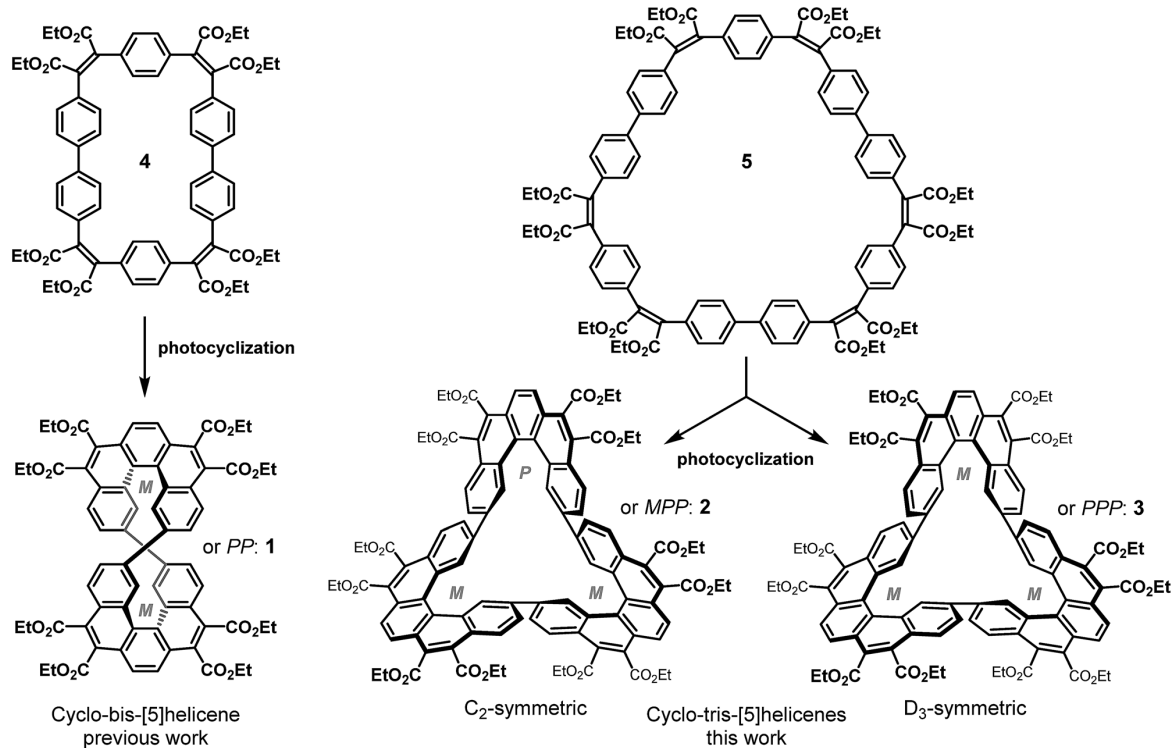
synthesis of a triple twisted annulene (540°) with small dihedral angles, and thus retaining full conjugation, and a diatropic ring current within the twisted π system in the periphery.

In the last five years, we have developed an efficient and versatile synthetic approach for the formation of large carboxy-substituted polycyclic arenes. It relies on Perkin reactions that yield flexible diarylmaleate-type precursors, followed by catalyst- or light-induced cyclization reactions.^{12,13} This synthetic method has shown considerable potential for the construction of double helicenes^{14,15} as well as for the formation of large conjugated macrocycles.^{16,17} Recently, we have combined these two structural elements in a Perkin-assembled propeller-shaped macrocycle that incorporates two identical [5]helicene fragments.¹⁸ This dimeric cyclo-bis-[5]helicene **1** has been obtained as a racemic mixture of two enantiomers whose helicene fragments have identical helicity: PP or MM. The PM (meso) compound has not been observed, which is in line with the extreme distortion of its simulated structure.

This article presents the synthesis and study of trimeric homologs of macrocycle **1**: the C_2 -symmetric cyclo-tris-[5]helicenes **2** (MPP and PMM configurations), and the D_3 -symmetric cyclo-tris-[5]helicenes **3** (PPP and MMM configurations) which are diastereomers and have been obtained as racemic mixtures (Scheme 1). In contrast to the dimeric case (the non-observed meso isomer of **1**), three helicenes of different helicity can be cyclically linked without generating much distortion, thus both possible diastereomers are formed.



Scheme 2 Synthesis of diacetic three-block precursor and its use in the synthesis of four-block macrocycle. (a) High dilution, Ac_2O , NEt_3 , THF, reflux, 48 h, then EtOH , EtBr , DBU, reflux, 24 h, 21%; (b) SOCl_2 , MeOH , reflux, 4 h, 85%; then KOH , 1,4-dioxane, reflux, 75 min, 47%; (c) Ac_2O , NEt_3 , THF, reflux, 18 h, then EtOH , EtBr , DBU, reflux, 24 h, 65%; (d) KOH , H_2O , EtOH , reflux, 18 h, 100%; (e) high dilution, Ac_2O , NEt_3 , THF, reflux, 48 h, then EtOH , EtBr , DBU, reflux, 24 h, 55%.



Scheme 1 Cyclo-poly-[5]helicenes obtained by photocyclisation of flexible conjugated macrocycles.

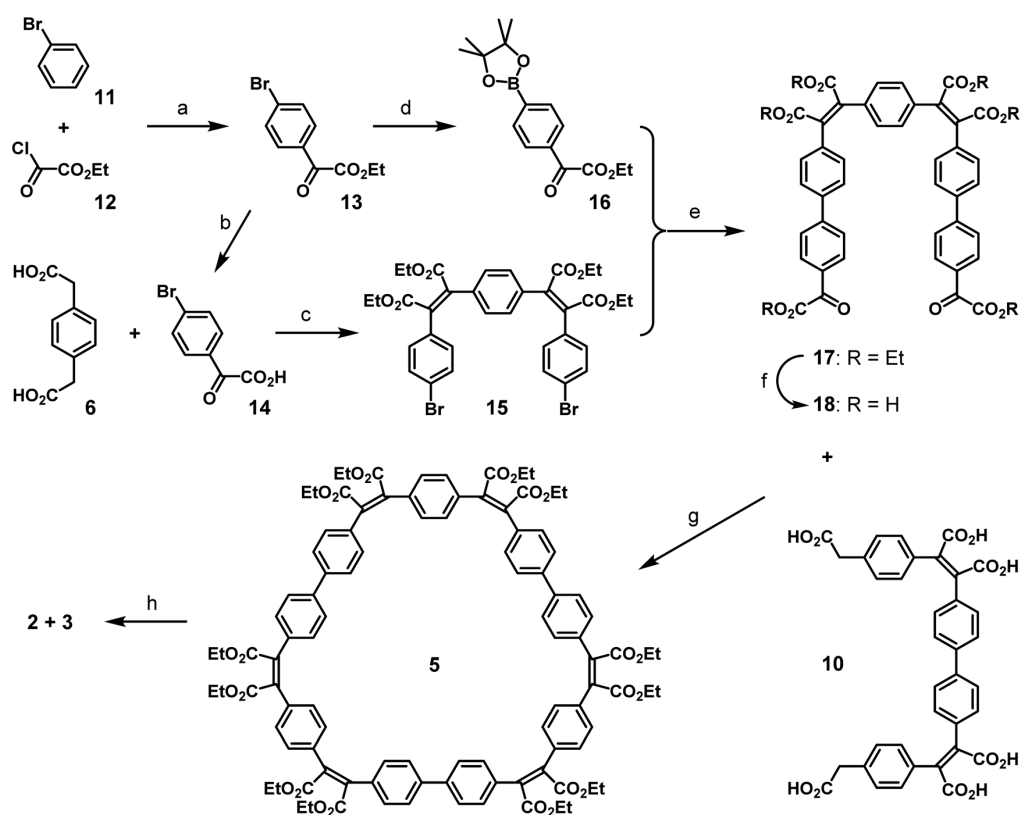
In both of these two rigid conjugated macrocycles, the adjacent terminal benzene rings at the interhelicene bonds are essentially coplanar, leading to an overall Möbius band geometry of π electron systems of both macrocycles. The C_2 -symmetric isomer has the geometry of a simple (singly twisted) Möbius band, whereas the D_3 -symmetric isomer has the geometry of a triply twisted Möbius band.

Results and discussion

The Perkin condensation of bifunctional arylene-diglyoxylic acids with bifunctional arylene-diacetic acids leads with surprisingly good size-selectivities and yields to the $2 + 2$ macrocyclic products, where four arylene moieties are connected by four maleic bridges. This approach has been used in the reported synthesis¹⁸ of the four-block flexible macrocycle **4** (Scheme 2, pathway A), with a moderate yield of 21%, precursor of the cyclic dimer of [5]helicene **1** (Scheme 1). Aiming at the formation of the trimeric counterparts **2** and **3** of the latter, the synthetic strategy based on the Perkin reaction involves one common macrocyclic intermediate **5** made of six building blocks: three 1,4-phenylenediacetic acid units **6** and three 4,4'-

bis(phenylglyoxylic acid) units **7**. The formation of a six-block macrocycle by Perkin reaction from bifunctional simple building blocks has been observed only once, as a minor side product of a four-block macrocycle composed exclusively of biphenyl units.¹⁸ A stepwise procedure is therefore necessary for the controlled synthesis of large six-block macrocycles by Perkin reaction. We focused on the combination of two complimentary linear bifunctional three-block intermediates ($3 + 3$ approach), which is more convergent than a $5 + 1$ approach and synthetically simpler than a $4 + 2$ approach due to the symmetry of the precursors.

We have recently reported the synthesis of three-block linear intermediates, bearing two acetic acid functions at their extremities for the formation of long phenacenes.¹⁷ The same synthetic strategy has been applied to the diacetic and diglyoxylic building blocks **6** and **7** in the synthesis of the three-block diacetic precursor **10**. 1,4-Phenylenediacetic acid **6** was first fully esterified in presence of methanol and SOCl_2 to give dimethyl 1,4-phenylenediacetic ester,¹⁹ which was then partially saponified with one equivalent of potassium hydroxide. The resulting mixture of remaining diester, diacetate and monoacetate monoester compounds was separated by selective pH-



Scheme 3 Synthesis of the second three-block precursor **18** and its combination with complementary three-block precursor **10** to form the six-block macrocycle **5**, precursor of cyclo-tris-[5]helicenes **2** and **3**. (a) AlCl_3 , CH_2Cl_2 , -10°C , 20 min, 71%; (b) NaHCO_3 , H_2O , EtOH , reflux, 16 h, 93%; (c) Ac_2O , NEt_3 , THF, reflux, 16 h, then EtOH , EtBr , DBU, reflux, 24 h, 83%; (d) $(\text{Bpin})_2$, $\text{PdCl}_2(\text{dppf})$, KOAc , 1,4-dioxane, 90°C , 2.5 h, 87% with traces of pinacol; (e) $\text{Pd}(\text{PPh}_3)_4$, K_3PO_4 , PhMe , reflux, 20 h, 45%; (f) NaHCO_3 , H_2O , EtOH , reflux, 24 h, 100%; (g) Ac_2O , NEt_3 , THF, reflux, 72 h, then EtOH , EtBr , DBU, reflux, 24 h, 29%; (h) I_2 , AcOEt , UV-irradiation, rt, 48 h, 18% (**2**) and 18% (**3**).

dependant solid-liquid extractions to finally give pure mono-protected phenylene diacetic acid **8**. The yield of this mono-deprotection reaction is satisfying (47%) as it can be carried out on a large scale (10 g) without complicated purification and 48% of the starting compound is recovered separately as diacid or diester. Mono-protected phenylene diacetic acid **8** reacted twice with diglyoxylic acid **7** by Perkin reaction to afford the three-block hexaester **9** in good yield (65%), and then full saponification by treatment with potassium hydroxide quantitatively formed the three-block diacetic acid precursor **10**. To verify its reactivity in the formation of macrocycles, it has been combined with the diglyoxylic building block **7** (Scheme 2, pathway B) by Perkin reaction in high dilution conditions to form the four-block macrocycle **4** with an improved yield of 55%, compared to 21% when single building blocks **6** and **7** are mixed under the same reaction conditions (Scheme 2, pathway A).¹⁸

The mono-protection of arylene-diglyoxylic acids for the Perkin reaction not yet having been developed, a different synthetic approach was pursued for the complimentary three-block diglyoxylic precursor **18** (Scheme 3). In biphenyl-based species, the central sigma C-C bond can easily be formed by usual palladium-catalyzed coupling reactions between adequately functionalized aryl fragments. Thus bromobenzene **11** was first functionalized with one glyoxylic ester function by a Friedel-Crafts reaction with ethyl oxalyl chloride **12** as an electrophile in presence of AlCl_3 following a recently reported procedure.²⁰ The glyoxylic ester function of the resulting ester **13** was saponified efficiently by treatment with sodium hydrogen carbonate and the resulting *para*-brominated phenylglyoxylic acid **14** reacted then twice with 1,4-phenylenediacetic acid **6** in Perkin conditions to give the dibrominated bis-maleate precursor **15** with a very good yield (83%). In parallel, *para*-brominated phenylglyoxylic ester **13** was transformed into the corresponding boronic ester **16** by palladium-catalyzed substitution of the bromo-substituent in presence of bis(pinacolato)diboron. In spite of non-removable traces of pinacol in the latter, it was coupled twice to the dibrominated bis-maleate precursor **15** by a double Suzuki reaction with $\text{Pd}(\text{PPh}_3)_4$ as a catalyst. The resulting bis-maleate hexaester **17** was obtained with a modest yield (45%) for this usually efficient reaction, because of partial saponification of the product in basic conditions, even in the absence of water. Full saponification of the hexa-ester **17** quantitatively afforded the three-block diglyoxylic acid precursor **18**.

The two three-block diacetic **10** and diglyoxylic **18** precursors were then coupled together by double Perkin reaction to form the six-block flexible conjugated macrocycle **5**. High dilution conditions were not used, because of the low solubility of compound **18**, but the cyclic product **5** was obtained with a very satisfying macrocyclization yield of 28%, after a difficult purification process. Irradiation of a 0.07 mM solution of **5** in ethyl acetate in the presence of iodine and oxygen for two days with pyrex-filtered light from a medium pressure mercury lamp afforded a mixture of the two *cyclo*-tris-[5]helicenes **2** and **3** with an average yield of 40%. ¹H-NMR analysis of this mixture revealed that these two rigid macrocycles are present in near-equal proportions. In spite of their structural differences,

compounds **2** and **3** could not be separated by chromatography, but recrystallization of this mixture in a large amount of ethanol surprisingly afforded crystals of pure racemic C_2 -symmetric *cyclo*-tris-[5]helicene **2**, and further purification of the remaining product in the mother liquor gave pure racemic D_3 -symmetric *cyclo*-tris-[5]helicene **3**, in 18% yield each. Racemic crystals suitable for X-ray structure determination (Fig. 1) where obtained by slow diffusion of methanol into a chloroform solution in the case of **2**, and by slow diffusion of cyclohexane into a toluene solution in the case of **3**.

Whereas the dimeric homolog **1** did not show any evidence of coplanarity and thus of conjugation between the two

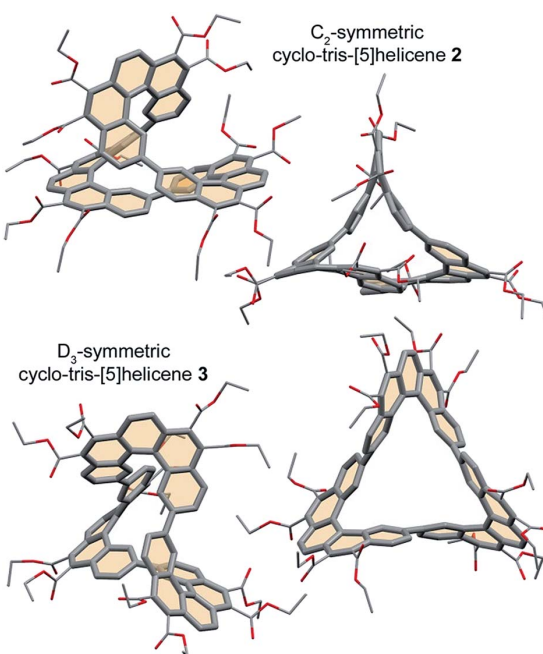


Fig. 1 Crystal structures of cyclo-tris-[5]helicenes **2** and **3** (PMM and MMM represented respectively).

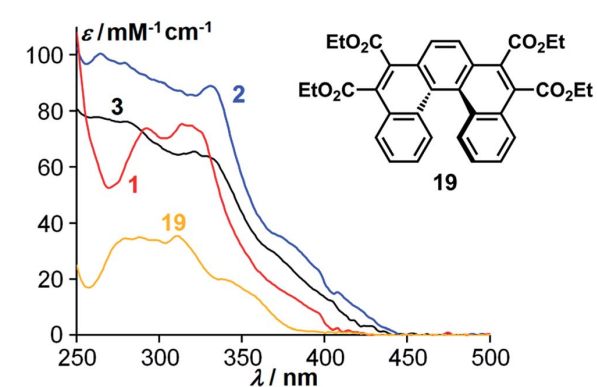


Fig. 2 Absorption spectra of a single [5]helicene tetraester **19** (yellow) and of the corresponding cyclic dimer **1** (red) and trimers **2** (blue) and **3** (black).

helicenes, the crystal structures of the trimers show that the two linked benzene rings of adjacent helicenes are almost coplanar. In these conditions, the conjugated π electron systems of these rigid macrocycles have persistent shapes of cyclic twisted ribbons.

A first evidence of the conjugation between the three helicenes composing the *cyclo*-tris-[5]helicenes **2** and **3** has been obtained from their optical absorption. The *cyclo*-bis-[5]helicene **1** was expected not to exhibit any conjugation between its two parts due to a lack of coplanarity at the junctions between helicenes. This was confirmed by the absorption spectra, where this cyclic dimer of ester-substituted [5]helicenes behaved approximately like two independent ester-substituted [5]helicenes²¹ (Fig. 2). In contrast, trimeric *cyclo*-tris-[5]helicenes **2** and **3** show a significantly modified absorption profile compared to the single [5]helicene.

For a closer inspection of the topology of **2** and **3**, we used our program ANEWWRITHM²² and determined the topological parameters L_k , T_w and W_r . Since both annulenes are not single stranded, there are different conjugation pathways that can be defined within the cyclic π system. We distinguish between the inner cyclic pathway with 24 π electrons (red line) and the outer pathway with 48 π electrons (blue line, Fig. 3). Thus, both conjugation pathways exhibit $4n \pi$ electrons. In Fig. 3 *cyclo*-tris-[5]helicenes are represented as topologically stretched 2D projections (**2'** and **3'**), as well as with their native 3D geometry (**2** and **3**). The stretched representation is easier to conceive, and it reveals that **2** is singly twisted and **3** is triply twisted. *Cyclo*-helicene **2** is composed of two helicene units of like helicity, and one unit with opposite helicity. In terms of the stretched representation, the opposite twists cancel, and a singly twisted Möbius ribbon results. The helicities of the three helicene units

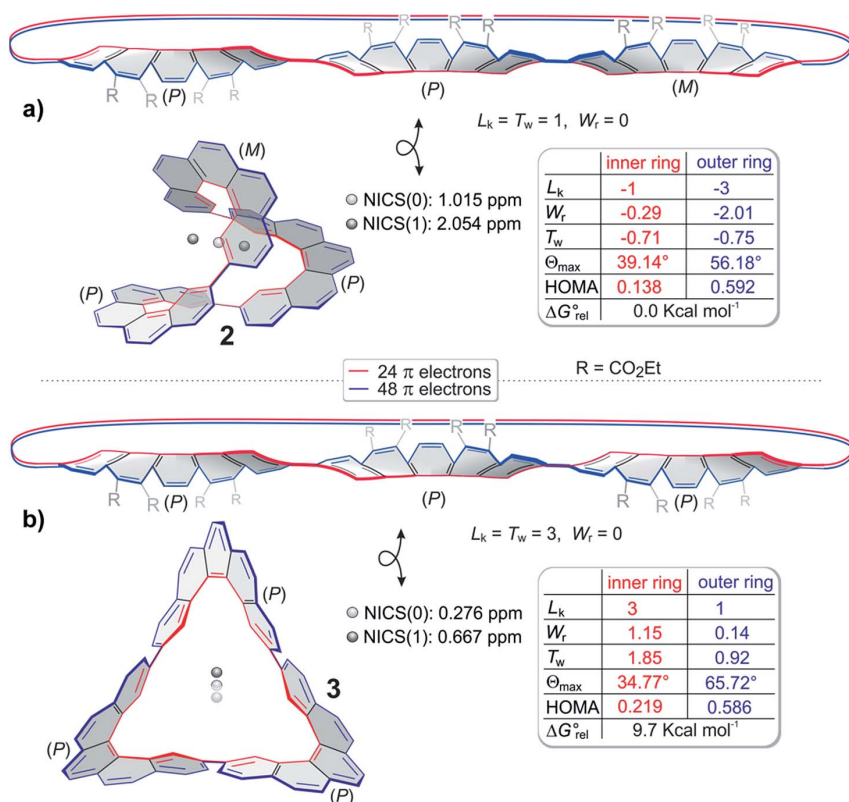


Fig. 3 Topologies and aromaticity parameters of *cyclo*-tris-[5]helicenes **2** and **3**. Geometries are optimized at the B3LYP/6-31G* level of density functional theory. The ester substituents are omitted for clarity. The topological parameters L_k , W_r and T_w are calculated with the program ANEWWRITHM.²² The looped double headed arrows define that both objects are topologically equivalent (homeomorphic). (a) top and (b) top: *cyclo*-tris-helicene **2** and **3** in topological stretched, writhe-free ($W_r = 0$) representations. In these forms the linking numbers L_k equal the twists T_w . (a) bottom and (b) bottom: 3D structures of **2** and **3**. In these "relaxed" structures a considerable part of the twist T_w is projected into writhe W_r . The topological parameters are given for the inner (red) and the outer conjugation path (blue). θ_{\max} is the largest dihedral angle between neighboring carbon atoms, and thus is a measure of the conjugation. Note that enantiomers have the same topological parameters, albeit with opposite algebraic sign, and inner and outer periphery exhibit different linking numbers L_k . E_{rel} are the relative energies of **2** and **3** at the B3LYP/6-31G* level of DFT. NICS values are calculated at the B3LYP/6-31G* level of DFT using the GIAO method.²³ NICS(0) was calculated at the center of gravity of molecules **2** and **3**. NICS(1) was calculated in a distance of 1 Å on an axis dissecting the center of gravity. In structure **3** the axis is identical to the C_2 axis, and in **2** the axis is orthogonal to the largest enclosed area obtained by all conceivable 2D projections (relative orientation of the molecule and the magnetic field leading to the largest ring current). HOMA values were calculated for the inner and outer periphery according to the published method.²⁴

in 3 are equal, and the twists add up to a triply twisted Möbius band. Note that the term “twist” has different meanings in the general English language and in topology. In the following we use the topological twist (as defined in the Calugeanou theorem: $L_k = T_w + W_r$) in combination with the symbol T_w . The topologically stretched geometries would be highly strained, and exhibit reduced overlap between neighbouring p orbitals. In the native geometry large part of the twist T_w is projected into writhe W_r by folding into a 3D geometry (Fig. 3). This topological transformation is obviously more efficient in 3 than in 2. Surprisingly, the triply twisted 3 is 5.8 kcal mol⁻¹ more stable than its singly twisted isomer 2. However, if dispersion is included (D3 method, see ESI†) the relative energies are reverse. Obviously, singly twisted 2 is more densely packed which leads to stabilization by an increased intramolecular dispersion interaction. The inner (red) and outer (blue) conjugation pathways in both *cyclo-tris-[5]helicenes* 2 and 3 exhibit odd linking numbers L_k (Möbius topology) however, they have different linking numbers L_k in the same molecule (Fig. 3).

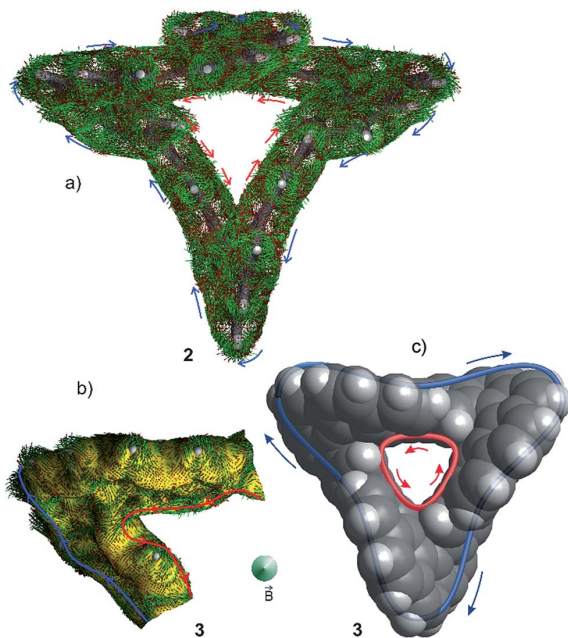


Fig. 4 Ring currents in cyclo-tris[5]helicene 2 and 3. The structures were optimized at the B3LYP/6-31G* level of density functional theory and the current density was determined with the CSGT method. The anisotropy of the induced current density was calculated using the ACID program at an isosurface value of 0.032. Current density vectors are plotted onto the ACID surface. The lengths of the green vectors with red arrowheads represent the current strengths. The magnetic field vector \mathbf{B} (large green arrowhead) points towards the viewer. (a) Current density vectors on the ACID surface of 2. The ACID hypersurface is removed for clarity. Bold blue arrows indicate the diamagnetic and red arrows the paramagnetic current flow. (b) ACID plot including current density vectors of a section of 3. The bold lines represent the general direction of the ring currents in the inner (red) and outer (blue) periphery. (c) Schematic view of the outer (diatropic) and inner (paratropic) current, plotted onto the van der Waals surface of 3.

Since the conjugation pathways in 2 and 3 include $4n$ electrons, and exhibit odd linking numbers L_k , they should be Möbius aromatic. ACID (anisotropy of the induced current density)^{25–27} calculations reveal that the situation is more complicated. Similar to the paragon of aromatic compounds benzene, Möbius compound 3 exhibits a diatropic ring current in the outer π system, and a paratropic current in the inner σ system.^{26,28} In 3 these currents cancel, and almost no net ring current results (Fig. 4).²⁹ In benzene the paratropic current is located within the ring plane, and there are two maximum diatropic ring currents approximately 1 Å above and underneath the ring plane (along the two paths with the highest π electron density).^{30,31} In the triply twisted Möbius molecule 3, however, the current follows a path mainly restricted to outer part of the molecule, changing the side of the π system three times.³² As a consequence of the inner paratropic ring current in the σ system, the six inner protons (8.88 ppm) are deshielded by 0.58 ppm as compared to the corresponding two protons in the [5]helicene building block 19. The diatropic ring current in the outer periphery (blue) does not induce a strong shift of the remaining 18 protons, because they are not located in the range of the induced magnetic field. Similar arguments hold for the singly twisted Möbius compound 2. There is a diatropic ring current in the periphery and a paratropic current in the σ system in the inner conjugation path (Fig. 3). NICS values³³ calculated for Möbius structures 2 and 3 are close to zero (Fig. 3) and corroborate the fact that diatropic and paratropic ring currents almost cancel. Also in agreement with our ACID analysis are the bond length analyses of 2 and 3 using the HOMA method.²⁴ For both Möbius compounds, the HOMA values are considerably larger in the periphery (diatropic, aromatic) than in the inner conjugation path (paratropic, antiaromatic) (see Fig. 3a and b). The C–C bonds connecting the [5]helicene units in 2 and 3 exhibit a bond length of 1.48–1.49 Å which is considerably longer than the bond length in the prototypic aromatic molecule benzene (~1.40 Å). Upon distortion of D_{6h} benzene towards a D_{3h} 1,3,5-hexatriene structure with alternating C–C bond lengths of 1.553 Å and 1.337 Å, benzene retains 72% of its diatropic ring current.³³ We conclude that a corresponding bond length elongation by 0.01 Å in 2 and 3 does not significantly reduce the ring currents.

Conclusions

Highly twisted annulenes have been considered as very challenging targets because of the severe strain and weak π overlap induced by the twist. In contrast to this intuitive conclusion, we prove that even a triple twisted Möbius annulene with a 540° twist in its π system, is easily accessible by standard chemical synthesis. Within the inner and the outer conjugation path of the triply twisted system, no torsional angle between neighbouring p orbitals is larger than 35° and 66°. So, conjugation is still efficient. All conjugation pathways include $4n$ electrons and an odd linking number L_k . Hence, they should be Möbius aromatic. A detailed ring current analysis reveals that a paratropic current is induced in the inner σ system, and a diatropic current in the outer π periphery, which almost cancel. The

surprisingly low strain and considerable π overlap is due to a topological transformation of twist into writhe by folding of the Möbius ring into a 3D structure, a process which is similar to the supercoiling of DNA.³⁴ Annulenes with chiral π systems are interesting from another point of view. Theoretical calculations predict that upon irradiation with a strong laser pulse (even in the absence of a magnetic field), ring currents should be induced which are orders of magnitude larger than the currents induced in a superconducting NMR magnet.^{35,36} Moreover, peculiar nonlinear optical³⁷ and two photon absorption properties³⁸ have been predicted for Möbius annulenes.

Conflicts of interest

There are no conflicts to declare.

Acknowledgements

Funding by the Agence Nationale de la Recherche (13-JS07-0009-01) and the German Research Foundation (SFB677) are gratefully acknowledged.

Notes and references

- 1 E. Hückel, *Z. Phys.*, 1931, **70**, 204–286.
- 2 E. Hückel, *Z. Phys.*, 1932, **76**, 628–648.
- 3 E. Heilbronner and E. Hückel, *Tetrahedron Lett.*, 1964, **29**, 1923–1928.
- 4 D. Ajami, O. Oeckler, A. Simon and R. Herges, *Nature*, 2003, **426**, 819–821.
- 5 D. Ajami, K. Hess, F. Köhler, C. Näther, O. Oeckler, A. Simon, C. Yamamoto, Y. Okamoto and R. Herges, *Chem.-Eur. J.*, 2006, **12**, 5434–5445.
- 6 R. Herges, *Chem. Rev.*, 2006, **106**, 4820–4842.
- 7 T. Tanaka and A. Osuka, *Chem. Rev.*, 2017, **117**, 2584–2640.
- 8 G. R. Schaller, F. Topić, K. Rissanen, Y. Okamoto, J. Shen and R. Herges, *Nat. Chem.*, 2014, **6**, 608–613.
- 9 S. M. Rappaport and H. S. Rzepa, *J. Am. Chem. Soc.*, 2007, **130**, 7613–7619.
- 10 P. W. Fowler and H. S. Rzepa, *Phys. Chem. Chem. Phys.*, 2006, **8**, 1775–1777.
- 11 G. Calugareanu, *Czech. Math. J.*, 1961, **11**, 588–625.
- 12 P. Sarkar, F. Durola and H. Bock, *Chem. Commun.*, 2013, **49**, 7552–7554.
- 13 T. S. Moreira, M. Ferreira, A. Dall'armellina, R. Cristiano, H. Gallardo, E. A. Hillard, H. Bock and F. Durola, *Eur. J. Org. Chem.*, 2017, 4548–4551.
- 14 H. Bock, S. Huet, P. Dechambenoit, E. A. Hillard and F. Durola, *Eur. J. Org. Chem.*, 2015, 1033–1039.
- 15 M. Ferreira, G. Naulet, H. Gallardo, P. Dechambenoit, H. Bock and F. Durola, *Angew. Chem., Int. Ed.*, 2017, **56**, 3379–3382.
- 16 A. Robert, P. Dechambenoit, H. Bock and F. Durola, *Can. J. Chem.*, 2017, **95**, 450–453.
- 17 G. Naulet, A. Robert, P. Dechambenoit, H. Bock and F. Durola, *Eur. J. Org. Chem.*, 2018, 619–626.
- 18 A. Robert, P. Dechambenoit, E. A. Hillard, H. Bock and F. Durola, *Chem. Commun.*, 2017, **53**, 11540–11543.
- 19 M. Neeb, C. Hohn, F. R. Ehrmann, A. Härtsch, A. Heine, F. Diederich and G. Klebe, *Bioorg. Med. Chem.*, 2016, **24**, 4900–4910.
- 20 M. Sasikumar, D. Bharath, G. S. Kumar, N. R. Chereddy, S. Chithiravel, K. Krishnamoorthy, B. Shanigaram, K. Bhanuprakash and V. J. Rao, *Synth. Met.*, 2016, **220**, 236–246.
- 21 M. G. Belarmino Cabral, D. Pereira de Oliveira Santos, R. Cristiano, H. Gallardo, A. Bentaleb, E. A. Hillard, F. Durola and H. Bock, *ChemPlusChem*, 2017, **82**, 342–346.
- 22 F. Köhler, Dissertation, University of Kiel, 2008The algorithm is based on a method developed by K. Klenin and J. Langowski, *Biopolymers*, 2000, **54**, 307–317.
- 23 Z. Chen, C. S. Wannere, C. Corminboeuf, R. Puchta and P. v. R. Schleyer, *Chem. Rev.*, 2005, **105**, 3842–3888.
- 24 T. M. Krygowski and M. K. Cyrański, *Chem. Rev.*, 2001, **101**, 1385–1420.
- 25 R. Herges and D. Geuenich, *J. Phys. Chem. A*, 2001, **105**, 3214–3220.
- 26 D. Geuenich, K. Hess, F. Köhler and R. Herges, *Chem. Rev.*, 2005, **105**, 3758–3772.
- 27 R. Herges, Magnetic Properties of aromatic compounds and aromatic transition states, in *The Chemical Bond : Chemical Bonding Across the Periodic Table*, ed. G. Frenking and S. Shaik, Wiley-VCH-Verlag, 2014.
- 28 E. Steiner and P. W. Fowler, *Int. J. Quantum Chem.*, 1995, **60**, 609–616.
- 29 A partial cancelling of the paratropic and diatropic ring current is also observed in benzene, explaining the rather small downfield shift of the protons in benzene as compared to hexatriene: S. Pelloni, A. Ligabue and P. Lazzaretti, *Org. Lett.*, 2004, **6**, 4451–4454.
- 30 J. S. Waugh and R. W. Fessenden, *J. Am. Chem. Soc.*, 1957, **79**, 846–849.
- 31 C. E. Johnson and F. A. Bovey, *J. Chem. Phys.*, 1958, **29**, 1012–1014.
- 32 Note that the ring currents don't exhibit a topology because they are not bands with two edges.
- 33 D. E. Bean and P. W. Fowler, *J. Phys. Chem. A*, 2011, **115**, 13649–13656.
- 34 O. M. J. Lilley, *Biochem. Soc. Trans.*, 1986, **14**, 489–493.
- 35 I. Barth, J. Manz, Y. Shigeta and K. Yagi, *J. Am. Chem. Soc.*, 2006, **128**, 7043–7049.
- 36 H. Mineo and Y. Fujimura, *J. Phys. Chem. Lett.*, 2017, **8**, 2019–2025.
- 37 Z. S. Yoon, J. H. Kwon, M.-C. Yoon, M. K. Koh, S. B. Noh, J. L. Sessler, J. T. Lee, D. Seidel, A. Aguilar, S. Shimizu, M. Suzuki, A. Osuka and D. Kim, *J. Am. Chem. Soc.*, 2006, **128**, 14128–14134.
- 38 V. Kundu, M. M. Alam and P. P. Thankachan, *Phys. Chem. Chem. Phys.*, 2015, **17**, 6827–6833.

5.5 Erweiterte π -Systeme

Konjugierte Oligomere und allgemein Konzepte erweiterter π -Systeme sind schon lange und nicht nur für die Polymerchemie von außerordentlich großem Interesse.^[250–256] Einen großen Einfluss in diesem Bereich haben Polyphenylene. Sie sind leicht zugänglich und bieten komplexe definierte Strukturen für verschiedenste nanostrukturelle Anwendungen.^[257,258] So wird z.B. derivatisiertes Hexaphenylbenzol (HPB) für photochemische und chemische Schalter,^[259] molekulare Rezeptoren,^[260] Flüssigkristalle (LCs),^[261] in Licht emittierenden Dioden (LEDs)^[262–266] und sogar in molekularen Maschinen eingesetzt.^[267,268]

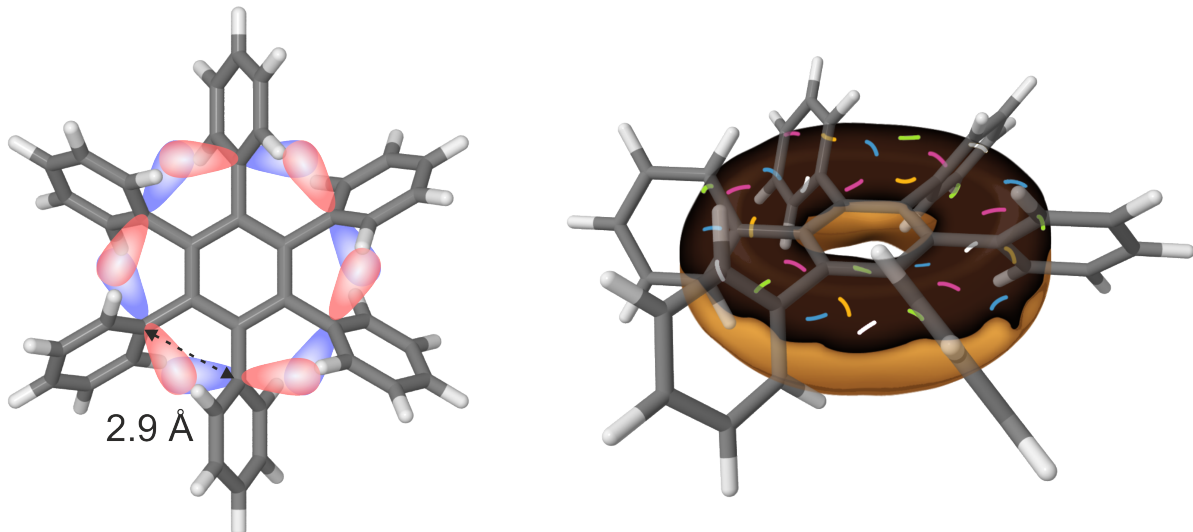


Abb. 5.5: Links: Überlappung der p_z -Orbitale der *ipso*-Kohlenstoffe mit unterschrittenem vdW-Radius; Rechts: Perspektivische Versinnbildlichung der toroidalen Delokalisierung der π -Elektronen durch einen Donut.

Strukturanalysen des propellerartigen HPB zeigen zusätzlich, dass die *ipso*-Kohlenstoffe einen Abstand zueinander von 2.9 Å^[269] aufweisen, welcher deutlich unterhalb des vdW-Radius von 3.4 – 3.5 Å^[270,271] liegt. Die somit mögliche Überlappung der zugehörigen π -Orbitale erklärt, dass die Elektronen eines kationisch radikalischen Zustand des HPB einer toroidalen Delokalisation unterliegen.^[272–277] In Anlehnung an die HPBs wurden alternative Konzepte erweiterter π -Systeme mit Heteroarylsubstituenten (Hexaarylbenzol (HAB)) entwickelt,^[261,278,279] welche bisher jedoch wenig erforscht sind. Thiophene werden schon lange in diversen konjugierten Polymeren eingesetzt,^[280–284] und könnten dank ihrer interessanten optischen und elektrochemischen Eigenschaften^[285,286] auch auf das Konzept der toroidalen Delokalisierung überprüft werden.

5.6 Twisted Thienylene–Phenylene Structures: Through-Space Orbital Coupling in Toroidal and Catenated Topologies

T. D. Leitner, Y. Gmeinder, F. Röhricht, R. Herges, E. Mena-Osteritz und P. Bäuerle

Eur. J. Org. Chem. **2020**, 3, 285–294.

DOI:10.1002/ejoc.201901637

Supporting Information: Anhang SI 8

Wissenschaftliche Beiträge: DFT-Geometrieoptimierungen der vorgestellten Strukturen als Hilfestellung bei der Aufklärung der Einkristallstrukturanalyse, TD-DFT-Simulationen zur Definition der elektronischen Übergänge, ACID-Plots als beschreibende Methode der Konjugation durch den Raum und etwaiger Ringströme, Qualitative Analyse der Orbitalbeiträge zum Ringstrom basierend auf der Gruppentheorie, (anteilig) Verfassen des Manuskripts.

Zusammenfassung

Die Synthese und Charakterisierung von Molekülen, welche toroidale und verkettete Delokalisierung von π -Elektronen durch den Raum (through space) aufweisen, wird in dieser Publikation dargelegt. Hierfür wurden bekannte Polyphenylene und neue Polythienylene mittels Einkristallstrukturanalysen sowie theoretischen Methoden untersucht und verglichen. Diese sterisch stark anspruchsvollen Verbindungen weisen Abstände der *ipso*-Kohlenstoffe von unter 3 Å auf. Die Summe der VAN-DER-WAALS-Radii betragen 3.4 - 3.5 Å, was somit ein gutes Indiz für eine Überlappung der p_z -Orbitale ist. Dies konnten die Kristallstrukturen mit propellerartigen Geometrien auch für die neuen Thienylverbindungen bestätigen. Geometrieeoptimierungen erklärten die Unordnung, da je nach Ausrichtung der Thienylgruppen unterschiedliche, nahezu isoenergetische Konformere und somit verschiedene Packungen im Festkörper vorliegen können.

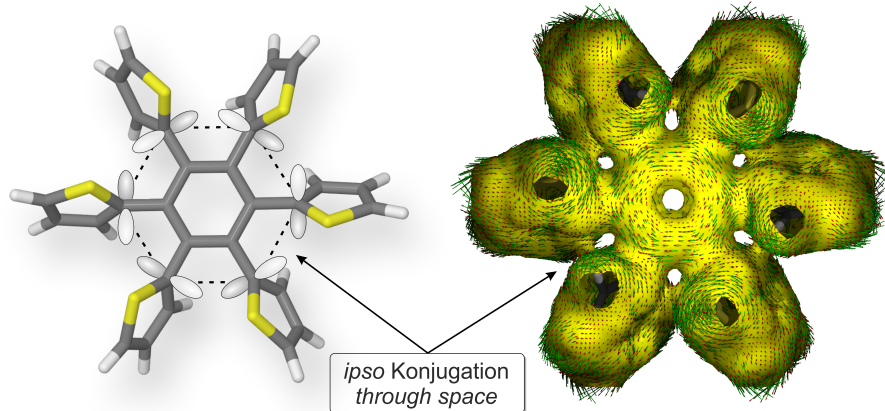


Abb. 5.6: Abbildung der toroidalen Konjugation am Beispiel von Hexathienylbenzol schematisch (links) und durch eine ACID-Analyse.

Für die Untersuchung der elektronischen Delokalisierung wurde die ACID-Methode angewandt. Wie erhofft zeigte sich eine vorhandene toroidale *through space*-Kopplung zwischen den p_z -Orbitalen der *ipso*-Kohlenstoffe sowohl bei den Polyphenylen als auch bei den Thienylanalogen. Besonders hervorzuheben ist die verkettete (Ring in Ring) Topologie der Konjugation bei den zehnfach substituierten Biphenylen. Nähtere Untersuchung der sechsfach substituierten Benzole zeigte jedoch keine Ringströme entlang der Konjugationstopologie. Eine qualitative Orbitalanalyse erklärte dies: der diatropen Ringstrom aller *ipso*-Kohlenstoffe wird durch sechs lokale paratropen Ströme zwischen dem zentralem Benzolring und den *ipso*-Kohlenstoffen ausgelöscht. Exakt dies konnte auch durch eine gruppentheoretische Betrachtung der Orbitalsymmetrie untermauert werden. Nach Störungstheorie erster Ordnung durch ein Magnetfeld geben die irreduziblen Darstellungen der ersten zehn $HOMO_n \rightarrow LUMO$ Übergänge nahezu gleichviel Anlass für paratropen sowie diatropen Ringströme.

Extended π -Systems | Very Important Paper |

Twisted Thienylene–Phenylene Structures: Through-Space Orbital Coupling in Toroidal and Catenated Topologies

Tanja D. Leitner,^[a] Yannick Gmeinder,^[a] Fynn Röhricht,^[b] Rainer Herges,^[b] Elena Mena-Osteritz,^[a] and Peter Bäuerle^{*[a]}

Abstract: Sterically crowded and twisted thienylene-phenylenes were synthesized and characterized in comparison to corresponding polyphenylene nanostructures. Spectroscopic, dif-

fraction, and theoretical studies gave evidence of through-space delocalization of π -electrons of peripheral (hetero)aromatic rings in toroidal and catenated topologies.

Introduction

Since many years, the synthesis of polyphenylene nanostructures has attracted great attention due to the improved accessibility of highly complicated distinct structures.^[1] Popular representatives of this class of compounds are hexaphenylbenzenes (HPB), that are strong candidates for application as photochemical and chemical switches,^[2] redox materials,^[3,4] liquid crystalline materials^[5], molecular receptors^[6] as well as in organic light-emitting diodes^[7,8] or molecular machines.^[9,10] Related hexathiénylbenzenes (HTB) are also known in literature.^[5,11] Although conjugated oligomers based on thiophenes show exceptional optical and electrochemical properties,^[12] compared to HPBs HTBs were much less investigated. HPB is known to show a propeller-shaped geometry due to six peripheral aromatic rings.^[13] In the radical cationic state, the affected π -electrons undergo toroidal delocalization of charge and energy, which was proven experimentally and theoretically.^[13–18] In this respect, stable radical cations of the investigated HPBs showed characteristic near-infrared charge-resonance absorption.^[19,20] Furthermore, it was found that the involved *ipso*-carbon atoms showed a distance of 2.9 Å from each other^[21] which is closer than the combined calculated van der Waals radii of 3.4–3.5 Å.^[22] Therefore, this finding indicates an overlap of the respective π -orbitals of the *ipso*-C atoms that can lead to toroidal delocalization^[17] as Akita et al. also showed for thiophene-containing hexaarylbenzenes (HAB).^[23]

Herein, we now present synthesis and characterization of deca(2-thienyl)biphenyl **1** and comparison to decaphenylbiphenyl **4**, which was already synthesized by Becker et al. in 1965 and can be seen as an evident expansion of the HAB system.^[24] Nevertheless, it took quite a long time until the structure of **4** was fully elucidated by Pascal et al.^[25] Ethynyl intermediates **2** and **5**^[26,27] and parent structures hexa(2-thienyl)benzene **3**^[11] and hexaphenylbenzene **6**^[1] are included in the discussion for comparison (Figure 1). Supported by single-crystal X-ray structure analysis and theoretical calculations, we found evidence of p_z -orbital overlapping opening the possibility of toroidal through-space conjugation of π -electrons in these compounds. Particularly intriguing are the catenated and twisted topologies of this phenomenon for biphenyls **1** and **4**. Toroidal delocalization and stabilization have only been described for charged HABs so far.^[16]

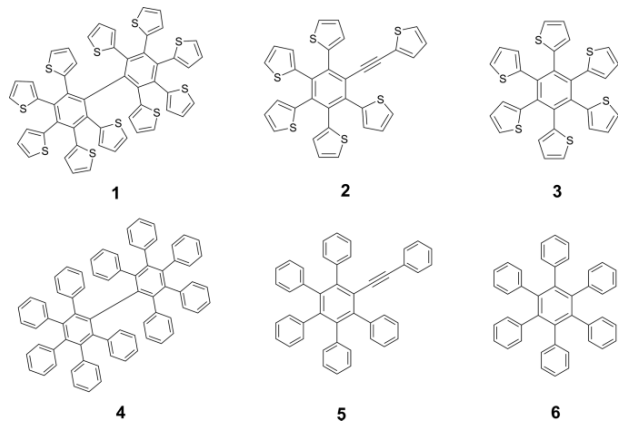


Figure 1. Sterically crowded phenylene-thienylene structures **1–3** and their phenylene counterparts **4–6** under investigation.

Results and Discussion

Synthetic Procedures

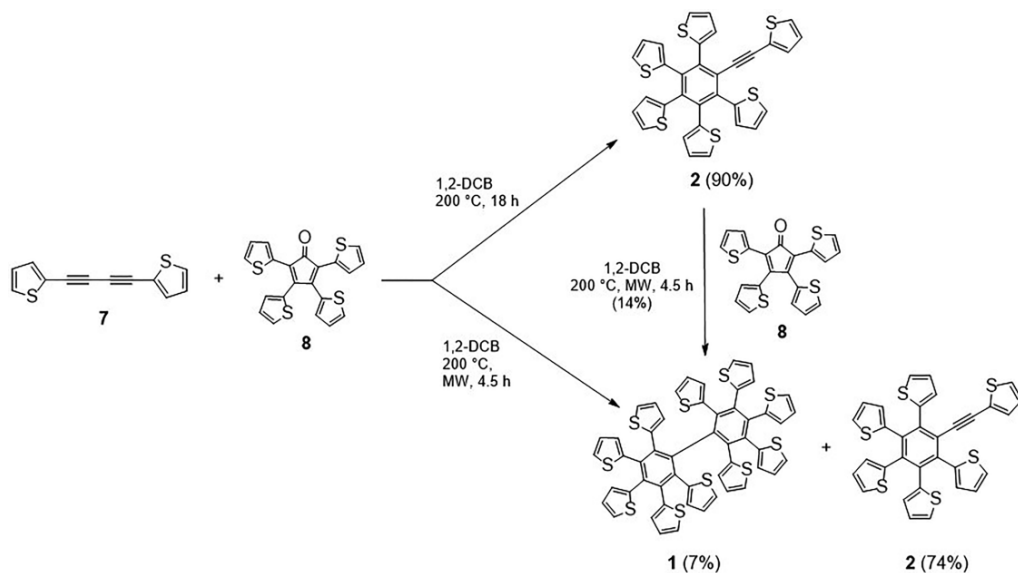
Preparation of deca(2-thienyl)biphenyl **1** is illustrated in Scheme 1. 1,4-Di(thien-2-yl)buta-1,3-diyne **7**^[28] and tetra(2-thi-

[a] Institute of Organic Chemistry II and Advanced Materials, University of Ulm, Albert-Einstein-Allee 11, 89081 Ulm, Germany
E-mail: peter.baeruerle@uni-ulm.de
<https://www.uni-ulm.de/navi/navi-oc2/>

[b] Otto Diels-Institute of Organic Chemistry, Christian-Albrechts University Kiel, Otto-Hahn-Platz 4, 24098 Kiel, Germany
E-mail: rherges@oc.uni-kiel.de
http://scholle.oc.uni-kiel.de/herges/pages_de

Supporting information and ORCID(s) from the author(s) for this article are available on the WWW under <https://doi.org/10.1002/ejoc.201901637>.

© 2019 The Authors. Published by Wiley-VCH Verlag GmbH & Co. KGaA. This is an open access article under the terms of the Creative Commons Attribution License, which permits use, distribution and reproduction in any medium, provided the original work is properly cited.

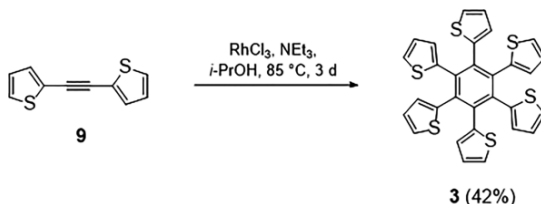


Scheme 1. Synthesis of thiylene-phenylenes **1** and **2**.

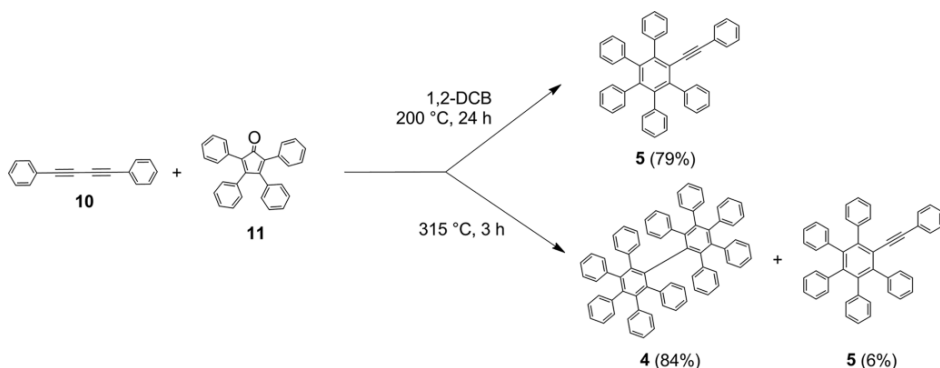
enylycyclopentadienone **8**^[29] were synthesized following modified literature procedures. Diels-Alder cycloaddition of butadiyne **7** and 2.5 equivalents of cyclopentadienone **8** in the microwave at 200 °C gave desired deca(2-thienyl)biphenyl **1** in 7 % yield accompanied with ethynylene derivative **2** as intermediate of the reaction and product of a single Diels-Alder cycloaddition (74 % yield). Both products were isolated by column and high-pressure liquid chromatography (HPLC). Because cyclopentadienone **8** decomposes above 200 °C, no higher temperature could be applied for the conversion. After reducing the excess of cyclopentadienone **8** from 2.5 to 1.5 equivalents, ethynylene derivative **2** was isolated in 90 % yield. This intentionally synthesized intermediate was subsequently converted into deca(2-thienyl)biphenyl **1** in 14 % yield by performing a separate second Diels-Alder cycloaddition with cyclopentadienone **8**.

Synthesis of basic hexa(2-thienyl)benzene **3** was achieved in 42 % yield by RhCl₃-catalyzed cyclotrimerization of di(2-thienyl)ethynylene **9** in a modified literature procedure

(Scheme 2).^[11] Phenylene derivative decaphenyl/biphenyl **4** was synthesized in 84 % yield through twofold Diels-Alder cycloaddition reaction of 1,4-diphenylbuta-1,3-diyne **10** and tetracyclone **11** at 315 °C in the melt and therefore is the main product of the reaction.^[24] Ethynylene derivative **5** was synthesized in 79 % yield in a single Diels-Alder cycloaddition of diyne **10** and tetracyclone **11** at 200 °C in 1,2-dichlorobenzene (Scheme 3).^[26,27] Hexaphenyl/benzene **6** was synthesized from tolane according to a modified literature procedure.^[30]



Scheme 2. Synthesis of basic hexa(2-thienyl)benzene **3**.



Scheme 3. Synthesis of phenylene derivatives **4** and **5**.

Structural Characterization of Derivatives 1–6 by NMR and High-Resolution Mass Spectra

Interestingly, all six derivatives **1–6** showed up-field shifted signals in ^1H -NMR spectra at room temperature (Supporting information, SI, Figure S1–S7). This behaviour was most pronounced for deca(2-thienyl)biphenyl **1**, for which one set of signals belonging to protons in 3-position of thiophenes (integral of four) appeared at $\delta = 6.25$ ppm and therefore showed the largest up-field shift in the series (Figure S1). At 230 K this signal was furthermore shifted to $\delta = 6.0$ ppm (Figure S2). This shielding effect is induced by aromatic ring current^[31] arising from a preferred conformation, in which the protons in 3-position of the inner four thiophenes are lying above and beneath the centre of the two nearly perpendicularly arranged phenylene rings (Figure 2). The structures of **1–6** were further confirmed by high-resolution mass spectra (HRMS, Figure S8–S13).

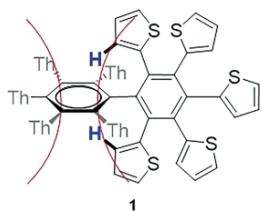


Figure 2. Protons in 3-position of inner thiophenes (blue) of deca(2-thienyl)biphenyl **1** deshielded by the aromatic ring current of the adjacent phenylene unit.

Structural Characterization of Thiophene-Based Derivatives 1–3 by X-ray Structure Analysis and Evidence for Toroidal Non-Covalent p_z -Orbital Overlapping

The molecular structures of the novel thienylene-phenylene derivatives **1–3** were investigated by single-crystal X-ray structure analysis and compared to structures of the phenyl derivatives **4**,^[25] **5**,^[27] and **6**^[32] which are literature known. The interesting question was if the exchange of the propeller-like arranged peripheral phenyl substituents in **4–6** by thiophenes in **1–3** would result in different geometric constraints.

Single crystals of hexa(2-thienyl)benzene **3** were obtained by slow diffusion of *n*-hexane into a solution of **3** in dichloromethane. The molecules crystallize in the *Pna*2₁ space group with four molecules in the unit cell (Table S1, Figure 3d). Three of the thiophene rings in the molecule showed orientational disorder causing two conformers: in the first one at 52 % probability all thiophenes point into the same direction (Figure 3a, c), whereas in the second one at 48 % probability, we observe an alternating up and down orientation of the thiophenes related to the plane of the benzene ring (Figure 3b).

The bond lengths in the central benzene ring vary between 1.402–1.412 Å and the bond lengths between the benzenoid carbons and the *ipso*-Cs of the thiophenes range from 1.474–1.493 Å. Nevertheless, the torsion angles between the central benzene and the thiophene rings showed values between 51.4(7) and 75.8(4) degrees allowing for some interaction between them (*vide infra*). Hexa(2-thienyl)benzene **3** showed the

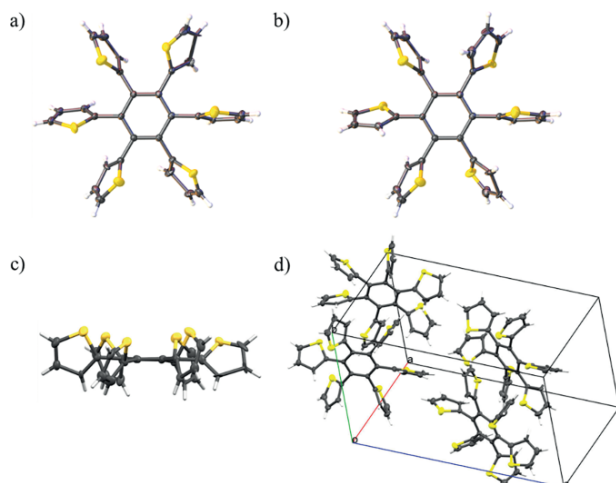


Figure 3. Molecular structure of hexa(2-thienyl)benzene **3**: front view (a) and side view (c) of the conformer with all thiophenes pointing into the same direction. Front view (b) of the conformer with alternating up and down orientation of the thiophenes. (d) Unit cell with four molecules. Ellipsoids were depicted in all cases.

lowest deviation in the values of short contacts between the *ipso*-Cs with values between 2.869(5)–2.918(5) Å. This might be due to the highest symmetry of this molecule in the series of **1–3**. Moreover, intramolecular short contacts occur between C-C, C-S, and S-S atoms at distances between 3.148–3.552 Å. Due to the propeller-like conformation of the thiophenes, the p_z -orbitals of their *ipso*-C atoms are almost aligned pointing to each other and forming a toroid. The short distances between the *ipso*-C atoms (< 3 Å) are of relevance because coupling between the p_z -orbitals should be present at these distances and electron delocalization in this toroid seems to occur (*vide infra*).

The packing mode of the molecules revealed quasi-herringbone intermolecular interactions between the thiophene π -system and α -H atoms of thiophenes in adjacent molecules (cyan-dotted lines in Figure 4a, c). In the perpendicular direction, the molecules organize in stacked columns showing short contacts between S- and H-atoms. Some S- π interactions at distances of 3.517 and 3.580 Å can be found as well (labelled by orange and

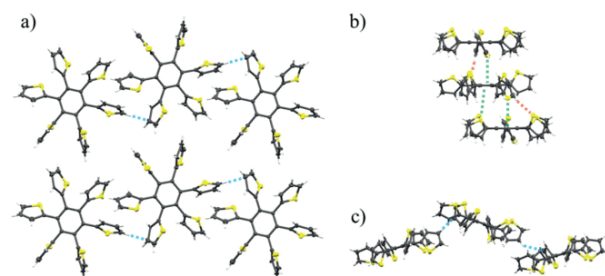


Figure 4. Packing mode of hexa(2-thienyl)benzene **3** perpendicular (a), parallel (b), and (c) in the [5 0 3] plane. Contacts between atoms at distances below van der Waals radii are labelled by dotted lines (cyan, orange, and green lines corresponding to H-C, H-S, and S- π contacts, respectively). Ellipsoids were depicted in all cases.

green-dotted lines, respectively, in Figure 4b). In phenylated counterpart HPB **6**, the peripheral phenyl rings are tilted by 75° or 79° in average,^[32] a value, which is substantially higher than that in thiienyl-substituted derivative **3** (ca. 65°, *vide supra*).

Single crystals of (2-thienyl)ethynylbenzene **2** were obtained by slow evaporation from a dichloromethane (DCM) solution. Ethynylene **2** crystallizes in the triclinic space group $P\bar{1}$ with two molecules in the unit cell (Table S2, Figure 5c). The thiophene ring located in the *para*-position to the ethynyl substituent showed orientational disorder causing two conformers. The prevailing conformer with 67 % probability is depicted in Figure 5. The bond lengths in the central benzene ring vary between 1.404–1.411 Å and those between the benzenoid Cs and the *ipso*-Cs of the thiophene rings range from 1.476(4)–1.484(4) Å. Related to the central benzene unit, the torsion angles of the thiophene rings showed values between 67.0(5)° and 70.0(4)°. The separated thiophene attached at the ethynyl-bridge is distorted by 46.4° from the benzene plane. *Intramolecular* short contacts of 2.831(4)–2.924(3) Å have been found between the *ipso*-Cs indicating p_z -orbital overlapping as in the case of HTB **3**. As well several *intramolecular* C-C and C-S interactions have been found at distances between 3.21–3.39 Å.

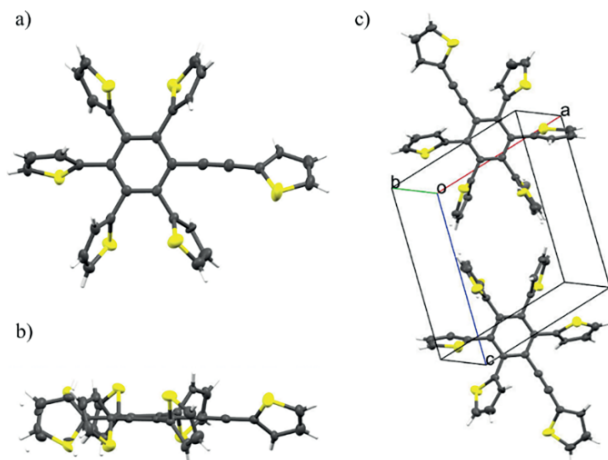


Figure 5. Molecular structure of (2-thienyl)ethynylbenzene **2**: front view (a), side view (b), and unit cell (c). Ellipsoids were depicted in all cases.

In the bulk, the molecules pack in dimers with an antiparallel orientation such that $\pi-\pi$ stacking between the thiienyl-ethynyl substituents have been found (pink-dotted lines in Figure 6a). Moreover, several H-C *intermolecular* interactions force the dimers to order in a plane (cyan-dotted lines in Figure 6a). In the perpendicular direction, the molecules interact through short H-C contacts with the dimers in the planes above and below (cyan-dotted lines in Figure 6b). In the case of the crystal structure of **2**, both, *intra-* and *intermolecular* interactions are relevant.

Corresponding phenylene derivative **5** as well showed two independent conformers in single-crystal X-ray structure analysis.^[27] In one conformer the central and ethynylene-linked rings are coplanar which contrasts with thiienyl derivative **2** (46°). The arrangement of the phenyl substituents in **5**, which adopt dihe-

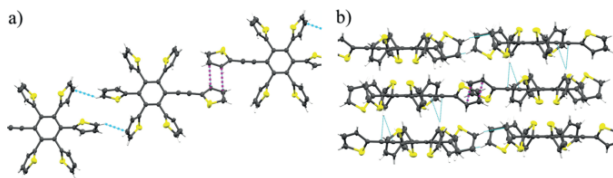


Figure 6. Packing mode of (2-thienyl)ethynylbenzene **2** perpendicular (a) and parallel (b) to plane [16 17 8]. Contacts between atoms at distances below van der Waals radii are labelled by dotted lines (cyan lines for H-C contacts, pink lines for C-C contacts, denoting $\pi-\pi$ stacking). Ellipsoids were depicted in both cases.

dral angles between 56°–70°, is quite similar to the thiophenes in **2** (67°–70°).

Single crystals of deca(2-thienyl)biphenyl **1** were obtained by slow diffusion of *n*-hexane into a solution of **1** in DCM. Crystals belong to the triclinic space group $P\bar{1}$ with two molecules in the unit cell. Eight out of ten thiophene rings in the molecule showed orientational disorder causing two conformers with almost equal probability (51 % and 49 %) (Figure 7, for clarity only one conformer is shown). The thiienyl substituents in each half of the molecule have torsion angles between 55°–85° and arrange as expected propeller-like. The torsion angle between the planes of the two benzene rings amounts to 80° (Figure 7a). The inter-ring bond length of 1.50(5) Å in the biphenyl unit of **1** is comparable to 1.501(4) Å^[25] in polyphenyl **4** and to 1.49(5) Å in non-constrained 1,1'-biphenyl.^[33] The interring bonds between the phenyl and the thiophene rings vary between 1.44(3)–1.52(1) Å and are larger than the 1.44 Å observed in non-constrained 2,5-diphenylthiophene^[34] due to the closely packed and distorted thiophene rings in **1**.

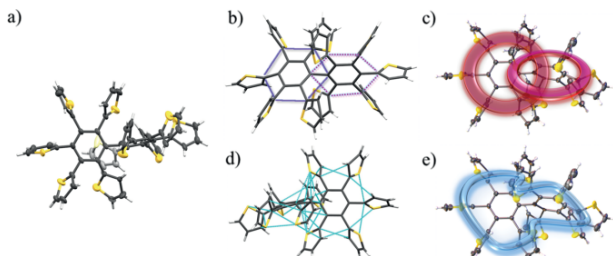


Figure 7. Molecular structure of deca(2-thienyl)biphenyl **1** with ellipsoids: (a) front view. Short contacts between the *ipso*-C atoms are labelled with magenta and purple lines in (b) and their catenated topology is sketched in (c). The remaining *intramolecular* short contacts between the *ipso*-C and S- or β -C-atoms are labelled with cyan rings in (d). Their twisted toroidal topology over all ten thiophene rings is sketched in (e).

Like in case of derivatives **2** and **3**, *intramolecular* short contacts at distances far below the sum of van der Waals radii have been found between *ipso*-Cs at 2.82(1)–3.04(1) Å (Figure 7b) and C-C and C-S short contacts between 2.897–3.545 Å (Figure 7d). The image of the interacting p_z -orbitals of the *ipso*-C atoms in **1** resembles two rings in a catenated topology (Figure 7c). Remarkably, as well $\pi-\pi$ stacking between the parallelly stacked four inner thiophene rings (numbered 1–1' and 5–5' in Figure 8a) at distances as short as 3.16(2) can be observed giving rise to a second pathway for the *intramolecular* interactions

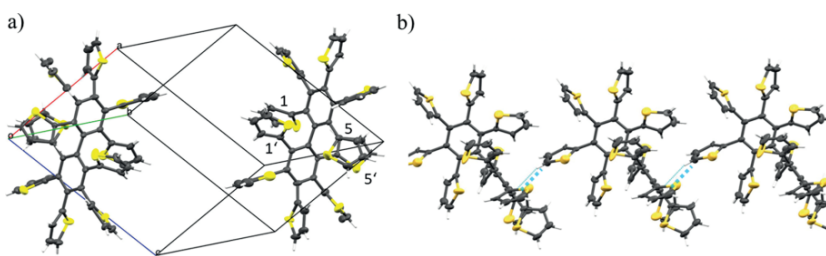


Figure 8. Unit cell of decathiényl/biphenyl **1** (a) and packing mode perpendicular to plane [010] (b). Four of the thiophene rings are labelled in a) (see text). Contacts between H-C atoms at distances below van der Waals radii are labelled by cyan-dotted lines in b). Ellipsoids were depicted in both cases.

involving all ten thiophene rings in a twisted toroidal topology (Figure 7e).

In the bulk, the molecules pack in perfectly aligned rows perpendicular to the [0 1 0] plane. Surprisingly, only one H-C *intermolecular* interaction can be found between molecules in these rows (cyan-dotted lines in Figure 8b) opposite to the numerous *intramolecular* short contacts (*vide supra*). The lack of significant *intermolecular* interactions in the crystal structure analysis of **1** indicates that the *intramolecular* short contacts are structurally inherent of biphenyl **1** lacking relevant influence from packing effects. The *intramolecular* interactions found for biphenyl **1** apparently contribute to their molecular stabilization energy.

The structural characterization of thiophene-based derivatives **1–3** by analysis of *intramolecular* non-bonding interactions of adjacent *ipso*-carbons, which were substantially shorter than the sum of the van der Waals radii, showed evidence for continuous overlap of the respective tilted p_z -orbitals of the *ipso*-Cs in a toroidal topology. This phenomenon is as well reflected in the corresponding occupied MOs (Figure 9) and was already discussed by Rathore et al. from X-ray structure analysis of HPB **6**.^[20] Comparison of the torsion angle and bond lengths of the central biphenyl unit in derivatives **1** and **4** revealed an orthogonal arrangement and thereby a larger distortion for decaphenylbiphenyl **4** (90°) than for deca(2-thienyl)biphenyl **1** (77°) whereas the bond lengths are practically not affected.

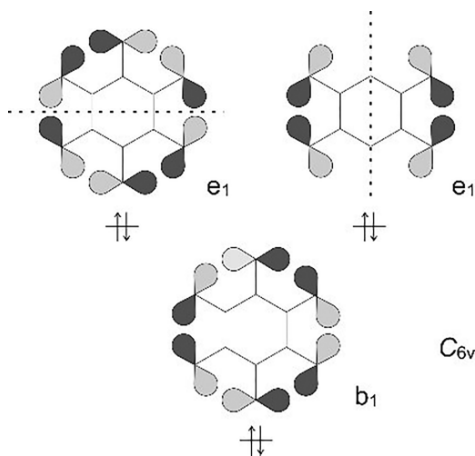


Figure 9. Schematic representation of the three occupied MOs that result from in-plane overlap of the p_z -orbitals of the *ipso* C atoms.

Theoretical Calculations on Structures **1**, **3**, **4** and **6**. Geometry Optimizations, Energies, and Evidence for Toroidal Through-Space Conjugation

Quantum chemical calculations were performed on sterically crowded thienylene-based structures **1** and **3** and compared to their polyphenylene counterparts **4** and **6**. Because of disorder in the crystal structures, the orientations of the thiophene rings in structures **1–3** are not unambiguous. Geometry optimizations at the M062X-D3/def2TZVP level of density functional theory (DFT) revealed that the two conformers of hexa(2-thienyl)benzene **3**, in which either all sulfur atoms point towards the same direction or they point up and down in an alternating sequence are almost isoenergetic ($\Delta E = 0.11 \text{ kcal mol}^{-1}$, Figure 10).

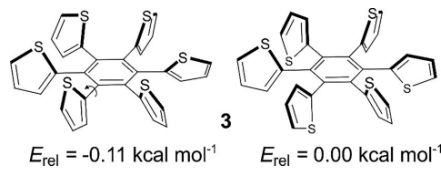


Figure 10. Symmetrical conformers of hexa(2-thienyl)benzene **3**. All sulfur atoms pointing in one direction (left) or the sulfur atoms point up and down in alternating sequence (right).

The two symmetrical conformers are indeed obtained in crystal structure analysis, although other less symmetrical conformers are conceivable. According to our calculations (geometry optimizations of all possible structures at the M062X-D3/def2T-ZVP level of DFT), corresponding energy differences in deca(2-thienyl)biphenyl **1** and decaphenylbiphenyl **4** are somewhat larger but still in the range of solid-state packing effects.

For investigation of electron delocalization, our ACID (Anisotropy of the Induced Current Density) method was employed.^[35,36] The ACID scalar field is interpreted as the density of delocalized electrons and can be plotted as isosurface (yellow surface in Figure 11). For the sake of simplicity and to save computer time, the conformations with the highest symmetry of derivatives **1**, **3**, **4**, and **6** were analyzed. As expected, the ACID plots of derivatives **3** and **6** exhibited strong π -electron delocalization in each phenyl or thienylene ring and a diatropic ring current in the central benzene ring. Furthermore, a noticeably, although subtle, through-space conjugation between the *ipso*-Cs of the outer rings (Figure 11) was found, which theoretically confirms the toroidal delocalization proposed in the literature.^[13–18]

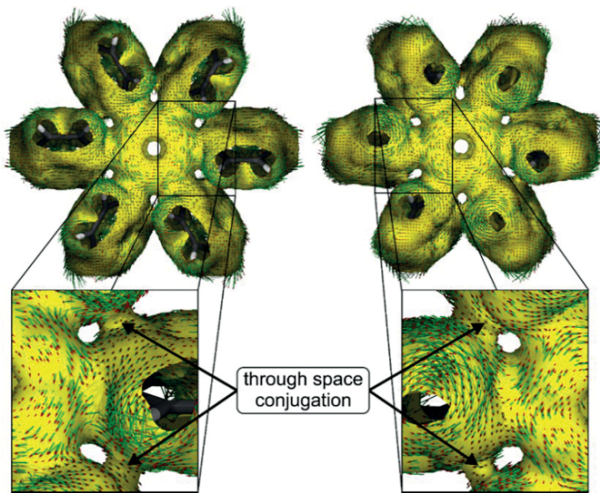


Figure 11. ACID plots of hexa(2-thienyl)benzene **3** (left) and hexaphenylbenzene **6** (right) at isosurface values of IV=0.008. The magnetic field is orthogonal to the central benzene ring. The current density is plotted as green arrows with red arrowheads on top of the ACID isosurface. The length of the arrows is proportional to the current. The wave function was calculated at the B3LYP/6-311G**-level of density theory and the current density tensor field was computed with the option IOp (10/93=1) implemented in the Gaussian program. The *ipso* through-space conjugation is clearly visible (see enlargement). However, there is no diatropic current following the *ipso* conjugation pathway.

Notwithstanding the clearly visible toroidal through-space *ipso*-conjugation, there is no ring current induced along the *ipso*-Cs in the outer periphery (Figure 11). A simple qualitative orbital consideration, however, predicts that the *ipso* p_z-orbitals of each phenyl substituent should form the basis of a six-electron, in-plane aromatic π-system (Figure 9). Hence, a diatropic ring current should be induced in a magnetic field. Orbital-separated ACID plots based on e₁ and b₁, which include the *ipso* p_z-orbitals, confirm this picture (Figure S19; for an analogous treatment of hexaphenylbenzene **6**, see Figure S18). The diatropic ring currents in the σ-system of the benzene ring and the *ipso* through-bond conjugation induce six local paratropic currents (red circles in Figure S18 and S19). However, if the complete set of MOs is included in ACID plots these currents vanish. Obviously, there are paratropic ring currents induced by other MOs that cancel the diatropic *ipso* C-atom current.

Orbital contributions to ring currents can be qualitatively analyzed based on their symmetry. If the product of the occupied and unoccupied pair of MOs involved in the transition transforms as the same representation as the rotation around a Cartesian axis, the contribution is paratropic, if it transforms as the translation along one of the axes the contribution is diatropic.^[37,38] The contributions from HOMO-2 → LUMO and HOMO-3 → LUMO excitations are paratropic and therefore cancel the diatropic contribution of the b_{2u} → LUMO excitation. This might be the reason why the effects due to homoconjugation do not give rise to measurable effects in NMR. Therefore, we calculated ¹³C-¹³C coupling constants using the GIAO method. The resulting 1.06 Hz were well below the detection limit of about 4–5 Hz in 2D ¹³C-¹³C INADEQUATE NMR experi-

ments allowing for the determination of through-bond carbon–carbon connectivities.^[39]

Tenfold-substituted biphenyls **1** and **4** exhibited similar through-bond, but topologically even more intriguing toroidal delocalization as shown in Figure 12. ACID plots revealed that through-space conjugation between the *ipso*-Cs of the deca-phenyl and deca(2-thienyl)benzene units exhibit the topology of catenated wedding rings.

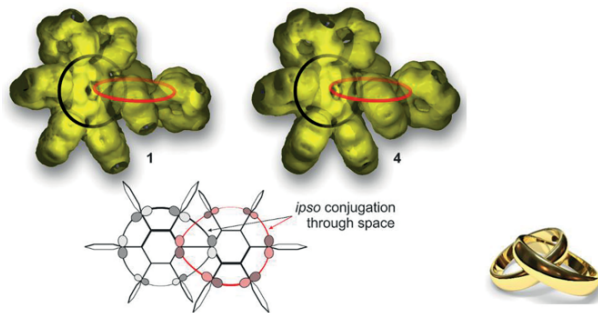


Figure 12. ACID plots of deca(2-thienyl)biphenyl **1** (top left) and decaphenylbiphenyl **4** (top right), at isosurface values of IV: 0.0015. The topology of the through-space conjugation of the *ipso*-C atoms is isomorphic to a pair of catenated wedding rings (bottom).

Optical and Electrochemical Properties

The optoelectronic properties of biphenylene derivatives **1** and **4** and of corresponding ethynylene derivatives **2** and **5** were investigated and compared to the parent structures hexa(2-thienyl)benzene **3** and hexaphenylbenzene **6**. Absorption and emission maxima, optical energy gaps, oxidation potentials, and the calculated frontier orbital energies are summarized in Table 1. The absorption maxima in DCM solutions of intermediates **2** and **5** are red-shifted compared to target derivatives **1** and **4** due to a higher delocalization in the elongated π-system (Figure 13). Derivatives containing thiophene units (**1**, **2**, and **3**) showed red-shifted absorption compared to the corresponding phenylene derivatives (**4**, **5** and **6**) and consequently lower optical gap energies. The unstructured absorption bands at lower energy of biphenyls **1** and **4** showed bathochromic shifts and smaller energy gaps compared with parent compounds **3** and **6** which can be rationalized by a partial electronic delocalization over the entire molecule in **1** and **4** with, fairly speaking,

Table 1. Optical and electrochemical data of thienylene derivatives **1–3** and phenylene counterparts **4–6**.

	λ_{abs} [nm] ^[a]	E_g^{opt} [eV]	λ_{em} [nm] ^[b]	$E_{\text{p}}^{\text{ox1}}$ [V]	$E_{\text{p}}^{\text{ox2}}$ [V]	E_{HOMO} [eV]	E_{LUMO} [eV] ^[c]
1	240, 294, 337(s)	3.45	424	0.91	1.07	-5.95	-2.50
2	240, 307, 347	3.32	425	0.99	—	-6.03	-2.71
3	240, 289, 320(s)	3.68	420	1.04	—	-5.94	-2.26
4	254, 277(s)	4.04	352	1.26	—	-6.31	-2.27
5	259, 304, 319	3.72	344	1.19	—	-6.23	-2.51
6	254, 282(s)	4.26	333	1.36	—	-6.14	-1.88

[a] Measured in DCM, maximum in italics, (s) denotes shoulder. [b] Measured in DCM. [c] Calculated with E_g^{opt} .

very low transition probability. The gain in vibronic structure in the absorption spectra of **2** and **5** accounts for a better planarization of the π -system compared to the higher torsion of the aromatic units in all other derivatives.

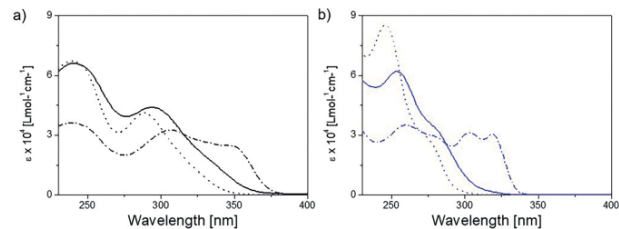


Figure 13. UV/Vis absorption spectra of (a) deca(2-thienyl)biphenyl **1** (black line), ethynylene derivative **2** (black dashed line), and hexathienylbenzene **3** (black dotted line); (b) decaphenyl/biphenyl **4** (blue line), ethynylene derivative **5** (blue dashed line), and hexaphenyl/benzene **6** (blue dotted line) measured in dichloromethane at room temperature.

In order to gain a better understanding of the experimentally observed optical transitions, theoretical calculations were performed on hexa(2-thienyl)benzene **3** (C_6 -symmetry) and hexaphenylbenzene **6** (D_6 -symmetry). After optimization at the M062X-D3/def2TZVP level of DFT, time-dependent DFT calculations at the same level of theory including 30 singlet excitations each were performed (Figure 14). The lowest energy excitations for **3** ($\lambda_{\max}^{\text{calc}}=317$ nm) and in **6** ($\lambda_{\max}^{\text{calc}}=286$ nm) are in good agreement with the experimental values ($\lambda_{\max}=320$ nm and 282 nm, respectively) and can be characterized as HOMO \rightarrow LUMO transitions. Both molecules exhibit degenerate HOMOs and LUMOs, which give rise to three transitions, one of which is allowed (*B* in **3** and E_2 in **6**). Fluorescence spectra of all compounds were analyzed in DCM solution (Table 1, Figure S20). Whereas hexa(hetero)arylbzenes **3** and **6** were only very weakly fluorescent, thiophene-based derivatives **1** and **2** showed stronger fluorescence and unstructured, strongly bathochromically shifted emission spectra compared to the corresponding polyphenylene derivatives **4** and **5**.

Redox potentials of biphenylene derivatives **1** and **4** and of corresponding ethynylene intermediates **2** and **5** were determined by cyclic voltammetry and compared to parent hexathienylbenzene **3** and hexaphenylbenzene **6** (Figure S21). All derivatives showed irreversible oxidation waves, which indicate the formation of reactive radical cations undergoing subsequent follow-up reactions due to free terminal positions. In the negative potential regime, no reductions were visible in the electrochemical window. The first oxidation potential (0.91–1.04 V) of the three thiophene derivatives **1–3** expectedly were at lower values than those of the polyphenylene derivatives **4–6** (1.19–1.36 V). Only for deca(2-thienyl)biphenyl **1** two separated (irreversible) oxidation waves at 0.91 V and 1.07 V were detected indicating that each half unit of the molecule is consecutively oxidized by one electron.

The analysis of the optical and redox properties of the six derivatives **1–6** clearly revealed that the replacement of phenylenes in **4–6** by thienylene substituents in **1–3** leads to bathochromic shifts in the optical spectra and lower oxidation potentials in electrochemistry due to the higher electron-donating effect of thiophenes.

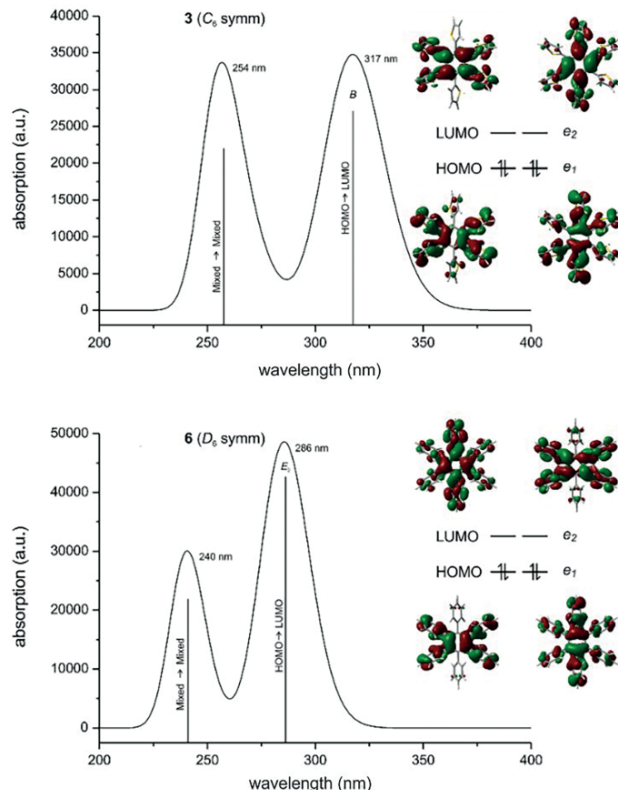


Figure 14. Theoretically calculated UV/Vis absorption spectra of **3** (top, C_6 symm.) and **6** (bottom, D_6 symm.). The insets represent the degenerated frontier orbitals that are involved in the corresponding transitions.

Conclusions

The synthesis of sterically crowded and congested thienylene–phenylene structures **1–3** has been presented and their structural characterization compared to the polyphenylene counterparts **4–6**. Single crystal X-ray structure analysis revealed propeller-like arrangement of the substituents around the central basic benzene (**2**, **3**, **5**, **6**) or biphenyl units (**1**, **4**), respectively. Typically, steric congestion and distortion effects of the thiophene-based derivatives **1–3** are smaller than in **4–6** due to the smaller geometric extension of thiophene compared to benzene rings. Evidence for through-space π -conjugation in a toroidal topology involving all *ipso*-carbons has been found theoretically for benzenoid derivatives **3** and **6** in their neutral state. For more complex biphenyls **1** and **4** through-space π -conjugation in a catenated toroidal topology was rationalized from advanced theoretical calculations (ACID) and suggested by the X-ray structure analysis. The characterization of the optoelectronic properties revealed the expected influence of the more electron-rich thiophene units in **1–3** compared to **4–6**. Finally, we expect that the subtle and small conjugation effects for the neutral molecules under investigation here should be much larger in charged species. In this respect, model compounds are underway in our laboratories.

Experimental Section

Materials and Methods: 1,2-Dichlorobenzene (Merck) was dried with CaCl_2 and distilled prior to use. Dichloromethane, petroleum ether, and *n*-hexane were purchased from VWR and distilled prior to use. Hexaphenylbenzene **6**,^[40] 1,4-Di(thien-2-yl)buta-1,3-diyne **7**,^[28] 2,3,4,5-tetra(thien-2-yl)cyclopenta-2,4-dien-1-one **8**,^[29] di(thien-2-yl)acetylene **9**,^[41] 1,4-diphenylbuta-1,3-diyne **10**,^[28] and tetracyclone **11**^[42] were prepared according to literature. Thin-layer chromatography was performed on aluminum plates, precoated with silica gel, Merck Si60 F254. Preparative column chromatography was carried out on glass columns packed with silica gel, Merck Silica 60, particle size 40–63 μm . HPLC was performed on a Shimadzu CBM-20A equipped with a SPD-20A UV/VIS detector and a LC-8A solvent system with a Macherey-Nagel column (Nucleosil 100-5 NO2). Melting points were measured using a Büchi Melting Point M-565. Thermogravimetric analyses (TGA) were performed on a TGA/SDTA 851e from Mettler Toledo. NMR spectra were recorded on a Bruker Avance 400 (^1H NMR: 400 MHz, ^{13}C NMR: 101 MHz) at 293 K. Chemical shift values (δ) are given in parts per million (ppm) and were calibrated on residual non-deuterated solvent peaks (^1H NMR: $\delta_{\text{H}} = 5.32$ for CD_2Cl_2 ; ^{13}C NMR: $\delta_{\text{C}} = 54.00$ for CD_2Cl_2) as an internal standard. The splitting patterns are labeled as follows: d (doublet), dd (doublet of doublet) and m (multiplet). High-resolution MALDI mass spectra (HRMS) were recorded on a MS Bruker Reflex 2 (Bruker Daltonik GmbH, Bremen, Germany), using *trans*-2-[3-(4-*tert*-butylphenyl)-2-methyl-2-propenylidene]malononitrile (DCTB) as a matrix. Cyclic voltammetry experiments were carried out using a computer-controlled Autolab PGSTAT30 potentiostat in a three-electrode single-compartment cell with a platinum working electrode, a platinum wire counter electrode, and an Ag/AgCl reference electrode. All potentials were internally referenced to the ferrocene/ferricinium couple. UV/Vis absorption spectra were recorded on a Perkin Elmer Lambda 19 spectrometer. Fluorescence spectra were recorded on a Perkin Elmer LS 55 Luminescence Spectrometer.

Synthetic Methods

2,2',2'',2''',2'''',2''''',2'''''''-([1,1'-Biphenyl]-2,2',3,3',4,4',5,5',6,6'-deca-yl)decathiophene (1). **Synthesis route 1:** A mixture of 1,4-di(thien-2-yl)buta-1,3-diyne **7** (50.0 mg, 0.23 mmol) and 2,3,4,5-tetra(thien-2-yl)cyclopenta-2,4-dien-1-one **8** (238 mg, 0.58 mmol) in 2.5 mL of dry 1,2-dichlorobenzene was stirred for 4.5 h at 200 °C in the microwave under Ar atmosphere. After cooling to room temperature, the solvent was removed under reduced pressure and the crude product was subjected to flash column chromatography (SiO_2 , petroleum ether/dichloromethane, 5:3). Further impurities had to be removed by HPLC (*n*-hexane/dichloromethane, 5:3). The desired biphenyl **1** (16 mg, 0.02 mmol, 7 %) was obtained as a white solid. 2,2',2'',2''',2''''-[6-(Thien-2-ylethynyl)benzene-1,2,3,4,5-pentayl]pentathiophene **2** (103 mg, 0.17 mmol, 74 %) was obtained as main product.

Synthesis Route 2: A mixture of 2,2',2'',2''',2''''-[6-(thien-2-ylethynyl)benzene-1,2,3,4,5-penta-yl]pentathiophene **2** (40.0 mg, 0.07 mmol) and 2,3,4,5-tetra(thien-2-yl)cyclopenta-2,4-dien-1-one **8** (68.7 mg, 0.17 mmol) in 8 mL of dry 1,2-dichlorobenzene was stirred for 4.5 h at 200 °C in the microwave under Ar atmosphere. After cooling to room temperature, the solvent was removed under reduced pressure and the crude product was subjected to flash column chromatography (SiO_2 , petroleum ether/dichloromethane, 5:3). Further impurities had to be removed by HPLC (*n*-hexane/dichloromethane, 5:3). The desired biphenyl **1** (10 mg, 0.01 mmol, 14 % yield) was obtained as a white solid. Mp 335–339 °C; ^1H -NMR (400 MHz, CD_2Cl_2): $\delta = 7.17$ (dd, $J = 5.1, 1.2 \text{ Hz}$, 4H), 7.07–7.04 (m,

5H), 6.67–6.61 (m, 11H), 6.51 (dd, $J = 3.5, 1.2 \text{ Hz}$, 2H), 6.47 (dd, $J = 3.5, 1.2 \text{ Hz}$, 4H), 6.24 (dd, $J = 3.6, 1.2 \text{ Hz}$, 4H); ^{13}C NMR (101 MHz, CD_2Cl_2): $\delta = 142.1, 141.5, 140.9, 140.0, 137.8, 137.6, 136.7, 131.1, 129.8, 129.7, 126.8, 126.54, 126.3, 126.2, 126.1, 125.6$; HRMS (MALDI-FT-ICR) m/z: calcd. for $\text{C}_{52}\text{H}_{30}\text{S}_{10}$, 973.95491; found 973.95476 [M]⁺ ($\delta\text{m}/\text{m} = 0.2 \text{ ppm}$), 1224.09250 [M + DCTB]⁺; CCDC 1884726.

2,2',2'',2''',[6-(Thien-2-ylethynyl)benzene-1,2,3,4,5-pentayl]pentathiophene (2). A mixture of 1,4-di(thien-2-yl)buta-1,3-diyne **7** (100 mg, 0.47 mmol) and 2,3,4,5-tetra(thien-2-yl)cyclopenta-2,4-dien-1-one **8** (286 mg, 0.70 mmol) in 2.5 mL of dry 1,2-dichlorobenzene was stirred for 18 h under reflux under Ar atmosphere. After cooling to room temperature, the solvent was removed under reduced pressure and the crude product was subjected to flash column chromatography (SiO_2 , petroleum ether/dichloromethane, 3:2). The desired product **2** (250 mg, 0.42 mmol, 90 %) was obtained as a white solid after recrystallization from dichloromethane/*n*-hexane and HPLC (*n*-hexane/dichloromethane, 3:2). Additionally, 2,2',2'',2''',[6-(1,1'-biphenyl)-2,2',3,3',4,4',5,5',6,6'-decayl]decathiophene **1** (11.0 mg, 0.01 mmol, 2 % yield) was obtained as side product. Melts under decomposition, T_d 323 °C (TGA) ^1H -NMR (400 MHz, CD_2Cl_2): $\delta = 7.34$ (dd, $J = 5.1, 1.2 \text{ Hz}$, 2H), 7.23 (dd, $J = 5.2, 1.2 \text{ Hz}$, 1H), 7.12 (dd, $J = 5.1, 1.2 \text{ Hz}$, 2H), 7.09 (dd, $J = 5.1, 1.2 \text{ Hz}$, 1H), 7.03 (dd, $J = 3.5, 1.2 \text{ Hz}$, 2H), 6.97 (dd, $J = 5.1, 3.5 \text{ Hz}$, 2H), 6.89 (dd, $J = 5.2, 3.7 \text{ Hz}$, 1H), 6.79 (dd, $J = 3.7, 1.2 \text{ Hz}$, 1H), 6.71 (dd, $J = 5.1, 3.5 \text{ Hz}$, 2H), 6.68–6.66 (m, 3H), 6.62 (dd, $J = 3.5, 1.2 \text{ Hz}$, 1H); ^{13}C NMR (101 MHz, CD_2Cl_2): $\delta = 140.8, 140.5, 140.4, 138.4, 137.4, 137.4, 132.7, 130.2, 130.1, 129.8, 128.7, 127.6, 126.9, 126.8, 126.8, 126.6, 126.3, 126.2, 123.3, 92.4, 92.3$; HRMS (MALDI-FT-ICR) m/z: calcd. for $\text{C}_{32}\text{H}_{18}\text{S}_6$, 593.97273; found 593.97099 [M]⁺ ($\delta\text{m}/\text{m} = 0.3 \text{ ppm}$), 844.11555 [M + DCTB]⁺; CCDC 1884740.

Hexa(thien-2-yl)benzene (3). All steps were carried out under Ar atmosphere. Di(thien-2-yl)acetylene **9** (0.09 g, 0.47 mmol) was dissolved in 4 mL of 2-propanol. Rhodium(III)chloride (7.1 mg, 0.03 mmol) and triethylamine (0.5 mL) was added and the solution was stirred for 3 days at 85 °C. The solution was poured into 20 mL of water, extracted with dichloromethane and dried with Na_2SO_4 . The product was purified by column chromatography (SiO_2 , 1. petroleum ether and 2. petroleum ether/ethyl acetate, 20:1) and isolated as colourless solid (152 mg, 0.27 mmol, 41 % yield). No melting up to 450 °C. ^1H -NMR (400 MHz, CDCl_3): $\delta = 7.08$ (dd, $J = 5.1, 1.2 \text{ Hz}$, 1H, H-5), 6.68 (dd, $J = 5.0, 3.5 \text{ Hz}$, 1H, H-4), 6.58 (dd, $J = 3.5, 1.2 \text{ Hz}$, 1H, H-3); ^{13}C NMR (101 MHz, CD_2Cl_2): $\delta = 141.1, 137.7, 129.1, 126.6, 126.2$; HRMS (MALDI-FT-ICR) m/z: calcd. for $\text{C}_{30}\text{H}_{18}\text{S}_6$, 569.97273; found 569.97241 [M]⁺ ($\delta\text{m}/\text{m} = 0.6 \text{ ppm}$); CCDC 1884759.

3',3'',4',4'',5',5'',6',6''-Octaphenyl-1,1':2',1'':2'',1'''-quaterphenyl (4). In a Schlenk-tube a mixture of 1,4-diphenylbuta-1,3-diyne **10** (70.0 mg, 0.35 mmol) and tetracyclone **11** (399 mg, 1.04 mmol) was stirred in the melt for 3 h at 315 °C under Ar atmosphere. After cooling to room temperature, the crude product was subjected to flash column chromatography (SiO_2 , petroleum ether/dichloromethane, 3:2). After recrystallization from dichloromethane/*n*-hexane the desired quaterphenyl **4** (265 mg, 0.29 mmol, 84 % yield) was obtained as a white solid (Lit. 60 %).^[24] Additionally, 3',4',5'-triphenyl-6'-(phenylethynyl)-1,1':2',1''-terphenyl **5** (11.0 mg, 0.02 mmol, 6 % yield) was obtained as side product. Mp 329–332 °C (Lit. 322–324 °C);^[24] ^1H -NMR (400 MHz, CD_2Cl_2): $\delta = 7.00$ –6.94 (m, 4H), 6.94–6.88 (m, 9H), 6.83–6.76 (m, 18H), 6.75–6.69 (m, 13H), 6.69–6.65 (m, 8H); ^{13}C NMR (101 MHz, CD_2Cl_2): $\delta = 142.2, 141.7, 141.4, 141.1, 140.8, 140.3, 137.8, 132.8, 132.2, 131.9, 126.8, 126.7, 126.1, 125.6, 125.5$; HRMS (MALDI-FT-ICR) m/z: calcd. for $\text{C}_{72}\text{H}_{50}$, 914.39070; found 914.38938 [M]⁺ ($\delta\text{m}/\text{m} = 1.4 \text{ ppm}$), 824.34257 [M-2(C_6H_5) + 2 H^+ + K^+ + Na^+], 937.37828 [M + Na^+], 953.35234 [M + K^+].

3',4',5'-Triphenyl-6'-(phenylethynyl)-1,1':2',1''-terphenyl (5): In a Schlenk-tube a mixture of 1,4-(diphenyl)buta-1,3-diyne **10** (200 mg, 0.99 mmol) and tetracyclone **11** (1.14 g, 2.97 mmol) in 6 mL of dry 1,2-dichlorobenzene was stirred for 24 h at 200 °C under Ar atmosphere. After cooling to room temperature, the solvent was removed under reduced pressure and the crude product was subjected to flash column chromatography (SiO_2 , petroleum ether/dichloromethane, 3:2). After recrystallization from dichloromethane/*n*-hexane the desired ethynylene **5** (438 mg, 0.78 mmol, 79 % yield) was obtained as a white solid (Lit. 66%).^[26] Mp 264–266 °C (Lit. 258 °C);^[26] ^1H -NMR (400 MHz, CD_2Cl_2): δ = 7.31–7.27 (m, 4H), 7.26–7.23 (m, 3H), 7.23–7.19 (m, 3H), 7.17–7.09 (m, 3H), 6.94–6.89 (m, 10H), 6.90–6.84 (m, 5H), 6.70–6.66 (m, 2H); ^{13}C NMR (101 MHz, CD_2Cl_2): δ = 143.8, 141.9, 141.2, 140.8, 140.7, 140.6, 131.8, 131.7, 131.5, 131.3, 128.6, 128.5, 127.6, 127.2, 127.1, 127.0, 126.1, 126.0, 123.8, 123.1, 97.2, 89.8. MS (MALDI-TOF) m/z: calcd. for $\text{C}_{44}\text{H}_{30}$, 558.724; found 558.921 [M]⁺ ($\delta\text{m}/\text{m}$ = 0.4 ppm).

Computational Methods: General. The geometry optimizations were performed with the Minnesota density functional M062X^[43] with dispersion correction (D3)^[44] and a large triple zeta basis def2TZVP, because this level performed well in Grimme's latest study for basic properties.^[45] These calculations were carried out with Turbomole 7.2^[46] including the resolution-of-identity (RI) with multipole accelerated RI-J (mrij) to speed up the calculations.

ACID. The anisotropy of the current density was calculated using our ACID^[35] method implemented in the Gaussian09 D.01^[47] program using NMR calculations with Continuous Set of Gauge Transformations (CSGT)^[48] and the IOp(10/93) option. For an adequate description of the expected through-space conjugation the Pople basis 6-311+G** with diffuse functions and the standard B3LYP^[49] density functional was employed. The orientation of the magnetic field vector is orthogonal to the peripheral ring current and pointing towards the viewer.

UV/Vis spectra. TD-DFT calculations (30 singlet excitations) were performed using Gaussian09 D.01 at the same level of theory as used for geometry optimization. The spectra are simulated by an overlay of Gauss functions with a half-width of 0.2 eV.

Acknowledgments

T. L. gratefully acknowledges financial support by the State of Baden-Württemberg and the University of Ulm. Special acknowledgment goes to B. Müller (Inorganic Chemistry II, University of Ulm) for recording single-crystal X-ray structure analyses and to Prof. K. Müllen (Max-Planck-Institute Mainz, Germany) for valuable discussions.

Keywords: ACID calculations · Phenylenes · Through-space conjugation · Toroidal p_z -orbital coupling · X-ray structure analysis

- [1] A. J. Berresheim, M. Müller, K. Müllen, *Chem. Rev.* **1999**, *99*, 1747–1785.
- [2] A. E. Keirstead, J. W. Bridgewater, Y. Terazono, G. Kodis, S. Straight, P. A. Liddell, A. L. Moore, T. A. Moore, D. Gust, *J. Am. Chem. Soc.* **2010**, *132*, 6588–6595.
- [3] R. Rathore, C. L. Burns, I. A. Guzei, *J. Org. Chem.* **2004**, *69*, 1524–1530.
- [4] S. Fukuzumi, K. Ohkubo, J. Otera, *J. Org. Chem.* **2001**, *66*, 1450–1454.
- [5] Y. Geng, A. Fechtenkötter, K. Müllen, *J. Mater. Chem.* **2001**, *11*, 1634–1641.
- [6] S. R. Waldvogel, A. R. Wartini, P. H. Rasmussen, J. A. Rebek, *Tetrahedron Lett.* **1999**, *40*, 3515–3518.

- [7] Y. Zou, T. Ye, D. Ma, J. Qin, C. Yang, *J. Mater. Chem.* **2012**, *22*, 23485–23491.
- [8] X. Sun, X. Xu, W. Qiu, G. Yu, H. Zhang, X. Gao, S. Chen, Y. Song, Y. Liu, *J. Mater. Chem.* **2008**, *18*, 2709–2715.
- [9] J. D. Badjić, V. Balzani, A. Credi, J. N. Lowe, S. Silvi, J. F. Stoddart, *Chem. Eur. J.* **2004**, *10*, 1926–1935.
- [10] V. Balzani, M. Clemente-León, A. Credi, J. N. Lowe, J. D. Badjić, J. F. Stoddart, D. J. Williams, *Chem. Eur. J.* **2003**, *9*, 5348–5360.
- [11] K. Yoshida, I. Morimoto, K. Mitsudo, H. Tanaka, *Tetrahedron Lett.* **2008**, *49*, 2363–2365.
- [12] *Handbook of Oligo- and Polythiophenes*, D. Fichou (Eds.), Wiley-VCH, Weinheim, **1999**.
- [13] T. Kosaka, Y. Inoue, T. Mori, *J. Phys. Chem. Lett.* **2016**, *7*, 783–788.
- [14] S. V. Rosokha, I. S. Neretin, D. Sun, J. K. Kochi, *J. Am. Chem. Soc.* **2006**, *128*, 9394–9407.
- [15] D. Sun, S. V. Rosokha, J. K. Kochi, *Angew. Chem. Int. Ed.* **2005**, *44*, 5133–5136; *Angew. Chem.* **2005**, *117*, 5263–5266.
- [16] C. Lambert, *Angew. Chem. Int. Ed.* **2005**, *44*, 7337–7339; *Angew. Chem.* **2005**, *117*, 7503–7505.
- [17] V. J. Chebny, R. Shukla, R. Rathore, *J. Phys. Chem. A* **2006**, *110*, 13003–13006.
- [18] C. Rios, R. Salcedo, *Molecules* **2014**, *19*, 3274–3296.
- [19] R. Rathore, J. K. Kochi, *Can. J. Chem.* **1999**, *121*, 913–921.
- [20] R. Rathore, C. L. Burns, S. A. Abdelwahed, *Org. Lett.* **2004**, *6*, 1689–1692.
- [21] E. M. Larson, R. B. von Dreele, P. Hanson, J. D. Gust, *Acta Crystallogr., Sect. C: Cryst. Struct. Commun.* **1990**, *46*, 784–788.
- [22] a) A. Bondi, *J. Phys. Chem.* **1964**, *68*, 441–451; b) S. Alvarez, *Dalton Trans.* **2013**, *42*, 8617–8636.
- [23] Y. Tanaka, T. Koike, M. Akita, *Chem. Commun.* **2010**, *46*, 4529–4531.
- [24] M. A. Ogliaruso, E. I. Becker, *Org. Chem.* **1965**, *30*, 3354–3360.
- [25] L. Tong, H. Lau, D. M. Ho, R. A. Pascal Jr., *J. Am. Chem. Soc.* **1998**, *120*, 6000–6006.
- [26] W. Dilthey, W. Schommer, W. Hirschen, H. Dierich, *Ber. Dtsch. Chem. Ges.* **1935**, *68*, 1159–1162.
- [27] S. Brydges, B. Gildea, J. P. Grealis, H. Müller-Bunz, M. Stradiotto, M. Casey, M. J. McGlinchey, *Can. J. Chem.* **2013**, *91*, 1098–1111.
- [28] X. Chen, H. Zhang, J. Chen, H. Gong, *Chem. Lett.* **2015**, *44*, 129–131.
- [29] T. Kawase, T. Ohsawa, T. Enomoto, M. Oda, *Chem. Lett.* **1994**, *23*, 1333–1336.
- [30] H. Pepermans, R. Willem, M. Gielen, C. Hoogzand, *Magn. Reson. Chem.* **1988**, *26*, 311–318.
- [31] J. A. N. F. Gomes, R. B. Mallion, *Chem. Rev.* **2001**, *101*, 1349–1384.
- [32] R. Hu, J. W. Y. Lam, Y. Liu, X. Zhang, B. Z. Tang, *Chem. Eur. J.* **2013**, *19*, 5617–5624.
- [33] H. Camleau, J. L. Baudour, *Acta Crystallogr., Sect. A* **1979**, *35*, 426–432.
- [34] P. Pouzet, I. Erdelmeier, D. Ginderow, J.-P. Mornon, P. M. Dansette, D. Mansuy, *J. Heterocycl. Chem.* **1997**, *34*, 1567–1573.
- [35] R. Herges, D. Geuenich, *J. Phys. Chem. A* **2001**, *105*, 3214–3220.
- [36] D. Geuenich, K. Hess, F. Köhler, R. Herges, *Chem. Rev.* **2005**, *105*, 3758–3772.
- [37] E. Steiner, P. W. Fowler, *J. Phys. Chem. A* **2001**, *105*, 9553–9562.
- [38] Magnetic properties of aromatic compounds and aromatic transition states (Eds.: R. Herges, G. Freking, S. Shaik), *Chemical Bond* **2014**, *2*, p. 383–420, Wiley VCH Weinheim.
- [39] N. C. Nielsen, H. Thøgersen, O. W. Sørensen, *J. Am. Chem. Soc.* **1995**, *117*, 11365–11366.
- [40] J. A. Hyatt, *Org. Prep. Proced. Int.* **1991**, *23*, 460–463.
- [41] A. Carpita, A. Lessi, R. Rossi, *Synthesis* **1984**, *7*, 571–572.
- [42] H. Wang, Y. Liang, H. Xie, L. Feng, H. Lu, S. Feng, *J. Mater. Chem. C* **2014**, *2*, 5601–5606.
- [43] Y. Zhao, D. G. Truhlar, *Theor. Chem. Acc.* **2008**, *120*, 215–241.
- [44] S. Grimme, J. Antony, S. Ehrlich, H. Krieg, *J. Chem. Phys.* **2010**, *132*, 154104.
- [45] L. Goerigk, A. Hansen, C. Bauer, S. Ehrlich, A. Najibi, S. Grimme, *Phys. Chem. Chem. Phys.* **2017**, *19*, 32184–32215.
- [46] *Turbomole7.2: TURBOMOLE V7.2 2017*, a development of University of Karlsruhe and Forschungszentrum Karlsruhe GmbH, 1989–2007, TURBOMOLE GmbH, since 2007; available from <http://www.turbomole.com>.
- [47] M. J. Frisch, G. W. Trucks, H. B. Schlegel, G. E. Scuseria, M. A. Robb, J. R. Cheeseman, G. Scalmani, V. Barone, B. Mennucci, G. A. Petersson, H. Na-

katsuji, M. Caricato, X. Li, H. P. Hratchian, A. F. Izmaylov, J. Bloino, G. Zheng, J. L. Sonnenberg, M. Hada, M. Ehara, K. Toyota, R. Fukuda, J. Hasegawa, M. Ishida, T. Nakajima, Y. Honda, O. Kitao, H. Nakai, T. Vreven, J. A. Montgomery Jr., J. E. Peralta, F. Ogliaro, M. Bearpark, J. J. Heyd, E. Brothers, K. N. Kudin, V. N. Staroverov, R. Kobayashi, J. Normand, K. Raghavachari, A. Rendell, J. C. Burant, S. S. Iyengar, J. Tomasi, M. Cossi, N. Rega, J. M. Millam, M. Klene, J. E. Knox, J. B. Cross, V. Bakken, C. Adamo, J. Jaramillo, R. Gomperts, R. E. Stratmann, O. Yazev, A. J. Austin, R. Cammi,

C. Pomelli, J. W. Ochterski, R. L. Martin, K. Morokuma, V. G. Zakrzewski, G. A. Voth, P. Salvador, J. J. Dannenberg, S. Dapprich, A. D. Daniels, Ö. Farkas, J. B. Foresman, J. V. Ortiz, J. Cioslowski, D. J. Fox, *Gaussian 09, Revision D.01*, Gaussian, Inc., Wallingford CT, 2013.

[48] T. A. Keith, R. F. W. Bader, *Chem. Phys. Lett.* **1992**, 194, 1–8.

[49] A. D. Becke, *J. Chem. Phys.* **1993**, 98, 5648–5652.

Received: November 6, 2019

6

Sonstige Publikationen in chronologischer Reihenfolge

Heterodiazocines: Synthesis and Photochromic Properties, *Trans* to *Cis* Switching within the Bio-optical Window

M. Hammerich, C. Schütt, C. Stähler, P. Lentes, F. Röhricht, R. Höppner und R. Herges

J. Am. Chem. Soc. **2016**, *138*, 13111–13114.

DOI:10.1021/jacs.6b05846

Wissenschaftliche Beiträge: Im Rahmen der eigenen Bachelorarbeit entstanden: DFT-Geometrieoptimierung der DACs, Simulation der UV/Vis-Spektren mittels TD-DFT, Synthese der Dinitroprecursor für die Diazocinsynthese.

Structural Monitoring of the Onset of Excited-State Aromaticity in a Liquid Crystal Phase

M. Hada, S. Saito, S. Tanaka, R. Sato, M. Yoshimura, K. Mouri, K. Matsuo, S. Yamaguchi, M. Hara, Y. Hayashi, F. Röhricht, R. Herges, Y. Shigeta, K. Onda und R. J. D. Miller

J. Am. Chem. Soc. **2017**, *139*, 15792–15800.

DOI:10.1021/jacs.7b08021

Wissenschaftliche Beiträge: Plots mit ACID.

Synthesis of dipolar molecular rotors as linkers for metal-organic frameworks

S. Hamer, F. Röhricht, M. Jakoby, I. A. Howard, X. Zhang, C. Näther und R. Herges

Beilstein J. Org. Chem. **2019**, *15*, 133–1338.

DOI:10.3762/bjoc.15.132

Wissenschaftliche Beiträge: DFT-Geometrieoptimierung der dipolaren molekularen Rotoren, Bestimmung der Dipolmomente, Modellrechnungen zur Bewertung der Dipol-Dipol-Wechselwirkung in *metal-organic-framework*-typischen Abständen und der freien Drehbarkeit entlang der Linkerachse.

Spin Switching with Triazolate-Strapped Ferrous Porphyrins

M. K. Peters, S. Hamer, T. Jäkel, F. Röhricht, F. D. Sönnichsen, C. v. Essen, M. Lahtinen, C. Näther, K. Rissanen und R. Herges

Inorg. Chem. **2019**, *58*, 5265–5272.

DOI:10.1021/acs.inorgchem.9b00349

Wissenschaftliche Beiträge: DFT-Modellrechnungen als Beitrag zum optimalen Design des Spinschalters, konformationelle Analyse der Verbrückung.

Norbornadiene-functionalized triazatriangulenium and trioxatriangulenium platforms

R. Löw, T. Rusch, T. Moje, F. Röhricht, O. Magnussen und R. Herges

Beilstein J. Org. Chem. **2019**, *15*, 1815–1821.

DOI:10.3762/bjoc.15.175

Wissenschaftliche Beiträge: DFT-Geometrieoptimierungen der vorgestellten Moleküle, Diskussion und Hilfestellung bei Ergründung des Schaltmechanismus.

Reversible coordination-induced spin-state switching in complexes on metal surfaces

A. Köbke, F. Gutzeit, F. Röhricht, A. Schlimm, J. Grundwald, F. Tuczak, M. Studniarek, D. Longo, F. Choueikani, E. Otero, P. Ohresser, S. Rohlf, S. Johannsen, F. Diekamnn, K. Rossnagel, A. Weismann, T. Jasper-Toennies, C. Näther, R. Herges, R. Berndt und M. Gruber

Nat. Nanotechnol. **2020**, *15*, 18–21.

DOI:10.1038/s41565-019-0594-8

Wissenschaftliche Beiträge: DFT-Single-Point-Rechnungen von vorhandenen Strukturen zur Bestimmung und Darstellung der Molekülorbitale und daraus resultierenden HOMO-LUMO-Lücke.

Rotation of Ethoxy and Ethyl Moieties on a Molecular Platform on Au(111)

T. Jasper-Toennies, M. Gruber, S. Johannsen, T. Frederiksen, A. Garcia-Lekue, T. Jäkel, F. Röhricht, R. Herges und R. Berndt

ACS Nano **2020**, *14* (4), 3907–3916.

DOI:10.1021/acsnano.0c00029

Wissenschaftliche Beiträge: DFT-Rechnungen als Hilfestellung zur Bestimmung der Geometrien, Rotationsbarrieren und Vibrationsmoden.

Synthesis of 4-substituted azopyridine-functionalized Ni(II)-porphyrins as molecular spin switches

J. Ludwig, T. Moje, F. Röhricht und R. Herges

Beilstein J. Org. Chem. **2020**, *16* (4), 2589–2597.

DOI:10.3762/bjoc.16.210

Wissenschaftliche Beiträge: DFT-Rechnungen zur Aufklärung eines Spin-Switching-Experiments.

Zusammenfassung und Ausblick

7

Diese Dissertation zeigt, wie zielführend quantenmechanische Methoden mit ihren breit gefächerten Möglichkeiten für das Design neuer molekularer Strukturen, die Vorhersage ihrer Eigenschaften und die Erklärung von bisher unbekannten Phänomenen eingesetzt werden konnten. Die Arbeit ist dabei grob in zwei Themengebiete gegliedert. Zum Einen wurde die Dichtefunktionaltheorie (DFT) genutzt, um photoschaltbare Moleküle anwendungsspezifisch zu designen, photophysikalische Eigenschaften vorherzusagen und experimentelle Ergebnisse zu beleuchten. Zum Anderen wurde in dieser Arbeit die von HERGES *et al.* entwickelte Anisotropie der induzierten Stromdichte (*ansitropy of the induced current density*, ACID)-Software^[197,198] für die Aufklärung von elektronischer Delokalisierung und von Ringströmen verwendet.

7.1 Neue Photoschalter

Mit der Entdeckung des Diazocins von DUVAL 1910 und der erst 100 Jahre späteren photophysikalischen Charakterisierung von SIEWERTSEN wurde eine neue Klasse photoschaltbarer Systeme gefunden.^[92,93] Der bedeutendste Unterschied zum Azobenzol ist die inverse thermodynamische *cis*-Stabilität, welche eine enorme Vielfalt für neue Anwendungen ermöglicht. Hinzu kommt die im Vergleich zum Azobenzol außerordentlich hohe Effizienz der Photoisomerisierung und die bathochrome Verschiebung der relevanten Anregungswellenlängen der *trans*-Isomere bis in den Bereich roten Lichts.^[93,94]

Hetero-Diazocene

Da die Synthese der -CH₂-CH₂- überbrückten Stammsysteme häufig zu Problemen bei der Reproduzierbarkeit und der Synthese unsymmetrisch substituierter Funktionalisierung führte,^[93,100,287–290] wurde von HAMMERICH *et al.* ein systematischer Ansatz mit Heteroatomen in der Verbrückung (-CH₂-O-/CH₂-S-) entwickelt.^[99] Bereits vor der Synthese sagten DFT-Rechnungen (B3LYP/6-31G*) für die neuen Systeme ähnliche Eigenschaften wie für das Stamm-diazocin voraus. Neben gut separierten $n\pi^*$ -Absorptionsbanden (*time dependent* (TD)-DFT), *cis*-Stabilität und Ringspannungsenergien ähnlich dem Stammsystem wurde zusätzlich ein bisher unberücksichtigtes Konformer der *trans*-Konfiguration, die chair-Konformation, untersucht. Dieses weist ein ähnliches Absorptionsspektrum wie das der *cis*-Konfiguration auf und sollte somit

für eine effiziente photochemische Anreicherung der *trans*-Konfiguration möglichst geringfügig populiert vorliegen, da sonst direkt die Rückisomerisierung angeregt würde. Diese direkte Anregung der Rückisomerisierung konnte im Fall des S-Diazocins auch die im Vergleich zum Stamm- und O-Diazocin geringere Anreicherung der metastabilen *trans*-Konfiguration im photostationären Zustand (*photostationary state*, PSS) erklären. Bei dem S-Diazocin sind chair und twist nahezu isoenergetisch. Deshalb wird bei der Anreicherung des *trans*-Isomers mit geeigneter Wellenlänge auch der chair populiert und mit derselben Wellenlänge zur Rückisomerisierung angeregt.

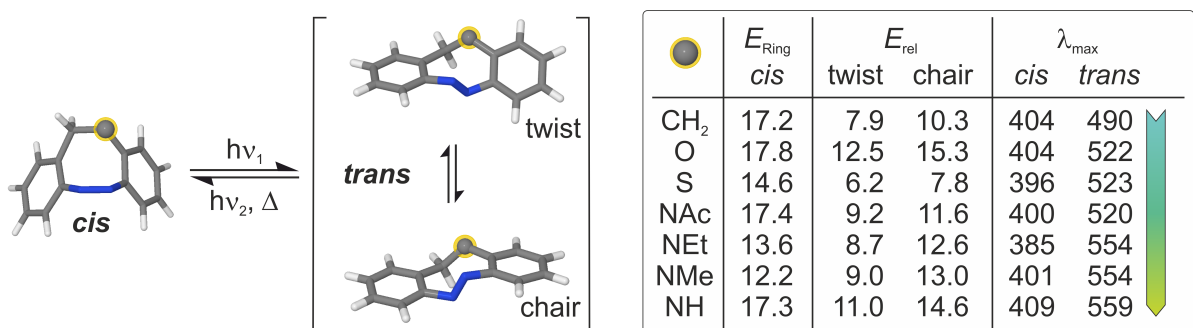


Abb. 7.1: Die Isomerisierung der Diazocene von der thermodynamisch stabilen *cis*-Konfiguration mit Licht geeigneter Wellenlängen zur metastabilen *trans*-Spezies kann zu zwei Konformeren (twist und chair) führen, wobei der twist meistens thermodynamisch präferiert wird. Die isodesmischen Ringspannungsenergien (*cis*-Form) und die rel. Energien (E_{rel} zum *cis*-Isomer) sind in kcal mol⁻¹ (M062X-D3/def2TZVP) angegeben.^[291] Die exp. Absorptionsmaxima der am stärksten rot-verschobenen $n\pi^*$ -Absorptionsbanden sind für beide Isomere angegeben.^[99,291]

Um das Konzept der Heterodiazocene zu erweitern, wurde 2019 innerhalb dieser Arbeit ein Stickstoff-verbrücktes Diazocin entwickelt (Brücke: -CH₂-NR-), welches gegenüber den O- und S-Diazocinen weitere Substitutionsmöglichkeiten am Brückenstickstoff bietet.^[291] Dies ist besonders für eine pharmazeutische Anwendung interessant, da die tricyclische Struktur vielen bereits bekannten Pharmakophoren ähnelt. Zur Berechnung der Eigenschaften der N-Diazocene wurde das weit verbreitete Standardniveau B3LYP/6-31G*, welches auch für vorherige Berechnung der Heterodiazocene verwendet wurde, durch M062X-D3/def2TZVP abgelöst. Der Wechsel hierzu wurde durch die überzeugenden Ergebnissen aus einem von GRIMME *et al.* durchgeführten Benchmarking an seiner eigens entwickelten GMTKN55-Datenbank nahegelegt.^[68] Hier drin erzielte M062X-D3 deutlich bessere Ergebnisse als das bisher verwendete Funktional B3LYP in der Kategorie grundlegende Eigenschaften und Reaktionen von kleinen Systemen. Die quantenchemischen Rechnungen dieser Arbeit konnten mit dem neuen Niveau vorhersagen, dass die N-Diazocene viele der gewünschten Eigenschaften und zusätzlich bis in den nahen Infrarot (NIR)-Bereich bathochrom verschobene Absorptionsbanden aufweisen. Diese Absorptionen liegen weiter im biooptischen Fenster als von den bisher etablierten Diazocinen bekannt, was für eine pharmakologischen Anwendung zusätzlich vielversprechend ist.

Durch die Kombination von experimentellen Daten der Kooperationspartner und der theoretischen Berechnung dieser Arbeit konnte der Mechanismus der Isomerisierungsreaktion weitgehend aufgeklärt werden. Es existieren grundsätzlich drei Spezies *cis*-boat, *trans*-twist und *trans*-chair, die photochemisch bzw. thermisch ineinander überführt werden können. Durch Einführen der Heteroatome in die Brücke wird die Symmetrie der Heterodiazocine erniedrigt und damit die Zahl der möglichen Isomere erhöht. Im Fall der N-Diazocine kommt hinzu, dass der Substituent am Stickstoff äquatorial bzw. axial stehen kann.

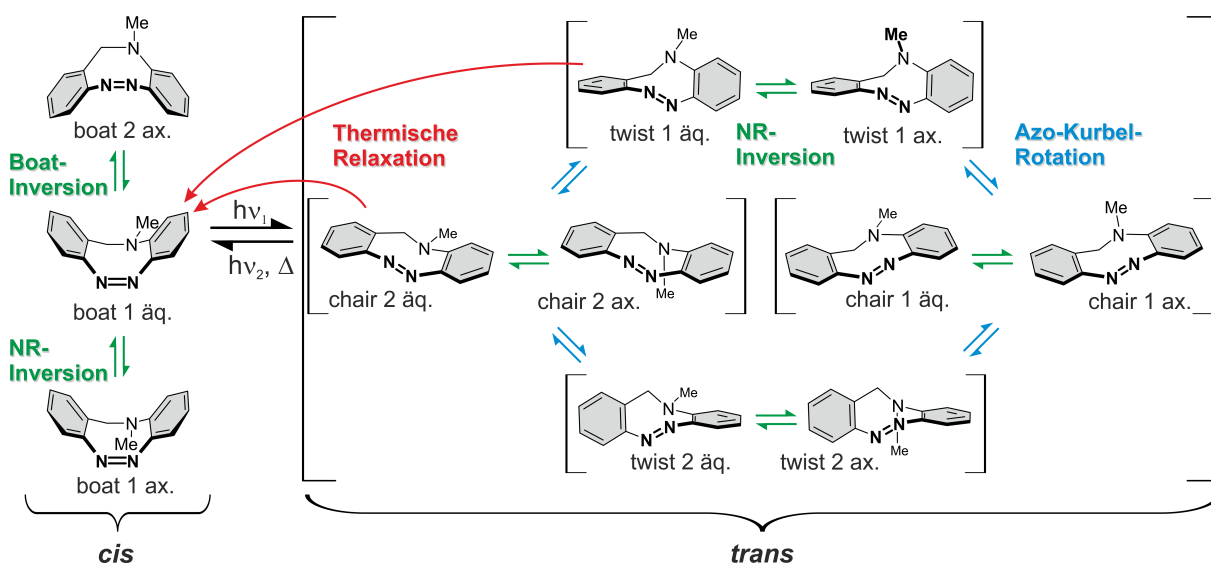


Abb. 7.2: Konfigurations- und Konformationsraum der N-Diazocine am Beispiel von N-Methyl-Diazocin: die am Brückenstickstoffatom axial bzw. äquatorial substituierten boat-Konformere der *cis*-Konfiguration können durch eine boat-Inversion des zentralen Achtrings oder die Inversion am Stickstoff ineinander übergehen. Auf der komplexeren Hyperfläche der *trans*-Konfiguration können die axial und äquatoriale Konformere des jeweiligen Enantiomers durch Inversion am Stickstoff ineinander übergehen. Die Racemisierung zwischen den enantiomeren chair-Konformeren ist nicht direkt sondern nur über eines der twist-Konformere durch eine kurbelartige Rotation der Azofunktion möglich. Analoges gilt für die twist-Konformere. Die thermische Relaxation vom metastabilen *trans* zum *cis* geschieht durch nahezu isoenergetische Übergangszustände entweder vom twist oder vom chair.

Durch theoretische Studien der möglichen Konfigurationen sowie deren Konformationen aller N-Diazocine (Bsp. N-Methyl-Diazocin s. Abb. 7.2) konnte diese Dissertation zeigen, dass die zwei *cis*-boat-Konformere schnell (auf der NMR-Zeitskala) durch Durchschwingen des Achtrings und zusätzlich durch die Inversion am sp^3 -hybridisierten-Stickstoff so ineinander transformieren, dass im thermodynamischen Gleichgewicht fast ausschließlich das stabilere äquatoriale Enantiomerenpaar vorliegen sollte. Der konformativ Raum der *trans*-Spezies ist deutlich komplexer. Hier können die verschiedenen Kombinationen aus axial, äquatorial, twist, chair und den jeweiligen Enantiomeren theoretisch zu sehr vielen dynamischen Konformationsumwandlungen führen. Ein großer Teil hiervon konnte durch die Kombination experimenteller NMR-Untersuchungen der Kooperationspartner und DFT-Rechnungen dieser Arbeit aufgeklärt werden. Es zeigte sich eine auf der NMR-Zeitskala schnelle Umwandlung der chair- in die twist-Spezies (und umge-

kehrt), was geringe Energiebarrieren der Rechnungen für alle N-Diazocene hierfür vorhersagten. Eine direkte Konversion von einem chair- bzw. twist- in das korrespondierende Enantiomer (*Racemisierung*) konnten die Rechnungen, bestätigt durch die Experimente der Kooperationspartner, ausschließen. Ebenso wie beim *cis*-boat war eine Inversion am Brückenstickstoff (ax. \rightleftharpoons äq.) bei Raumtemperatur durch breite Signale im NMR zu beobachten. Bei Temperaturerniedrigung wurde die Inversion jedoch teilweise so ausgesetzt, dass nur das thermodynamisch stabile Konformer im NMR zu beobachten ist. Da die Inversion am sp^3 -hybridisierten-Stickstoff von der DFT bekanntermaßen schlecht beschrieben wird,^[109] wurden hierzu keine weitergehenden theoretischen Untersuchungen durchgeführt. Einen Ausweg könnten zukünftig andere quantenchemische Rechnungen (z. B. MØLLER-PLESSET, MP; oder Coupled Cluster, CC) darstellen, um dieses Verhalten besser zu beschreiben. Erste Studien, die Inversion in der *cis*-Konfiguration des N-Methyl-Diazocins zu beschreiben, erzielten mit MP2 sowie CC2 (MP2 bzw. CC2/aug-cc-pVTZ//M062X-D3/def2TZVP) im Vergleich zur DFT (M062X-D3/def2TZVP: 0.9 kcal mol⁻¹) viel besser zu den NMR-Experimenten passende Energiebarrieren von ca. 5-6 kcal mol⁻¹. Dies zeigt, dass die DFT zwar in vielerlei Hinsicht akkurat und zeitsparend Ergebnisse erzielt, ein Vergleich mit anderen quantenchemischen Methoden besonders in Spezialfällen sehr sinnvoll ist. Da Vertreter der N-Diazocene bereits jetzt für Pharmakophore gewünschte Eigenschaften wie gute Wasserlöslichkeit, Absorptionsbanden im biooptischen Fenster und gute Schalteigenschaften in wässriger Umgebung aufweisen, erscheinen weitere Untersuchungen vielversprechend. Hierfür könnten zunächst die vorhandenen und gut charakterisierten N-Diazocene unverändert auf biologisch inhibierende Eigenschaften in Bioassays untersucht werden. Auf Grund der strukturellen Ähnlichkeit des tricyclischen Kerns (s. Abb. 7.3) zu bereits bekannten und auf verschiedene biologische Aktivität, wie z.B. Prostaglandin-, Histamin-, Serotonin- oder Dopaminrezeptoren, untersuchten Verbindungen,^[292,293] wäre der Einsatz als Inhibitor bei diesen Rezeptoren aussichtsreich. Dabei könnten die thermodynamisch stabileren *cis*-Isomere inhibierende Eigenschaften aufweisen, welche durch Belichtung mit geeigneter Wellenlänge orts- und zeitaufgelöst durch Isomerisierung zu den *trans*-Isomeren deaktiviert werden könnten. Um etwaige biologische Aktivität für andere Rezeptoren zu erforschen oder eine gesteigerte Selektivität und Affinität zu entwickeln, wären weiterführende theoretische Studien am N-Diazocin möglich. Hier könnte ein breit angelegtes Screening von z. B. unterschiedlich Resten am Brückenstickstoff zielführend sein. Mit Hilfe von DFT-Rechnungen könnten so zeitsparend akkurate Strukturen erhalten werden, welche bereits bekannten inhibierenden Geometrien ähneln. Zusätzlich könnten diese erhaltenen Strukturen in Computer-Dockingstudien an einer Vielzahl von Rezeptorbindetaschen mit Hilfe der Softwaresuite SCHRÖDINGER untersucht werden. Ein so präevaluiertes Design könnte bereits im Vorweg einer aufwendigen und langwierigen Synthese bei gleichzeitiger Einsparung von Kosten und Arbeit die Chancen für das Auffinden eines photoschaltbaren Inhibitors erhöhen.

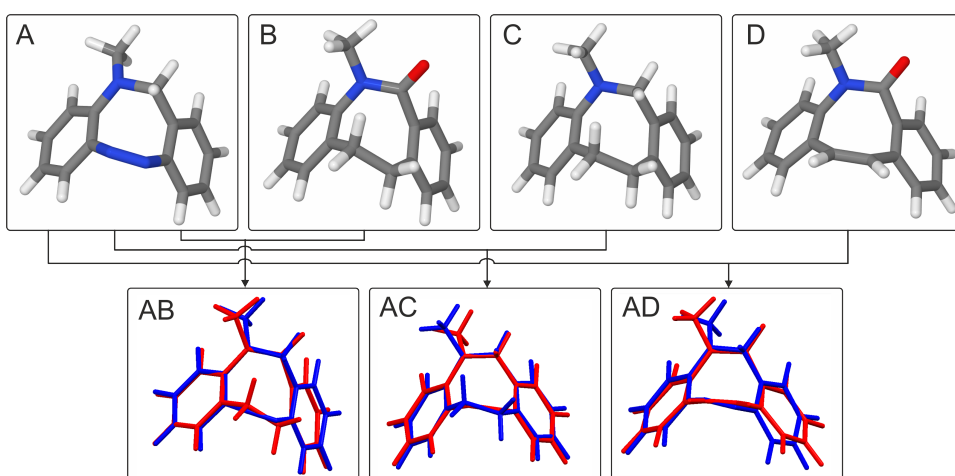


Abb. 7.3: Strukturvergleich des N-Methyl-Diazocins (A) mit dem tricyclischen Kern bereits in Rezeptor- bzw. Inhibitorstudien eingesetzten Dibenzoazocinen (B: Dihydro-Dibenzoazocinon,^[292,293] C: Dihydro-Dibenzoazocin,^[292] D: Dibenzoazocinon^[293]).

Doppelt verbrückte Diazocene

Die vorgestellten Heterodiazocene weisen in vielerlei Hinsicht überlegene Eigenschaften gegenüber dem Stammdiazocin auf. Sie sind jedoch nicht in der Lage, gerichtet zu schalten. Deshalb wurde parallel dazu im Arbeitskreis HERGES ein Diazocinsystem entwickelt, welches auf dem Stammsystem basierend zusätzlich zur einfachen Überbrückung noch mehr Starrheit durch eine weitere Verbrückung erhält. Diese sogenannten Diindandiazocene Moleküle zeigen eine gerichtete Schaltung^[102] und zusätzlich eine enorm hohe Konversionseffizienz von Licht in chemische Energie.

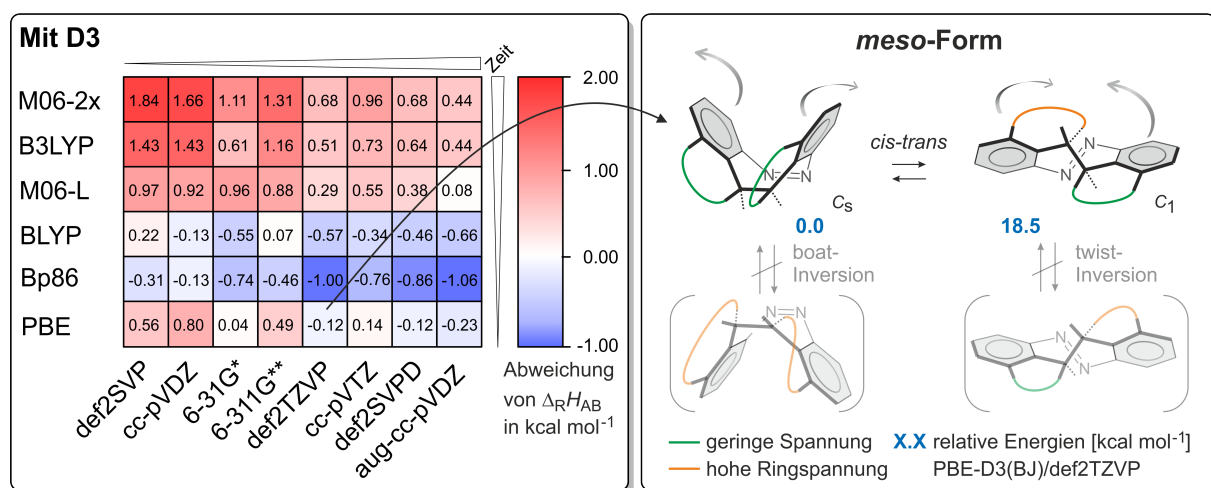


Abb. 7.4: Links: Auszug des Benchmarkings verschiedener DFT-Niveaus an der Isomerisierungsenthalpie von Azobenzol: Dargestellt sind die Abweichungen vom experimentellen Wert. Rechts: Konformationsraum der Konfigurationen des *meso*-Diindandiazocin. Die boat-Inversionen des *cis*-Isomers wird durch Ringspannung sehr ungünstig. Durch Spannung eines Indanringes bei der Isomerisierung entsteht eine relative Energie von 18.5 kcal mol⁻¹ gegenüber der *cis*-Spezies. Die *trans*-Konfiguration ist auf Grund des Designs in nur einem Konformer günstig.

Ein Grund für die hohe Effizienz der Energiekonversion ist die bisher größte ermittelte Quantenausbeute für photoschaltbare Systeme, welche sogar größer als die von Rhodopsin ist. Gepaart mit hohen Konversionsraten und dem erheblichen energetischen Unterschied von $18.5 \text{ kcal mol}^{-1}$ zwischen der stabilen und metastabilen Konfiguration wird eine Energieumwandlung von 18 % erreicht.^[294] Um den energetischen Unterschied der beiden Isomere quantenchemisch möglichst akkurat zu beschreiben, wurde in dieser Arbeit nicht allein auf das generelle Benchmarking von GRIMME^[68] zurückgegriffen, sondern ein Eigenes entwickelt. Da die Diazocine strukturell nahe Verwandte des Azobenzols sind, wurden 96 verschiedene Niveaus der DFT mit den experimentellen Ergebnisse der Isomerisierungsenthalpie von Azobenzol ($\Delta_R H_{AB}$, Auszug s. Abb. 7.4, links) verglichen. Zusätzlich konnte dank erhaltener Einkristallstrukturen der Diindandiazocine ein Strukturvergleich der vielversprechendsten Niveaus des eigenen Benchmarkings durchgeführt werden. So erzielte diese Arbeit das Ergebnis, dass ein weniger rechenintensives Niveau PBE-D3(BJ)/def2TZVP den besten Kompromiss aus Genauigkeit und Aufwand für die Beschreibung der Diindandiazocine darstellt. Ein Einsatz dieser Methode empfiehlt sich daher auch für Berechnungen von anderen Diazocinen.

7.2 Schaltverhalten auf Oberflächen

Da die Schaltung von photoresponsiven Molekülen oder allgemein funktionalen Strukturen nicht nur in Lösung, sondern auch auf Oberflächen für verschiedene Anwendungen von großem Interesse ist, wurden innerhalb des von HERGES entwickelten Plattform-Konzeptes verschiedene Funktionalisierungen auf Triazatriangulene oder Trioxatriangulene aufgebracht.^[102,103,123,127–132,177,295–299] Der Vorteil dieses Konzeptes ist der modulare Aufbau, welcher orthogonal zur Oberfläche stehende Substitutionen am zentralen Kohlenstoffatom der Plattformen ermöglicht. So können durch verschiedene Spacer der Abstand zur Oberfläche und die Kopplung zum Metallsubstrat gezielt eingestellt und je nach gewünschter Anwendung z. B. photoschaltbare Kopfgruppen auf die Plattform und somit auf Oberflächen aufgebracht werden.

Beschleunigte Relaxation auf Gold(111)-Oberflächen

Eine Applikation dieses Plattform-Konzepts sollte der Oberflächentransport von Partikeln sein, welcher durch eine photoinduzierte Schlagbewegung einer schaltbaren Gruppe realisiert werden sollte. Die chemische Umsetzung basierte dabei auf der Zusammensetzung einer Triazatriangulen-Plattform mit Ethinyl-Spacer und dem gut untersuchten Azobenzol.^[125] Experimentell festgestellt wurde bei diesem Setup jedoch ein bisher unerklärtes Phänomen: die auf Gold(111)-Oberflächen aufgetragene, selbst organisierende Monolage (*self-assembled monolayer*) weist eine um mehrere Größenordnungen beschleunigte, thermische Relaxation des Azobenzol auf.^[134,135,137,138]

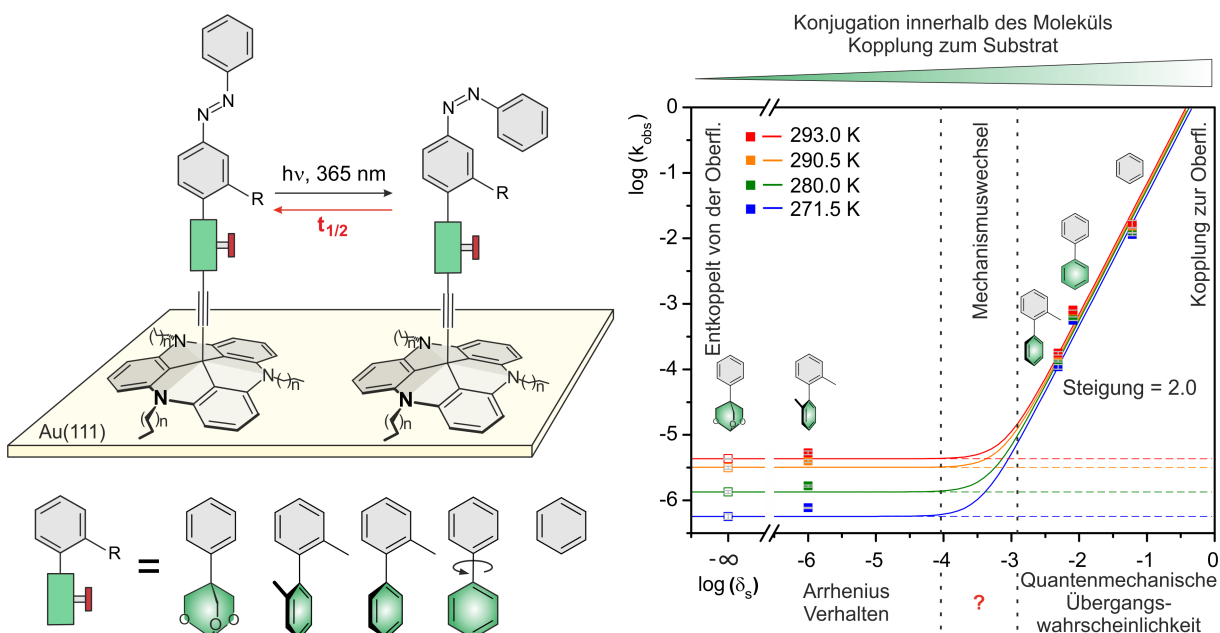


Abb. 7.5: Darstellung der verschiedenen untersuchten TATA-Moleküle (links) und der zugehörigen Korrelation der observierten Relaxationskonstante (k_{obs}) mit der delokalisierte Triplet-Spindichte in der Plattform (δ_S).

Um dieses Phänomen näher zu untersuchen, wurden innerhalb dieser Arbeit ähnliche Moleküle mit Hilfe von DFT-Rechnungen konzeptioniert, welche unterschiedlich starke Konjugation zwischen Plattform und Schalter aufweisen. Die Hypothese, dass die beschleunigte Relaxation in Zusammenhang mit der durch die Stärke der Konjugation gesteuerten Kopplung der funktionellen Gruppe und dem Substrat steht, konnte durch die experimentellen Ergebnisse der synthetisierten Moleküle auf Gold bestätigen werden. Einen wesentlichen Beitrag zur physikalischen Beschreibung des Phänomens lieferten die berechneten Werte der delokalisierten Spindichte der Tripletstruktur in der Plattform. Hieraus ließ sich erst die quadratische Abhängigkeit der Ratenkonstante vom Anteil der delokalisierten Spindichte ableiten. So konnte gezeigt werden, dass ein Substrat-vermitteltes *intersystem crossing* der Ursprung der beschleunigten Relaxation ist. Die Gold(111)-Oberflächen katalysierte Reaktion wird damit je nach Kopplung des Schalters zum Leitungsband des Substrats durch klassisches ARRHENIUS-Verhalten (entkoppelt) oder durch die quantenmechanische Übergangswahrscheinlichkeit (gekoppelt) beschrieben. Ein solcher Mechanismus war bis dato unbekannt und beschreibt einen völlig neuen, im Rahmen dieser Arbeit aufgedeckten Typ von Katalyse.

Eine Möglichkeit, dieses Phänomen weitergehend zu untersuchen, wäre der Einsatz weiterer Regulierungseinheiten (s. Abb. 7.5, links, grünes Ventil). Dabei wäre es interessant, möglichst den Bereich zwischen klassisch adiabatischem Verhalten und dem neuen Mechanismus zu untersuchen. Hierzu könnten erneut quantenmechanische Methoden verwendet werden, um Moleküle zu entwickeln, welche mit ihrem Anteil delokalisierte Spindichte im Bereich des Mechanismuswechsels liegen.

Da dieser neue Katalysetyp bisher nur mit Azobenzol als photochromer Gruppe nachgewiesen werden konnte, sollten für fortschreitende Untersuchungen bei ähnlichem Aufbau andere schaltbare Systeme eingesetzt werden. Hierfür konnten zwei andere photoresponsive Gruppen auf die Plattformen aufgebracht werden. Zum einen wurde das bekannte Stammdiazocin in unterschiedlich stark konjugierten Positionen (*meta* und *para*) und zum anderen ein Norbornadien auf der Plattform positioniert.^[301,302]

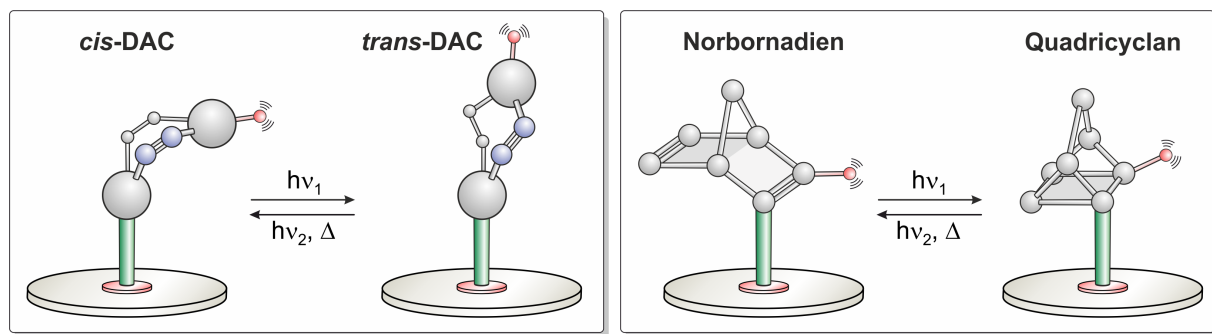


Abb. 7.6: Schematische Darstellung anderer Schalter auf Plattformen zur Untersuchung des neuen Katalysemechanismus.

Interessant ist das Diazocinsystem, da es thermodynamisch als *cis*-Isomer stabil ist und von der *trans* zur *cis*-Konfiguration thermisch relaxiert. DFT-Rechnungen dieser Arbeit, welche durch experimentelle Bestimmung der thermischen Relaxationsbarrieren in Lösung von dem Kooperationspartner LÖW bestätigt wurden, zeigten für die beiden unterschiedlich substituierten Diazocinsysteme sehr ähnliche Barrieren und somit eine ideale Grundlage, etwaigen Einfluss einer Substrat-vermittelten Katalyse zu untersuchen. Erste Rastertunnelmikroskop (*scanning tunneling microscope*)-Experimente der Kooperationspartnerin RUSCH zeigten dazu, dass auch diese Moleküle selbst organisierende Monolagen bilden und somit mittels Oberflächen-sensitiven Methoden auf ihre kinetischen Schalteigenschaften untersucht werden könnten. Die Möglichkeit einen grundsätzlich anderen Reaktionstyp zu betrachten, bietet das Konzept mit Norbornadien als Kopfgruppe. Bei diesem Konzept könnte statt einer *cis/trans*-Isomerisierung die photochemische [2+2] Cycloaddition von Norbornadien zum Quadricyclan und die thermische Relaxation ([2+2] Cycloreversion) zurück zum Norbornadien auf der Oberfläche untersucht werden. Erste theoretische Ergebnisse dieser Arbeit hierzu sowie die Synthese und anschließende erfolgreiche Vermessung von intakten Monolagen durch Kooperationspartner konnten bereits publiziert werden. Somit wurden in Kooperation zwei mögliche neue Systeme für die Untersuchung des neuartigen Gold-vermittelten Katalysetyps entwickelt. Der nächste Schritt für quantenmechanische Rechnungen zu diesen neuen Systemen ist analog zu den Azobenzol-Ethinylen-Triazatriangulenen die Ausführung und Auswertung von Spindichte-Rechnungen von Triplett-Strukturen. So würden bereits vor der Durchführung von zeitaufwendigen Experimenten, Einblicke in das Schaltverhalten ermöglicht sowie etwaige Reaktionspfade über eine Triplett-Hyperfläche untersucht werden.

Laterale Schalter und Rotoren auf Oberflächen

Ein 2015 entwickeltes Molekül besteht aus zwei lateral über ein Azobenzol verknüpfte Triazatriangulen-Plattformen, mit dem das Konzept einer muskelartigen Bewegung (Bewegung der Plattformen) auf Oberflächen realisiert werden sollte.^[177] Die geplante Adsorption der Moleküle auf Goldoberflächen, bei der das reversible Schaltverhalten erhalten blieb, konnte 2019 realisiert werden. Die Bewegung der Plattformen war jedoch trotz nachgewiesener Schaltung nicht zu beobachten.^[300] Problematisch war zunächst die strukturelle Interpretation der STM-Bilder, welche schließlich durch die in dieser Arbeit durchgeföhrten quantenchemischen Rechnungen erst ermöglicht worden ist.

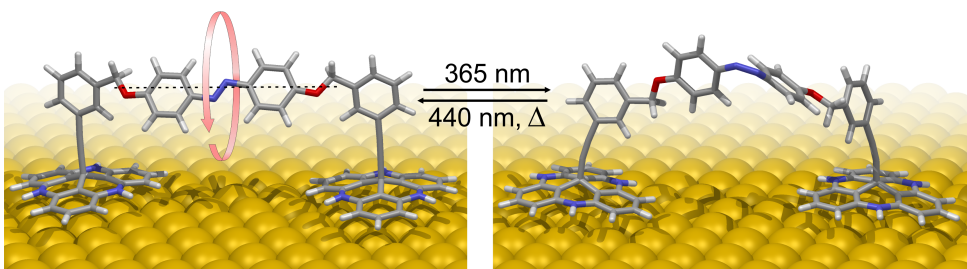


Abb. 7.7: Darstellung vom freien Schaltmechanismus des über zwei TATA-Plattformen mit freier Rotationsachse verbundenen Azobenzols.

Die Rechnungen zu diesem Moleköl zeigten, dass ein lateraler Rotor mit freier altitudinaler Drehbarkeit (s. Abb. 7.7) im thermischen Gleichgewicht vorliegt. Dieser Rotor kann mittels Photoanregung zur *cis*-Konfiguration isomerisieren, wodurch die freie Rotation aufgehoben wird. Dabei verändern die Plattformen ihre Position auf der Oberfläche nicht, lediglich der Aufbau ändert seine Konformation. Grund dafür ist die enge Packung der Moleküle auf der Oberfläche, die eine Verschiebung der Plattformen und damit die muskelartige Bewegung verhindert. Dieses Konzept ermöglicht eine elektronische, zur Oberfläche entkoppelte schaltbare altitudinale Rotation.

7.3 Konzepte von Delokalisierung und Aromatizität

Die 2001 von HERGES *et al.* entwickelte ACID-Methode ermöglicht es, qualitativ wie quantitativ Rückschlüsse auf die Delokalisierung von Elektronen in Molekülen zu ziehen und ist somit sehr gut für die Erklärung und Beschreibung von konjugierten Systemen geeignet.^[197,198,303] Zusätzlich ist die Methode durch die Visualisierung von para- oder diatropen Ringströmen unverzichtbar geworden, um verschiedene Konzepte von Aromatizität nachzuweisen.^[304–310] Deshalb wurde die ACID-Methode in verschiedenen Nebenprojekten dieser Doktorarbeit verwendet, um elektronische Delokalisierung und Konjugation zu visualisieren, zu analysieren und auf Aromatizität zu überprüfen.

Möbius-Topologie und -aromatizität

Zusammen mit verschiedenen anderen Methoden konnte ACID in dieser Arbeit dazu entscheidend beitragen MÖBIUS-Aromatizität^[246] in neuen Molekülen zu belegen, welche von den Kooperationspartnern DUROLA *et al.* aus drei [5]Helicen-Untereinheiten zu PPM- und PPP-Tris-[5]helicens zusammengesetzt wurden.^[311] In diesen Molekülen gibt es unterschiedliche Elektronenpfade, welche ein- bzw. dreifach gedrehte (*Twist*) MÖBIUS-Topologie mit ungerader Verknüpfungszahl^[312,313] innerhalb des intakten konjugierten $4n$ -Elektronensystems aufweisen. Durch die weiterführenden ACID- und HOMA (*harmonic oscillator model of aromaticity*)^[183,184]-Analysen konnte im inneren σ -Elektronenpfad paratropen und im äußeren π -Pfad diatropen Ringstrom nachgewiesen werden. Dies ist dem HÜCKEL-aromatichen Benzol äußerst ähnlich,^[314–316] die Ströme jedoch heben sich in den vorliegenden MÖBIUS-Systemen komplett auf, was durch ^1H -NMR-Experimente der genannten Partner und durch in dieser Arbeit ermittelte Werte für die kernunabhängige chemische Verschiebung (*nucleus-independent chemical shift*, NICS)^[180–182] belegt wird.

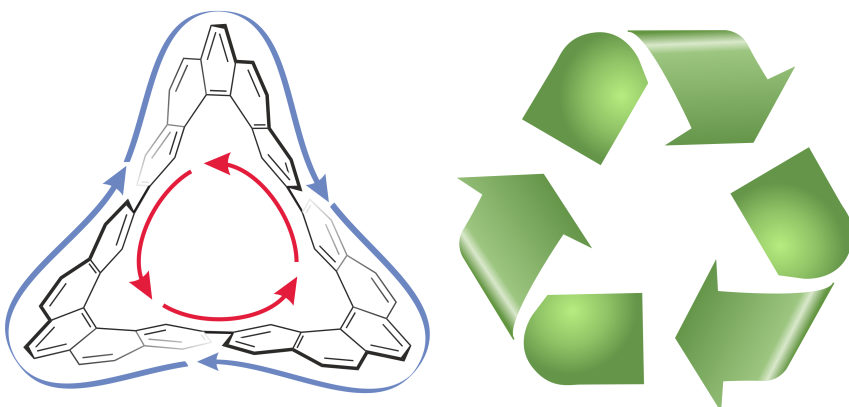


Abb. 7.8: Ähnlichkeit der PPP-Tris-[5]helicens Struktur mit dem alltäglichen Recyclingsymbol. Beide Strukturen weisen MÖBIUS-Topologie auf. Im Molekül gibt es unterschiedliche $4n\pi$ -Elektronenpfade mit ungerader Verknüpfungszahl: der innere weist diatropen somit MÖBIUS-antiaromatischen und der äußere Pfad paratropen somit MÖBIUS-aromatischen Ringstrom auf.

Insgesamt ergibt sich demnach ein sehr spezielles System: Einerseits ist es nach der Theorie MÖBIUS-aromatisch, in der Gesamtheit aber ein nicht aromatisches System. Um solche komplexen topologischen Moleküle weitergehend mit ACID zu untersuchen und herauszufinden, warum z. B. der paratropen innere Strom so stark ausgeprägt ist, könnten zunächst weitere [n]Helicene mit unterschiedlicher Anzahl an Untereinheiten untersucht werden. Zusätzlich könnten für ein allgemeineres Verständnis von großen cyclischen Elektronenpfaden bekannte Nanogürtel-Systeme^[317,318] systematisch mit ACID analysiert werden. Dabei ließen sich exemplarisch Cyclacene^[319–321] oder ähnliche, bereits synthetisierte oder vorgeschlagene Gürtelsysteme auf Ringströme untersuchen. Abbildung 7.9 zeigt weitere Modellsysteme (z. B. das [10]Cyclacen aus

Kapitel 5.3, Abb. 5.3), die mit der ACID-Methode untersucht werden sollten, um die Ringströme in komplizierten, verdrillten Systemen zu verstehen.

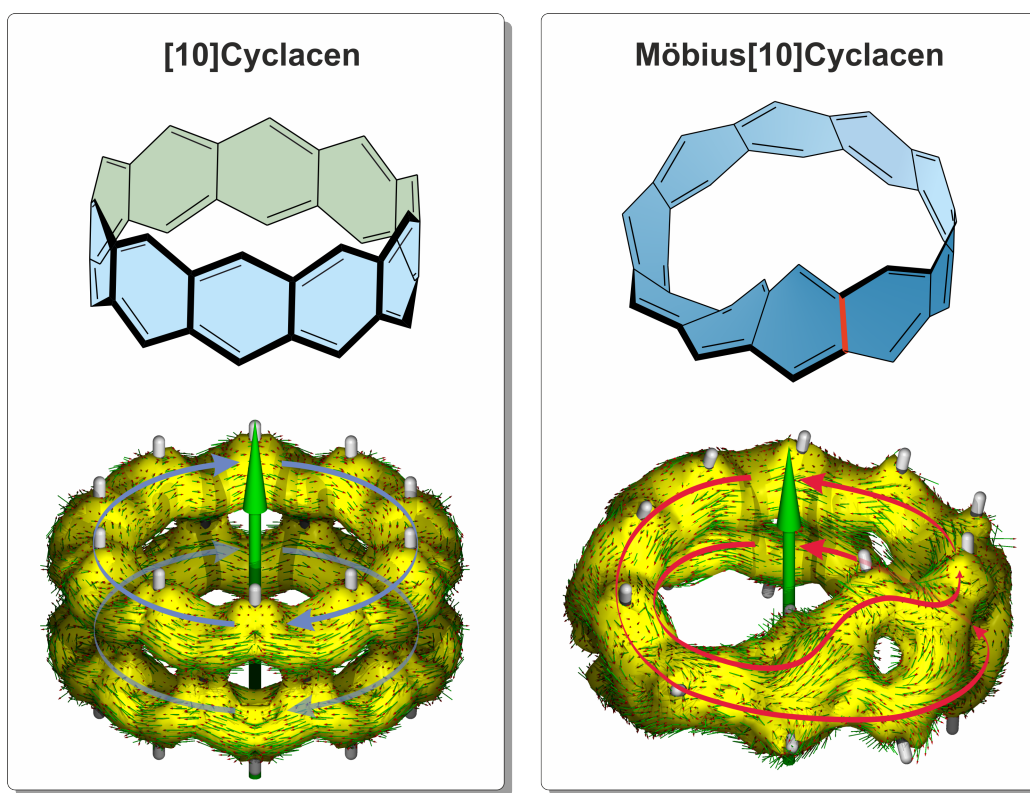


Abb. 7.9: ACID-Vergleich des [10]Cyclacens mit seinem MÖBIUS-Analogon (Strukturen: PBE/def2SVP; ACID: B3LYP/6-311+G*, Isooberflächenwert (*isosurface value*, IV) : 0.050, Magnetfeldvektor: grüner Pfeil): Links ist HÜCKEL-aromatisches Verhalten in zwei getrennt voneinander existenten 20π -Elektronensystemen mit diatropen Ringstrom zu erkennen. Komplizierter ist die Analyse der Stromdichtevektoren für das MÖBIUS-[10]Cyclacen: Die Ringstromanalyse zeigt keinen klar auswertbaren Verlauf.

Stereo- und Regiochemie-Vorhersage

Der Einsatz von ACID ist aber nicht nur auf Ringströme begrenzt, sondern liefert auch allgemein Informationen zur Delokalisierung oder Ausbildung von Konjugation.^[198,322] Dank quantitativer ACID-Analyse Auswertung konnte eine Erklärung für die Regiochemie der DIELS-ALDER-Reaktion von Isobenzofuran mit Chlorinen erbracht werden.^[323] So konnte die Addition an die vom aromatischen System separierte und dadurch reaktivere Bindung eindeutig erklärt und vorhergesagt werden (rote Pfeile Abb. 7.10).

Je nachdem ob das Molekül als freie Base oder mit eingelagertem Nickel vorliegt, entstehe ein anderes Regioisomer (s. Abb. 7.10 rechts). Zusätzlich wurde durch umfangreiche Berechnungen aller möglichen Stereo- und Regioisomere, sowie deren zugehörigen Übergangszustände (*transition states*, TS) durch diese Arbeit eine nahezu exakte Vorhersage der erst einfachen und dann doppelten Addition getroffen. Entscheidend hierfür war die Erkenntnis der Ausbildung eines

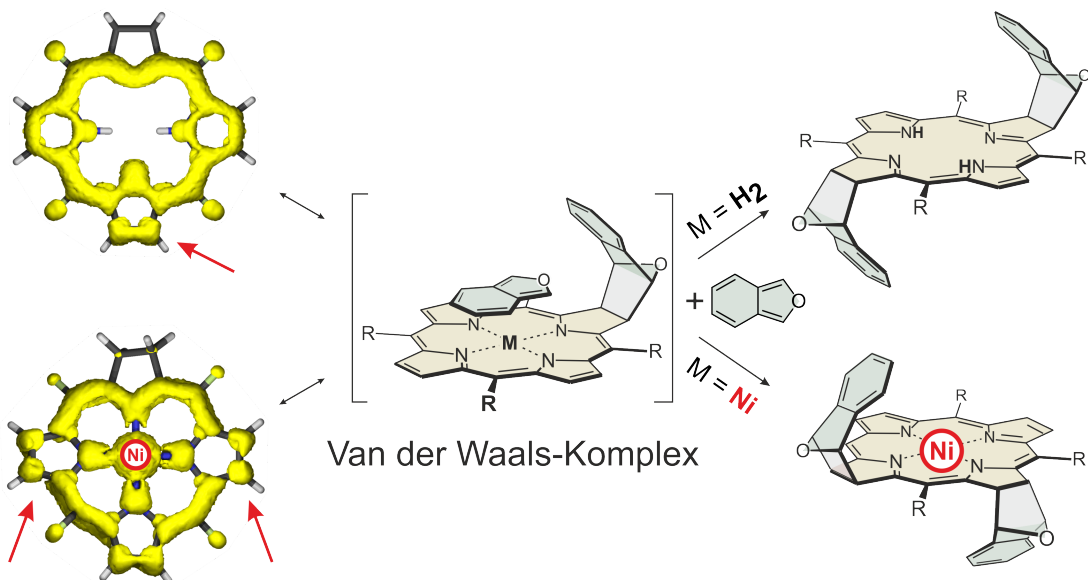


Abb. 7.10: Regioselektivität der Addition von Isobenzofuran an Chlorine mit und ohne Nickel als Metallzentrum. Die ACID-Plots der Edukte zeigen die schwächer konjugierten *meso*-Positionen (rote Pfeile), welche die entsprechenden C=C-Doppelbindungen vom restlichen 18- π -Elektronensystem separieren und daher mit dem Isobenzofuran reagieren. Entscheidend für die Reaktionsberechnung ist der dargestellte VAN-DER-WAALS-Komplex, welcher sich vor der Reaktionen bildet und somit berücksichtigt werden muss.

VAN-DER-WAALS-Komplexe, dessen Berechnung zwingend den Einsatz einer Dispersionskorrektur (z. B. nach Grimme D3) erfordert,^[324,325] da die einfache Dichtefunktionaltheorie die London-Dispersions-Wechselwirkung häufig nicht ausreichend berücksichtigt.^[325–327]

Lediglich für die zweifache Addition an der freien Base wurde ein anderer Reaktionsausgang beobachtet als von der theoretischen Betrachtung vorausgesagt wurde. Da eine Auswertung bisher nur über die Reaktionsenthalpien erfolgte, sind weiterführende quantenchemische Rechnungen zielführend, um die theoretische Voraussage des Reaktionsausgangs noch weiter zu präzisieren. Neben der Einführung von entropischen Effekten durch Frequenzanalysen wäre auch eine Lösungsmittel-Korrektur denkbar, um dieses Ziel zu erreichen.

Through Space-Konjugation

In einem weiteren Projekt konnte elektronische Delokalisierung zwischen zwei Atomen ohne kovalente Bindung erfolgreich mit der ACID-Methode visualisiert werden. In Hexaphenylbenzol konnte schon von anderen das Konzept der toroidalen *through space*-Konjugation zwischen den *ipso*-Kohlenstoffen vermutet bzw. teilweise nachgewiesen werden.^[272–274,328] Basierend auf diesem Konzept wurden durch BÄUERLE *et al.* mehrere komplexe Moleküle synthetisiert, die elektronenreiche Thiophene als Substituenten tragen und auf Biphenylenkernen als zentralen Baustein aufbauen.

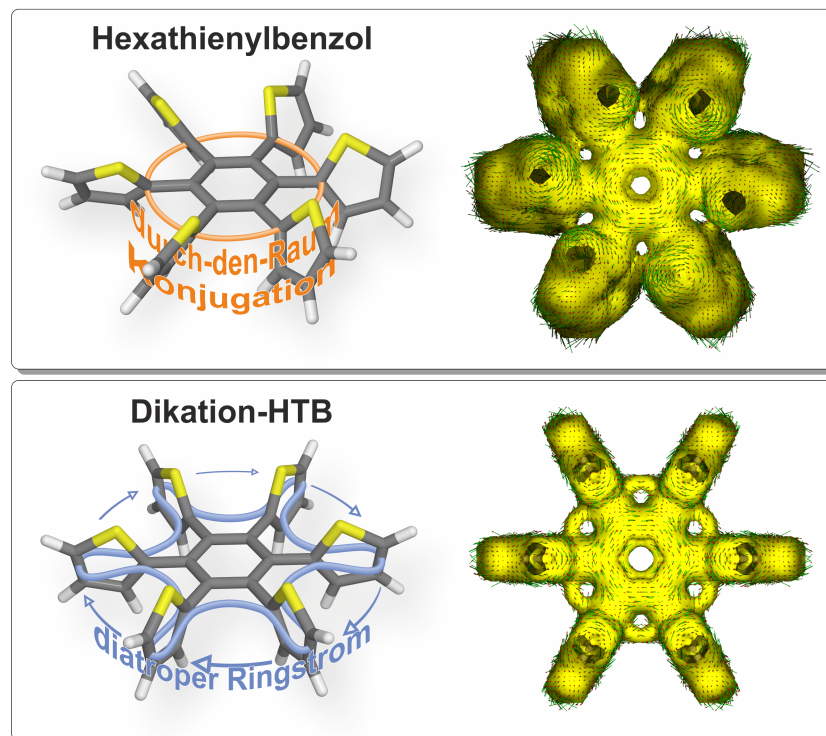


Abb. 7.11: Schematische Darstellung der ACID-Ergebnisse für Hexathiarylbenzol (HTB). Der ACID-Plot des neutralen HTB (oben, Struktur M062X-D3/def2TZVP, ACID: B3LYP/6-311+G*, Magnetfeldvektor zeigt zum Betrachter) zeigt die schwach vorhandene (IV: 0.008) *through space*-Konjugation. ACID zeigt für das Dikation des HTB (unten, in c_{6v} optimiert, ACID: B3LYP/6-311+G*/M062X-D3/def2TZVP, Magnetfeldvektor zeigt zum Betrachter) die deutlich stärker ausgeprägte Konjugation (IV: 0.015) mit zusätzlich diatropem Ringstrom.

Erstmals konnte ACID in dieser Arbeit graphisch die Überlappung der Orbitale durch den freien Raum (s. Abb. 7.11, oben) bei dem bereits etablierten Hexaphenylbenzol, dem neuen Hexathiarylbenzol und im besonderen Fall der Biphenyle eine verkettete toroidale Konjugation der *ipso*-Kohlenstoffe abbilden.^[329] Weitere Rechnungen sagen voraus, dass die entsprechenden, geladenen Moleküle (z. B. Radikalkationen oder Dikationen) sehr viel stärkere *through-space*-Ringströme zwischen den *ipso*-Kohlenstoffatomen aufweisen. Modellrechnungen hierzu am Dikation (s. Abb. 7.11, unten) sehen vielversprechend aus. Diese weisen deutlich erhöhte *through space*-Konjugation mit diatropem Ringstrom auf. Die Beispiele zeigen, dass mit der ACID-Methode elektronische Effekte analysiert und visualisiert werden können, die sich einer einfachen Valenzband- oder Molekülorbital-Betrachtung entziehen. Dies macht sie zu einem wertvollen Werkzeug für das Design von optoelektronischen Materialien.

Anhang

8

Begleitmaterial (Supporting Information) zu den Publikationen

Nitrogen Bridged Diazocines: Photochromes Switching within the Near-Infrared Region with High Quantum Yields in Organic Solvents and in Water

P. Lentes, E. Stadtler, F. Röhricht, A. Brahms, J. Gröbner, F. D. Sönnichsen, G. Gescheidt und
R. Herges

J. Am. Chem. Soc. **2019**, *141*, 13592–13600.

DOI:10.1021/jacs.9b06104

DVD: Kapitel 1

Hyperlink: Supporting Information

Efficient Conversion of Light to Chemical Energy: Directional, Chiral Photoswitches with Very High Quantum Yields

W. Moormann, T. Tellkamp, E. Stadler, F. Röhricht, C. Näther, R. Puttreddy, K. Rissanend, G. Gescheidt und R. Herges

Angew. Chem. **2020**, *59*, 15081-15086.

DOI:10.1002/anie.202005361

Deutsche Version: DOI:10.1002/ange.202005361

DVD: Kapitel 2

Hyperlink: Supporting Information

Long-Distance Rate Acceleration by Bulk Gold

A. Schlimm, R. Löw, T. Rusch, F. Röhricht, T. Strunskus, T. Tellkamp, F. Sönnichsen, U. Mathe,
O. Magnussen, F. Tuczek und R. Herges

Angew. Chem. Int. Ed. **2019**, *58*, 6574–6578.

DOI:10.1002/anie.201814342

DVD: Kapitel 3

Hyperlink: Supporting Information

Diazocine-functionalized TATA platforms

R. Löw, T. Rusch, F. Röhricht, O. Magnussen und R. Herges

Beilstein J. Org. Chem. **2019**, *15*, 1485–1490.

DOI:10.3762/bjoc.15.150

DVD: Kapitel 4

Hyperlink: Supporting Information

Ordered Adlayers of a Combined Lateral Switch and Rotor

T. R. Rusch, A. Schlimm, N. R. Krekiehn, B. M. Flöser, F. Röhricht, M. Hammerich, I. Lautenschläger, T. Strunskus, R. Herges, F. Tuczek und O. Magnussen

J. Phys. Chem. C **2019**, *123*, 13720–13730.

DOI:10.1021/acs.jpcc.9b02469

DVD: Kapitel 5

Hyperlink: Supporting Information

One-Pot Approach to Chlorins, Isobacteriochlorins, Bacteriochlorins, and Pyrrocorphins

M. K. Peters, F. Röhricht, C. Näther und R. Herges

Org. Lett. **2018**, *20*, 7879–7883.

DOI:10.1021/acs.orglett.8b03433

DVD: Kapitel 6

Hyperlink: Supporting Information

Cyclic tris-[5]helicenes with single and triple twisted Möbius topologies and Möbius aromaticity

G. Naulet, L. Sturm, A. Robert, P. Dechambenoit, F. Röhricht, R. Herges, H. Bock und F. Durola

Chem. Science **2018**, 9, 8930–8936.

DOI:10.1039/c8sc02877j

DVD: Kapitel 7

Hyperlink: Supporting Information

Twisted Thienylene–Phenylene Structures: Through-Space Orbital Coupling in Toroidal and Catenated Topologies

T. D. Leitner, Y. Gmeinder, F. Röhricht, R. Herges, E. Mena-Osteritz und P. Bäuerle

Eur. J. Org. Chem. **2020**, 3, 285–294.

DOI:10.1002/ejoc.201901637

DVD: Kapitel 8

Hyperlink: Supporting Information

Literaturverzeichnis

- [1] R. Huber, *Angew. Chem.* **1989**, *101*, 849–871.
- [2] J. Deisenhofer, H. Michel, *Angew. Chem. Int. Ed.* **1989**, *28*, 829–847.
- [3] H. Kinzel, *Biol. unserer Zeit* **1981**, *11*, 48–57.
- [4] F. Lipmann, In *Advances in Enzymology and Related Areas of Molecular Biology*. John Wiley & Sons, Ltd **2006**, 99–162.
- [5] R. D. Vale, R. A. Milligan, *Science* **2000**, *288*, 88–95.
- [6] R. D. Vale, *Cell* **2003**, *112*, 467–480.
- [7] A. S. Shah, Y. Ben-Shahar, T. O. Moninger, J. N. Kline, M. J. Welsh, *Science* **2009**, *325*, 1131–1134.
- [8] M. v. Delius, D. A. Leigh, *Chem. Soc. Rev.* **2011**, *40*, 3656–3676.
- [9] A. J. Berdis, *Chem. Rev.* **2009**, *109*, 2862–2879.
- [10] K. S. Murakami, S. A. Darst, *Curr. Opin. Struct. Biol.* **2003**, *13*, 31–39.
- [11] K. Kinbara, T. Aida, *Chem. Rev.* **2005**, *105*, 1377–1400.
- [12] G. Moore, *Proc. IEEE* **1998**, *86*, 82–85.
- [13] P. K. Bondyopadhyay, *Proc. IEEE* **1998**, *86*, 78–81.
- [14] M. M. Waldrop, *Nature News* **2016**, *530*, 144.
- [15] Y. Xia, *Angew. Chem. Int. Ed.* **2014**, *53*, 12265–12265.
- [16] M. Seifert, *Angew. Chem. Int. Ed.* **2017**, *56*, 7351–7351.
- [17] S. Shinkai, T. Nakaji, Y. Nishida, T. Ogawa, O. Manabe, *J. Am. Chem. Soc.* **1980**, *102*, 5860–5865.
- [18] P. L. Anelli, N. Spencer, J. F. Stoddart, *J. Am. Chem. Soc.* **1991**, *113*, 5131–5133.

Literaturverzeichnis

- [19] T. R. Kelly, H. De Silva, R. A. Silva, *Nature* **1999**, *401*, 150–152.
- [20] N. Kourumura, R. W. J. Zijlstra, R. A. van Delden, N. Harada, B. L. Feringa, *Nature* **1999**, *401*, 152–155.
- [21] J. D. Badjić, V. Balzani, A. Credi, S. Silvi, J. F. Stoddart, *Science* **2004**, *303*, 1845–1849.
- [22] V. Ferri, M. Elbing, G. Pace, M. D. Dickey, M. Zharnikov, P. Samorì, M. Mayor, M. A. Rampi, *Angew. Chem.* **2008**, *120*, 3455–3457.
- [23] Y. Shirai, A. J. Osgood, Y. Zhao, K. F. Kelly, J. M. Tour, *Nano Lett.* **2005**, *5*, 2330–2334.
- [24] T. Kudernac, N. Ruangsrapichat, M. Parschau, B. Maciá, N. Katsonis, S. R. Harutyunyan, K.-H. Ernst, B. L. Feringa, *Nature* **2011**, *479*, 208–211.
- [25] T. Muraoka, K. Kinbara, Y. Kobayashi, T. Aida, *J. Am. Chem. Soc.* **2003**, *125*, 5612–5613.
- [26] J. Berná, D. A. Leigh, M. Lubomska, S. M. Mendoza, E. M. Pérez, P. Rudolf, G. Teobaldi, F. Zerbetto, *Nat. Mater.* **2005**, *4*, 704–710.
- [27] Y. Liu, A. H. Flood, P. A. Bonvallet, S. A. Vignon, B. H. Northrop, H.-R. Tseng, J. O. Jeppesen, T. J. Huang, B. Brough, M. Baller, S. Magonov, S. D. Solares, W. A. Goddard, C.-M. Ho, J. F. Stoddart, *J. Am. Chem. Soc.* **2005**, *127*, 9745–9759.
- [28] Q. Li, G. Fuks, E. Moulin, M. Maaloum, M. Rawiso, I. Kulic, J. T. Foy, N. Giuseppone, *Nat. Nanotechnol.* **2015**, *10*, 161–165.
- [29] B. Lewandowski, G. D. Bo, J. W. Ward, M. Papmeyer, S. Kuschel, M. J. Aldegunde, P. M. E. Gramlich, D. Heckmann, S. M. Goldup, D. M. D’Souza, A. E. Fernandes, D. A. Leigh, *Science* **2013**, *339*, 189–193.
- [30] G. De Bo, M. A. Y. Gall, M. O. Kitching, S. Kuschel, D. A. Leigh, D. J. Tetlow, J. W. Ward, *J. Am. Chem. Soc.* **2017**, *139*, 10875–10879.
- [31] D. A. Leigh, *Angew. Chem. Int. Ed.* **2016**, *55*, 14506–14508.
- [32] V. Balzani, A. Credi, F. M. Raymo, J. F. Stoddart, *Angew. Chem. Int. Ed.* **2000**, *39*, 3348–3391.
- [33] W. R. Browne, B. L. Feringa, *Nat. Nano.* **2006**, *1*, 25–35.
- [34] E. R. Kay, D. A. Leigh, F. Zerbetto, *Angew. Chem. Int. Ed.* **2007**, *46*, 72–191.
- [35] E. R. Kay, D. A. Leigh, *Angew. Chem.* **2015**, *127*, 10218–10226.
- [36] J.-P. Sauvage, *Angew. Chem. Int. Ed.* **2017**, *56*, 11080–11093.

- [37] Y. Hirshberg, E. Fischer, *J. Chem. Soc.* **1954**, 3129–3137.
- [38] R. Klajn, *Chem. Soc. Rev.* **2014**, *43*, 148–184.
- [39] M. Schulz-Senft, P. J. Gates, F. D. Sönnichsen, A. Staubitz, *Dyes Pigm.* **2017**, *136*, 292–301.
- [40] M. Irie, *Chem. Rev.* **2000**, *100*, 1685–1716.
- [41] M. Irie, *Pure Appl. Chem.* **1996**, *68*, 1367–1371.
- [42] M. Irie, M. Mohri, *J. Org. Chem.* **1988**, *53*, 803–808.
- [43] A. R. Santos, R. Ballardini, P. Belser, M. T. Gandolfi, V. M. Iyer, L. Moggi, *Photochem. Photobiol. Sci.* **2009**, *8*, 1734–1742.
- [44] Y. Yokoyama, *Chem. Rev.* **2000**, *100*, 1717–1740.
- [45] B. L. Feringa, R. A. van Delden, N. Koumura, E. M. Geertsema, *Chem. Rev.* **2000**, *100*, 1789–1816.
- [46] W. G. Dauben, R. L. Cargill, *Tetrahedron* **1961**, *15*, 197–201.
- [47] J. Orrego-Hernández, A. Dreos, K. Moth-Poulsen, *Acc. Chem. Res.* **2020**, *53*, 1478–1487.
- [48] G. N. Lewis, T. T. Magel, D. Lipkin, *J. Am. Chem. Soc.* **1940**, *62*, 2973–2980.
- [49] D. H. Waldeck, *Chem. Rev.* **1991**, *91*, 415–436.
- [50] H. Meier, *Angew. Chem. Int. Ed.* **1992**, *31*, 1399–1420.
- [51] H. Weir, M. Williams, R. M. Parrish, E. G. Hohenstein, T. J. Martínez, *J. Phys. Chem. B* **2020**, *124*, 5476–5487.
- [52] G. S. Hartley, *Nature* **1937**, *140*, 281–281.
- [53] E. Fischer, M. Frankel, R. Wolovsky, *J. Chem. Phys.* **1955**, *23*, 1367–1367.
- [54] J. Griffiths, *Chem. Soc. Rev.* **1972**, *1*, 481–493.
- [55] P. Cattaneo, M. Persico, *Phys. Chem. Chem. Phys.* **1999**, *1*, 4739–4743.
- [56] T. Ishikawa, T. Noro, T. Shoda, *The Journal of Chemical Physics* **2001**, *115*, 7503–7512.
- [57] H. M. Dharmika Bandara, S. C. Burdette, *Chem. Soc. Rev.* **2012**, *41*, 1809–1825.
- [58] S. Ornes, *PNAS* **2018**, *115*, 9327–9330.

Literaturverzeichnis

- [59] E. R. Kay, D. A. Leigh, *Angew. Chem. Int. Ed.* **2015**, *54*, 10080–10088.
- [60] A. Lehmann, C. D. Maranas, *Ind. Eng. Chem. Res.* **2004**, *43*, 3419–3432.
- [61] M. Jacoby, *Chemical & Engineering News* **2015**, *93*.
- [62] B. Oruganti, J. Wang, B. Durbejj, *Int. J. Quantum Chem.* **2018**, *118*, e25405.
- [63] I. E. Steinmark, *RSC Education* **2017**.
- [64] N. S. V. Barbosa, E. R. d. A. Lima, F. W. Tavares, In *Reference Module in Chemistry, Molecular Sciences and Chemical Engineering*. Elsevier **2017**.
- [65] S. Grimme, P. R. Schreiner, *Angew. Chem. Int. Ed.* **2018**, *57*, 4170–4176.
- [66] F. Jensen, *Introduction to Computational Chemistry: Second Edition*, 2. Aufl., JW, Chichester, England ; Hoboken, NJ **2011**.
- [67] W. Thiel, *WIREs Comput. Mol. Sci.* **2014**, *4*, 145–157.
- [68] L. Goerigk, A. Hansen, C. Bauer, S. Ehrlich, A. Najibi, S. Grimme, *Phys. Chem. Chem. Phys.* **2017**, *19*, 32184–32215.
- [69] L. Goerigk, N. Mehta, *Aust. J. Chem.* **2019**, *72*, 563–573.
- [70] P. Hohenberg, W. Kohn, *Phys. Rev.* **1964**, *136*, B864–B871.
- [71] W. Kohn, L. J. Sham, *Phys. Rev.* **1965**, *140*, A1133–A1138.
- [72] J. Tao, J. P. Perdew, V. N. Staroverov, G. E. Scuseria, *Phys. Rev. Lett.* **2003**, *91*, 146401.
- [73] D. C. Patton, M. R. Pederson, *Phys. Rev. A* **1997**, *56*, R2495–R2498.
- [74] Y. Zhang, W. Pan, W. Yang, *J. Chem. Phys.* **1997**, *107*, 7921–7925.
- [75] J. M. Pérez-Jordá, E. San-Fabián, A. J. Pérez-Jiménez, *J. Chem. Phys.* **1999**, *110*, 1916–1920.
- [76] J. P. Perdew, K. Schmidt, *AIP Conference Proceedings* **2001**, *577*, 1–20.
- [77] R. Peverati, D. G. Truhlar, *Philosophical Transactions of the Royal Society A: Mathematical, Physical and Engineering Sciences* **2014**, *372*, 20120476.
- [78] A. D. Becke, *Phys. Rev. A* **1988**, *38*, 3098–3100.
- [79] C. Lee, W. Yang, R. G. Parr, *Phys. Rev. B* **1988**, *37*, 785–789.
- [80] B. Miehlich, A. Savin, H. Stoll, H. Preuss, *Chem. Phys. Lett.* **1989**, *157*, 200–206.

- [81] J. P. Perdew, K. Burke, M. Ernzerhof, *Phys. Rev. Lett.* **1996**, *77*, 3865–3868.
- [82] Y. Zhao, D. G. Truhlar, *J. Chem. Phys.* **2006**, *125*, 194101.
- [83] J. Jaramillo, G. E. Scuseria, M. Ernzerhof, *J. Chem. Phys.* **2003**, *118*, 1068–1073.
- [84] J. K. Desmarais, J.-P. Flament, A. Erba, *J. Phys. Chem. Lett.* **2019**, *10*, 3580–3585.
- [85] M. Ernzerhof, G. E. Scuseria, *J. Chem. Phys.* **1999**, *110*, 5029–5036.
- [86] C. Adamo, V. Barone, *J. Chem. Phys.* **1999**, *110*, 6158–6170.
- [87] A. D. Becke, *J. Chem. Phys.* **1993**, *98*, 5648–5652.
- [88] Y. Zhao, D. G. Truhlar, *Theor Chem Account* **2008**, *120*, 215–241.
- [89] L. Goerigk, S. Grimme, *WIREs Comput. Mol. Sci.* **2014**, *4*, 576–600.
- [90] S. Grimme, *J. Chem. Phys.* **2006**, *124*, 034108.
- [91] R. Car, *Nat. Chem.* **2016**, *8*, 820–821.
- [92] H. Duval, *Bull. Soc. Chim. Fr.* **1910**, *4*, 727–732.
- [93] R. Siewertsen, H. Neumann, B. Buchheim-Stehn, R. Herges, C. Näther, F. Renth, F. Temps, *J. Am. Chem. Soc.* **2009**, *131*, 15594–15595.
- [94] R. Siewertsen, *Dissertation*, Christian-Albrechts-Universität zu Kiel **2011**.
- [95] X.-M. Liu, X.-Y. Jin, Z.-X. Zhang, J. Wang, F.-Q. Bai, *RSC Adv.* **2018**, *8*, 11580–11588.
- [96] V. Ladányi, P. Dvořák, J. A. Anshori, L. Vetráková, J. Wirz, D. Heger, *Photochem. Photobiol. Sci.* **2017**, *16*, 1757–1761.
- [97] J. Harada, K. Ogawa, S. Tomoda, *Acta Crystallogr. B Struct. Sci.* **1997**, *53*, 662–672.
- [98] J. Harada, K. Ogawa, *J. Am. Chem. Soc.* **2004**, *126*, 3539–3544.
- [99] M. Hammerich, C. Schütt, C. Stähler, P. Lentes, F. Röhricht, R. Höppner, R. Herges, *J. Am. Chem. Soc.* **2016**, *138*, 13111–13114.
- [100] H. Sell, C. Näther, R. Herges, *Beilstein J. Org. Chem.* **2013**, *9*, 1–7.
- [101] R. R. Anderson, J. A. Parrish, *J. Invest. Dermatol.* **1981**, *77*, 13–19.
- [102] T. Tellkamp, *Dissertation*, Christian-Albrechts-Universität zu Kiel **2014**.
- [103] T. Tellkamp, J. Shen, Y. Okamoto, R. Herges, *Eur. J. Org. Chem.* **2014**, *2014*, 5456–5461.

Literaturverzeichnis

- [104] A. A. Beharry, G. A. Woolley, *Chem. Soc. Rev.* **2011**, *40*, 4422–4437.
- [105] W. Szymański, J. M. Beierle, H. A. V. Kistemaker, W. A. Velema, B. L. Feringa, *Chem. Rev.* **2013**, *113*, 6114–6178.
- [106] K. Hüll, J. Morstein, D. Trauner, *Chem. Rev.* **2018**, *118*, 10710–10747.
- [107] M. Schehr, C. Ianes, J. Weisner, L. Heintze, M. P. Müller, C. Pichlo, J. Charl, E. Brune, J. Ewert, M. Lehr, U. Baumann, D. Rauh, U. Knippschild, C. Peifer, R. Herges, *Photochemical & Photobiological Sciences* **2019**, *18*, 1398–1407.
- [108] L. Heintze, D. Schmidt, T. Rodat, L. Witt, J. Ewert, M. Kriegs, R. Herges, C. Peifer, *Int. J. Mol. Sci.* **2020**, *21*, 8961.
- [109] Z. Rappoport, *The Chemistry of Anilines, Part 1*, John Wiley & Sons **2007**.
- [110] R. Conrad, W. Seiler, *J. Atmos. Chem.* **1988**, *6*, 83–94.
- [111] A. Engel, H. W. Bange, M. Cunliffe, S. M. Burrows, G. Friedrichs, L. Galgani, H. Herrmann, N. Hertkorn, M. Johnson, P. S. Liss, P. K. Quinn, M. Schartau, A. Soloviev, C. Stolle, R. C. Upstill-Goddard, M. van Pinxteren, B. Zäncker, *Front. Mar. Sci.* **2017**, *4*.
- [112] O. Wurl, W. Ekau, W. M. Landing, C. J. Zappa, *Elem Sci Anth* **2017**, *5*, 31.
- [113] F. Haber, G. v. Oordt, *Zeitschrift für anorganische Chemie* **1905**, *44*, 341–378.
- [114] F. Haber, R. L. Rossignol, *Zeitschrift für Elektrochemie und angewandte physikalische Chemie* **1913**, *19*, 53–72.
- [115] H. S. Taylor, E. F. Armstrong, *Proceedings of the Royal Society of London. Series A, Containing Papers of a Mathematical and Physical Character* **1925**, *108*, 105–111.
- [116] F. Spausta, In F. Spausta, Hg., *Treibstoffe für Verbrennungsmotoren: Erster Band: Flüssige Treibstoffe und ihre Herstellung*. Springer, Vienna **1953**, 164–188.
- [117] J. Smidt, W. Hafner, R. Jira, J. Sedlmeier, R. Sieber, R. Rüttinger, H. Kojer, *Angew. Chem.* **1959**, *71*, 176–182.
- [118] G. N. Schrauzer, P. Glockner, S. Eichler, *Angew. Chem. Int. Ed.* **1964**, *3*, 185–191.
- [119] J. K. Stille, R. Divakaruni, *J. Organomet. Chem.* **1979**, *169*, 239–248.
- [120] P. W. Voorhees, *J. Stat. Phys.* **1985**, *38*, 231–252.
- [121] S. A. Beyramabadi, H. Eshtiagh-Hosseini, M. R. Housaindokht, A. Morsali, *Organometallics* **2008**, *27*, 72–79.

- [122] J. L. Casci, C. M. Lok, M. D. Shannon, *Catal. Today* **2009**, *145*, 38–44.
- [123] B. Baisch, D. Raffa, U. Jung, O. M. Magnussen, C. Nicolas, J. Lacour, J. Kubitschke, R. Herges, *J. Am. Chem. Soc.* **2009**, *131*, 442–443.
- [124] S. Kuhn, B. Baisch, U. Jung, T. Johannsen, J. Kubitschke, R. Herges, O. Magnussen, *Phys. Chem. Chem. Phys.* **2010**, *12*, 4481.
- [125] U. Jung, S. Kuhn, U. Cornelissen, F. Tuczek, T. Strunskus, V. Zaporojtchenko, J. Kubitschke, R. Herges, O. Magnussen, *Langmuir* **2011**, *27*, 5899–5908.
- [126] S. Kuhn, U. Jung, S. Ulrich, R. Herges, O. Magnussen, *Chem. Commun.* **2011**, *47*, 8880–8882.
- [127] M. Hammerich, T. Rusch, N. R. Krekiehn, A. Bloedorn, O. M. Magnussen, R. Herges, *ChemPhysChem* **2016**, *17*, 1870–1874.
- [128] T. Jasper-Tönnies, A. Garcia-Lekue, T. Frederiksen, S. Ulrich, R. Herges, R. Berndt, *Phys. Rev. Lett.* **2017**, *119*, 066801.
- [129] T. Jasper-Tönnies, I. Poltavsky, S. Ulrich, T. Moje, A. Tkatchenko, R. Herges, R. Berndt, *J. Chem. Phys.* **2018**, *149*, 244705.
- [130] T. Jasper-Tönnies, A. Garcia-Lekue, T. Frederiksen, S. Ulrich, R. Herges, R. Berndt, *J. Phys.: Condens. Matter* **2019**, *31*, 18LT01.
- [131] T. Jasper-Toennies, M. Gruber, S. Johannsen, T. Frederiksen, A. Garcia-Lekue, T. Jäkel, F. Roehricht, R. Herges, R. Berndt, *ACS Nano* **2020**, *14*, 3907–3916.
- [132] T. Jasper-Tönnies, M. Gruber, S. Ulrich, R. Herges, R. Berndt, *Angew. Chem. Int. Ed.* **2020**, *59*, 7008–7017.
- [133] A. Köhntopp, M. Dittner, F. Temps, *J. Phys. Chem. Lett.* **2016**, *7*, 1088–1095.
- [134] U. Jung, J. Kubitschke, R. Herges, O. Magnussen, *Electrochim. Acta* **2013**, *112*, 869–880.
- [135] S. Ulrich, U. Jung, T. Strunskus, C. Schütt, A. Bloedorn, S. Lemke, E. Ludwig, L. Kipp, F. Faupel, O. Magnussen, R. Herges, *Phys. Chem. Chem. Phys.* **2015**, *17*, 17053–17062.
- [136] T. R. Rusch, M. Hammerich, R. Herges, O. M. Magnussen, *Chem. Commun.* **2019**, *55*, 9511–9514.
- [137] U. Jung, C. Schütt, O. Filinova, J. Kubitschke, R. Herges, O. Magnussen, *J. Phys. Chem. C* **2012**, *116*, 25943–25948.

Literaturverzeichnis

- [138] H. Jacob, S. Ulrich, U. Jung, S. Lemke, T. Rusch, C. Schütt, F. Petersen, T. Strunskus, O. Magnussen, R. Herges, e. al, *Phys. Chem. Chem. Phys.* **2014**, *16*, 22643–22650.
- [139] A. Cembran, F. Bernardi, M. Garavelli, L. Gagliardi, G. Orlandi, *J. Am. Chem. Soc.* **2004**, *126*, 3234–3243.
- [140] M. Quick, A. L. Dobryakov, M. Gerecke, C. Richter, F. Berndt, I. N. Ioffe, A. A. Granovsky, R. Mahrwald, N. P. Ernsting, S. A. Kovalenko, *J. Phys. Chem. B* **2014**, *118*, 8756–8771.
- [141] J. Dokić, M. Gothe, J. Wirth, M. V. Peters, J. Schwarz, S. Hecht, P. Saalfrank, *J. Phys. Chem. A* **2009**, *113*, 6763–6773.
- [142] A. Muzdalov, *Dissertation*, Universität Potsdam **2017**.
- [143] D. L. Isac, A. Airinei, M. Homocianu, N. Fifere, C. Cojocaru, C. Hulubei, *J. Photochem. Photobiol., A* **2020**, *390*, 112300.
- [144] C. Schütt, *Dissertation*, Christian-Albrechts-Universität zu Kiel **2016**.
- [145] A. Franke, *Dissertation*, Christian-Albrechts-Universität zu Kiel **2010**.
- [146] N. Hauptmann, K. Scheil, T. G. Gopakumar, F. L. Otte, C. Schütt, R. Herges, R. Berndt, *J. Am. Chem. Soc.* **2013**, *135*, 8814–8817.
- [147] A. Schlimm, R. Löw, T. Rusch, F. Röhricht, T. Strunskus, T. Tellkamp, F. Sönnichsen, U. Manthe, O. Magnussen, F. Tuczek, R. Herges, *Angew. Chem. Int. Ed.* **2019**, *58*, 6574–6578.
- [148] M. J. Comstock, N. Levy, A. Kirakosian, J. Cho, F. Lauterwasser, J. H. Harvey, D. A. Strubbe, J. M. J. Fréchet, D. Trauner, S. G. Louie, M. F. Crommie, *Phys. Rev. Lett.* **2007**, *99*, 038301.
- [149] P. Tegeder, *J. Phys.: Condens. Matter* **2012**, *24*, 394001.
- [150] G. Floß, G. Granucci, P. Saalfrank, *J. Chem. Phys.* **2012**, *137*, 234701.
- [151] E. Benassi, G. Granucci, M. Persico, S. Corni, *J. Phys. Chem. C* **2015**, *119*, 5962–5974.
- [152] M. J. Comstock, N. Levy, J. Cho, L. Berbil-Bautista, M. F. Crommie, D. A. Poulsen, J. M. J. Fréchet, *Appl. Phys. Lett.* **2008**, *92*, 123107.
- [153] S. Hagen, P. Kate, F. Leyssner, D. Nandi, M. Wolf, P. Tegeder, *J. Chem. Phys.* **2008**, *129*, 164102.
- [154] M. Wolf, P. Tegeder, *Surf. Sci.* **2009**, *603*, 1506–1517.

- [155] R. Schmidt, S. Hagen, D. Brete, R. Carley, C. Gahl, J. Dokić, P. Saalfrank, S. Hecht, P. Tegeder, M. Weinelt, *Phys. Chem. Chem. Phys.* **2010**, *12*, 4488–4497.
- [156] F. Leyssner, S. Hagen, L. Óvári, J. Dokić, P. Saalfrank, M. V. Peters, S. Hecht, T. Klamroth, P. Tegeder, *J. Phys. Chem. C* **2010**, *114*, 1231–1239.
- [157] E. R. McNellis, G. Mercurio, S. Hagen, F. Leyssner, J. Meyer, S. Soubatch, M. Wolf, K. Reuter, P. Tegeder, F. S. Tautz, *Chem. Phys. Lett.* **2010**, *499*, 247–249.
- [158] S. D. Evans, S. R. Johnson, H. Ringsdorf, L. M. Williams, H. Wolf, *Langmuir* **1998**, *14*, 6436–6440.
- [159] M. Ito, T. Xin Wei, P.-L. Chen, H. Akiyama, M. Matsumoto, K. Tamada, Y. Yamamoto, *J. Mater. Chem.* **2005**, *15*, 478–483.
- [160] G. Pace, V. Ferri, C. Grave, M. Elbing, C. v. Hänisch, M. Zharnikov, M. Mayor, M. A. Rampi, P. Samorì, *PNAS* **2007**, *104*, 9937–9942.
- [161] A. S. Kumar, T. Ye, T. Takami, B.-C. Yu, A. K. Flatt, J. M. Tour, P. S. Weiss, *Nano Lett.* **2008**, *8*, 1644–1648.
- [162] S. Yasuda, T. Nakamura, M. Matsumoto, H. Shigekawa, *J. Am. Chem. Soc.* **2003**, *125*, 16430–16433.
- [163] H. Akiyama, K. Tamada, J. Nagasawa, K. Abe, T. Tamaki, *J. Phys. Chem. B* **2003**, *107*, 130–135.
- [164] K. Lee, F. Pan, G. T. Carroll, N. J. Turro, J. T. Koberstein, *Langmuir* **2004**, *20*, 1812–1818.
- [165] U. Jung, O. Filinova, S. Kuhn, D. Zargarani, C. Bornholdt, R. Herges, O. Magnussen, *Langmuir* **2010**, *26*, 13913–13923.
- [166] N. Heinemann, J. Grunau, T. Leißner, O. Andreyev, S. Kuhn, U. Jung, D. Zargarani, R. Herges, O. Magnussen, M. Bauer, *Chem. Phys.* **2012**, *402*, 22–28.
- [167] D. T. Valley, M. Onstott, S. Malyk, A. V. Benderskii, *Langmuir* **2013**, *29*, 11623–11631.
- [168] Y. Yao, J. M. Tour, *J. Org. Chem.* **1999**, *64*, 1968–1971.
- [169] D. Takamatsu, Y. Yamakoshi, K.-i. Fukui, *J. Phys. Chem. B* **2006**, *110*, 1968–1970.
- [170] T. Kitagawa, Y. Idomoto, H. Matsubara, D. Hobara, T. Kakiuchi, T. Okazaki, K. Komatsu, *J. Org. Chem.* **2006**, *71*, 1362–1369.
- [171] S. Wagner, F. Leyssner, C. Kördel, S. Zarwell, R. Schmidt, M. Weinelt, K. Rück-Braun, M. Wolf, P. Tegeder, *Phys. Chem. Chem. Phys.* **2009**, *11*, 6242–6248.

Literaturverzeichnis

- [172] X. Zheng, M. E. Mulcahy, D. Horinek, F. Galeotti, T. F. Magnera, J. Michl, *J. Am. Chem. Soc.* **2004**, *126*, 4540–4542.
- [173] G. London, G. T. Carroll, T. F. Landaluce, M. M. Pollard, P. Rudolf, B. L. Feringa, *Chem. Commun.* **2009**, *0*, 1712–1714.
- [174] G. T. Carroll, G. London, T. F. Landaluce, P. Rudolf, B. L. Feringa, *ACS Nano* **2011**, *5*, 622–630.
- [175] M. Valášek, M. Mayor, *Chemistry – A European Journal* **2017**, *23*.
- [176] C. J. Murphy, Z. C. Smith, A. Pronschinski, E. A. Lewis, M. L. Liriano, C. Wong, C. J. Ivimey, M. Duffy, W. Musial, A. J. Therrien, S. W. T. Iii, E. C. H. Sykes, *Phys. Chem. Chem. Phys.* **2015**, *17*, 31931–31937.
- [177] M. Hammerich, R. Herges, *J. Org. Chem.* **2015**, *80*, 11233–11236.
- [178] H. J. Dauben, J. D. Wilson, J. L. Laity, *J. Am. Chem. Soc.* **1969**, *91*, 1991–1998.
- [179] W. H. Flygare, *Chem. Rev.* **1974**, *74*, 653–687.
- [180] P. v. R. Schleyer, C. Maerker, A. Dransfeld, H. Jiao, N. J. R. van Eikema Hommes, *J. Am. Chem. Soc.* **1996**, *118*, 6317–6318.
- [181] A. Stanger, *J. Org. Chem.* **2006**, *71*, 883–893.
- [182] A. Stanger, G. Monaco, R. Zanasi, *ChemPhysChem* **2020**, *21*, 65–82.
- [183] J. Kruszewski, T. M. Krygowski, *Tetrahedron Lett.* **1972**, *13*, 3839–3842.
- [184] T. M. Krygowski, M. K. Cyrański, *Chem. Rev.* **2001**, *101*, 1385–1420.
- [185] A. Pasquarello, M. Schlüter, R. C. Haddon, *Science* **1992**, *257*, 1660–1661.
- [186] T. A. Keith, R. F. W. Bader, *Chem. Phys. Lett.* **1992**, *194*, 1–8.
- [187] T. A. Keith, R. F. W. Bader, *J. Chem. Phys.* **1993**, *99*, 3669–3682.
- [188] R. Zanasi, P. W. Fowler, *Chem. Phys. Lett.* **1995**, *238*, 270–280.
- [189] E. Steiner, P. W. Fowler, *Int. J. Quantum Chem.* **1996**, *60*, 609–616.
- [190] P. W. FOWLER, E. STEINER, I. CERNUSAK, *Mol. Phys.* **1997**, *91*, 401–412.
- [191] P. W. Fowler, R. Zanasi, B. Cadioli, E. Steiner, *Chem. Phys. Lett.* **1996**, *251*, 132–140.
- [192] B. R. ZANASI, P. LAZZERETTI, *Mol. Phys.* **1997**, *92*, 609–618.

- [193] P. W. Fowler, E. Steiner, B. Cadioli, R. Zanasi, *J. Phys. Chem. A* **1998**, *102*, 7297–7302.
- [194] A. Ligabue, U. Pincelli, P. Lazzeretti, R. Zanasi, *J. Am. Chem. Soc.* **1999**, *121*, 5513–5518.
- [195] S. Fias, P. W. Fowler, J. L. Delgado, U. Hahn, P. Bultinck, *Chemistry – A European Journal* **2008**, *14*, 3093–3099.
- [196] E.-U. Wallenborn, R. F. Haldimann, F.-G. Klärner, F. Diederich, *Chemistry – A European Journal* **1998**, *4*, 2258–2265.
- [197] R. Herges, D. Geuenich, *J. Phys. Chem. A* **2001**, *105*, 3214–3220.
- [198] D. Geuenich, K. Hess, F. Köhler, R. Herges, *Chem. Rev.* **2005**, *105*, 3758–3772.
- [199] D. Weiß, E. Täuscher, H. Brandl, *Chem. unserer Zeit* **2019**, *53*, 12–21.
- [200] R. Herges, *Nachr. Chem.* **2011**, *59*, 817–821.
- [201] S. Venkataramani, U. Jana, M. Dommaschk, F. D. Sönnichsen, F. Tuczek, R. Herges, *Science* **2011**, *331*, 445–448.
- [202] M. Dommaschk, F. Gutzeit, S. Boretius, R. Haag, R. Herges, *Chem. Commun.* **2014**, *50*, 12476–12478.
- [203] M. Dommaschk, V. Thoms, C. Schütt, C. Näther, R. Puttreddy, K. Rissanen, R. Herges, *Inorg. Chem.* **2015**, *54*, 9390–9392.
- [204] M. Dommaschk, M. Peters, F. Gutzeit, C. Schütt, C. Näther, F. D. Sönnichsen, S. Tiwari, C. Riedel, S. Boretius, R. Herges, *J. Am. Chem. Soc.* **2015**, *137*, 7552–7555.
- [205] G. Heitmann, C. Schütt, J. Gröbner, L. Huber, R. Herges, *Dalton Trans.* **2016**, *45*, 11407–11412.
- [206] J. Ludwig, J. Gröbner, M. Dommaschk, L. M. Huber, M. K. Peters, J.-B. Hövener, R. Herges, *J. Porphyrins Phthalocyanines* **2019**, *24*, 480–488.
- [207] J. Ludwig, T. Moje, F. Röhricht, R. Herges, *Beilstein Arch.* **2020**, *2020*, 96.
- [208] R. Bonnett, *Chem. Soc. Rev.* **1995**, *24*, 19–33.
- [209] E. D. Sternberg, D. Dolphin, C. Brückner, *Tetrahedron* **1998**, *54*, 4151–4202.
- [210] O. Mazor, A. Brandis, V. Plaks, E. Neumark, V. Rosenbach-Belkin, Y. Salomon, A. Scherz, *Photochem. Photobiol.* **2005**, *81*, 342–351.
- [211] H. Brandl, E. Täuscher, D. Weiß, *Chem. unserer Zeit* **2016**, *50*, 130–139.

Literaturverzeichnis

- [212] A. Hirth, U. Michelsen, D. Wöhrle, *Chem. unserer Zeit* **1999**, *33*, 84–94.
- [213] L. B. Josefsen, R. W. Boyle, Photodynamic Therapy and the Development of Metal-Based Photosensitisers **2008**, URL <https://www.hindawi.com/journals/mbd/2008/276109/>.
- [214] J. L. Sessler, D. Seidel, *Angew. Chem.* **2003**, *115*, 5292–5333.
- [215] G. Sedghi, V. M. García-Suárez, L. J. Esdaile, H. L. Anderson, C. J. Lambert, S. Martín, D. Bethell, S. J. Higgins, M. Elliott, N. Bennett, J. E. Macdonald, R. J. Nichols, *Nat. Nanotechnol.* **2011**, *6*, 517–523.
- [216] M. Rehahn, *Chem. unserer Zeit* **2003**, *37*, 18–30.
- [217] M. U. Winters, E. Dahlstedt, H. E. Blades, C. J. Wilson, M. J. Frampton, H. L. Anderson, B. Albinsson, *J. Am. Chem. Soc.* **2007**, *129*, 4291–4297.
- [218] G. Sedghi, L. J. Esdaile, H. L. Anderson, S. Martin, D. Bethell, S. J. Higgins, R. J. Nichols, *Adv. Mater.* **2012**, *24*, 653–657.
- [219] M. Noori, A. C. Aragonès, G. Di Palma, N. Darwish, S. W. D. Bailey, Q. Al-Galiby, I. Grace, D. B. Amabilino, A. González-Campo, I. Díez-Pérez, C. J. Lambert, *Sci. Rep.* **2016**, *6*, 37352.
- [220] A. C. Aragonès, A. Martín-Rodríguez, D. Aravena, J. Puigmartí-Luis, D. B. Amabilino, N. Aliaga-Alcalde, A. González-Campo, E. Ruiz, I. Díez-Pérez, *Angew. Chem. Int. Ed.* **2020**, *59*, 19193–19201.
- [221] J. Sukegawa, C. Schubert, X. Zhu, H. Tsuji, D. M. Guldi, E. Nakamura, *Nat. Chem.* **2014**, *6*, 899–905.
- [222] L.-L. Li, E. Wei-Guang Diau, *Chem. Soc. Rev.* **2013**, *42*, 291–304.
- [223] A. J. Esswein, D. G. Nocera, *Chem. Rev.* **2007**, *107*, 4022–4047.
- [224] D. Gust, T. A. Moore, A. L. Moore, *Acc. Chem. Res.* **2009**, *42*, 1890–1898.
- [225] L. Moretti, B. Kudisch, Y. Terazono, A. L. Moore, T. A. Moore, D. Gust, G. Cerullo, G. D. Scholes, M. Maiuri, *J. Phys. Chem. Lett.* **2020**, *11*, 3443–3450.
- [226] K. König, *J. Microsc.* **2000**, *200*, 83–104.
- [227] D. Holten, D. F. Bocian, J. S. Lindsey, *Acc. Chem. Res.* **2002**, *35*, 57–69.
- [228] M. Gouterman, *J. Mol. Spectrosc.* **1961**, *6*, 138–163.

- [229] M. Taniguchi, J. S. Lindsey, *Chem. Rev.* **2017**, *117*, 344–535.
- [230] A. M. G. Silva, A. C. Tomé, M. G. P. M. S. Neves, A. M. S. Silva, J. A. S. Cavaleiro, *J. Org. Chem.* **2002**, *67*, 726–732.
- [231] A. M. G. Silva, A. C. Tomé, M. G. P. M. S. Neves, A. M. S. Silva, J. A. S. Cavaleiro, *J. Org. Chem.* **2005**, *70*, 2306–2314.
- [232] X. Liu, C. Li, X. Peng, Y. Zhou, Z. Zeng, Y. Li, T. Zhang, B. Zhang, Y. Dong, D. Sun, P. Cheng, Y. Feng, *Dyes Pigm.* **2013**, *98*, 181–189.
- [233] A. C. Tomé, P. S. S. Lacerda, M. G. P. M. S. Neves, J. A. S. Cavaleiro, *Chem. Commun.* **1997**, *0*, 1199–1200.
- [234] K. Matsumoto, S. Kimura, *Heterocycl. Commun.* **2000**, *6*, 31–34.
- [235] A. M. G. Silva, J. A. S. Cavaleiro, In G. W. Gribble, J. A. Joule, Hg., *Progress in Heterocyclic Chemistry*, Bd. 19. Elsevier **2008**, 44–69.
- [236] A. Sobanski, R. Schmieder, F. Vögtle, *Chem. unserer Zeit* **2000**, *34*, 160–169.
- [237] H. L. Frisch, E. Wasserman **1961**, *7*.
- [238] D. M. Walba, *Tetrahedron* **1985**, *41*, 3161–3212.
- [239] J.-C. Chambron, D. K. Mitchell, *J. Chem. Educ.* **1995**, *72*, 1059.
- [240] E. E. Fenlon, *Eur. J. Org. Chem.* **2008**, *2008*, 5023–5035.
- [241] K. Klenin, J. Langowski, *Biopolymers* **2000**, *54*, 307–317.
- [242] G. Călugăreanu, *Czechoslovak Mathematical Journal* **1961**, *11*, 588–625.
- [243] F. H. Crick, *Proceedings of the National Academy of Sciences* **1976**, *73*, 2639–2643.
- [244] F. B. Fuller, *PNAS* **1971**, *68*, 815–819.
- [245] F. B. Fuller, *PNAS* **1978**, *75*, 3557–3561.
- [246] E. Heilbronner, *Tetrahedron Lett.* **1964**, *5*, 1923–1928.
- [247] E. Hückel, *Z. Physik* **1931**, *70*, 204–286.
- [248] E. Hückel, *Z. Physik* **1932**, *76*, 628–648.
- [249] D. Ajami, O. Oeckler, A. Simon, R. Herges, *Nature* **2003**, *426*, 819–821.
- [250] O. Wennerstroem, *Macromolecules* **1985**, *18*, 1977–1980.

Literaturverzeichnis

- [251] J. J. S. Lamba, J. M. Tour, *J. Am. Chem. Soc.* **1994**, *116*, 11723–11736.
- [252] J. D. Stenger-Smith, P. Zarras, R. A. Hollins, A. P. Chafin, L. H. Merwin, R. Yee, G. A. Lindsay, W. N. Herman, R. F. Gratz, E. G. Nickel, *J. Polym. Sci., Part A: Polym. Chem.* **2000**, *38*, 2824–2839.
- [253] B. J. Schwartz, *Annu. Rev. Phys. Chem.* **2003**, *54*, 141–172.
- [254] P.-O. Morin, T. Bura, M. Leclerc, *Mater. Horiz.* **2015**, *3*, 11–20.
- [255] Y. J. Wang, G. Yu, *J. Polym. Sci., Part B: Polym. Phys.* **2019**, *57*, 1557–1558.
- [256] H. Bronstein, C. B. Nielsen, B. C. Schroeder, I. McCulloch, *Nature Reviews Chemistry* **2020**, *4*, 66–77.
- [257] A. J. Berresheim, M. Müller, K. Müllen, *Chem. Rev.* **1999**, *99*, 1747–1786.
- [258] J. Wu, A. C. Grimsdale, K. Müllen, *J. Mater. Chem.* **2005**, *15*, 41–52.
- [259] A. E. Keirstead, J. W. Bridgewater, Y. Terazono, G. Kodis, S. Straight, P. A. Liddell, A. L. Moore, T. A. Moore, D. Gust, *J. Am. Chem. Soc.* **2010**, *132*, 6588–6595.
- [260] S. R. Waldvogel, A. R. Wartini, P. H. Rasmussen, J. Rebek, *Tetrahedron Lett.* **1999**, *40*, 3515–3518.
- [261] Y. Geng, A. Fechtenkötter, K. Müllen, *J. Mater. Chem.* **2001**, *11*, 1634–1641.
- [262] S. Watanabe, J. Kido, *Chem. Lett.* **2007**, *36*, 590–591.
- [263] X. Sun, X. Xu, W. Qiu, G. Yu, H. Zhang, X. Gao, S. Chen, Y. Song, Y. Liu, *J. Mater. Chem.* **2008**, *18*, 2709–2715.
- [264] Y. Zou, T. Ye, D. Ma, J. Qin, C. Yang, *J. Mater. Chem.* **2012**, *22*, 23485–23491.
- [265] N. Ito, T. Kamata, H. Sasabe, M. Igarashi, J. Kido, *SID Symposium Digest of Technical Papers* **2019**, *50*, 1889–1890.
- [266] T. Kamata, H. Sasabe, N. Ito, Y. Sukegawa, A. Arai, T. Chiba, D. Yokoyama, J. Kido, *J. Mater. Chem. C* **2020**, *8*, 7200–7210.
- [267] V. Balzani, M. Clemente-León, A. Credi, J. N. Lowe, J. D. Badjić, J. F. Stoddart, D. J. Williams, *Chemistry – A European Journal* **2003**, *9*, 5348–5360.
- [268] J. D. Badjić, V. Balzani, A. Credi, J. N. Lowe, S. Silvi, J. F. Stoddart, *Chemistry – A European Journal* **2004**, *10*, 1926–1935.

- [269] E. M. Larson, R. B. Von Dreele, P. Hanson, J. D. Gust, *Acta Cryst C* **1990**, *46*, 784–788.
- [270] A. Bondi, *J. Phys. Chem.* **1964**, *68*, 441–451.
- [271] S. Alvarez, *Dalton Trans.* **2013**, *42*, 8617–8636.
- [272] T. Kosaka, Y. Inoue, T. Mori, *J. Phys. Chem. Lett.* **2016**, *7*, 783–788.
- [273] C. Lambert, *Angew. Chem. Int. Ed.* **2005**, *44*, 7337–7339.
- [274] V. J. Chebny, R. Shukla, R. Rathore, *J. Phys. Chem. A* **2006**, *110*, 13003–13006.
- [275] T. Kosaka, S. Iwai, Y. Inoue, T. Moriuchi, T. Mori, *J. Phys. Chem. A* **2018**, *122*, 7455–7463.
- [276] S. V. Rosokha, I. S. Neretin, D. Sun, J. K. Kochi, *J. Am. Chem. Soc.* **2006**, *128*, 9394–9407.
- [277] C. Rios, R. Salcedo, *Molecules* **2014**, *19*, 3274–3296.
- [278] K. Yoshida, I. Morimoto, K. Mitsudo, H. Tanaka, *Tetrahedron Lett.* **2008**, *49*, 2363–2365.
- [279] V. Vij, V. Bhalla, M. Kumar, *Chem. Rev.* **2016**, *116*, 9565–9627.
- [280] S. A. Chen, M. Y. Hua, *Macromolecules* **1993**, *26*, 7108–7110.
- [281] S. J. Higgins, *Chem. Soc. Rev.* **1997**, *26*, 247–257.
- [282] C. Bounioux, E. A. Katz, R. Y. Rozen, *Polym. Adv. Technol.* **2012**, *23*, 1129–1140.
- [283] H. Huang, N. Zhou, R. P. Ortiz, Z. Chen, S. Loser, S. Zhang, X. Guo, J. Casado, J. T. L. Navarrete, X. Yu, A. Facchetti, T. J. Marks, *Adv. Funct. Mater.* **2014**, *24*, 2782–2793.
- [284] Z. Deng, T. Ai, R. Li, W. Yuan, K. Zhang, H. Du, H. Zhang, *Polymers* **2019**, *11*, 1683.
- [285] A. Brzeczek, K. Piwowar, W. Domagala, M. M. Mikołajczyk, K. Walczak, P. Wagner, *RSC Adv.* **2016**, *6*, 36500–36509.
- [286] S. Tsumura, K. Ohira, K. Hashimoto, K. Imato, Y. Ooyama, *Mater. Chem. Front.* **2020**, *4*, 2762–2771.
- [287] W. W. Paudler, A. G. Zeiler, *J. Org. Chem.* **1969**, *34*, 3237–3239.
- [288] D. K. Joshi, M. J. Mitchell, D. Bruce, A. J. Lough, H. Yan, *Tetrahedron* **2012**, *68*, 8670–8676.
- [289] S. Samanta, C. Qin, A. J. Lough, G. A. Woolley, *Angew. Chem. Int. Ed.* **2012**, *51*, 6452–6455.

Literaturverzeichnis

- [290] F. Eljabu, J. Dhruval, H. Yan, *Bioorg. Med. Chem. Lett.* **2015**, *25*, 5594–5596.
- [291] P. Lentes, E. Stadler, F. Röhricht, A. Brahms, J. Gröbner, F. D. Sönnichsen, G. Gescheidt, R. Herges, *J. Am. Chem. Soc.* **2019**, *141*, 13592–13600.
- [292] R. Ruel, P. Lacombe, M. Abramovitz, C. Godbout, S. Lamontagne, C. Rochette, N. Sawyer, R. Stocco, N. M. Tremblay, K. M. Metters, M. Labelle, *Bioorg. Med. Chem. Lett.* **1999**, *9*, 2699–2704.
- [293] B. Biesczad, A. Siwek, M. Wilczek, D. Trzybiński, K. Woźniak, G. Satała, A. J. Bojarski, A. Mieczkowski, *Bioorg. Med. Chem. Lett.* **2020**, *30*, 127493.
- [294] W. Moormann, T. Tellkamp, E. Stadler, F. Röhricht, C. Näther, R. Puttreddy, K. Rissanen, G. Gescheidt, R. Herges, *Angew. Chem. Int. Ed.* **2020**, *n/a*.
- [295] J. Kubitschke, *Dissertation*, Christian-Albrechts-Universität zu Kiel **2010**.
- [296] J. Kubitschke, C. Näther, R. Herges, *Eur. J. Org. Chem.* **2010**, *2010*, 5041–5055.
- [297] F. L. Otte, S. Lemke, C. Schütt, N. R. Krekiehn, U. Jung, O. M. Magnussen, R. Herges, *J. Am. Chem. Soc.* **2014**, *136*, 11248–11251.
- [298] Z. Wei, X. Wang, A. Borges, M. Santella, T. Li, J. K. Sørensen, M. Vanin, W. Hu, Y. Liu, J. Ulstrup, G. C. Solomon, Q. Chi, T. Bjørnholm, K. Nørgaard, B. W. Laursen, *Langmuir* **2014**, *30*, 14868–14876.
- [299] M. Hammerich, *Dissertation*, Christian-Albrechts-Universität zu Kiel **2016**.
- [300] T. R. Rusch, A. Schlimm, N. R. Krekiehn, B. M. Flöser, F. Röhricht, M. Hammerich, I. Lautenschläger, T. Strunkus, R. Herges, F. Tuczak, O. M. Magnussen, *J. Phys. Chem. C* **2019**, *123*, 13720–13730.
- [301] R. Löw, T. Rusch, F. Röhricht, O. Magnussen, R. Herges, *Beilstein J. Org. Chem.* **2019**, *15*, 1485–1490.
- [302] R. Löw, T. Rusch, T. Moje, F. Röhricht, O. M. Magnussen, R. Herges, *Beilstein J. Org. Chem.* **2019**, *15*, 1815–1821.
- [303] R. Herges, In *The Chemical Bond*. John Wiley & Sons, Ltd **2014**, 383–420.
- [304] S. Furukawa, M. Fujita, Y. Kanatomi, M. Minoura, M. Hatanaka, K. Morokuma, K. Ishimura, M. Saito, *Communications Chemistry* **2018**, *1*, 1–7.
- [305] Z. Li, T. Y. Gopalakrishna, Y. Han, Y. Gu, L. Yuan, W. Zeng, D. Casanova, J. Wu, *J. Am. Chem. Soc.* **2019**, *141*, 16266–16270.

- [306] J. Lin, L. Ding, Q. Zhuo, H. Zhang, H. Xia, *Organometallics* **2019**, *38*, 2264–2271.
- [307] X. Jiang, S. D. Laffoon, D. Chen, S. Pérez-Estrada, A. S. Danis, J. Rodríguez-López, M. A. Garcia-Garibay, J. Zhu, J. S. Moore, *J. Am. Chem. Soc.* **2020**, *142*, 6493–6498.
- [308] P. J. Mayer, O. El Bakouri, T. Holczbauer, G. F. Samu, C. Janáky, H. Ottosson, G. London, *J. Org. Chem.* **2020**, *85*, 5158–5172.
- [309] Z. Liu, T. Lu, S. Hua, Y. Yu, *J. Phys. Chem. C* **2019**, *123*, 18593–18599.
- [310] S. Nishigaki, Y. Shibata, A. Nakajima, H. Okajima, Y. Masumoto, T. Osawa, A. Muranaka, H. Sugiyama, A. Horikawa, H. Uekusa, H. Koshino, M. Uchiyama, A. Sakamoto, K. Tanaka, *J. Am. Chem. Soc.* **2019**, *141*, 14955–14960.
- [311] G. Naulet, L. Sturm, A. Robert, P. Dechambenoit, F. Röhricht, R. Herges, H. Bock, F. Durola, *Chem. Sci.* **2018**, *9*, 8930–8936.
- [312] G. R. Schaller, R. Herges, *Chem. Commun.* **2013**, *49*, 1254–1260.
- [313] P. W. Fowler, H. S. Rzepa, *Phys. Chem. Chem. Phys.* **2006**, *8*, 1775–1777.
- [314] S. Pelloni, A. Ligabue, P. Lazzeretti, *Org. Lett.* **2004**, *6*, 4451–4454.
- [315] C. E. Johnson, F. A. Bovey, *J. Chem. Phys.* **1958**, *29*, 1012–1014.
- [316] J. S. Waugh, R. W. Fessenden, *J. Am. Chem. Soc.* **1957**, *79*, 846–849.
- [317] H. A. Wegner, *Angew. Chem. Int. Ed.* **2017**, *56*, 10995–10996.
- [318] X. Lu, J. Wu, *Chem* **2017**, *2*, 619–620.
- [319] F. H. Kohnke, A. M. Z. Slawin, J. F. Stoddart, D. J. Williams, *Angew. Chem. Int. Ed.* **1987**, *26*, 892–894.
- [320] H. S. Choi, K. S. Kim, *Angew. Chem. Int. Ed.* **1999**, *38*, 2256–2258.
- [321] J. R. Dias, *Mol. Phys.* **2018**, *116*, 423–448.
- [322] S. Bhowmik, M. Kosa, A. Mizrahi, N. Fridman, M. Saphier, A. Stanger, Z. Gross, *Inorg. Chem.* **2017**, *56*, 2287–2296.
- [323] M. K. Peters, F. Röhricht, C. Näther, R. Herges, *Org. Lett.* **2018**, *20*, 7879–7883.
- [324] S. Grimme, J. Antony, S. Ehrlich, H. Krieg, *J. Chem. Phys.* **2010**, *132*, 154104.
- [325] S. Grimme, *WIREs Comput. Mol. Sci.* **2011**, *1*, 211–228.

Literaturverzeichnis

- [326] E. J. Meijer, M. Sprik, *J. Chem. Phys.* **1996**, *105*, 8684–8689.
- [327] S. M. Cybulski, C. E. Seversen, *J. Chem. Phys.* **2004**, *122*, 014117.
- [328] Y. Tanaka, T. Koike, M. Akita, *Chem. Commun.* **2010**, *46*, 4529–4531.
- [329] T. D. Leitner, Y. Gmeinder, F. Röhricht, R. Herges, E. Mena-Osteritz, P. Bäuerle, *Eur. J. Org. Chem.* **2020**, *2020*, 285–294.
- [330] J. J. Piet, H. A. M. Biemans, J. M. Warman, E. W. Meijer, *Chem. Phys. Lett.* **1998**, *289*, 13–18.